

Gluonic Profile and Confining String in Static Mesons and Baryons at Finite Temperature

Ahmed Saad El Bakry Mahmoud

**Centre for the Subatomic Structure of Matter
School of Chemistry & Physics
University of Adelaide**

Contents

Statement of originality	11
Dedication	12
Abstract	13
1 Quantum Chromodynamics	14
2 Lattice Gauge Theory	20
2.1 Outline	20
2.2 Introduction	20
2.3 Path integral formulation	20
2.4 Gauge field	21
2.5 Fermion field	22
2.6 Correlation functions	24
2.7 Continuum limit	25
2.8 Quenched approximation	27
2.9 Numerical simulation errors	27
2.10 Markov chain	28
2.11 Metropolis algorithm	29
2.12 Hybrid heat bath/Overrelaxation	30
2.12.1 Heat-bath algorithm	30
2.12.2 Overrelaxation	34
3 Systematic Uncertainties in Wilson-loop	35
3.1 Outline	35
3.2 Introduction	35
3.3 Flux distribution calculation	35
3.4 Source-shape dependence	36
3.5 Stringless operators	40
3.6 Lattice QCD at finite temperature	45
3.7 Conclusion	48
4 Bosonic String Model	49
4.1 Outline	49
4.2 Introduction	49
4.3 Mesonic string	51
4.3.1 Quark-antiquark potential	51

4.3.2	Width of the string	52
4.4	The Baryonic string picture	54
4.4.1	Width of the junction	57
4.5	Summary and Conclusion	64
5	Noise Reduction in Loop Correlators	65
5.1	Outline	65
5.2	Four-dimensional smearing of the gauge field	65
5.2.1	Smearing and cooling	66
5.2.2	Smearing radius	66
5.2.3	Calibration of smearing algorithms	68
5.2.4	Quark–antiquark potential	68
5.3	Link integration	74
5.4	Multi-level algorithm	77
5.5	Conclusion	78
6	Gluonic Profile of Static Mesons	80
6.1	Outline	80
6.2	Introduction	80
6.3	Colour field measurements	82
6.4	Action density	82
6.4.1	Tube profile (qualitative picture)	82
6.4.2	Tube growth in width	92
6.5	Conclusion	94
7	Bosonic Strings and the UV Filtering of QCD	96
7.1	Outline	96
7.2	Introduction	96
7.3	Quark–antiquark potential	98
7.4	The Gluonic profile	101
7.5	Conclusion	107
8	On The Ground State of Yang-Mills Theory	109
8.1	Outline	109
8.2	Introduction	109
8.3	Wilson loop operator	111
8.4	Numerical results and discussions	114
8.5	Conclusion	119
9	Gluonic Profile of Static Baryons	121
9.1	Outline	121
9.2	Introduction	122
9.3	Measurements	124
9.4	Statistics	124
9.5	Forces in the static baryon	125
9.6	Action Density	129
9.6.1	Flux iso-surface profile	129
9.6.2	Flux radius profile	139

9.6.3	Flux amplitude profile	142
9.6.4	The broadening of the flux width	144
9.6.5	Planes aspect ratio	147
9.7	Delocalization of the junction	149
9.8	Conclusion	154
10	Summary and Conclusion	157
A	Transition Form Factors	161
A.1	Introduction	161
A.2	The Vector-current-Hadron vertex function	161
A.2.1	Transition form factors	165
A.2.2	The ratio method	167
	Bibliography	169

NOTE: Pagination of the digital copy does not correspond with the pagination of the print copy.

List of Figures

3.1	The three-quark Wilson loop operator.	36
3.2	Spatial points [1] where vacuum field fluctuations are maximally suppressed in the three-quark system as measured by the correlation function $C(\vec{y})$.	37
3.3	The rendered gluonic field distribution via Eq. (3.3.3) mimics the form of the spatial link configurations in Wilson loop [2].	37
3.4	The ground-state overlap of the 3Q system [3]. $C_0 = \langle W_{3Q}(T) \rangle^{T+1} / \langle W_{3Q}(T+1) \rangle^T$, with the smeared link (upper data) and unsmeared link (lower data) [3]. The horizontal axis has been taken as L_{min} , with the minimal length of the flux tubes linking the three quarks. For each 3Q configuration C_0 is largely enhanced as $0.8 < C_0 < 1$ by smearing.	39
3.5	The static mesonic state is constructed via two Polyakov loops winding around the time in opposite directions.	43
3.6	(a) Average Polyakov loop over several successive Monte Carlo measurements [4], below the transition temperature (in the confined phase), (b) above the transition temperature.	44
3.7	$g\langle\bar{q}\sigma_{\mu\nu}G_{\mu\nu}q\rangle$ plotted against temperature T from Ref. [5]. The vertical dashed line denotes the critical temperature $T_c = 280$ MeV in quenched QCD.	47
4.1	The mean-square width, Eq. (4.3.17), of the flux tube evaluated at all planes ξ_1 perpendicular to the quark-antiquark line. The separation distance between the pair is $R a^{-1} = 10$.	54
4.2	Fluctuating flux tubes of three static color sources Q. The junction position ϕ is measured relative to the classical location which minimizes the total strings length (Fermat point).	55
4.3	World sheet spanned by one of the strings during time evolution up to the junction.	56
4.4	The world sheets of the strings in a baryon and a meson. The string in the static meson is modelled as being composed of two strings connected by a junction in the middle.	60
4.5	The Δ and Y baryonic strings configurations. The delocalization of the junction in the Y-shaped string system trace a filled Δ shaped energy distribution with maximal effect at the junction of the system. The Δ string configuration implies an energy distribution of maximum effect at the edges.	62

5.1 (a) Plot of the logarithm of the average value of $n(\rho = 0.06)/n(\rho)$ versus $\ln(\rho/0.06)$. The line corresponds to a fit to a straight line passing through the origin.	69
5.2 The quark–antiquark potential measured at each depicted smearing level. The lines correspond to fits of the potential obtained from the string picture of Eq. (4.3.7) for each data set as described in the text. The upper plot is at $T = 0.8 T_c$ while the lower plot is at $T = 0.9 T_c$	71
5.3 The $q\bar{q}$ force measured for all the smearing levels up to a distance of 1.4 fm. The temperature is $T = 0.8 T_c$, and $\beta = 6$. The line denotes the force as predicted by the string model at finite temperature, Eq. (4.3.7).	72
5.4 The diameter of smearing $2 R_s$ versus the number of sweeps n_s for the improved stout-link algorithm with $\rho = 0.06$ as in Eq. (5.2.9).	73
5.5 The Polyakov loop correlators measured using the heatbath integration (above), and fast link integration (below).	75
6.1 The flux-distribution $\bar{\mathcal{C}}(\vec{\rho}, \vec{r}_1, \vec{r}_2)$ as given by the characterization Eq. (6.3.3) in the plane of the quark–antiquark pair $\vec{\rho}(x, y, z = z_0)$, for separation distances R (a) 0.5 fm, (b) 0.6 fm, to (d) 0.8 fm at $T = 0.8 T_c$. The spheres refer to the positions of the quark and antiquark.	83
6.2 The flux-contour-line distribution in the plane of the quark–antiquark pair z_0 , for separation distances of (a) 0.9 fm, (b) 1.0 fm. The spheres denote the positions of the $q\bar{q}$ pair, $T = 0.9 T_c$	85
6.3 The flux iso-surface passing through the quarks, plotted together with a surface plot for the density distribution in the $q\bar{q}$ plane (inverted). The measurements are taken on 80 sweeps of smearing for separation distance $R = 9 a$, and $T = 0.8 T_c$. The lattice spatial extent is 36^3 at $\beta = 6$, $a = 0.1$ fm.	86
6.4 The density distribution $\mathcal{C}(\vec{\rho})$ for separation distance of $R = 12 a$, $T = 0.9 T_c$, plotted for the transverse planes $x = 1$, $x = 3$, and $x = 6$. The lines correspond to the Gaussian fits to the density in each plane $\vec{\rho}(x_i, y, z_0)$	87
6.5 The width difference $\delta W^2 = W^2(x_i) - W^2(x_0)$ for $q\bar{q}$ separations (a) 0.7 fm, (b) 0.8 fm, (c) 0.9 fm, and (d) 1 fm, $\beta = 6$, $T = 0.9 T_c$ for each depicted smearing level. The line denotes the width difference δW^2 as predicted by the string model Eq. (4.3.17). The lowest smearing level provides the best estimate of the width difference.	89
6.6 Similar to Fig. 6.5, the change in width is plotted for $q\bar{q}$ separations (a) 1.1 fm, (b) 1.2 fm, (c) 1.3 fm, and (d) 1.4 fm.	90
6.7 The width $W^2(x_i)$ for $q\bar{q}$ separations $R = 6 a$ to $R = 13 a$ at four consecutive planes (a) $x = 1$, (b) $x = 2$, (c) $x = 3$, and (d) $x = 4$. $\beta = 6$, $T = 0.9 T_c$. The line denotes the string model, Eq. (4.3.17), fit of R_0 to the data as described in the text.	93

7.1	(a) The temporal link U_4 is updated based on the neighboring links. The shaded area represents the 3D spatial smeared lattice. The heat bath starts from links of a low action configuration. The overrelaxation or reflection steps starts updates the time links based on action minimal	99
7.2	(a) The quark–antiquark potential measured at each depicted smearing level for 3 dimensional smearing (above) and 4 dimensional smearing (below). The lines correspond to the string picture predictions of Eq. (4.3.8). The standard value of the string tension is used.	100
7.3	Plot of the density distribution $\mathcal{C}(\vec{\rho})$ in the middle plane for source separation $R = 9a$, $T = 0.9T_c$	102
7.4	The mean square width of the flux tube $W_n^2(R/2)$ in the middle plane between the quarks. The lattice data, corresponding to the action density minimization, approach the string model predictions at short distances. At large distances the predicted linear divergence of the flux tube width is manifest in lattice data.	103
7.5	The normalized width of the flux tube $W_n^2(x_i)$ versus $q\bar{q}$ separations measured in the planes (a) $x = 2$, (b) $x = 3$, (c) $x = 4$. $\beta = 6$, $T = 0.9T_c$. The coordinates x_i are lattice coordinates (lattice units) and are measured from the quark position $x = 0$. The line denotes the one parameter string model, Eq. (7.4.1), fit to lattice data for $R \geq 1$ fm. The numbers in the legend denote the number of smearing sweeps.	104
7.6	The normalized width of the flux tube $W_n^2(x_i)$ versus $q\bar{q}$ separations measured in the plane $x = 3$. The temporal links have not been smeared in the evaluation of Polyakov loops, rather the temporal links have been integrated out. This time, the Polyakov loops are taken from the unsmeared configurations and correlated with the smeared action density. The legend denotes the number of smearing sweeps of the QCD vacuum.	105
7.7	The change of the tube’s width $\delta W^2 = W^2(x_i) - W^2(x_0)$ measured from the central plane for the depicted $q\bar{q}$ separations. The smearing level of the lattice data is illustrated. $\beta = 6$, $T = 0.9T_c$. The line denotes the width difference δW^2 as predicted by the string model Eq. (7.4.1).	106
7.8	The measured change in the ultraviolet cutoff R_0 along the flux tube normalized by a factor $(\pi\sigma)^{-1}$	107
8.1	Schematic representation of link-blocking	112
8.2	Schematic representation of smearing the spatial links in the Wilson loop. Each spatial link $U_\mu(x)$, $\mu \neq 4$ is smeared with the operators $(S^n)U$. The temporal links are left unsmeared. While not indicated in the figure, the links U^\dagger at the top of the figure are also smeared.	113
8.3	Schematic diagram of the smearing profile. h is the minimum number of smearing sweeps applied at the last link giving rise to smearing radius L_1 . n is the maximum number of smearing sweeps in the middle resulting in the radius L_2	113

- 8.4 The overlap with the ground state C_0 , the distance between the quark anti-quark source is $R = 10 a$, $\beta = 6$ 115
- 8.5 The overlap with the ground state C_0 , for $R = 1$ fm. The lines connect the states corresponding to variation of the ellipse semi-major axis for each rectangular base corresponding to sweeps $h = 15$ and $h = 18$. . . 116
- 8.6 Comparison between non-uniformly smeared profiles $n \neq h$ and flat states $n = h$ represented by the smooth line. The quark source separation distance $R = 1.0$ fm. 117
- 8.7 The flux tube operator Eq. (8.3.8). Each operator consists of a family of five Gaussians. The operators correspond to the states $(h = 13, n = 34)$, $(h = 15, n = 32)$, $(h = 20, n = 34)$ and $(h = 24, n = 33)$. These states maximize the value of the overlap with the ground state. The source separation distance $R = 1.0$ fm. 117
- 8.8 Same as Fig. 8.6, for quark-antiquark separation distance $R = 1.2$ fm. 118
- 8.9 The overlap with the ground state C_0 versus the physical width of the flux-tube operator in the middle L_2 of the tube. Each line corresponds to a fixed ratio between the width of the tube in the middle and at the last link L_1 . The quark-antiquark separation distance of $R = 1.2$ fm is considered here. 118
- 9.1 Schematic diagram for the isosceles configuration of the 3Q system. The large spheres represent the motion of the diffused field of characteristic smearing radius of R_s centred at the quarks (small spheres). 126
- 9.2 The force for the isosceles 3Q configurations with base lengths (a) $A = 0.6$ fm, (b) $A = 0.8$ fm and (c) $A = 1.0$ fm, respectively. The x -axis denotes the position R of the third quark. Smearing effects are manifest for $R < 0.95$ fm, $R < 0.85$ fm and $R < 0.75$ fm for $A = 0.6$ fm, $A = 0.8$ fm, and $A = 1.0$ fm. Only subtle smearing effects remain beyond these distance scales. 127
- 9.3 Surface plot (inverted) of the flux distribution $\mathcal{C}(\vec{\rho})$ of Eq. (9.3.1) evaluated in the plane of the (3Q) system $\vec{\rho}(x, y, 0)$, for isosceles configuration of base length $A = 0.4$ fm and separation distances (a) $R = 0.6$ fm, (b) $R = 0.8$ fm and (c) $R = 1.0$ fm, at $T = 0.8 T_c$. The spheres refer to the positions of the quarks. 130
- 9.4 The flux action iso-surface at the quark positions, plotted together with a surface plot for the density distribution $\mathcal{C}(\vec{\rho})$, in the 3Q plane at temperature $T = 0.9 T_c$, for equilateral triangular configuration $R = 1.1$ fm and $A = 1.0$ fm. 131
- 9.5 Surface plot in the plane of the 3Q system $\vec{\rho}(x, y, z = 0)$ and iso-surface of the flux distribution $\mathcal{C}(\vec{\rho}; \vec{r}_1, \vec{r}_2, \vec{r}_3)$ for the isosceles configuration with $A = 1$ fm and the third quark separation distance R as indicated. $T = 0.8 T_c$ 132
- 9.6 Comparison of the flux contour lines of the density distribution in the 3Q plane \mathcal{C} for triangular base $A = 1.0$ fm and third quark separation $R = 0.9$ fm at (a) $T = 0.8 T_c$ and (b) $T = 0.9 T_c$, in the $z = 0$ plane. As illustrated in Fig. 9.3, the maximal effect is near the Fermat point. 133

9.7 The density distribution $\mathcal{C}'(\vec{\rho})$ for the isosceles configuration with the base, $A = 1.0$ fm, and height $R = 0.8$ fm at $T/T_c = 0.8$ ($n_{\text{sw}} = 60$ sweeps). Data are plotted for the transverse planes $x = 1$ to $x = 6$. The lines correspond to the Gaussian fits to the density in each plane $\vec{\rho}(x_i, y, 0)$. The highest amplitude lies close to the Fermat point plane $x = 2.88$ of this 3Q configuration.	134
9.8 The radius profile of the flux-tube measured in the plane of the quarks for each isosceles configuration with base $A = 6a$, $A = 8a$ and $A = 10a$ ($a = 0.1$ fm), at two temperatures $T/T_c = 0.8$ (above) and $T/T_c = 0.9$ (below). The legend (in the upper right corner graph) signifies the third quark's position.	139
9.9 The radius profile of the flux-tube displaying a Y-shape like profile for quark configurations of base $A = 1.0$ fm and the third quark position $R = 1.3$ fm at temperature $T/T_c = 0.8$. In the background are the corresponding flux action-density contours.	141
9.10 Same as Fig. 9.8 for isosceles configuration bases of $A = 0.6$ fm, and $A = 1.0$ fm. The upper and lower figures compare the measured radius profile for two levels of smearing, 60 sweeps and 80 sweeps, respectively. The radius is in lattice units.	141
9.11 The profile of the action density amplitude, $H_y(x_i)$ (scaled by a factor of 10^1) for each isosceles configuration with base $A = 0.6$ fm, $A = 0.8$ fm and $A = 1.0$ fm, for the two temperatures $T/T_c = 0.8$ (upper), $T/T_c = 0.9$ (lower). The legend signifies the third quark position.	143
9.12 The squared flux distribution width at the depicted planes, $x_i = 2, 3$ and 7, are compared for two smearing levels. The isosceles configuration base length is $A = 1.0$ fm at temperature $T/T_c = 0.9$. Smearing merely shifts the profile by a constant. The broadening pattern is not affected.	145
9.13 The squared flux-tube width at the depicted planes for the isosceles configuration $A = 0.8$ fm compared at two temperatures $T/T_c = 0.8$ (top) and $T/T_c = 0.9$ (bottom). The plane coordinates are indicated in the legend.	146
9.14 Same as Fig. 9.13 for a larger isosceles base length of $A = 1.0$ fm.	146
9.15 Comparison of the mean square width of the flux distribution at three distinct planes, $x = 2, 3$, and 7, for two isosceles bases $A = 0.6$ fm and $A = 0.8$ fm. The upper graphs show the comparison at $T/T_c = 0.9$ whereas the lower are at $T/T_c = 0.8$	147
9.16 Comparison of the ratio, α (Eq. (9.6.7)), of the mean squared width of the flux distribution parallel and perpendicular to the quark plane for three isosceles bases $A = 0.6$ fm, $A = 0.8$ fm and $A = 1.0$ fm. The upper graphs show comparison at $T/T_c = 0.8$ whereas the lower are at $T/T_c = 0.9$	148

- 9.17 Surface plot of the flux density surface in the quark plane, $\rho(x, y, z = 0)$, together with contour lines. The contour lines are projected onto the surface plot. The density of the contour lines increases near the edges in accord with the gradient of the density scalar field along the x -axis. The flux contours of the maximum value are the inner most lines inside the triangle. As the density plot illustrates, the flux-tube configuration is a filled Δ -shape with maximum action expulsion inside the triangle near the Fermat point of the configuration. These measurements are taken for an isosceles quark geometry of base $A = 0.8$, height $R = 1.2$ fm and temperature $T = 0.9 T_c$ 151
- 9.18 Schematic diagram for the isosceles configuration of the 3Q system. L_1 , L_2 and L_3 are distances from the Fermat point to the quark positions. 152

Statement of originality

This work contains no material which has been accepted for the award of any other degree or diploma in any university or other tertiary institution and, to the best of my knowledge and belief, contains no material previously published or written by another person, except where due reference has been made in the text.

I give consent to this copy of my thesis, when deposited in the University Library, being available for loan and photocopying, subject to the provisions of the Copyright Act 1968.

I give also permission for the digital version of my thesis to be made available on the web, via the university's digital research repository, the library catalogue and also through web search engines, unless permission has been granted by the University to restrict access for a period of time.

Ahmed Saad El Bakry Mahmoud

Dedication

To my family.

Abstract

The distribution of the gluon action density in mesonic systems is investigated at finite temperature. The simulations are performed in pure SU(3) Yang-Mills gauge theory for two temperatures below the deconfinement phase. The action-density isosurfaces display a prolate-spheroid-like shape. The curved width profile of the flux tube is found to be consistent with the prediction of the free bosonic string model at large distances.

In the intermediate source separation distance, where the free string picture poorly describes the flux tube width profile, we find the topological characteristics of the flux tube converge and compare favourably with the predictions of the free bosonic string upon reducing the vacuum action towards the classical instanton vacuum. As a byproduct of these calculations, we find the broadening of the QCD flux tube to be independent of the UV filtering at large distances. Our results exhibit a linearly divergent pattern in agreement with the string picture predictions.

We investigate the overlap of the ground state meson potential with sets of mesonic-trial wave functions. We construct trial states with non-uniform smearing profiles in the Wilson loop operator at $T = 0$. The non-uniformly UV-regulated flux-tube operators are found to optimize the overlap with the ground state.

The gluon flux distribution of a static three quark system has been revealed at temperatures near the end of the QCD plateau, $T/T_c \approx 0.8$, and another just before the deconfinement point, $T/T_c \approx 0.9$. The flux distributions at short distance separations between the quarks display an action-density profile consistent with a rounded filled Δ shape iso-surface. However the Δ shape action iso-surface distributions are found to persist even at large inter-quark separations. The action density distribution in the quark plane exhibits a nonuniform pattern for all quark separations considered. We systematically measure and compare the main aspects of the profile of the flux distribution at the two considered temperature scales for three sets of isosceles triangle quark configurations. The radii, amplitudes and rate of change of the width of the flux distribution are found to reverse their behavior as the temperature increases from the end of the QCD plateau towards the deconfinement point. Remarkably, we find the mean square width of the flux distribution shrinks and localizes for quark separations larger than 1.0 fm at $T/T_c \approx 0.8$ which results in an identifiable Y-shaped radius profile. Near the deconfinement point, the action-density delocalizes and the width broadens linearly with the quark separation at large quark separations.

We present a method to include the thermal effects into the junction width of the baryonic string model. The profile of the baryonic gluonic distribution is compared with the width of the string picture's junction fluctuations. The comparison reveals that the best fits to the junction fluctuations of the baryonic string are near the Fermat point of the triangle made up by the quarks. This result supports the underlying picture of Y-shaped string-like flux tubes connected at a junction.

Chapter 1

Quantum Chromodynamics

Quantum chromodynamics (QCD) is the current proposed theory of the strong interactions. The strong force binds the quarks and gluons and is responsible for the formation of hadrons such as protons and neutrons. The strong interaction mediates the interactions between the hadrons themselves and is the fundamental force that dominates the atomic nuclei. Although quarks and gluons have not been observed as free states, an immense bulk of experimental data supports QCD as the true theory of strong interactions. QCD is a nonlinear gauge theory that is practically analytically unsolvable. A perturbative expansion gives accurate predictions in the quantum field theory of QED which describes a much weaker force. Perturbative expansions, however, are constrained to short distance predictions in the case of strong interactions. This has led to the introduction of non-perturbative approximations that are based on discretising four-dimensional space-time into a lattice of points, giving rise to the theory called lattice QCD, which can be simulated on computers. Lattice QCD provides a first principles approach for determining the properties of QCD. Alternative popular approaches to lattice QCD are the light-front formulation of QCD [6, 7, 8, 9] and Schwinger-Dyson equations [10, 11, 12, 13] which are usually employed in constructing QCD-based quark models.

The concept of colour arose during the phenomenological studies of the rapidly growing abundance of newly discovered elementary particles in particle accelerators. Gell Man and Zweig [14] found that the known hadrons can be grouped into octets and decuplets representing multiplets of the $SU(3)$ group. The Gell-Man [15] classification for hadrons resulted in non-trivial predictions which have been confirmed experimentally, such as the prediction of the Ω^- hyperon. This discovery happened in a way reminiscent of the discovery of missing elements which filled out cells in Mendeleev's table.

Although in experiments we observe octets and decuplets, the particles belonging to the fundamental representation of $SU(3)$ and its conjugate (triplets and anti-triplets) have not been observed in asymptotic states. These fundamental particles have been called quarks. The existence of the quarks can be inferred based on purely algebraic results of tensor products of several representations: $3 \otimes \bar{3} = 8 + 1$ and $3 \otimes 3 \otimes 3 = 10 + 8 + 8 + 1$. This leads to mesons which are bound states of a quark and anti-quark, while baryons consist of three quarks. In the constituent quark model, hadrons are formed as a bound state of quarks in a similar manner as the nuclei are composed of nucleons.

In order to explain the electric charges and other quantum numbers of the observed hadrons, Gell-Man and Zweig postulated [14, 15] the existence of three distinct species (called flavours) of quarks: the up (u), down (d) and the strange (s) quarks. In fact, the discovery of additional hadrons confirmed the existence of another three flavours corresponding to new quantum numbers: charm(c), bottom(b) and top(t). The fractional electric charges are then ascribed to the quarks $e_u = e_c = e_t = 2/3$, $e_d = e_s = e_b = -1/3$. Spin $S = -1$ for the strange quark isospin=0, $S = 0$ and isospin=1/2 for up (u) and down (d) quarks.

Despite the phenomenological success of the flavour symmetry in classifying the spectrum of elementary particles, the dynamics that binds the quarks could not be explained within the framework of this symmetry. Apart from that, two main difficulties in the constituent quark model were far from being resolved. The first difficulty is that quarks do not exist in nature as free asymptotic states. The second, on the other hand, has to do with the observation of bound states such as the Δ^{++} -isobar which according to the Pauli exclusion principle should not exist. According to the constituent quark model this particular bound state consists of three u quarks in S wave with the same spin orientation.

To restore the Pauli principle, the quark of each flavour (u , d , and s) has to occur naturally in three colour forms. Thus, on top of the approximate $SU(3)$ flavour symmetry, there exists an exact $SU(3)$ colour symmetry. The wave functions of the baryons are in anti-symmetric form $\epsilon^{ijk}q^i q^j q^k$ ($i, j, k = 1, 2, 3$ are the colour indices).

The field theory that encompasses the ideas of QCD is Yang-Mills theory [16, 17]. In this theory, the principle of local gauge invariance [18, 19, 20, 21] is generalized to the non-Abelian gauge group [22, 23]. For the electromagnetic interaction, local gauge invariance is the underlying principle for the observed electromagnetic dynamics in which the intermediate interaction proceeds via the exchange of massless vector bosons (photons). The extension of the principle of local gauge invariance to weak and strong interactions has encountered a remarkable success in constructing a renormalizable quantum gauge field theory [24] free of the Landau-pole problem [25]. The strong interactions proceed via the exchange of massless vector particles “called gluons” between the quarks. The gluons belong to the octet representation of the $SU(3)$ colour group and are self-interacting.

A full-fledged quantum field theory now exists that describes electromagnetic (EM) weak and strong forces between elementary particles, the standard model (SM) of particle physics. The SM, generalized for massive neutrinos, is in good agreement with the current experimental tests. Quantum chromodynamics (the gauge field theory that describes the strong interactions of coloured quarks and gluons) is the $SU(3)$ component of the $SU(3) \times SU(2) \times U(1)$ standard model of particle physics. The QCD lagrangian [17] is given by

$$\mathcal{L}_{QCD} = \sum_q \bar{\psi}_{q,a} (i\gamma^\mu \partial_\mu \delta_{ab} - g_s \gamma^\mu t_{ab}^C A_\mu^C - m_q \delta_{ab}) \psi_{q,b} - \frac{1}{4} F_{\mu\nu}^A F^{A\mu\nu}. \quad (1.0.1)$$

The γ^μ are the Dirac γ -matrices. The $\psi_{q,a}$ are quark-field spinors for a quark of flavour q and mass m_q , with a colour-index a that runs from $a = 1$ to $a = N_c = 3$ since the quarks come in three colours. Quarks are said to be in the fundamental

representation of $SU(3)$ colour group. The A_μ^C corresponds to the gluon fields with C running from 1 to $N_c^2 - 1$, thus there are eight kinds of gluon. Gluons are said to be in the adjoint representation of $SU(3)$ colour group. The t_{ab}^C correspond to eight 3×3 matrices and are the generators of the $SU(3)$ group. The gluon interactions thus rotate the quark's colour in $SU(3)$ space. The quantity g_s is the QCD coupling. The field strength tensor $F_{\mu\nu}^A$ is given by

$$F_{\mu\nu}^A = \partial_\mu A_\nu^A - \partial_\nu A_\mu^A - g_s f_{ABC} A_\mu^B A_\nu^C, \quad (1.0.2)$$

where the f_{ABC} are the structure constants of the $SU(3)$ group. The fundamental parameters of QCD are the coupling g_s and the quark masses m_q .

The calculations of the charge renormalization of this gauge theory indicated [26, 27] that the effective charge does not grow with momentum but rather decreases. The decrease of the strength of coupling by decreasing the separation distance between quarks is a peculiar property of QCD that is referred to as asymptotic freedom. In the scale of small length, the quarks and gluons interact weakly and can be considered as nearly free. The immediate consequence of this property is that it is possible to perform perturbative calculations of the observables for phenomena governed by small separation distances. The perturbative calculations of QCD successfully accounts for the scaling violation [28, 29, 30] observed in deep inelastic scattering between leptons and nucleons. However, in the infrared (IR) region of the theory, the coupling is strong. The large value of the coupling renders the perturbative calculations ineffective.

The two different regions of QCD are described by the running of the coupling. This means that the coupling constant is a function of the length or momentum scale. The renormalized coupling constant [31] is a scale dependent quantity with the one-loop value given by

$$\alpha_s(k^2) = \frac{\alpha_s(q^2)}{1 + \alpha_s(q^2) \frac{(33-2n_f)}{12\pi} \ln(\frac{k^2}{q^2})}. \quad (1.0.3)$$

The fine structure α_s is related to the coupling as

$$\alpha_s(k^2) = \frac{g^2(k^2)}{4\pi}. \quad (1.0.4)$$

Similarly, $\alpha_s(q^2)$ is related to the coupling defined at the scale q^2 , and the two parameters (α_s and q^2) are not independent from each other. However, the running coupling can be fixed for all momentum transfers by one parameter, with a relation between the scale q^2 and introduced scale Λ_{QCD} such that

$$\alpha_s(q^2) = \frac{12\pi}{(33-2n_f) \ln(\frac{-q^2}{\Lambda_{QCD}^2})}. \quad (1.0.5)$$

The exact value of Λ_{QCD} may be determined from experiment.

The fundamental property of the IR region of the QCD vacuum is that it confines quarks. Quark confinement is a terminology which describes the fact that quarks have never been observed in a free state in Nature. If one of the quarks in a given hadron is pulled away from its neighbors, the colour-force field stretches between that

quark and its neighbours. This causes a dramatic increase in the system's energy. This does not proceed to infinity. At a certain point the energy is high enough to produce the mass of new quark pairs that are again assembled into confined states.

Confinement is a large distance phenomenon in which the perturbative approach no longer gives precise calculations. Wilson [32] was the first to show that QCD calculations can be made nonperturbatively by reformulating the theory on a lattice instead of the whole continuous space-time and employing numerical methods. Although numerical simulations of lattice gauge theory have confirmed [32] quark confinement, neither a derivation of quark confinement from first principles has been found, nor has any proposed scenario or mechanism of confinement generally been accepted.

The confinement mechanism of quarks is still an outstanding problem in QCD. There are many mechanisms that address the confinement of quarks via a special class of gauge configurations such as instantons [33], merons [34, 35], abelian monopoles [36], centre vortices [37], and dyons [38]. These topological objects dominate the QCD vacuum in the infrared region and may play an important role in the confinement mechanism, giving rise to a linearly rising potential. Technically, this should correspond to a Wilson loop area law or exponential decay of Polyakov loop correlators. The advent of new algorithms and lattice techniques made it possible to study these objects and therefore directly scrutinize the proposed confinement mechanism for each of these topological excitations.

Instantons [39] are topologically nontrivial solutions of the Yang-Mills equations that absolutely minimize the energy functional. Instantons describe the quantum tunnelling between degenerate vacuums in gauge theories, and can cause confinement of the charges [40]. The instanton is believed to be composed of two merons. It can be also shown [41, 42] that effective theories based on ensembles of merons can produce confinement.

Dyons are gluon field configurations with asymptotic Coulomb-like chromo-electric and magnetic fields, and are saddle points of the Yang-Mills partition function at $T \neq 0$. In this mechanism, an ensemble of dyons, in particular the dual (magnetic) gluons, will constitute a plasma which acquires a Debye mass. This will give rise to an exponential decay of the Polyakov line correlations, or in other words, a linearly rising potential [43, 44].

The maximal centre projected QCD is to perform a gauge-fixing condition that preserves the centre symmetry of the gauge group. The centre vortices are the topological objects that carry the centre of the group as a charge. Lattice simulations show that these objects are linked to the so-called string tension and hence the linearly rising potential between quarks. This is based on the observation that the string tension vanished upon removal of centre vortices [45]. This phenomenon is usually called centre dominance. Also, the suppression of these objects in the deconfinement phase [46] supports the important role played by these objects in the confinement mechanism.

The dual superconductor model [47] is a scenario speculated in the 70s [47, 48, 49, 50, 51, 52] to conceive the phenomena of quark confinement in terms of the dual theory of superconductivity in electromagnetism. The theoretical framework of the theory of dual superconductivity is described by the dual Landau-Ginzburg model [53] (equivalent to and sometimes called the dual Abelian Higgs model [54]).

In the dual superconductor the role of electric and magnetic fields are exchanged. The confinement mechanism in the dual superconductivity picture of the QCD vacuum [55, 56, 57, 58] proceeds in the same manner as the condensation of electric charges to Cooper pairs gives rise to superconductivity. In dual superconductors, the confinement mechanism is realized through the condensation of magnetic monopoles [59] by the dual Meissner effect. The magnetic field lines are squeezed into flux tubes by virtue of this effect. The quark–antiquark potential will linearly rise since the energy contained in the tube is proportional to its length. According to this picture, the quark-antiquark pair are doomed to be confined in a bound state.

In a similar fashion to the maximal centre gauge fixing, an abelian projection to QCD [60] can be performed by gauge-fixing to the maximal abelian torus group. Then QCD becomes a $U(1) \times U(1)$ abelian gauge theory with magnetic monopoles. This idea is based essentially on the superconductivity scenario of confinement where 'tHooft conjectured [60] that the condensation of these abelian monopoles provides the confinement mechanism in QCD. Lattice studies [61] show that the large distance physics of QCD is contained in the abelian projected theory, in what is known as abelian dominance at large distances.

Another model inspired from the superconductivity property of the QCD vacuum, which squeezes the colour field into a thin stringlike object, is the effective string picture. This picture is expected to provide a good physical description of confining gauge theories in the low energy regime. In this picture the two confined colour charges are joined by a thin flux tube that fluctuates like a vibrating string. The dynamics of the string's worldsheet dynamics can be described based on an effective action. In this effective description, quantitative predictions about the potential between a confined quark-antiquark pair can be derived. These predictions have remained speculative for a long period of time. However, recent precise lattice simulations have measured [62, 63, 64, 65, 66] the properties of the static quark–antiquark potential to a sub-leading order, and confirmed properties related to the stringlike behaviour [67] of the QCD flux tube.

In addition to quark confinement, QCD exhibits another property which is chiral symmetry breaking [68, 69, 70, 71, 72]. The QCD Lagrangian with N_f massless flavours is known to possess a global symmetry under $U_R(N_f) \times U_L(N_f)$, independent rotations of left- and right-handed quark fields. This symmetry is called “chiral”. Chiral transformations involve rotations of Weyl spinors as well as axial $U_A(N_f)$ and vector $U_V(N_f)$ rotations of the whole 4 component Dirac spinors. The $U_A(N_f)$ mixes states with different parities; nevertheless, the experimental value of mass splitting in the vector ρ and axial a_1 meson for example is as large as 400 MeV. The chiral symmetry of the QCD lagrangian is broken down spontaneously. According to Goldstone's theorem [73] this entails the existence of light (pseudo) Goldstone pseudo-scalar hadrons. The lightest known hadrons to play this role are the pions. The order parameter associated with chiral symmetry breaking is the so-called chiral or quark condensate $\langle \bar{\psi} \psi \rangle$. As a composite operator, the symmetry is said to be dynamically broken. The condensate defines a quark Green function taken at one point which corresponds to a closed quark loop in momentum space. Chiral symmetry breaking implies that massless quarks develop a non-zero dynamical mass [74].

The two main characteristics of the QCD vacuum are the confinement of quarks and chiral symmetry breaking. Lattice studies [75, 76, 77, 78], however, have shown

that for sufficiently high temperature, the low temperature hadronic phase of QCD turns into a high temperature quark-gluon-plasma phase [79] in which quarks are liberated and chiral symmetry is restored [80].

Among these features, an important and not yet fully understood property of the confining flux-tubes concerns their thermal behaviour in the IR region. Lattice simulations have indicated a decrease in the slope of the linearly rising potential between a pair of colour sources with the increase in the temperature [81]. A natural and fundamental question to QCD and confinement is what happens to the flux tubes just before the deconfinement point? In fact the profiles of the flux tube for temperatures close to the deconfinement point are unknown. The major goal in this work is to reveal, based on first principles lattice QCD calculations, the profile of the confining flux tube in mesonic and baryonic systems. The obtained results of the gluonic distributions are then explained in the context of their stringlike behaviour.

The organization of this work is as follows. Chapter 2 will be devoted to a brief introduction to lattice gauge theory (LGT) and the corresponding simulation techniques. In Chapter 3, two approaches to reveal the colour field between colour charges, i.e. the Wilson loop operator and Polyakov lines, are discussed. This chapter also contains the basic principles of the lattice formulation of finite temperature field theory. The predictions of the bosonic string model for the changes with the temperature of the profile of the flux-tubes for both mesonic and baryonic systems are reviewed in Chapter 4. The thermal effects are included in the baryonic string model predictions. In Chapter 5, we introduce various noise reduction techniques for the Polyakov line correlators and show to what extent every technique is suitable and valid in extracting the correct physics.

In Chapter 6 and eventually Chapter 9, we present and discuss our finite temperature results on various profiles of the flux-tube for the meson and the baryon, respectively. The profile of the flux-tube at finite temperature is compared to the predictions of the free bosonic string model. In Chapter 7, the role played by the UV physics in the behaviour of the flux-tube is revealed and compared with the bosonic string picture predictions. In Chapter 8, the zero temperature regime is probed by using flux-tube profiles discovered at finite temperature at the end of the QCD plateau where the action density profile is non-uniform. The flux-tube is constructed by means of local smearing operators in the Wilson loop operator. The overlap with the ground state for these trial states is measured. Finally in Chapter 10, a brief summary is provided.

Chapter 2

Lattice Gauge Theory

2.1 Outline

The basic ideas of lattice gauge theory are briefly reviewed in this chapter. In addition to this, we discuss algorithms for generating a sequence of configurations distributed according to a Boltzmann probability distribution governed by the SU(3) Yang-Mills action which are used to measure the relevant observables in the theory. We first describe an algorithm which is generally applicable to any system, namely, the Metropolis algorithm. Then we describe the Hybrid heat bath/overrelaxation algorithm which is an efficient scheme for generating Markov chains, and is particularly suitable for pure non-Abelian gauge configuration generation.

2.2 Introduction

Lattice gauge theory [82, 83] is a framework to reduce the infinite number of degrees of freedom of a quantum field theory to a finite number. In the lattice formulation, the continuous space-time is replaced by a discrete mesh of points. The lattice has a finite size in its total extent. The lattice spacing introduces a natural ultraviolet regularization which preserves gauge-invariance. Lorentz invariance, nevertheless, is destroyed by lattice discretisation. In the continuum limit, relativistic invariance is restored and the renormalised quantities approach finite limits. The choice of the lattice parameters in numerical simulations is based on a skilful and economic choice between having a reasonably small lattice spacing and a large volume.

2.3 Path integral formulation

A field theory is solveable once all the relevant Green functions of the theory are computed. The path integral formulation provides an elegant representation of green functions,

$$\langle \Omega | \phi_1(x_1) \phi_2(x_2) \cdots | \Omega \rangle = \frac{1}{Z} \int [d\phi] e^{iS[\phi]} \phi_1(x_1) \phi_2(x_2) \cdots, \quad (2.3.1)$$

for generic fields (operators) ϕ , with

$$Z = \int [d\phi] e^{iS[\phi]}. \quad (2.3.2)$$

In order to carry out numerical techniques to extract the physical observables from the field theory given by the representation Eq. (2.3.1), the integral in Minkowski space has to be analytically continued to imaginary time (Euclidean space)

$$t \longrightarrow -it, \quad (2.3.3)$$

$$iS[\phi] \longrightarrow -S[\phi]. \quad (2.3.4)$$

The Euclidean path integral formulation allows application of techniques of statistical mechanics to the quantum fields on the lattice. The numerical evaluation can be done by the use of Monte Carlo methods by importance sampling of the equilibrium configurations of the classical fields corresponding to configurations chosen with the probability

$$P(\phi) = \frac{1}{Z_E} e^{-S^E[\phi]}. \quad (2.3.5)$$

The evaluation of the path integral is then a sum over the equilibrium configurations

$$\langle \Omega | \phi_1(x_1) \phi_2(x_2) \cdots | \Omega \rangle \approx \frac{1}{N} \sum_N \phi_1(x_1) \phi_2(x_2) \cdots. \quad (2.3.6)$$

In the next sections of this chapter, we will discuss the relevant algorithms for the construction of such configurations.

2.4 Gauge field

The elements of the local gauge group G are associated with the lattice sites. These parallel transporters are the elements describing the gauge fields. The link variable $U_\mu(x)$ denotes the group element linking the site x to the site $x + a_\mu$, where a_μ is a vector in the μ direction.

The gluon field A_μ is related to the parallel transporter in continuum

$$U_\mu(x) = \mathcal{P} e^{\int_x^{x+\hat{\mu}} A_\mu(z) dz}. \quad (2.4.1)$$

In QCD, the matrices $A_\mu(x)$ belong to the colour octet of the $SU(3)$ Lie algebra, i.e. $A_\mu(x) = \sum_{a=1,8} t^a A_\mu^a(x)$ with $t^a = \lambda^a/2$ and λ^a are Gell-Mann matrices.

In the continuum, the gauge action in Euclidean space-time for QCD is given by

$$S_G = \frac{1}{2} \int d^4x Tr(F_{\mu\nu}(x) F_{\mu\nu}(x)). \quad (2.4.2)$$

$F_{\mu\nu}$ is the field strength tensor

$$F_{\mu\nu} = \partial_\mu A_\nu(x) - \partial_\nu A_\mu + ig[A_\mu, A_\nu]. \quad (2.4.3)$$

The parallel transporters transform under gauge transformation

$$U_\mu \rightarrow U_\mu^g(x) = G(x) U_\mu(x) G^\dagger(x + a\hat{\mu}). \quad (2.4.4)$$

This means that path-ordered products of links along any path through the lattice will be only transformed by multiplying the matrices operating at ends of the paths and the traced product of links along a closed loop will be gauge invariant.

The gauge action is constructed from an arbitrary Wilson loop,

$$\begin{aligned} W_{\mu\nu} &= \frac{1}{N_c} \mathcal{P} \text{Tr} \left[\exp \left(-ig \oint_{\mathcal{C}} A(x) \cdot dx \right) \right], \\ &= \mathcal{P} \frac{1}{N_c} \text{Tr} \left[1 - ig \left(\oint_{\mathcal{C}} A(x) \cdot dx \right) - \frac{g^2}{2} \left(\oint_{\mathcal{C}} A(x) \right)^2 + \mathcal{O}(g^3) \right]. \end{aligned} \quad (2.4.5)$$

For convenience, consider the Abelian case of Stokes' theorem

$$\oint_{\mathcal{C}} A(x) \cdot dx = \int_a^b dx_{\mu} dx_{\nu} [D_{\mu} A_{\nu}(x + x_0) - D_{\nu} A_{\mu}(x + x_0)]. \quad (2.4.6)$$

Expanding around the centre point of Wilson loop x_0 in the coordinate gauge, $A \cdot x = 0$, we get

$$\begin{aligned} \oint_{\mathcal{C}} A(x) \cdot dx &= \int_a^b dx_{\mu} dx_{\nu} [F_{\mu\nu}(x_0) + (x_{\mu} D_{\mu} + x_{\nu} D_{\nu}) F_{\mu\nu}(x_0) + \\ &\quad \frac{1}{2} (x_{\mu}^2 D_{\mu}^2 + x_{\nu}^2 D_{\nu}^2) F_{\mu\nu}(x_0) + \mathcal{O}(a^2 g^2, a^4)]. \end{aligned} \quad (2.4.7)$$

Taking the contour to be simple plaquette, the integration bounds would then be $-a/2 \leq x_{\mu} \leq a/2, -a/2 \leq x_{\nu} \leq a/2$ respectively

$$\oint_{1 \times 1} A(x) \cdot dx = a^2 F_{\mu\nu}(x_0) + \frac{a^4}{24} (D_{\mu}^2 D_{\nu}^2) F_{\mu\nu}(x_0) + \mathcal{O}(a^6, A^2). \quad (2.4.8)$$

The real part of the trace of $W_{\mu\nu}$ gives the Wilson action

$$\begin{aligned} P_{\mu\nu} &= \frac{1}{N_c} \text{Tr} \left[\mathcal{I} - \frac{g^2}{2!} \oint_{\mathcal{C}} (A(x) \cdot dx)^2 + \dots \right] \\ &= 1 - \frac{g^2}{6} a^4 \text{Tr}(F_{\mu\nu}^2) - \frac{g^2}{6} \frac{a^6}{12} \text{Tr} (F_{\mu\nu}(x_0) (D_{\mu}^2 + D_{\nu}^2) F_{\mu\nu}(x_0)) + \dots \end{aligned} \quad (2.4.9)$$

Using this expansion, the Wilson gluonic action is then

$$S_{\text{Wil}} = \beta \sum_{x, \nu > \mu} (1 - P_{\mu\nu}) \rightarrow \frac{1}{2} \int d^4x \text{Tr}(F_{\nu\mu}^2) + \mathcal{O}(a^2), \quad (2.4.10)$$

provided $\beta = 2N_c/g^2$.

2.5 Fermion field

The continuum Dirac action is

$$S[\psi, \bar{\psi}] = \int d^4x \bar{\psi}(x) (D_{\mu} \gamma_{\mu} + m) \psi(x), \quad (2.5.1)$$

where D_μ is the covariant derivative. Replacing the derivative with symmetrized difference operators

$$\bar{\psi} \not{D} \psi = \frac{1}{2a} \bar{\psi} \sum_\mu [U_\mu(x) \psi(x + \hat{\mu}) - U_\mu^\dagger(x - \hat{\mu}) \psi(x - \hat{\mu})], \quad (2.5.2)$$

where $\hat{\mu}$ has length a . Expanding the gauge links, $U_\mu = 1 + iagA(x + \hat{\mu}/2) + \mathcal{O}(g^2)$. The simplest naive lattice action for fermions is

$$\begin{aligned} S &= \sum_x \left[m_q \bar{\psi}(x) \psi(x) + \frac{1}{2a} \sum_\mu \bar{\psi}(x) \gamma_\mu [U_\mu(x) \psi(x + \hat{\mu}) - U_\mu^\dagger(x - \hat{\mu}) \psi(x - \hat{\mu})] \right], \\ &= \sum_x \bar{\psi}(x) M[U]_{xy} \psi(y), \end{aligned} \quad (2.5.3)$$

where the fermion matrix, $M[U]_{xy}$ is

$$M_{ij} = m_q \delta_{ij} + \frac{1}{2a} \sum_\mu \gamma_\mu [U_\mu(x) \delta_{ij-\mu} - U_\mu^\dagger(x - \hat{\mu}) \delta_{ij+\hat{\mu}}]. \quad (2.5.4)$$

The propagator is the inverse of the matrix $M[U]_{xy}$,

$$\begin{aligned} S(k) &= \left[\frac{i}{a} \sum_\mu \gamma_\mu \sin(k_\mu a) + m \right]^{-1}, \\ &= \frac{-i/a \sum_\mu \gamma_\mu \sin(k_\mu a) + m}{\sum_\mu (1/a \sin(k_\mu a))^2 + m^2}. \end{aligned} \quad (2.5.5)$$

As $a \rightarrow 0$, the propagator vanishes except at $k = (0, 0, 0, 0)$ or any of the 15 other points where one or more of the components of k_μ equals π/a . In the vicinity of these momenta, the propagator has a distribution function having the form resembling that of a single particle propagator. These additional excitations are pure lattice artifacts. In fact, in d -space the number would be 2^d (0 and π/a for each dimension), i.e. it doubles for each additional dimension.

The fermion doubling problem can be overcome by cancelling out the lattice artifacts. This is done by introducing irrelevant operators at the expense of an explicit breaking of chiral symmetry even for $m_q \rightarrow 0$.

The naive lattice action for fermions can be modified by a term which vanishes in the continuum limit. This fermion action is known as the Wilson fermion action. It has $\mathcal{O}(a)$ errors and is defined as

$$\begin{aligned} S_W[U, \bar{\psi}, \psi] &= \sum_x [(m_q + 4r) \bar{\psi}(x) \psi(x) \\ &\quad - \frac{1}{2} \sum_\mu \bar{\psi}(x) (r - \gamma_\mu) U_\mu(x) \psi(x + \hat{\mu})] \\ &\quad + \bar{\psi}(x - \hat{\mu}) (r + \gamma_\mu) U_\mu^\dagger(x) \psi(x)]. \end{aligned} \quad (2.5.6)$$

$$(2.5.7)$$

This equation can be rewritten as

$$\begin{aligned} S_W[U, \bar{\psi}, \psi] &= \sum_{xy} \bar{\psi}(x) D_W(x, y) \psi(y), \\ D_W(x, y) &= (m_q + 4r) \delta_{x,y} - \frac{1}{2} \sum_{\mu} (r - \gamma_{\mu}) U_{\mu}(x) \delta_{y,x+\hat{\mu}} + (r + \gamma_{\mu}) U_{\mu}^{\dagger}(x - \hat{\mu}) \delta_{y,x-\hat{\mu}}, \end{aligned} \quad (2.5.8)$$

where r is the Wilson coefficient. The terms containing r are the irrelevant dimension operators introduced to eliminate the fermion doubling problem. Here m_q is the lattice bare mass related to the hopping parameter κ via

$$\kappa = \frac{1}{2m + 8r}, \quad m_q \equiv \frac{1}{2a} \left(\frac{1}{\kappa} - \frac{1}{\kappa_c} \right). \quad (2.5.9)$$

κ_c is the critical value for the hopping parameter. $\kappa_c = 1/8$ when the gluonic interactions are switched off ($U_{\mu}(x) \equiv I$). However, in the presence of the gluonic interaction, κ_c is defined as the value of κ at which the pion mass vanishes. In the latter case, the critical value diverges away from the tree value of an eighth.

2.6 Correlation functions

We consider a correlation function of the generic form

$$\begin{aligned} \langle O_1(U, \psi, \bar{\psi}) O_2(U, \psi, \bar{\psi}) \cdots \rangle &= \frac{1}{Z} \int [dU] [d\psi] [d\bar{\psi}] e^{-S_G[U] - S_F[U, \psi, \bar{\psi}]} \\ &\times \bar{\psi}_{\alpha} \bar{\psi}_{\beta} \cdots \Gamma_{\alpha' \beta' \cdots}^{\alpha \beta \cdots} (U) \psi_{\alpha'} \psi_{\beta'} \cdots, \end{aligned} \quad (2.6.1)$$

α and β are Dirac indices. The fermionic part of the action S_F is quadratic in the quark fields

$$S_F = \bar{\psi} M[U] \psi. \quad (2.6.2)$$

where M is the fermion matrix. The fermion functional integral is over Grassmann variables

$$\begin{aligned} \langle O_1(U, \psi, \bar{\psi}) O_2(U, \psi, \bar{\psi}) \cdots \rangle &= \frac{1}{Z} \int [dU] e^{-S_G[U]} \det(M[U]) \\ &\times \text{Tr} [M^{-1}[U] M^{-1}[U] \cdots \Gamma]. \end{aligned} \quad (2.6.3)$$

Computing correlation functions proceeds first via constructing sets of equilibrium gauge field configurations chosen with a probability proportional to $\exp(-S_G[U]) \det(M[U])$ or $\exp(-S_G[U])$ in the pure Yang-Mills theory which is the standard in the present work. Then the quark propagators $M^{-1}[U]$ are calculated. The final step is to average the hadron correlation function over the gauge field configurations.

Let $P(U', U)$ define the updating algorithm. Thermal equilibrium is equivalent to requiring the condition of detailed balance

$$P(U', U) e^{-S(U)} = \sum_{U'} P(U, U') e^{-S(U')}, \quad (2.6.4)$$

which is imposed at each step of the updating process. There are many algorithms in common use for updating gauge fields such as the Metropolis algorithm, and pseudo-heat bath algorithm [84]. In addition to those, there are also many algorithms for including the fermion determinant such as pseudo-fermion Langevin [85] equation, molecular dynamics [86] and hybrid methods [87].

The QCD vacuum admits topological features such as instantons, center vortices and abelian monopoles. These objects play important roles in the confinement mechanism and have become subject to direct investigation by lattice methods. In the thermal regime, the current computational capabilities reached a level such that it has become feasible to study the phase transition aspects such as the order of the transition, transition temperature, screening lengths in the quark gluon plasma phase and chiral symmetry restoration. The calculation of the vector currents on the lattice is a particularly important method to understand the structure of the hadron. In Appendix A we present our calculations of branching reactions of pseudo-scalar to vector transition form factor.

2.7 Continuum limit

The lattice spacing removes the infinities of the quantum field theory and renders the observables finite. This lattice regulator must be removed to approach the continuum limit. The coupling $g \rightarrow 0$ as the continuum limit is approached. To keep the observables finite, however, the infinities are absorbed into the renormalization parameters of the theory as is the case in the continuum field theory.

The lattice gauge theory is assumed to reproduce QCD in the continuum limit. Nevertheless, there can be an infinite number of lattice theories that all correspond to the same continuum field theory. The requirement that the lattice gauge theory reproduces QCD in the continuum limit is necessary but not sufficient to ensure a true realization of QCD [82]. This led to the consideration of the critical points of the partition function in Eq. (2.6.1). At these points the lattice gauge theory is expected to become blind to the details of the lattice structure itself.

The tuneable parameter in lattice gauge theory is the bare coupling constant which by certain choice, say g_0^c , will cause the correlation length, ξ , to diverge

$$\hat{\xi}(g_0) \xrightarrow[g_0 \rightarrow g_0^c]{} \infty. \quad (2.7.1)$$

A lattice gauge theory that does not possess these critical points cannot be a realization of the continuum field theory. This is because, at this critical parametric subspace, the physical quantities should be finite in the limit of zero lattice spacing a .

An observable on the lattice, \hat{O} , will depend on the parameters of the theory. The renormalized version of this observable is obtained via scaling with the corresponding canonical dimension

$$\left(\frac{1}{a}\right)^d \hat{O}(g_0(a)) = O(g_0(a), a) \quad (2.7.2)$$

The physical value of the observable, O_{phys} , has to be finite in the limit

$$\lim_{a \rightarrow 0} O(g_0(a), a) = O_{\text{phys}}. \quad (2.7.3)$$

This means that g_0 has to scale with a such that the critical coupling Eq. (2.7.1) is approached

$$g_0(a) \rightarrow g_0^c. \quad (2.7.4)$$

The renormalization group equations (RGE) scale the bare coupling with the lattice regulator such that physical quantities remain fixed. This is done at sufficiently small lattice spacing. The RGE reads

$$[a \frac{\partial}{\partial a} - \beta(g_0) \frac{\partial}{\partial g_0}] O(g_0(a), a) = 0, \quad (2.7.5)$$

with the Callan-Symanzik β -function defined as

$$\beta(g_0) = -a \frac{\partial g_0}{\partial a}. \quad (2.7.6)$$

To find $g_0(a)$, we need to calculate β -function which cannot be calculated exactly. However, the β function can be determined in perturbation theory. In two-loop perturbation theory, it is given by

$$\beta(g_0) = -\beta_0 g_0^3 - \beta_1 g_0^5 + \mathcal{O}(g_0^7), \quad (2.7.7)$$

with the QCD coefficients [82]

$$\begin{aligned} \beta_0 &= \frac{1}{16\pi^2} \left(\frac{11}{3} N_c - \frac{2}{3} n_f \right), \\ \beta_1 &= \frac{1}{(16\pi^2)^2} \left(\frac{34}{3} N_c^2 - \frac{10}{3} n_f N_c - \frac{N_c^2 - 1}{N_c} n_f \right), \end{aligned} \quad (2.7.8)$$

which are renormalization scheme independent. The positivity of the coefficients gives rise to a negative β -function. This means a reduction in the coupling constant as the lattice spacing decreases.

The explicit dependence of the coupling on the lattice spacing is obtained by integrating the RGE

$$a = \frac{1}{\lambda_L} (\beta_0 g_0^2)^{\frac{\beta_1}{2\beta_0^2}} e^{\frac{1}{-2\beta_0 g_0^2}}, \quad (2.7.9)$$

where λ_L an integration constant with the dimension of $1/a$, which has to be determined from simulation. This function has to be independent from the considered observable. This is ensured if the system is well within the scaling region. Scaling violation in this case amounts to the deviations from the RGE for finite lattice spacing and dependence on the measured observable.

In order to obtain the physical values of observables, they need to be scaled according to their dimension, with either the lattice spacing or λ_L , Eq. (2.7.9). We should use at least one quantity to set the scale. In many cases, the ρ -mass or string tension σ , or Sommer parameter r_0 is considered [88]. The string tension is adopted herein.

On the other hand, if it happened that the lattice spacing in certain simulations was made small enough for the system to be deep in the scaling region, the physical values can be directly extracted from the lattice without the need to perform the continuum limit, as the $\mathcal{O}(a)$ or $\mathcal{O}(a^2)$ errors of the action would be small.

2.8 Quenched approximation

The integration of the fermionic variables in the path integral ends up with the fermionic determinant which is a complicated non-local effective action depending only on the gauge fields. The integration of the fermionic degrees of freedom amounts to computing dynamical quark loops which are the quark loops generated from the gluons. The computations of these loops can be performed in principle on the lattice. However, the inclusion of dynamical quarks into the calculations increases the computational time considerably.

For a large number of lattice sites, a popular approximation is performed by equating the fermion determinant to 1, or in other words, all of dynamical fermion loops are eliminated. The quenched approximation can be satisfactory in processes which are dominated by heavy valence quarks. The quenching effects are nonperturbative effects and hence are not straightforward to estimate. For certain observables, however, the quenched approximation is a good approximation, for example, the light meson spectrum can be determined within quenched QCD.

Quenched QCD differs from full QCD only in the relative weights of the background gauge configurations, and it exhibits all the important features of full QCD including confinement, asymptotic freedom and spontaneous chiral symmetry breaking. The physical effect of quenching is the absence of all virtual quark loops. Certain quantities and phenomena which are sensitive to the effects of these loops, like string breaking [89], are not reproducible in the quenched approximation. The absence of string breaking leads to a different qualitative behavior of the two theories at large length scales.

In the present work we perform our analysis on quenched gauge configuration since the pair production may occur before the long string limit of the hadronic string is reached. Thus, in this case, the behavior of the pure Yang-Mills theory is more relevant to string picture, which we will investigate in detail.

2.9 Numerical simulation errors

Two types of errors arise in numerical simulations on the discrete lattice, namely, statistical and systematic errors. Statistical errors arise from the finite size of the Monte Carlo sample. For configurations which are statistically independent, the error on a measured observable will fall with \sqrt{N} , where N is the number of configurations used.

Lattice spacing also introduces systematic errors which arise from the discretization of the continuum theory. These types of errors can be reduced by improving the corresponding operators, usually by skilful strategic combination of loops, to eliminate the corresponding effects associated with $\mathcal{O}(a)$ errors. In addition, errors arise from uncertainties and approximations in the extrapolation to the continuum limit.

One systematic error which we will study in detail in Chapter 3 is the isolation of the ground state in the loop operators. This kind of error can be a source of significant uncertainties in calculating the gluonic distribution. The problem arises as a result of the practical constraints due to the limitation imposed by statistical

fluctuation over the evolution in Euclidean time in the operators.

2.10 Markov chain

The direct numerical evaluation of the Euclidean formulated Feynman path integral

$$\langle O_1(U, \psi, \bar{\psi}) O_2(U, \psi, \bar{\psi}) \dots \rangle_E = \frac{1}{Z_E} \int [dU][d\psi][d\bar{\psi}] e^{-S_G^E[U] - S_F^E[U, \psi, \bar{\psi}]} \times \bar{\psi}_\alpha \bar{\psi}_\beta \dots \Gamma_{\alpha'\beta'}^{\alpha\beta}(U) \psi_{\alpha'} \psi_{\beta'} \dots, \quad (2.10.1)$$

is time consuming and becomes practically impossible to calculate for large lattice sizes. Not all the configurations, however, contribute significantly to Eq. (4.3.5). In fact, most of them will have an action which is very large and one needs an efficient importance sampling technique to compute such integrals with the most relevant configurations. This amounts to calculating an ensemble average over a sequence of uncorrelated field configurations with a probability distribution given by Boltzmann factor $e^{-S_{QCD}^E}$. Configurations can be generated such that each configuration is an element of a Markov chain. Let $P(U_{ij}) \equiv P_{ij}$ be the probability of transition from configuration U_i to U_j for a set of configurations $\{U_{\tau_i}\}$ generated by Markov process with recurrence time τ_i [90]. The ensemble average of an observable evaluated on this set of states is

$$\langle O \rangle = \frac{1}{N} \sum_{i=1}^N O(U_{\tau_i}). \quad (2.10.2)$$

A Markov chain is said to be “irreducible” if any state is accessible from any other state. The state is called “aperiodic” if returning to this state need not occur at regular times. An irreducible, aperiodic and positive recurrent Markov chain is said to be ergodic. For an ergodic Markov chain, the limit

$$\lim_{N \rightarrow \infty} P_{ij}^N = \pi_j,$$

exists and is unique [90], where

$$\begin{aligned} \sum_j \pi_j &= 1, \\ \pi_j &= \sum_i \pi_i P_{ij}. \end{aligned} \quad (2.10.3)$$

This defines the equilibrium state, the resultant configuration is completely uncorrelated from the initial configuration used to start the Markov process. Also the system does not change after further updates with transition probabilities P_{ij} . If the chain is irreducible and its states are positive

$$\tau_i^2 \equiv \sum_{n=1}^{\infty} n^2 P_{ii}^n < \infty, \quad (2.10.4)$$

then the time average approaches the ensemble average

$$\langle O \rangle_N = \frac{1}{N} \sum_{i=1}^N \pi_i O(U_i), \quad (2.10.5)$$

with statistical uncertainty of order $O(\frac{1}{\sqrt{N}})$. For a Markov process to sample a probability distribution of the type that is found in lattice gauge theory, it is sufficient to require the transition probability P_{ij} to satisfy the detailed balance

$$\exp(-S(U_i))P(U_i \rightarrow U_j) = \exp(-S(U_j))P(U_j \rightarrow U_i). \quad (2.10.6)$$

2.11 Metropolis algorithm

Let U be a configuration which is to be updated. The new updated configuration U' is suggested with a transition probability $P_0(U \rightarrow U')$ which satisfies the condition

$$P_0(U \rightarrow U') = P_0(U' \rightarrow U). \quad (2.11.1)$$

If the new suggested configuration is such that $\exp(-S[U']) > \exp(-S[U])$ holds, i.e. the action decreases then the configuration U' is accepted. On the other hand, if the action increases, $\exp(-S[U']) < \exp(-S[U])$, then we accept U' with a probability $P(U')$ such that

$$P(U') = \frac{\exp(-S[U'])}{\exp(-S[U])}. \quad (2.11.2)$$

This algorithm has been proposed by Metropolis et al [91] and it is applicable to any system. The algorithm satisfies detailed balance and hence ensures the system reaches equilibrium. The transition probability from the state U to the state U' is given by the probability of accepting the configuration times the probability of suggesting this particular configuration $P_0(U \rightarrow U')$

$$P(U \rightarrow U') = P(U')P_0(U \rightarrow U'). \quad (2.11.3)$$

For a decrease in the action, $\exp(-S[U']) > \exp(-S[U])$, $P(U') = 1$. Otherwise, we have

$$P(U' \rightarrow U) = P_0(U' \rightarrow U) \frac{\exp(-S[U])}{\exp(-S[U'])}. \quad (2.11.4)$$

Since $P_0(U \rightarrow U') = P_0(U' \rightarrow U)$, then it follows that detailed balance is satisfied

$$\exp(-S[U])P(U \rightarrow U') = \exp(-S[U'])P(U' \rightarrow U). \quad (2.11.5)$$

Now, assume the action is increasing

$$\exp(-S[U']) < \exp(-S[U]). \quad (2.11.6)$$

Then

$$P(U \rightarrow U') = P_0(U \rightarrow U') \exp(-S[U'] - S[U]), \quad (2.11.7)$$

$$P(U' \rightarrow U) = P_0(U' \rightarrow U), \quad (2.11.8)$$

which implies that detailed balance holds again.

2.12 Hybrid heat bath/Overrelaxation

A combination of overrelaxation and heat bath steps is a standard simulation algorithm convenient for pure gauge systems. The overrelaxation is non-ergodic microcanonical update to accelerate the decorrelations of the configurations [92]. Both the heat bath and the microcanonical reflections (overrelaxations) are local updates. The heat bath step is ergodic and satisfies detailed balance and hence ensures thermal equilibrium.

2.12.1 Heat-bath algorithm

Generally speaking, it is not straightforward to find an efficient algorithm for generating the configurations of generic fields and actions over which the ensemble average Eq. (2.10.5) is evaluated. A convenient scheme for non-abelian pure gauge theories is the heat bath algorithm [84]. In this section, we discuss this algorithm for generating ergodic Markov chains for $SU(2)$ non-abelian pure gauge theories and generalize the discussion to $SU(N)$.

Each new configuration update is chosen from the canonical distribution

$$P(U \rightarrow U') \propto \exp(-S[U']). \quad (2.12.1)$$

Here, we begin with an $SU(2)$ theory. The $SU(3)$ case can be connected to $SU(2)$ by updating corresponding subgroups and will be discussed later.

$SU(2)$ heat bath

Consider an $SU(2)$ theory with a Wilson gauge action. A heat bath update for local $SU(2)$ colour matrix defines a way to produce the distribution

$$dP(U') \propto e^{\frac{1}{2}Tr(U'Q^\dagger)} dU'. \quad (2.12.2)$$

dU is the Haar measure, and Q is a real multiple of an $\hat{Q} \in SU(2)$ or in other words $Q = \sqrt{\det \hat{Q}} \hat{Q}$. Since the Haar measure is invariant under left and right multiplication with the gauge group elements, R can be considered as a scalar ¹

$$dP(U' \hat{Q}) \propto e^{\frac{1}{2}\sqrt{\det Q} Tr(U')} dU'.$$

The isomorphism φ between the group Q of normalized quaternions and $SU(2)$ is given below

$$U' = \varphi(a) = \begin{pmatrix} a_0 + ia_3 & ia_1 - a_2 \\ ia_1 + a_2 & a_0 - ia_3 \end{pmatrix}. \quad (2.12.5)$$

¹

$\int dU f(U) = \int dU f(GUH^{-1}), \quad G, H \in SU(N), \quad (2.12.3)$

and it is normalized,

$$\int dU = 1. \quad (2.12.4)$$

In the quaternionic representation of $SU(2)$, we have $\frac{1}{2}Tr(\varphi(a)) = a_0$. Hence, a distribution $\exp(ca_0)d\mu(a)$ with $d\mu$ being the Haar measure on Q and it takes the form

$$d\mu(a) = \frac{1}{2\pi^2} \delta(a^2 - 1) d^4 a. \quad (2.12.6)$$

It is easy to see that $\delta(a^2 - 1)d^4 a$ is proportional to $(1 - a_0^2)^{1/2} da_0 dn$, $a_0 \in [-1, 1]$ and dn is a uniform measure on S^2 .

$$dP(U' \hat{Q}) \propto \frac{1}{\pi^2} \delta(a^2 - 1) e^{\sqrt{\det Q} a_0} da_0 d^3 \mathbf{a}. \quad (2.12.7)$$

Setting $a_j = n_j \sqrt{1 - a_0^2}$ and $\eta = \sqrt{Q_0^2 + Q_j Q_j}$ it follows

$$dP(U' \hat{Q}) \propto \frac{1}{\pi^2} e^{\eta a_0} \sqrt{1 - a_0^2} da_0 d\mathbf{n}. \quad (2.12.8)$$

This entails generating a flat distribution in a_0 and a uniform distribution on S^2 . These produce a matrix U' , which is, according to Eq. (2.12.7), to be multiplied with \hat{Q} to obtain the new link variable. The \mathbf{n} vector can be generated by a pair (u_1, u_2) of numbers with a uniform distribution in $[0, 1)$ such that

$$\begin{aligned} n_1 &= 1 - 2u_1, \\ n_2 &= \sqrt{1 - n_1^2} \cos(2\pi u_2), \\ n_3 &= \sqrt{1 - n_1^2} \sin(2\pi u_2). \end{aligned} \quad (2.12.9)$$

Fabricius and Haan [93] and Kennedy and Pendleton [94] described an updating algorithm. For a variable y with the distribution

$$P(y) \propto \exp(-y) \sqrt{y} \theta(y). \quad (2.12.10)$$

we set $a_0 = 1 - y\eta$. The distribution of the generated a_0 then is given by

$$\begin{aligned} \bar{P}(a_0) da_0 &= P(y) dy, \\ \Rightarrow \bar{P}(a_0) &= P(y(a_0)) \frac{dy}{da_0}, \\ &\propto e^{\eta a_0} \sqrt{1 - a_0} \theta(1 - a_0). \end{aligned} \quad (2.12.11)$$

The factor $\sqrt{1 - a_0} \theta(1 - a_0)$ can be accommodated by an acceptance step. The proposal from Eq. (2.12.11) is then accepted if a flat random number c fulfills $2c^2 \leq 1 + a_0$. This corresponds to a $P_1(c) = \theta(2c^2 - 1 - a_0)$ and therefore

$$\begin{aligned} \int dc \bar{P}(a_0) P_1(c) &= \int_0^{\sqrt{(1-a_0)/2}} dc e^{\eta a_0} \sqrt{1 - a_0} \theta(1 - a_0) \theta(1 + a_0), \\ &= e^{\eta a_0} \sqrt{1 - a_0} \theta(1 - a_0) \\ &\propto P(a_0). \end{aligned} \quad (2.12.12)$$

Two distributions can be combined to reproduce the desired one. In order to create a value for a_0 , one generates a number a with a Gaussian distribution

$$P_1(a) \propto \exp(-a^2)\theta(a), \quad (2.12.13)$$

and a number b distributed like

$$P_2(b) \propto \exp(-b)\theta(b). \quad (2.12.14)$$

Transforming the variables to $y = a^2 + b$ and $z = a$ with the Jacobian

$$\det \frac{\partial(a, b)}{\partial(y, z)} = 1. \quad (2.12.15)$$

The covariant distribution of y and z is

$$\begin{aligned} P(y, z) &= P_1(a(y, z), b(y, z)) \times P_2(a(y, z), b(y, z)), \\ &= \exp(-z^2)\theta(z) \times \exp(-y + z^2)\theta(y - z^2), \\ &= \exp(-y)\theta(z)\theta(\sqrt{y} - z). \end{aligned} \quad (2.12.16)$$

The resulting distribution of y is obtained by integrating over z ,

$$P(y) = \int dz P(y, z) = \sqrt{y} \exp(-y)\theta(y). \quad (2.12.17)$$

The distributions P_1 is Gaussian. P_2 can be generated from uniformly distributed random numbers u by taking $b = -\log(1 - u)$.

SU(3) heat bath

The general form of the Wilson action is

$$S[U] = -\Re \text{Tr} \{ U(x, \mu) Q^\dagger(x, \mu) \} + \dots \quad (2.12.18)$$

The above action has two parts: one linearly proportional to the link variable $U(x, \mu) \in SU(3)$ ($N \geq 3$), which is updated, and the other part is independent.

The term $Q(x, \mu)$ is proportional to the sum of the six staples of the link

$$\begin{aligned} Q(x, \mu) &= \frac{\beta}{3} \sum_{\nu \neq \mu} \left\{ U(x, \nu) U(x + a\hat{\nu}, \mu) U^\dagger(x + a\hat{\mu}, \nu) + \right. \\ &\quad \left. U^\dagger(x - a\hat{\nu}, \nu) U(x - a\hat{\nu}, \mu) U(x - a\hat{\nu} + a\hat{\mu}, \nu) \right\}. \end{aligned} \quad (2.12.19)$$

The sum of the staples need not be a real multiple of an element of the gauge group. Factorizing the distribution for U into several flat distributions requires an elaborate method. Cabibbo and Marinari generalized the heat bath algorithm described above [95] by projecting into subgroups successively. The method for the $SU(3)$ group and can be applied to $SU(N)$ groups.

In this method, a set \mathcal{F} of $SU(2)$ subgroups of $SU(3)$ are selected such that no subset of $SU(3)$ is left invariant under left multiplication by \mathcal{F} , except for the whole group

$$\mathcal{F} = \{SU(2)_1, \dots, SU(2)_m\}, \quad m \geq 2. \quad (2.12.20)$$

By successive multiplication of an $SU(3)$ matrix with random matrices with the desired distribution from these subgroups we can reach any other $SU(3)$. The new link in each step comes by applying to the one from the previous step a member $A^{(k)} \in SU(2)_k$ of a subgroup

$$U^{(k)} = A^{(k)} U^{(k-1)}. \quad (2.12.21)$$

The matrices $A^{(k)}$ are selected according to the distribution

$$dP(A_k) = dA^{(k)} \frac{\exp\{-S[A^{(k)}U^{(k-1)}]\}}{\int_{SU(2)_k} dA \exp\{-S[AU^{(k-1)}]\}}. \quad (2.12.22)$$

The two subgroups of $SU(3)$ can be selected such as

$$A_1 = \begin{pmatrix} a_{11} & a_{12} & 0 \\ a_{21} & a_{22} & 0 \\ 0 & 0 & 1 \end{pmatrix}, \quad A_2 = \begin{pmatrix} 1 & 0 & 0 \\ 0 & a_{11} & a_{12} \\ 0 & a_{21} & a_{22} \end{pmatrix}, \quad (2.12.23)$$

where $a \in SU(2)$. Although the above stated condition implies only two subgroups, one may employ, as we do, a third subgroup

$$A_3 = \begin{pmatrix} a_{11} & 0 & a_{12} \\ 0 & 1 & 0 \\ a_{21} & 0 & a_{22} \end{pmatrix}. \quad (2.12.24)$$

This may lead to better autocorrelation times than the minimum of two subgroups.

In our choice of subgroups, it is obvious that

$$S[A^{(k)}U^{(k-1)}] = -\Re \operatorname{Tr}(av), \quad (2.12.25)$$

where v is the $(i, j) \in \{(1, 2), (2, 3), (1, 3)\}$ submatrix of $\Gamma = U^\dagger V$,

$$\gamma = \begin{pmatrix} \Gamma_{ii} & \Gamma_{ij} \\ \Gamma_{ji} & \Gamma_{jj} \end{pmatrix}. \quad (2.12.26)$$

By using the quaternionic representation of a_k and γ , we can recast this into the form

$$\begin{aligned} S[A^{(k)}U^{(k-1)}] &= -\Re \operatorname{Tr}(a\gamma) \\ &= -\Re(a_0\gamma_0 - a_jq_j) \\ &= -\frac{1}{2}\operatorname{Tr}(aq^\dagger), \end{aligned} \quad (2.12.27)$$

where q is a real multiple of an $SU(2)$ matrix. Its quaternionic components are given by

$$\begin{aligned} q_0 &= 2\Re\gamma_0, \\ q_j &= -2\Re q_j, \end{aligned} \quad (2.12.28)$$

and explicitly by

$$\begin{aligned} q_0 &= \Re\Gamma_{ii} + \Re\Gamma_{jj}, \\ q_1 &= -\Im\Gamma_{ij} - \Im\Gamma_{ji}, \\ q_2 &= -\Re\Gamma_{ii} + \Re\Gamma_{ji}, \\ q_3 &= -\Im\Gamma_{ii} + \Im\Gamma_{jj}. \end{aligned} \quad (2.12.29)$$

Equation (2.12.27) shows that Eq. (2.12.22) can be obtained by applying the described Fabricius-Haan algorithm for $SU(2)$.

2.12.2 Overrelaxation

The overrelaxation steps amount to updating the new link variable such that the action remains constant. This helps when we want to sweep quickly through the configuration space and accelerate the decorrelation of physical observables. For a pure $SU(2)$ gauge theory with a Wilson-like action, where Q is the sum of elements of the gauge group, we can update $U \rightarrow U'$ such that

$$Tr(U'Q^\dagger) = Tr(UQ^\dagger), \quad (2.12.30)$$

or equivalently

$$U' = \frac{2}{Tr(Q^\dagger Q)} Q U^\dagger Q. \quad (2.12.31)$$

For a general action of the form Eq. (2.12.18), in analogy to the heat bath case, microcanonical updates can be performed on some $SU(2)$ subgroups of the variable in question. We obtain a new U' by applying matrices A_k in accord to Eq. (2.12.23)

$$U' = A_3 A_2 A_1 U. \quad (2.12.32)$$

To ensure constant action, the condition over the $SU(2)$ matrices, a , corresponding to the A_k will be

$$Tr(aq^\dagger) = Tr(q^\dagger). \quad (2.12.33)$$

In the quaterionic form this reads

$$a = -1 + 2 \frac{2q_0}{Tr(qq^\dagger)} q. \quad (2.12.34)$$

A possible overflow in the implementation of these algorithms may arise due to a potentially small value of $Tr(qq^\dagger)$. A condition may be imposed during the implementation such that no reflection of the link variable occurs when the denominator becomes smaller than a given value.

The Hybrid Overrelaxation combines the two parts described above. The update step consists of one heat bath step followed by N_{OR} microcanonical reflection steps. N_{OR} is a simulation parameter that can be tuned to reduce the autocorrelation times and depends on lattice sizes.

Chapter 3

Systematic Uncertainties in Wilson-loop

3.1 Outline

In this Chapter, the measurement technique for calculating the gluonic distributions is described. The gluonic field distribution is calculated as a correlation between the flux probe operator and the operator used to construct the static mesonic and baryonic states. Wilson loops and Polyakov line operators correspond to two methodologically different ways to construct infinitely heavy quark states. In this chapter, we discuss both approaches to the problem of calculating the gluonic flux distribution and the systematic uncertainties due to the bias inherent in the shape of the Wilson loop. The basic elements of the field theory formulation at finite temperature are introduced.

3.2 Introduction

Revealing the form of the gluonic field distributions among interacting quarks is an active field of research. As a consequence of improvements in computational resources and analysis techniques, tackling this problem by employing lattice QCD techniques has become readily achievable. Several studies [2, 96, 97, 98, 99] have been conducted to explore the shape of these distributions and some studies [2, 99] have been devoted to improve the statistics. However, systematic effects due to the bias by the source shape in the operators remain under investigation.

3.3 Flux distribution calculation

In order to reveal the distribution of the gluonic field, a source operator representing the quark bound state has to be adopted. Wilson loop operators can account for a gauge invariant, colour singlet, and an infinitely heavy quark state. Consider a baryonic system which is constructed with a three quark Wilson loop [3, 100]. This quark operator consists of three quarks connected by strings of gauge field links which assume a particular shape. The generic form of the three-quark (3Q) Wilson loop operators (Fig. 3.1) is given by

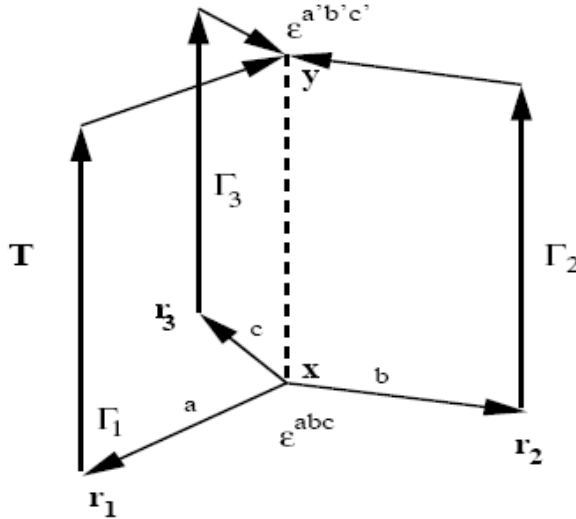


Figure 3.1: The three-quark Wilson loop operator.

$$W_{3Q} = \frac{1}{3!} \varepsilon_{abc} \varepsilon_{ab'c'} U_1^{aa'} U_2^{bb'} U_3^{cc'}, \quad (3.3.1)$$

with the path-ordered link variables

$$U_j = P \exp \{ig \int_{\Gamma_j} dx_\mu A^\mu(x)\}. \quad (3.3.2)$$

After the construction of the baryonic state, subsequent measurement by a gauge-invariant flux probe operator is taken at each point of the lattice. With the convenient choice of the components of the field strength, one can measure action density, energy density, chromo-electric or chromo-magnetic fields. The gluon flux density distribution is calculated through a correlation of the form

$$C(\vec{y}, \vec{r}_1, \vec{r}_2, \vec{r}_3, t) = \frac{\langle W_{3Q}(\vec{r}_1, \vec{r}_2, \vec{r}_3; t) S(y, t/2) \rangle}{\langle W_{3Q}(\vec{r}_1, \vec{r}_2, \vec{r}_3; t) \rangle \langle S(y, t/2) \rangle}, \quad (3.3.3)$$

where $\langle \dots \rangle$ denotes averaging over configurations, and $S(y, t/2)$ is a generic gauge-invariant density observed at spatial coordinate \vec{y} and Euclidean time $t/2$ measured relative to the origin of the three-quark Wilson loop. $C(\vec{y})$ is a scalar field in three dimensions. For values of \vec{y} well away from the quark positions \vec{r}_i , there are no correlations and $C \rightarrow 1$. C is found [1] generally to be positive and less than 1 in the interior of the heavy-quark baryon indicating expulsion of vacuum fluctuations (Fig. 3.2).

3.4 Source-shape dependence

As discussed in the previous chapter, systematic errors are possible in all lattice simulations, and these effects are obvious in the gluon-flux distribution calculations.

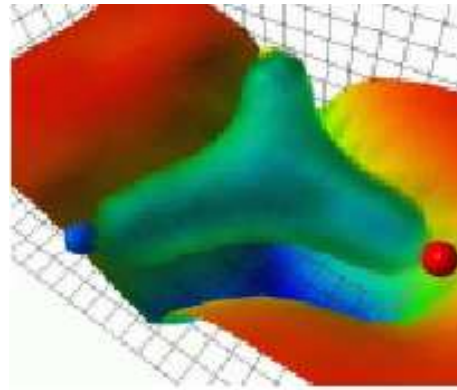


Figure 3.2: Spatial points [1] where vacuum field fluctuations are maximally suppressed in the three-quark system as measured by the correlation function $C(\vec{y})$.

NOTE:

This figure is included on page 37
of the print copy of the thesis held in
the University of Adelaide Library.

Figure 3.3: The rendered gluonic field distribution via Eq. (3.3.3) mimics the form of the spatial link configurations in Wilson loop [2].

The so-called source-shape dependence is the main systematic effect that is of concern in these calculations. Given a fixed quark geometry, many different spatial-link configurations can be adopted in the Wilson loop operator before evaluating the correlation function Eq. (3.3.3). The rendered colour field distribution mimics the form of the spatial links as illustrated in Fig. 3.3. This source-shape dependence is a consequence of two underlying difficulties regarding lattice simulations. The first difficulty concerns the isolation of the ground state, and the second is related to the control of the statistical fluctuations. Isolating the ground state of the three-quark colour source system is achieved by increasing the Wilson loop time t . As the time evolves, the excited components drop faster than the ground state components in the expectation values mentioned above. However, the ground state also decreases exponentially; this is the source of the ground state isolation difficulty.

Usually, the isolation of the ground state problem is tackled by the enhancement of the ground state through the use of smearing technique. One of the most popular technique for smearing is the so-called APE smearing [101]. In this technique, the link is iteratively updated by averaging it with its neighboring links via staples, then projecting back to $SU(3)$ by the Cabbibo Marinari [95] maximization of the $Tr(U_\mu(x) U_\mu'^\dagger(x))$. The transformation takes the form

$$U'_\mu(x) = (1 - \alpha)U_\mu(x) + \frac{\alpha}{4} \sum_{\mu \neq \nu} \Sigma_{\mu\nu}^\dagger(x),$$

with the sum of the staples

$$\Sigma_{\mu\nu}^\dagger = \{U_\nu(x)U_\mu(x + \hat{\nu})U_\nu^\dagger(x + \hat{\mu}) + U_\nu^\dagger(x - \hat{\nu})U_\mu(x - \hat{\nu})U_\mu^\dagger(x + \hat{\nu} - \hat{\mu})\}. \quad (3.4.1)$$

The new link variable $U_\mu(x)$ is obtained from the link variable $U'_\mu(x)$ via the projection \mathcal{P} onto the $SU(3)$ group

$$U_\mu(x) = \mathcal{P} U'_\mu(x). \quad (3.4.2)$$

The above transformation defines a single APE smearing sweep. The APE smearing is characterized by two parameters: α which determines the fraction of smearing and n_{APE} which defines the number of smearing sweeps. The two parameters are tuned so as to obtain the optimal enhancement of the ground state of the quark system.

Smearing the spatial links in Wilson loop operators is justified by the fact that the path of the links used to construct the three quark creation operator can not affect the eigenvalues of the transfer matrix. Thus, the freedom in the choice of the path links can be exploited in tuning the best states that enhance the ground state overlap. The smearing technique does not affect the physics itself, and it can be counted merely as a method for adopting the interpolating fields in the transfer matrix formalism [99].

Dependence on the choice of the source operator indicates that non-ground state contaminations contribute to the correlation function. On the other hand, enhancing the ground state by gauge smoothing techniques alone [63, 101] will not overcome the problem of biasing by the shape of the source [2, 99].

NOTE:
 This figure is included on page 39
 of the print copy of the thesis held in
 the University of Adelaide Library.

Figure 3.4: The ground-state overlap of the 3Q system [3]. $C_0 = \langle W_{3Q}(T) \rangle^{T+1} / \langle W_{3Q}(T+1) \rangle^T$, with the smeared link (upper data) and unsmeared link (lower data) [3]. The horizontal axis has been taken as L_{min} , with the minimal length of the flux tubes linking the three quarks. For each 3Q configuration C_0 is largely enhanced as $0.8 < C_0 < 1$ by smearing.

This is due to the fact that isolating the ground state requires a large time interval between the source and the sink as well as between the source and the sink and the flux probe. Let us illustrate the above discussion further:

Consider the two-point correlation function at $T > 0$

$$\begin{aligned} \langle \Omega | O(T) O(0) | \Omega \rangle &= \sum_n e^{-E_n T} \langle \Omega | O(0) | n \rangle \langle n | O(0) | \Omega \rangle, \\ &\xrightarrow[T \rightarrow \infty]{} e^{-E_0 T} \langle \Omega | O(0) | 0 \rangle \langle 0 | O(0) | \Omega \rangle. \end{aligned} \quad (3.4.3)$$

For the three-point function $T > t$

$$\begin{aligned} \langle \Omega | O(T) P(t) O(0) | \Omega \rangle &= \sum_{nn'} e^{-E_n(T-t)} e^{-E_{n'} t} \langle \Omega | O(0) | n \rangle \langle n | P(0) | n' \rangle \langle n' | O(0) | \Omega \rangle, \\ &\xrightarrow[T \rightarrow \infty]{} e^{-E_0 T} \langle \Omega | O(0) | 0 \rangle \langle 0 | P(0) | 0 \rangle \langle 0 | O(0) | \Omega \rangle. \end{aligned} \quad (3.4.4)$$

The correlation function which gives the field distribution is

$$\begin{aligned} C(t) &= \frac{\langle \Omega | O(T) P(t) O(0) | \Omega \rangle}{\langle \Omega | O(T) O(0) | \Omega \rangle \langle \Omega | P(0) | \Omega \rangle}, \\ &\xrightarrow[T \rightarrow \infty]{} \frac{\langle 0 | P(0) | 0 \rangle}{\langle \Omega | P(0) | \Omega \rangle}. \end{aligned} \quad (3.4.5)$$

The correlation function measures the ground state expectation value of the operator $P(0)$ to that of the vacuum, and the condition $0 \ll t \ll T$ is required to isolate the ground state. This requires a time interval much larger than that needed

for the two point function, which yields the potential, where one only needs $T \gg 0$. This clearly indicates that the dependence on the shape of the source operator in simulations is due to non-ground state contributions.

Although the smearing of the spatial links can be effective in enhancing the overlap with the ground state [102], the flux distribution calculation is very noisy [99]. Attempts to improve the statistics have been made, for example, in Ref. [98, 99], a maximal abelian projection has been used. The abelian projected theory is less noisy and is believed to preserves the long distance behaviour of the Wilson loop [61]. In other calculations [63], the noise reduction is achieved only via integrating out the time links. In these calculations, the time links are replaced by the mean field value which they take in the neighbourhood of the links that interact through the staples. One should note that these calculations are performed for SU(2) lattice gauge theory, where the noise level is much less than in the SU(3) case. In the calculations of Ref. [2], a gauge-independent high statistics approach is used to improve the statistics. This has been done by exploiting the lattice translational symmetries. That is, the correlation is computed in every node of the lattice, averaging the results over the four-volume. This is the only case where the time-oriented links have remained untouched to preserve the correct static quark potential at all separations.

The correlation function can be calculated by studying the ground state expectation values of the ground state of the Wilson loop for large Euclidean times. However, as mentioned above, this situation is not practically feasible. The numerical signal is drowned in statistical noise for large times. On the other hand, the adoption of Wilson loops imposes an inevitable choice on the string configuration of the quark source operator, which due to the limitation over the time possible to evolve the Wilson loop, would still affect the form of the calculated field distribution (see Fig. 3.3). The success in improving the statistics was limited to the potential calculations and this effect remained on the level of the flux distribution. Therefore, a new approach is warranted.

3.5 Stringless operators

The immediate idea that can be proposed is to use a different set of stringless gauge-invariant operators. There are particularly relevant types of gauge-invariant objects that construct an infinitely heavy quark which is well-known as the Polyakov loop or Wilson thermal line [103, 104]. The Polyakov line acquires its loop structure via the lattice periodicity over the time direction; i.e. by the product of link variables along loops winding around the time direction

$$P(x) = \text{Tr} \left[\prod_{n_t=1}^{N_t} U_4(x, n_t) \right]. \quad (3.5.1)$$

The trace guarantees the gauge-invariance

$$\begin{aligned} \tilde{P}(x) = & \text{Tr}[G(x, 1) U_4(x, 1) G^\dagger(x, 2) G(x, 2) U_4(x, 2) G^\dagger(x, 3) \dots \\ & G(x, N_t) U_4(x, N_t) G^\dagger(x, N_t + 1)]. \end{aligned} \quad (3.5.2)$$

$$\tilde{P}(x) = G(x, 1) \left[\prod_{n_t=1}^{N_t} U_4(x, n_t) \right] G^\dagger(x, N_t + 1) = P(x). \quad (3.5.3)$$

because of the periodicity

$$G(x, 1) = G(x, N_t + 1). \quad (3.5.4)$$

A physical meaning can be assigned to the Polyakov line by realizing an infinitely heavy quark sitting at a given point x in space and only propagating in the time direction. The Euclidean-Schrodinger equation is given by

$$\partial_t \Psi^{(Q)} = i A_0(x, t) \Psi^{(Q)}(x, t). \quad (3.5.5)$$

The time evolution operator $S(t)$ is then

$$S(t) = P \exp[i \int^t d\tau A_0(x, \tau)], \quad (3.5.6)$$

which is the continuum version of the Polyakov line. It describes the propagation of a static colour charge on the lattice.

Calculating the expectation value of the Polyakov line at finite temperature T , corresponds to the partition function of the system

$$\langle P(x) \rangle = Z_Q = \exp(-F_Q/T), \quad (3.5.7)$$

with the free energy of the system F_Q .

Let us find the form of the correlator which represents the creation at time $t = 0$ of two static colour sources, and separated by spatial distance R . This gauge-invariant colourless physical state can be represented by massive quark and antiquark creation operators acting on a chromodynamical vacuum state $|\Omega\rangle$,

$$|\chi^\dagger(\vec{x}, \vec{y}; t = 0)\rangle = \bar{\psi}^b(\vec{y}, t = 0) U^{ba}(\vec{x}, t = 0; \vec{y}, t = 0) \psi^a(\vec{x}, t = 0) |\Omega\rangle \quad (3.5.8)$$

with

$$U^{ab}(\vec{x}, t = 0, \vec{y}, t = 0) = \exp[i g \int_{\vec{x}}^{\vec{y}} dz^i A_i(\vec{z})]. \quad (3.5.9)$$

If the colour sources are propagated for time t and then annihilated, the correlation between the two states becomes

$$\begin{aligned} G = & \langle \Omega | \bar{\psi}^a(\vec{x}, t) U^{ab}(\vec{x}, \vec{y}; t) \times \\ & \psi^b(\vec{y}, t) \bar{\psi}^{b\prime}(\vec{y}, t = 0) U^{b'a'}(\vec{y}, t = 0; \vec{x}, t = 0) \psi^{a'}(\vec{x}, t = 0) | \Omega \rangle. \end{aligned} \quad (3.5.10)$$

The quarks interact while propagating through time. Inserting a complete set of eigenstates gives

$$G(x, y, t) = \sum_n \langle \Omega | \chi(x, y, t) | n \rangle \langle n | \chi^\dagger(x, y, 0) | \Omega \rangle. \quad (3.5.11)$$

Making use of the translational invariance and evaluating eigenstates of the Hamiltonian

$$\chi(x, y, t) = \exp(-iHt)\chi(x, y, 0)\exp(iHt), \quad (3.5.12)$$

the correlation is then

$$G(x, y, t) = \sum_n \lambda_n^2 \exp(-iE_n t), \quad (3.5.13)$$

where

$$\lambda_n^2 = |\langle \Omega | \chi(x, y, 0) | n \rangle|^2. \quad (3.5.14)$$

In a Euclidean space, $t \rightarrow -it$ and

$$G(x, y, t) = \sum_n \lambda_n^2 \exp(-E_n t). \quad (3.5.15)$$

E_n are the eigenstates of the Hamiltonian. It is the sum of kinetic, potential energy, and self energy of the system. The last equation is the vacuum expectation value at the hadronic level.

Consider Eq. (3.5.10) which has the formal path integral representation

$$G = \frac{1}{Z} \int D\mathcal{A} D\psi D\bar{\psi} \exp(-iS) \bar{\psi}^a(\vec{x}, t) U^{ab}(\vec{x}, \vec{y}; t) \psi^b(\vec{y}, t) \bar{\psi}^{b\prime}(\vec{y}, t=0) U^{b\prime a\prime}(\vec{y}, t=0; \vec{x}, t=0) \psi^{a\prime}(\vec{x}, t=0), \quad (3.5.16)$$

where the action is given by

$$S = S_G[\mathcal{A}] + S_F[\psi, \bar{\psi}, \mathcal{A}], \quad (3.5.17)$$

$$S_G[\mathcal{A}] = -\frac{1}{2} \int d^4x \text{Tr}(F_{\mu\nu}F^{\mu\nu}), \quad (3.5.18)$$

$$S_F[\psi, \bar{\psi}, \mathcal{A}] = \int d^4x \bar{\psi}(i\gamma^\mu D^\mu - M) \psi. \quad (3.5.19)$$

Performing integration over Grassmann variables yields

$$G = -\frac{1}{Z} \int D\mathcal{A} [S^{bb\prime}(y, t, t=0) U^{b\prime a\prime}(\vec{y}, \vec{x}, t=0) S^{a\prime a}(\vec{x}, t=0, t) U^{ab}(\vec{x}, \vec{y}, t)] \det(K[\mathcal{A}]) e^{iS_G+iS_F}, \quad (3.5.20)$$

where

$$K[\mathcal{A}] = (i\gamma^\mu D^\mu - M). \quad (3.5.21)$$

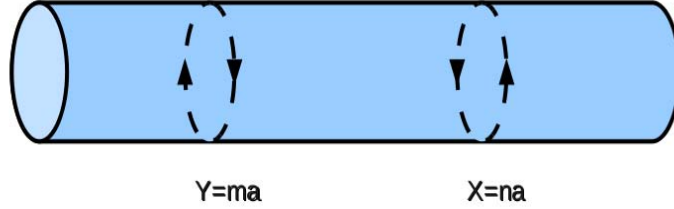


Figure 3.5: The static mesonic state is constructed via two Polyakov loops winding around the time in opposite directions.

In the quenched approximation

$$\det(K[A]) = 1. \quad (3.5.22)$$

In contrast, the correlation function for the Polyakov loop correlator is

$$G_p = -\frac{1}{Z} \int DA [S^{bb}((y, N_t), (y, 0)) S^{aa}((x, 0), (x, N_t))] \det(K[A]) \exp(iS_G + iS_F). \quad (3.5.23)$$

It is very important to note that despite the existence of a mathematical relation¹, the two correlators of Eq. (3.5.20) and Eq. (3.5.23) address different physics. While the Wilson loop utilizes the overlap of the interpolating fields in the transfer matrix formalism, the Polyakov loops correlator addresses physics of the free-energy of the system.

For $x_0 > y_0$ the free propagator is

$$S((x, x_0), (y, y_0)) = \mathcal{P} \exp[ig \int_{x_0}^{y_0} dx_0 A_0(x) \delta^3(x - y) P_+ e^{-m_q(x_0 - y_0)}]. \quad (3.5.24)$$

For $y_0 > x_0$

$$S((x, x_0), (y, y_0)) = \mathcal{P} \exp[ig \int_{x_0}^{y_0} dy_0 A_0(x) \delta^3(x - y) P_- e^{-m_q(y_0 - x_0)}]. \quad (3.5.25)$$

Substituting the propagators into Eq. (3.5.23) yields

$$G_p(x, y, t) = \exp(-2m_q N_t) \langle P(\vec{y}) P^\dagger(\vec{x}) \rangle, \quad (3.5.26)$$

¹Mathematically, the above correlation function can be related to Eq. (3.5.20) of the Wilson loop by setting $b = b'$ and $t = N_t$ and making use of the boundary condition over the time-coordinate

$$U^{ab}(\vec{x}, \vec{y}, t=0) U^{\star ba'}(\vec{y}, \vec{x}, t=N_t) = \delta^{aa'}.$$

NOTE:

This figure is included on page 44
of the print copy of the thesis held in
the University of Adelaide Library.

Figure 3.6: (a) Average Polyakov loop over several successive Monte Carlo measurements [4], below the transition temperature (in the confined phase), (b) above the transition temperature.

with

$$\begin{aligned} \langle P(y) P^\dagger(x) \rangle &= \frac{1}{Z} \int D A \exp(-S_G) \\ &\quad \left[\mathcal{P} \text{Tr} \left[\exp(i g \int_0^{N_t} dt A_0(y)) \right] \mathcal{P} \text{Tr} \left[\exp(-i g \int_0^{N_t} dt A_0(x)) \right] \right]. \end{aligned} \quad (3.5.27)$$

On the lattice, $P(x)$ is given by Eq. (3.5.1).

The above correlation function correlates two Polyakov loops with bases at $\vec{y} = \vec{m}a$ and $\vec{x} = \vec{n}a$ with a lattice spacing, and having opposite orientations. This correlator is the object that we wish to substitute in Eq. (3.3.3) instead of the Wilson loop W , if we are going to calculate the gluonic field distribution for mesonic systems.

One may follow a simple symmetry argument, regarding the centre symmetry, to find the form of these correlators for mesonic as well as baryonic systems. The lattice action as well as the above correlators Eq. (3.5.27) are invariant under the centre symmetry transformation. This symmetry is necessary but not a sufficient condition to ensure a non-vanishing value of the Polyakov correlator. Consider, for example, the elements of $SU(3)$ belonging to the centre C of the group. The centre C of the group G consists of all the elements z for which $z g z^{-1} = g$, with $g \in G$ and they are given by $\exp(2\pi i l/3) \in Z(3)$ where $l = 0, 1, 2$. The centre symmetry transformation

$$\tilde{U}_4(x, n_\tau = 1) = C U_4(x, n_\tau = 1) \quad (3.5.28)$$

takes all time-like link variables in a hyperplane for some fixed time $n_\tau = 1$ and transforms these links by a unitary 3×3 matrix Z belonging to the centre of the gauge group.

Now, if the ground state of the quantum system respects the symmetry of the classical action, then link configurations related by centre symmetry will occur with the same probability, and the same number of configurations will yield the values

$P_l = e^{2\pi i l/3}$ ($l = 0, 1, 2$) for one Polyakov loop. Since $\Sigma_l \exp(2\pi i l/3) = 0$, it follows that the expectation value of the Polyakov loop must vanish. Therefore, the correlators for baryonic systems must be necessarily invariant with respect to the centre symmetry in order to fulfil the necessary condition of a non-vanishing expectation value of the correlators. The form of the mesonic correlator is

$$\begin{aligned}\Gamma_{\text{Mesonic}} &= \langle \tilde{P}(\vec{x}) \tilde{P}^\dagger(\vec{y}) \rangle \\ &= \langle P(\vec{x}) P^\dagger(\vec{y}) \rangle.\end{aligned}\quad (3.5.29)$$

The three-loop correlator reads

$$\begin{aligned}\Gamma_{\text{Baryonic}} &= \langle \tilde{P}(\vec{x}) \tilde{P}(\vec{y}) \tilde{P}(\vec{z}) \rangle, \\ &= \langle e^{2i\pi l} P(\vec{x}) P(\vec{y}) P(\vec{z}) \rangle, \\ &= \langle P(\vec{x}) P(\vec{y}) P(\vec{z}) \rangle.\end{aligned}\quad (3.5.30)$$

This correlator constructs an infinitely heavy baryon.

Correlation functions of Polyakov loops define the free energy of a heavy quark and anti-quark. One generally considers the so-called colour averaged free energy

$$e^{-F(r,T)/T+C} = \frac{1}{9} \langle P(\vec{x}) P^\dagger(\vec{y}) \rangle, \quad (3.5.31)$$

where P is the traced Polyakov loop defined in Eq. (3.5.1), and C is a renormalization constant.

The idea of unravelling the gluon-flux distribution using Polyakov thermal loops brings us to the regime of finite temperature QCD, where certain considerations regarding the finite-temperature lattice QCD, such as determining the lattice temperature, should be taken into account.

3.6 Lattice QCD at finite temperature

In order to employ statistical mechanics techniques in the path-integral representation of the field theory of the partition function

$$Z = \int [d\phi] e^{iS[\phi]}, \quad (3.6.1)$$

the theory has to be formulated in Euclidean space-time. The Euclidean Lagrangian,

$$\mathcal{L}_{QCD}^E = \sum_{k=1}^{n_f} \psi_{q,a} (\gamma_\mu^E D_\mu + m_q)_{ab} \psi_b^k + \frac{1}{4} \sum_{a=1}^{N_c^2-1} F_{\mu\nu}^a(x) F_a^{\mu\nu}(x), \quad (3.6.2)$$

is obtained from the Minkowski expression by rotation to imaginary time τ

$$t \longrightarrow -i\tau. \quad (3.6.3)$$

The anti-commuting relations for the Euclidean γ matrices are

$$\{\gamma_\mu^E, \gamma_\nu^E\} = 2\delta_{\mu\nu}. \quad (3.6.4)$$

Finite temperature field theory is defined by the Matsubara formalism [105] for finite temperature statistical systems. The temperature is defined through restricting the Euclidean time interval to $[0, \frac{1}{T}]$. The grand canonical partition function Z can be written as

$$Z = \text{Tr}(e^{-H/T}) = \int [d\phi] e^{-S[\phi]}. \quad (3.6.5)$$

The thermodynamical expectation value of an operator O is

$$\langle O(\bar{\psi}, \psi; A) \rangle = \frac{\text{Tr}(O(\bar{\psi}, \psi; A))}{Z}. \quad (3.6.6)$$

This expression is formally equivalent to the path-integral representation of the expectation value of the operator O

$$\langle O(\bar{\psi}, \psi; A) \rangle = \frac{1}{Z^E} \int DAD\bar{\psi}D\psi O(\bar{\psi}, \psi; A) e^{-S_{QCD}^E}. \quad (3.6.7)$$

with the Euclidean action

$$S_{QCD}^E(T, V) = \int_0^{\beta=1/T} d\tau \int_V d^3x \mathcal{L}_{QCD}^E \quad (3.6.8)$$

and the partition function

$$Z^E(T, V) = \int \mathcal{D}A \mathcal{D}\bar{\psi} \mathcal{D}\psi e^{-S_{QCD}^E(T, V)}. \quad (3.6.9)$$

Therefore, one can calculate the expectation value of a given operator within QCD at finite temperature by restricting the Euclidean time extension. Due to the trace operation in Eq. (3.6.6), bosonic and fermionic fields must obey periodic and anti-periodic boundary conditions in Euclidean time direction respectively.

Studying QCD at finite temperature in Monte Carlo simulation requires a careful choice of the spatial and temporal extensions of the lattice to be used as the latter determines the temperature. In general, these principles should be considered:

- The choice of the spatial volume should be large enough so as to ignore the finite volume size effects.
- The bare coupling constant should be small enough to approximate the continuum physics. For a given number of lattice sites, the lattice extension will depend on the lattice spacing, and consequently, on the value of the bare coupling.
- To study QCD at high temperatures, the temporal extension is typically smaller than the spatial one.

- Varying the physical temperature can be done either by varying the number of temporal slices N_t , or by varying the bare coupling g_0 . Changing the temperature by varying β has the disadvantage that the volume (in physical units) does change as well. The temperature can be changed without altering the volume of the system $V = (N_x)^3$ in the former method. However, the disadvantage of this approach is that N_t is an integer. In addition, many lattice gauge codes require even values of N_t , so that the variation possibilities of the temperature $\frac{1}{N_t a} - \frac{1}{(N_t+1)a} \simeq \frac{1}{(N_t)^2 a} = \frac{T}{N_t}$ may become coarse.

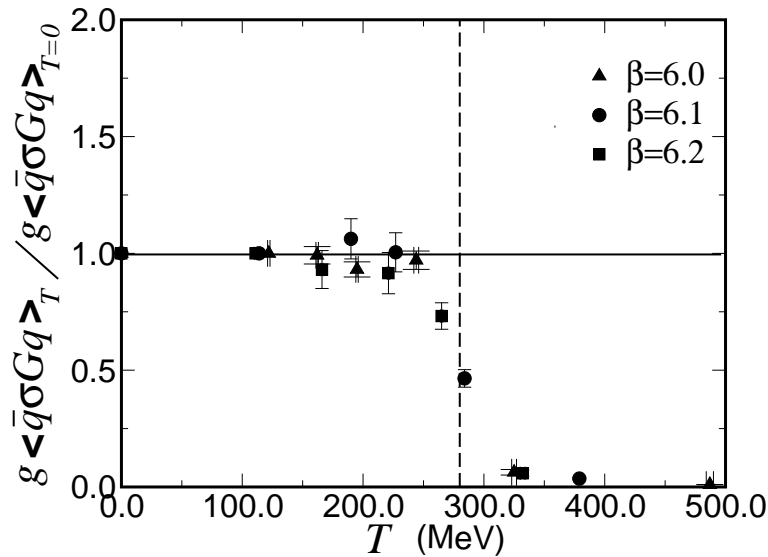


Figure 3.7: $g\langle\bar{q}\sigma_{\mu\nu}G_{\mu\nu}q\rangle$ plotted against temperature T from Ref. [5]. The vertical dashed line denotes the critical temperature $T_c = 280$ MeV in quenched QCD.

In order to find the critical temperature at phase transition one studies the temperature dependence of an order parameter such as a Polyakov loop or quark-gluon condensate... etc. If the QCD coupling, $6/g_0^2$, is large enough, then the lattice spacing is related to the bare coupling by

$$a = \frac{1}{\lambda_L} R(g_0), \quad (3.6.10)$$

with

$$R(g_0) = (\beta_0 g_0^2)^{-\beta_1/2\beta_0^2} e^{-(1/2\beta_0 g_0^2)}, \quad (3.6.11)$$

where Λ_L is a physical scale in terms of which dimensional quantities can be measured, and β_0 , β_1 are given by

$$\beta_0 = \frac{1}{16\pi^2} \left(11 - \frac{2}{3} N_F\right), \quad (3.6.12)$$

$$\beta_1 = \frac{1}{(16\pi^2)^2} (102 - \frac{38}{3} N_F), \quad (3.6.13)$$

and the temperature is given by

$$T = \frac{1}{N_\tau a} = \frac{\lambda_L}{N_\tau R(g_0)}. \quad (3.6.14)$$

Let g_c be the critical coupling at which the phase transition takes place. Then the critical temperature is given by

$$T_c = \frac{\lambda_L}{N_\tau R(g_c)}. \quad (3.6.15)$$

In Ref. [106] the thermal effects on the quark-gluon mixed condensate $g\langle\bar{q}\sigma_{\mu\nu}G_{\mu\nu}q\rangle$, as well as $\langle q\bar{q}\rangle$ are studied using $SU(3)_c$ lattice QCD with Kogut-Susskind [107] fermions at the quenched level. The phase transition is signalled by a sharp decrease in both condensates observed at $T_c = 280$ MeV. Of particular note is that the thermal effects below T_c are found to be weak. If the above calculated value of the transition temperature is adopted, i.e. $T_c = 280$ MeV, then the number of lattice slices would roughly be $N_\tau = 10$, for a lattice spacing $a = 0.1$ fm.

3.7 Conclusion

The properties of colour flux tubes can be unravelled following the construction of the static meson or baryon. Wilson loop and Polyakov lines operators correspond to two distinct approaches to construct these heavy quark states. The Wilson loop utilizes the overlap in the transfer matrix formalism, and the calculated flux distribution using this operator suffers from biasing by the shape of the interpolating fields. On the other hand, the Polyakov loop correlators addresses the free energy of the static meson or baryon and provide a set of unbiased operators to unravel the shape of the gluonic distribution. However, these sets of operators suffer from a bad signal to noise ratio and a suitable noise reduction technique, depending on the source separation and temperature scale, has to be employed. This can be very expensive in terms of the computational resources especially at low temperatures, as we will discuss in Chapter 5. The loop operator is exponentially suppressed with the increase of the separation distance between the sources and the temporal extent of the lattice. The study of these gauge-invariant objects may still be practically feasible for temperatures near the deconfinement phase of QCD. This has two advantages: the first is that we can unravel the changes in the shape of the glue distribution due to the changes in the temperature. The second is that the analysis near the end of the QCD plateau may provide insights about the corresponding distribution at zero temperature.

Chapter 4

Bosonic String Model

4.1 Outline

The dual superconductivity scenario of quark confinement implies the formation of a stringlike flux tube between the quark–antiquark pair. An effective bosonic-string description can be given for the colour-electric flux tube. The string picture has measurable effects on both the levels of the quark anti-quark potential as well as on the width of the field distribution. The picture also describes the thermal dependence of both quantities. In this chapter, we review the expectations of the string picture for both mesonic and baryonic systems. We also present a method to include the thermal effects into the junction width, based on the baryonic string model.

4.2 Introduction

With the proliferation of the newly discovered particles in particle accelerators and cosmic rays in the 1960s, regularities were soon found among particles properties. The Chew-Frautschi plots of the angular momentum J vs M^2 yielded parallel lines now well known as Regge trajectories. Veneziano [108] proposed a simple formula for scattering which accounted for Regge trajectories. This motivated the proposal of the hadronic string theory, where the hadrons are explained as excitation of relativistic strings.

Though the hadronic string theory encountered a success in accounting for Regge trajectories as well as the Veneziano formula, it ran quickly into difficulties. The consistency with quantum mechanics and Lorentz invariance requires the space time dimension to be 26. In addition to that, the spectrum of string theories includes massless spin 2 particles which are not hadrons. String theories had lost their appeal as candidate theories of hadrons. Instead they were proposed with a supersymmetric extension in the context of unification of all known forces including gravitation.

In conjunction with these developments, the quark model emerged, with the discovery of $SU(3)$ colour symmetry as an exact symmetry. The model was eventually expanded into a fully-fledged relativistic quantum field theory in which the analogue of photons are the gluons which belong to the 8 dimensional adjoint representation of the colour group.

Quantum chromodynamics has a very peculiar property, that of quark confinement. The quarks do not exist in Nature as asymptotic states. Until now, it is not clear how the quark confinement could be physically realized. The dual superconductor model of the QCD vacuum [52, 49, 109] is one of the classic pictures which provides a confinement scenario based on the formation of a thin stringlike colour-electric flux tube.

In fact, the formation of stringlike defects is not a peculiar property of the QCD flux tubes, and is realized in many physical phenomena such as vortices in superfluids [110], flux tubes in superconductors [111], vortices in Bose Einstein condensates [112], Nielsen-Olesen vortices of field theory [47], and cosmic strings [113]. The physical parameters of each of these models fix the properties of this stringlike object.

However, quantum mechanical effects become relevant in certain phases of the model, giving rise to interesting measurable effects. To find a consistent quantum description within the quantization scheme used in bosonic string theories, we encounter the difficulty that this is only possible in 26 dimensions.

Shortly after Nambu [114] suggested a formal relation between gauge-invariant loops and strings. Lüscher and Weiss [67] developed their effective string description. They showed that there is universal long distance correction to the confining linear potential [115]

$$V(R) = \sigma R - \frac{(D-2)\pi}{24} \frac{1}{R}. \quad (4.2.1)$$

This should be distinguished from the non-universal Coulomb term at short distances, which depends on the details of the gauge group.

The stringy signatures of the flux tubes can be investigated in lattice gauge theories by measuring average values of Wilson loops or Polyakov loop correlators. In the former approach one uses a transfer matrix interpretation in studying configurations with a static pair of a quark and an antiquark.

Early attempts to verify Lüscher predictions on the lattice occurred in the 1980s when Ambjorn and De Forcrand [116, 117] reported having measured the Lüscher term in numerical simulations, although these measurements have been criticized for being not very accurate. Lüscher and Weiss developed the Multi-level algorithm which enables exponential noise reduction [118]. The Lüscher term has now been measured with unprecedented accuracy in SU(3) gauge theory [119]. Even so, this does not provide a clear indication of the type of true QCD string theory. A variety of string theories with different boundary conditions give rise to the Lüscher term was shown by Dietz and Filk [120]. Naik [121] also showed that AdS/CFT correspondence yields a Lüscher term. On the other hand, non-bosonic strings were ruled out by Lucini et al [122].

Polchininski and Strominger [123] suggested to handle such string-like defects by an effective string theory. This proceeds in a similar fashion to the effective field description of the low energy dynamics of pions and nucleons wherein one retains the symmetry features of QCD, like chiral symmetry, but otherwise relax other constraints like the renormalizability of the allowed action.

4.3 Mesonic string

4.3.1 Quark–antiquark potential

The correlation function of two Polyakov loops on the lattice determines the interaction potential between the colour sources

$$\begin{aligned} \langle P(0) P^\dagger(R) \rangle &= \int d[U] P(0) P^\dagger(R) \exp(-S_w), \\ &= \exp(-V(R, T)/T). \end{aligned} \quad (4.3.1)$$

S_w is the plaquette action and T is the physical temperature. The self-interactions of the glue exchanged between two color sources in QCD can result in the squeezing of the glue into a thin one-dimensional stringlike object. The immediate consequence of this string picture is that a functional form can be ascribed to the Polyakov-loop correlators, namely, the partition function of the string. The correlators are expressed as functional integrals over all the world sheet configurations swept by the string,

$$\langle P(0) P^\dagger(R) \rangle = \int_{\mathcal{C}} [D X] \exp(-S(X)). \quad (4.3.2)$$

The vector $X^\mu(\zeta_1, \zeta_2)$ maps the region $\mathcal{C} \subset \mathbb{R}^2$ into \mathbb{R}^4 , with a Dirichlet boundary condition $X(\zeta_1, \zeta_2 = 0) = X(\zeta_1, \zeta_2 = R) = 0$, and a periodic boundary condition along the time direction $X(\zeta_1 = 0, \zeta_2) = X(\zeta_1 = L_T = \frac{1}{T}, \zeta_2)$, and S is the string action and can be chosen to be proportional to the surface area, i.e., the Nambu-Goto action,

$$S[X] = \sigma \int d\zeta_1 \int d\zeta_2 \sqrt{g}, \quad (4.3.3)$$

where $g_{\alpha\beta}$ is the two-dimensional induced metric on the world sheet embedded in the background \mathbb{R}^4

$$\begin{aligned} g_{\alpha\beta} &= \frac{\partial X}{\partial \zeta_\alpha} \cdot \frac{\partial X}{\partial \zeta_\beta}, \quad (\alpha, \beta = 1, 2), \\ g &= \det(g_{\alpha\beta}). \end{aligned}$$

Gauge fixing is required for the path integral of Eq. (4.3.2) to be well defined with respect to Weyl and reparametrization invariance. The physical gauge $X^1 = \zeta_1, X^4 = \zeta_2$ would restrict the string fluctuations to transverse directions to \mathcal{C} . At the quantum level, Weyl invariance is broken in four dimensions; however, the anomaly is known to vanish at large distances [124]. The action after gauge fixing reads

$$S[X] = \sigma \int_0^L d\zeta_1 \int_0^R d\zeta_2 (1 + (\partial_{\zeta_1} X_\perp)^2 + (\partial_{\zeta_2} X_\perp)^2)^{\frac{1}{2}}. \quad (4.3.4)$$

Expanding the square root in powers of σRL_T

$$S[X] = \sigma R L_T + \frac{\sigma}{2} \int_0^{L_T} d\zeta_1 \int_0^R d\zeta_2 (\nabla X_\perp)^2 + \dots, \quad (4.3.5)$$

the action decomposes into the classical configuration and fluctuation part, and the string higher-order self interactions. A leading-order approximation can be made by neglecting the self-interaction terms; the path integral Eq. (4.3.5) is then

$$\langle P(0) P^\dagger(R) \rangle = e^{-\sigma R L_T} [\det(-\frac{1}{2} \nabla^2)]^{-1}. \quad (4.3.6)$$

The determinant of the Laplacian on the cylinder has been regulated using a lattice regulator in Ref. [117]. The potential is obtained in closed form for a length scale comparable to the thermodynamic scale in [125]. The effective potential is

$$\begin{aligned} V(R, T) = & \left(\sigma - \frac{\pi}{3} T^2 + \frac{2}{3} T^2 \tan^{-1} \left(\frac{1}{2 R T} \right) \right) R \\ & - \left(\frac{\pi}{12} - \frac{1}{6} \tan^{-1} (2 R T) \right) \frac{1}{R} \\ & - \frac{T}{2} \log(1 + (2 R T)^2) + \mu. \end{aligned} \quad (4.3.7)$$

In the zeta function regularization scheme, the potential in four dimensions is given by

$$V(R) = 2 T \log \eta \left(\frac{i}{2 T R} \right) + \sigma R + \mu(T), \quad (4.3.8)$$

with the Dedekind eta function

$$\eta(\tau) = q^{\frac{1}{24}} \prod_{n=1}^{\infty} (1 - q^n); \quad q = e^{-2\frac{\pi}{T R}}, \quad (4.3.9)$$

and $\mu(T)$ is a renormalization parameter. The limit of large string length [117] entails taking the temperature-dependent string tension to be

$$\sigma(T) = \sigma - \frac{\pi}{3} T^2. \quad (4.3.10)$$

The free-string model predicts a temperature-dependent quark–antiquark potential that is featured by the existence of a logarithmic term in addition to a leading-order decrease in the string tension by an amount $\frac{\pi}{3} T^2$.

4.3.2 Width of the string

The vibration modes of the stringlike object render an effective width for the flux tube. A well known prediction made by Lüscher, Münster and Weisz [126], based on the effective bosonic string model, has shown that the mean-square width of the vibrating flux tube at the centre plane grows logarithmically as a function of the interquark separation in four dimensions

$$w^2 \sim \frac{1}{\pi \sigma} \log \left(\frac{R}{\lambda} \right), \quad (4.3.11)$$

where λ is an ultra-violet scale. With the increase of the temperature, higher order gluonic degrees of freedom are present and the effective width of the corresponding

string is expected to manifest an intricate behaviour involving both the distance and the temperature. The mean square width of the string is defined as

$$\begin{aligned} W^2(\xi; \tau) &= \langle X^2(\xi; \tau) \rangle, \\ &= \frac{\int_C [D X] X^2 \exp(-S[X])}{\int_C [D X] \exp(-S[X])}, \end{aligned} \quad (4.3.12)$$

where $\xi = (\xi_1, i\xi_2)$ is a complex parametrization of the world sheet, such that $\xi_1 \in [-R/2, R/2]$, $\xi_2 \in [-L_T/2, L_T/2]$, with $\tau = \frac{L_T}{R}$ being the modular parameter of the cylinder, and $L_T = 1/T$ is the temporal extent governing the inverse temperature.

Casselle et al. [65] and Gliozi [127] have worked out the delocalization of the string for all the planes transverse to the line joining the quark pair by the corresponding Green function. This technique proceeds by removing the divergence in the quadratic operator in Eq. (4.3.12) by the use of the Schwinger [128] point-split regularization, then taking the limiting action for the Nambu-Goto model as that of the corresponding Gaussian model. The quadratic operator is then the correlator of the free bosonic string theory in two dimensions

$$\begin{aligned} \langle X^2(\xi; \tau) \rangle &= (\xi) \cdot X(\xi + \epsilon) \rangle, \\ &= G(\xi, \xi + \epsilon). \end{aligned} \quad (4.3.13)$$

This Green function is the solution of the Laplace equation on the cylinder with a Dirichlet boundary condition,

$$G(\xi, \xi_0) = \frac{-1}{2\pi} \log |f(\xi, \xi_0)|. \quad (4.3.14)$$

The conformal map reads [129],

$$f(\xi, \xi_0) = \frac{\theta_1[\pi(\xi - \xi_0)/R; \tau]}{\theta_2[\pi(\xi - \bar{\xi}_0)/R; \tau]}, \quad (4.3.15)$$

where the Jacobi θ functions are

$$\begin{aligned} \theta_1(\xi; \tau) &= 2 \sum_{n=0}^{\infty} (-1)^n q^{n(n+1)+\frac{1}{4}} \sin((2n+1)\xi), \\ \theta_2(\xi; \tau) &= 2 \sum_{n=0}^{\infty} q^{n(n+1)+\frac{1}{4}} \cos((2n+1)\xi), \end{aligned} \quad (4.3.16)$$

with $q = e^{\frac{-\pi}{2}\tau}$. The expectation value of the mean square width would then read

$$W^2(\xi_1, \tau) = \frac{D-2}{2\pi\sigma} \log\left(\frac{R}{R_0}\right) + \frac{D-2}{2\pi\sigma} \log \left| \frac{\theta_2(\pi \xi_1/R; \tau)}{\theta_1'(0; \tau)} \right|. \quad (4.3.17)$$

This expression converges for modular parameters close to 1, and contains, in addition to the logarithmic divergence term, a correction term that encodes the dependence of the width at different transverse planes on the modular parameter of the cylinder. At finite temperature, this term is contributing to the width at all the planes. Figure 4.1 is a plot of the mean-square width calculated at ξ_1 values via Eq. (4.3.17). The plot shows the profile for several modular parameters and fixed separation between the two Polyakov loops.

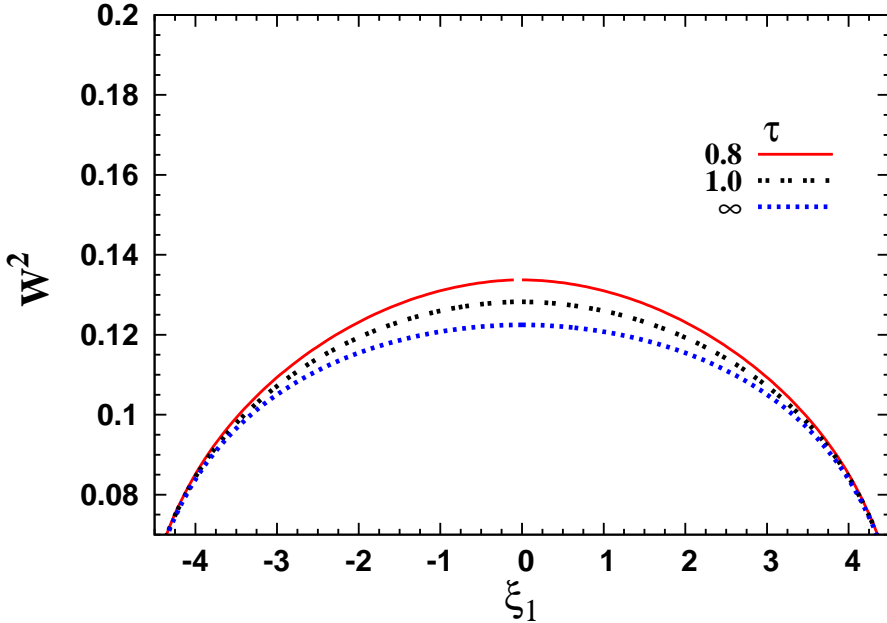


Figure 4.1: The mean-square width, Eq. (4.3.17), of the flux tube evaluated at all planes ξ_1 perpendicular to the quark–antiquark line. The separation distance between the pair is $R a^{-1} = 10$.

The string model predicts an increase in the width with the increase of the temperature. The increase in the width is maximum at the central plane which is seen as an increase in the curvature in the profile of the string fluctuations. At zero temperature $L_T \rightarrow \infty$, Eq. (4.3.17) converges well, and the second term in Eq. (4.3.17) still contributes to the whole shape of the fluctuations at all planes except the middle; and the contribution of this term at zero temperature is

$$\frac{D-2}{2\pi} \log \left| \cos \left(\frac{\pi \xi_1}{R} \right) \right|, \quad (4.3.18)$$

which is seen from the plot of Fig. 4.1 to be subtle in the middle region and have more pronounced effects on the width near the quark positions.

4.4 The Baryonic string picture

The Y-ansatz for the flux-tube shape can be derived from the strong coupling approximation [130, 131, 132] and is consistent with the dual superconducting picture

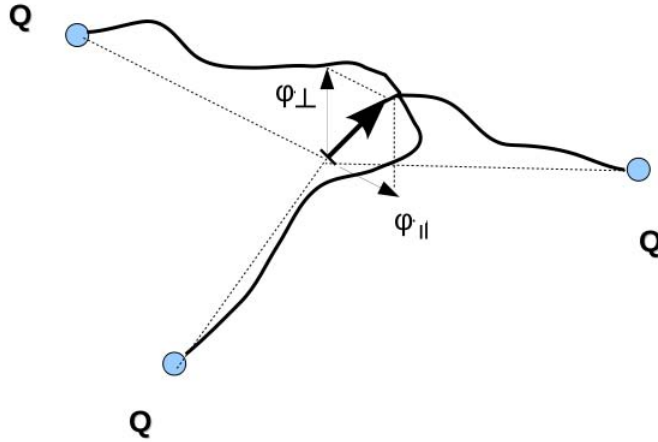


Figure 4.2: Fluctuating flux tubes of three static color sources Q . The junction position ϕ is measured relative to the classical location which minimizes the total strings length (Fermat point).

of QCD. The Y-shaped string is the most relevant to the IR region and amounts to three squeezed flux tubes that meet at a junction.

In the baryonic string model, the quarks are connected by three strings that meet at a junction as in Fig. 4.2. The classical configuration is the one that minimizes the area of the string world sheets. The position of the junction is thus determined by the requirement of the minimal total string length (Fermat point). Each string's worldsheet (blade) consists of a static quark line and the worldline of the fluctuating junction as illustrated in Fig. 4.3.

The parameters s and t (time) label the position on string world-sheet (blade) i . The position of the junction is given by $s = L_i + e_i \cdot \varphi(t)$, where L_i is the length of the blade and the scalar product $e_i \cdot \varphi(t)$ of the 4-vector $\varphi(t)$ and the unit directional vectors as illustrated in Figs. 4.3 and 4.4. The label i denotes the blades.

From continuity, the boundary conditions for the transverse fluctuations $\xi_i(t, s)$ is

$$\xi_i(t, L_i + e_i \cdot \varphi(t)) = \varphi_{\perp i}(t), \quad (4.4.1)$$

where, $\varphi_{\perp i} \equiv \varphi - e_i(e_i \cdot \varphi)$. The transverse fluctuations $\xi_i(t, s)$ vanish at the location of the quarks ($s = 0$), and are periodic in the time t , with period L_T .

In this model, the junction is assumed to have a finite mass m . This results in a static energy and a kinetic energy term. Expanding the NG action around the equilibrium configuration yields

$$S = S_{\parallel} + \frac{\sigma}{2} \sum_{i,j} \int_{\Gamma_i} d^2\zeta \frac{\partial \xi_i}{\partial \zeta_j} \cdot \frac{\partial \xi_i}{\partial \zeta_j} + m \left(L_T + \frac{1}{2} \int_0^{L_T} dt |\dot{\varphi}|^2 \right), \quad (4.4.2)$$

where again ζ_1, ζ_2 are world sheet parameters and

$$S_{\parallel} = \sigma \sum_i \left(L_i L_T + \int dt e_i \cdot \varphi(t) \right) = \sigma L_Y L_T. \quad (4.4.3)$$

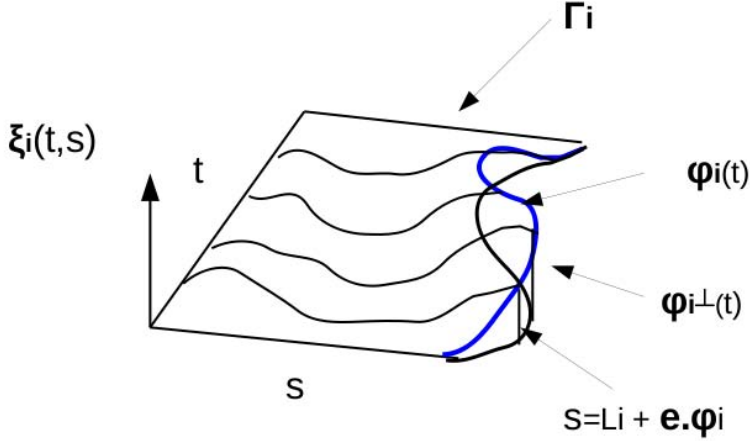


Figure 4.3: World sheet spanned by one of the strings during time evolution up to the junction.

where, $L_Y = \sum_i L_i$ above denotes the total string length.

The system's partition function is given by

$$Z = e^{-(\sigma L_Y + m) L_T} \int D\varphi \exp \left(-\frac{m}{2} \int dt |\dot{\varphi}|^2 \right) \prod_{i=1}^3 Z_i(\varphi). \quad (4.4.4)$$

Here $Z_i(\varphi)$ denotes the partition function for the fluctuations of a given blade that is bounded by the junction worldline $\varphi(t)$:

$$Z_i(\varphi) = \int D\xi_i \exp \left(-\frac{\sigma}{2} \int |\partial \xi_i|^2 \right). \quad (4.4.5)$$

The string partition functions $Z_i(\varphi)$ are Gaussian functional integrals and can be calculated according to

$$Z_i(\varphi) = e^{-\frac{\sigma}{2} \int |\partial \xi_{\min, i}|^2} |\det(-\Delta_{\Gamma_i})|^{-(D-2)/2}, \quad (4.4.6)$$

where $\xi_{\min, i}$ is the minimal-area solution for given $\varphi(t)$. Δ_{Γ_i} denotes the Laplacian acting on the domain (blade) Γ_i . $\xi_{\min, i}(t, s)$ is harmonic and satisfies the boundary conditions Eq. (4.4.1) [133].

The world sheets Γ_a are general domains that can be conformally mapped into rectangles:

$$f_a(z) = z + \frac{1}{\sqrt{L_T}} \sum_{\omega=0} \frac{e_i \cdot \varphi_\omega}{\sinh(\omega L_i)} e^{\omega z} + \mathcal{O}(\varphi^2). \quad (4.4.7)$$

Jahn and de Forcrand [133] calculated the Casimir energy for the baryonic potential V_{qqq} . This has been done by evaluating the determinant of the Laplacian in Eq. (4.4.6) by conformally mapping the resulting domains to rectangles. The baryonic potential V_{qqq} then reads

$$V_{qqq}(L_1, L_2, L_3) = \sigma \sum_i L_i + V_{\parallel} + V_{\perp} + O(L_i^{-2}),$$

with

$$\begin{aligned} V_{\parallel} &= -\frac{\pi}{24} \sum_i \frac{1}{L_i} + \int_0^\infty \frac{dw}{2\pi} \ln \left[\frac{1}{3} \sum_{i < j} \coth(wL_i) \coth(wL_j) \right], \\ V_{\perp} &= -\frac{\pi}{24} \sum_i \frac{1}{L_i} + \int_0^\infty \frac{dw}{2\pi} \ln \left[\frac{1}{3} \sum_i \coth(wL_i) \right]. \end{aligned} \quad (4.4.8)$$

4.4.1 Width of the junction

The thickness of the fluctuating baryonic junction can be calculated based on the bosonic string model. This entails evaluating the expectation value

$$\langle \varphi^2 \rangle = \frac{\int D\varphi \varphi^2 e^{-S}}{\int D\varphi e^{-S}}. \quad (4.4.9)$$

The string width can be decomposed into perpendicular contributions $\langle \varphi_{\perp}^2 \rangle$ to the i -th quark world sheet, and $\langle \varphi_{\parallel}^2 \rangle$ are the mean-square width of the parallel fluctuations within the plane of the quarks, as illustrated in Fig 4.2:

$$\langle \varphi^2 \rangle = \langle \varphi_{\perp}^2 \rangle + \langle \varphi_{\parallel}^2 \rangle. \quad (4.4.10)$$

Leading-order approximation

The action S is defined in Eq. (4.4.2) and can also be read from the partition function Eq. (4.4.4). The thickness of the string [134] at the junction can be calculated by taking the expectation value of φ^2 [see Eq. (4.4.2)]

$$\langle \varphi^2 \rangle = \frac{\int D\varphi \varphi^2 e^{-S}}{\int D\varphi e^{-S}}. \quad (4.4.11)$$

To do this, we have to consider integrals

$$\begin{aligned} Z \equiv \sum_i Z_i(\varphi) &= \int D\varphi \exp\left(-\frac{m}{2} \int_0^{L_T} dt |\dot{\varphi}|^2 + \sum_{i=1} \left(-\frac{\sigma}{2} \int d^2\zeta \right. \right. \\ &\quad \left. \sum_{\alpha} \frac{\partial \xi_{\min,i}}{\partial \zeta_{\alpha}} \cdot \frac{\partial \xi_{\min,i}}{\partial \zeta_i} + \frac{D-2}{24\pi} \sum_w w^3 \coth(wL_i) |e_i \cdot \varphi_w|^2 \right)). \end{aligned} \quad (4.4.12)$$

The integral over φ is decomposed in Eq. (4.4.12) using $|\varphi_{w,\perp i}|^2 = |\varphi_w|^2 - |\varphi_w \cdot e_i|^2$ into parallel and perpendicular components to the plane of the quarks. The mean-square value of the perpendicular fluctuations is

$$\langle \varphi_{\perp}^2 \rangle = \frac{2}{L_T} \sum_{w>0} \frac{1}{m w^2 + \sigma w \sum_i \coth(w L_i)}, \quad (4.4.13)$$

with $w = 2\pi n/L_T$. The parallel fluctuations read

$$\langle \varphi_{\parallel}^2 \rangle = \frac{1}{\sigma \pi} \sum_{w>0} \frac{1}{w} \frac{\tilde{m}w + (1 - aw^2)C_1}{\tilde{m}^2 w^2 + 2\tilde{m}w(1 - aw^2)C_1 - 4aw^2(C_1)^2 + \frac{4}{3}(1 + aw^2)^2 C_2} \quad (4.4.14)$$

where

$$\tilde{m} = \frac{2m}{3\sigma}, \quad a = \frac{2}{12\pi\sigma}, \quad (4.4.15)$$

$$C_1 = \frac{1}{3} \sum_i \coth(w L_i), \quad (4.4.16)$$

$$C_2 = \frac{1}{3} \sum_{i < j} \alpha_{ij} \coth(w L_i) \coth(w L_j), \quad (4.4.17)$$

with the geometrical coefficients

$$\alpha_{ij} = \sin^2 \left(2\pi \frac{(i-j)}{n} \right). \quad (4.4.18)$$

In contrast to the perpendicular fluctuations, the mean-square width of the parallel fluctuations does depend on the geometrical setup of the quarks.

Convolution of the junction fluctuations

Here, we present a method for the inclusion of the thermal effects into the mean-square width of the baryonic junction. The mean-square width of the fluctuations in the mesonic limit does not account for the temperature effects. Evidently, Eq. (4.4.13) does not reproduce equation Eq. (4.3.17). Moreover, Eq. (4.4.13) and Eq. (4.4.14) indicates a decrease in the junction width with the increase of the temperature.

In the limit $L_T \rightarrow \infty$, for general n string system of identical lengths $L = L_i$, the perpendicular contribution reads

$$\langle \varphi_{\perp}^2 \rangle = \frac{D-n}{\pi n} \int_0^{\infty} dw \frac{1}{mw^2 + n\sigma w \coth(wL)}. \quad (4.4.19)$$

In the leading order, the integral simplifies to

$$\langle \varphi_{\perp}^2 \rangle = \frac{D-n}{n\pi\sigma} \ln \frac{L}{L_0}. \quad (4.4.20)$$

The arbitrary constant is contained in L_0 which generally will depend on the dimension and the number of strings and the ultraviolet properties of the corresponding gauge model [135]. This indicates that the width of the junction, orthogonal to the plane swept by the quarks, grows logarithmically with the distance.

The above equation is consistent with the mesonic string fluctuations of Eq. (4.3.17). This can be shown by first considering the limit $L_T \rightarrow \infty$. Then Eq. (4.3.17) becomes

$$W^2(\xi_1, \tau) = \frac{D-2}{2\pi\sigma} \log\left(\frac{R}{R_0}\right) + \frac{D-2}{2\pi\sigma} \log|\cos\left(\frac{\pi\xi_1}{R}\right)|. \quad (4.4.21)$$

The mean-square width, W_0^2 , determined at the symmetry point of the string world sheet depends only on the first term

$$W_0^2 = \frac{(D-2)}{2\pi\sigma} \ln \frac{R}{R_0}. \quad (4.4.22)$$

By dividing the string connecting a quark and an antiquark into two parts of equal length connected in the middle by a junction, $L = 2L' = 2R$, see Fig. 4.4, one can relate Eq. (4.4.22) and (4.4.20). These equations coincide provided that the constants are identified as $L_0 = 2R_0$. The parameter m which has been absorbed into L_0 , therefore, scales linearly with the parameter R_0 . Nevertheless, the mean-square width of the fluctuations in the mesonic limit does not account for the temperature dependent effects. Evidently, Eq. (4.4.13) does not reproduce equation Eq. (4.3.17) unless we assume a temperature dependence for the mass of the junction. One therefore should consider the higher-order terms in the conformal mapping Eq. (4.4.7) in the calculation scheme.

To keep the form of the formulas as simple as possible, the temperature dependence in the higher-order terms of the conformal mapping from a fluctuating blade to a rectangular one can be accounted for by assuming a smoothing scalar function ψ such that $\varphi \rightarrow \int_{-\infty}^{\infty} \phi(\tau) \psi(t - \tau) d\tau$. The form of this function can be found from the mesonic limit. The integration over Fourier modes of the fluctuating junction ϕ can be performed in a similar way as detailed in Ref. [134].

The general domains Γ_a describing the world sheet of each blade can now be conformally mapped into rectangles using the convoluting scalar function ψ

$$f_i(z) = z + \frac{1}{\sqrt{L_T}} \sum_{\omega=0} \frac{e_k \cdot \varphi_{\omega} \psi(\omega, L_i)}{\sinh(\omega L_i)} e^{\omega z}. \quad (4.4.23)$$

The mean-square width of the perpendicular fluctuation of the junction acquires a simple modification after solving for the position of the junction $\xi_{min,i}$ for each blade

$$\xi_{min,i} = \frac{1}{\sqrt{L_T}} \sum_w \varphi_{w,\perp i} \frac{\sinh(ws)}{\sinh(wL_i)} e^{iwt} + \mathcal{O}(\varphi^2), \quad (4.4.24)$$

with the convoluted position

$$\xi_{min,i} = \frac{1}{\sqrt{L_T}} \sum_w \varphi_{w,\perp i} \psi(w, L_i) \frac{\sinh(ws)}{\sinh(wL_i)} e^{iwt}. \quad (4.4.25)$$

Following the same procedure as Ref. [134] for the calculation of the thickness of the junction, this results in a simple modification for the perpendicular fluctuations of Eq. (4.4.13) to

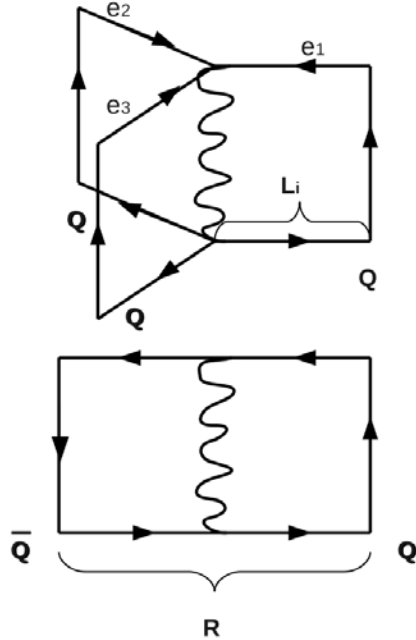


Figure 4.4: The world sheets of the strings in a baryon and a meson. The string in the static meson is modelled as being composed of two strings connected by a junction in the middle.

$$\langle \varphi_{\perp}^2 \rangle = \frac{2}{L_T} \sum_{w>0} \frac{1}{mw^2 + \sigma w \sum_i \coth(wL_i) \psi(w, L_i)}. \quad (4.4.26)$$

The form of this convoluting scalar can be derived from the mesonic limit. At the centre point between the quark and anti-quark we have $\psi(w, L_i) = \psi(w, L_j)$. The mesonic string picture at finite temperature, Eq. (4.3.17), implies the mean-square width at the symmetry point of the string is given by

$$w^2(\xi_1, \tau) = \frac{1}{\pi\sigma} \log\left(\frac{R}{R_0}\right) + \frac{1}{\pi\sigma} \log|\chi(\tau)|, \quad (4.4.27)$$

with $\chi(\tau) = \frac{\theta_2(0; \tau)}{\theta'_1(0; \tau)}$. Equating both expressions of Eq. (4.4.26) and Eq. (4.4.27), with $R = 2L_i = L$, expanding the logarithm in the right hand side and solving for $\psi(w, L_i)$ yields the following expression

$$\psi(w, L_i) = \frac{-kw}{2\sigma \coth(wL_i)} - \frac{(wL_T - \pi)}{2wL_T \coth(wL_i)} \left(\frac{2L_i \chi(\tau_i) + 1}{2L_i \chi(\tau_i) - 1} \right)^{wL_T/\pi-1}. \quad (4.4.28)$$

As indicated above, the parameter m shifts the mean-square width of the fluctuations by a constant. The parameter m can be chosen such that R_0 cancels out from both sides of Eqs. (4.4.26) and (4.4.27).

A similar procedure can be applied to the mean-square width of the parallel fluctuations, Eq. (4.4.14). This results in the following expression

$$\langle \varphi_{\parallel}^2 \rangle = \frac{1}{\sigma\pi} \sum_{w>0} \frac{1}{w} \frac{\tilde{m}w + (1 - aw^2)C_1}{\tilde{m}^2w^2 + 2\tilde{m}w(1 - aw^2)C_1 - 4aw^2(C_1)^2 + \frac{4}{3}(1 + aw^2)^2C_2}, \quad (4.4.29)$$

where

$$\tilde{m} = \frac{2}{3} \frac{m}{\sigma}, \quad a = \frac{2}{12\pi\sigma}, \quad (4.4.30)$$

$$C_1 = \frac{1}{3} \sum_i \coth(wL_i) \psi(w, L_i), \quad (4.4.31)$$

$$C_2 = \frac{1}{3} \sum_{i < j} \alpha_{ij} \coth(wL_i) \psi(w, L_i) \coth(wL_j) \psi(w, L_j), \quad (4.4.32)$$

which includes thermal effects into the solutions worked out in detail in Ref. [134] for the junction fluctuations at zero temperature.

In fact, the thermal effects on the level of three-quark potentials has been discussed by Andreev [136] from the gauge-string duality perspective. The consideration of the multi-quark potentials using collective coordinates for the junction allowed for the calculations of baryonic potentials for the $SU(N)$ gauge group as well as the pseudo-potentials at finite temperature. To the best of our knowledge, these pseudo-potentials, in addition to the above prediction of the baryonic string model for the width of the junction, remain to be investigated on the lattice.

Nevertheless, the first test of the baryonic string model predictions with the lattice data for the potential of three static quarks at zero temperature has been reported in Ref. [137]. The Y-ansatz has been discussed in detail for different three-quark geometries. Moreover, the precise numerical measurements of the 3-state Potts model in these calculations made it possible to verify the subleading Lüscher-like corrections that come from Eq. (4.4.8). These numerical simulations present an indication that when the separation between any two quarks is large, the flux-tubes behave as a system of three strings that meet at a junction. In addition, these calculations confirmed the universal (gauge-group independent) Lüscher-like correction, $1/L_Y = \frac{\pi}{24} \sum_i \frac{1}{L_i}$, to the Y-ansatz, and hence the validity of the baryonic string picture at zero temperature and large distances.

In the strong coupling regime of gauge theories in $D = 3$ or $D = 4$, the flux tube between a quark–antiquark pair has a constant width at large source separations. The flux-tube undergoes a roughening transition with the decrease of the coupling constant. The rough phase of the flux-tube is characterized by strong fluctuations of the collective coordinates describing the position of the underlying string. In this phase the width of the flux tube is no longer constant and increases logarithmically with the increase of the inter-quark separation [126].

At zero temperature, the string model assumptions are valid in the rough phase of the LGT where collective coordinates for the flux tube are used [119, 63, 64, 65, 66]. Near the deconfinement point, the mesonic results are indicating [135, 129, 138, 139, 140] a linear growth of the flux tube width in agreement with string model

predictions. This must mean that at high the temperatures, near the deconfinement point, the string model assumptions are still working.

In the case of baryon, on the other hand, the strong coupling results, as well as lattice results, are indicating a Y-ansatz at large sources separation distances at zero temperature. The use of the collective co-ordinates for the junction in this Y-shape string model is thus a good assumption at zero temperature. In addition to that, the mesonic results near the deconfinement point indicate that the use of collective co-ordinates for the flux tube itself is successful in predicting the large distance features of the flux-tubes. The Y-shaped string model is then expected to be a working picture at high temperatures, and the observed features of the gluonic distribution are expected to arise as a result of the vibration of this underlying Y-shaped string system.

Figure 4.5 illustrates two possible baryonic string configurations that can give rise to two different types of Δ -shaped action density distribution. In the first baryonic picture, Fig. 4.5. (a), a string connecting each pair of quarks forms. At large quark separations, the vibrations of each of the individual strings in this model is expected to give rise to an energy distribution analogous to the quark–antiquark pair at the edges of the triangle. The width profile of this system is related to the properties of the flux tube of the corresponding mesonic system. As we will see in Chapter 9, the lattice data at a temperature near the end of the QCD plateau indicate shrinking in the width profile, and this shrinking cannot be realized in this string picture, since the lattice data at the same temperature do not indicate this

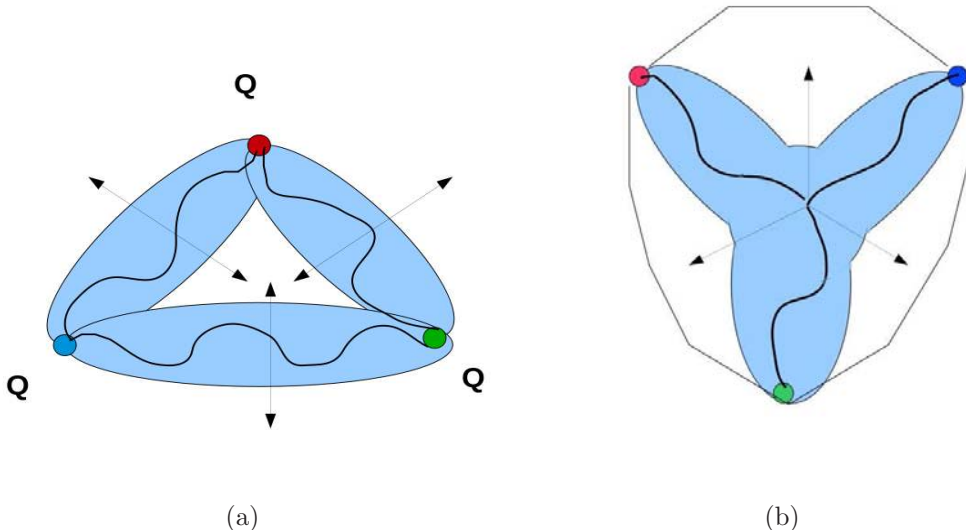


Figure 4.5: The Δ and Y baryonic strings configurations. The delocalization of the junction in the Y-shaped string system trace a filled Δ shaped energy distribution with maximal effect at the junction of the system. The Δ string configuration implies an energy distribution of maximum effect at the edges.

behaviour in the mesonic case of Chapter 6.

The validity of the Y-shaped 3-string model at finite temperature is based mainly on the analysis of the lattice data [141] reported in Chapter 9. In Chapter 9, the action density distribution of three static-quark system is not of the shape of tubes that form around the perimeter of the three-quark system indicating a direct sum of $q\bar{q}$ forces and hence implying the baryonic string picture of Fig. 4.5 (a). In fact, the lattice data [141] of Chapter 9 indicate a filled Δ shape where the maximal effect on the action density is at the centre of the three-quark system, not at the edges. Moreover, for the temperatures at the end of the QCD plateau, the flux-tube radius profile shows an underlying Y-shape. We note that the width profile is not related to the iso-surface profile; the width is the quantity of direct relevance to the predictions of the string model.

The analysis of the radius profile of the flux tube exhibits an underlying Y-shape as well as a maximal vacuum suppression near the Fermat point. This provide solid ground to interpret the observed filled Δ -shape as coming about through the delocalization of the Y-junction, tracing out a filled Δ shape, and hence justifies the need to generalize the 3-string Y-shaped baryonic string model.

Apart from the numerical lattice data, a mechanism that suggests a possible transition or switching between the two baryonic string arrangements, i.e a Δ -shape string configuration to a Y-shape string configuration, has been ruled out in Ref. [142] on purely phenomenological grounds.

The justifications for generalizing the string model formulas to include the temperature dependence can be summarized in the following main points:

- The strong coupling results [130, 131, 132] as well as the lattice results [137] at zero temperature support the Y-shaped string picture for the flux tubes in the baryon. In addition to this, the success of the string model near the deconfinement point in the meson indicates that the assumptions of the rough phase of Yang-Mills theory still holds, which implies the use of the collective co-ordinates for the flux-tubes that has been observed at zero temperature.
- Observation of a filled Δ -shape gluonic distribution with maximum expulsion of the vacuum fluctuations localized near the Fermat Point of the triangular configuration [141].
- The analysis of the gluonic field distribution in the baryon shows that the aspect ratio between the parallel and perpendicular mean-square width to the quark planes is greater than unity [141] (as we will see in Chapter 9), this indicates a strong restoring force in the quark plane of the three string system. This supports that the filled Δ -shape profile comes from the vibration of a Y-shaped string system.
- Theoretical difficulties [142] in the mechanisms that show switching from the Y-shape string model to the Δ -shape string model exist and this has not been observed on the lattice.

In addition to the above points there are also the following reasons that are in support of the Y-shaped string model at finite temperature

- The abelian projected theory shows a Y-shaped underlying current at $T/T_c = 0.8$ [143].
- Multi-junction systems are expected to appear for quark systems greater than three or number of strings greater than three [134].
- The Δ -shaped spatial links do not define a gauge-invariant state in the 3Q Wilson loop operator.
- As we will see in Chapter 9, the above generalized model is successful in accounting for the width profile of the junction.

4.5 Summary and Conclusion

In this chapter we presented a detailed overview of the predictions of the bosonic string model for both the mesonic and baryonic systems. The free string model predicts a temperature-dependent quark anti-quark potential that is featured by a leading-order decrease in the string tension by an amount $\frac{\pi}{3} T^2$. The string model predicts an increase in the width with the increase of the temperature and a subsequent increase in the curvature in the profile of the string fluctuations. The mean-square width of the thin string-like flux tube turns from logarithmic growth at $T = 0$ into linear growth with the increase of source separation at high temperature. The formula of the baryonic string model for the width of the junction has been extended to a high temperature regime by convoluting the leading-order junction fluctuations with a smoothing function whose form can be found from the mesonic limit.

The major goal in the next chapters will be to confront the bosonic string predictions for the thermal delocalizations of the flux tube for both static mesons and baryons as well as the $q\bar{q}$ force with lattice gauge theory results.

Chapter 5

Noise Reduction in Loop Correlators

5.1 Outline

Throughout this investigation, we study the gluonic field strength after constructing static mesons and baryons with the use of Polyakov loop operators. Polyakov loops are an unbaised set of operators that are known to suffer from a bad signal to noise ratio. Four-dimensional smearing or cooling of the gauge field can be used to enhance the signal to noise ratio. However, these methods have the problem of the associated loss of short distance physics. In this chapter, we study this noise reduction technique in detail, such that it can be used to extract the correct physics in a systematic and controlled manner. We report the effects of smearing on the static $q\bar{q}$ potential and find that associated effects become subtle for source separations greater than the diameter of smearing. In the remainder of this chapter we discuss the link-integration method which is an effective technique for noise reduction at small quark separations. Also we describe the Multi-level algorithm which is the most effective technique for noise reduction at low temperatures.

5.2 Four-dimensional smearing of the gauge field

As it was discussed in the last chapter, the translational-invariance through the lattice hyper-torus can be exploited to decrease the statistical errors by computing the correlations of Eq. (3.3.3) on every node of the lattice, and averaging the results over the volume of the four-dimensional torus. To further improve the signal to noise ratio in the gluonic correlation function, local action reduction by smearing the gauge links can be performed on the whole four-dimensional lattice. Although smearing the gauge field results in the elimination of the short distance physics, the main focus in this investigation is to resolve the nature of the flux distributions in the infrared (IR) region of the theory.

In this chapter, we show that the effects on the large distance correlations can be kept minor with the appropriate choice of smearing levels. Similar techniques have been adopted in Ref. [144] in the determination of the large distance $Q\bar{Q}$ force in vacuum with different levels of HYP smearing. In Sec. IV-A, we show that for a

given distance scale, the measured quark–antiquark force at large distances can be left with negligible changes for a range of smearing levels. Alternatively to Ref. [145] where the Cabibbo–Marinari cooling has been employed, we choose to smear the gauge field by an overimproved stout-link smearing algorithm [146]. The use of this algorithm should ensure that the four-dimensional smearing has a minimal effect on the topology of the gauge field [146]. In standard stout-link smearing [147], all the links are simultaneously updated. Each sweep of update consists of a replacement of all the links by the smeared links

$$\tilde{U}_\mu(x) = \exp(iQ_\mu(x)) U_\mu(x), \quad (5.2.1)$$

with

$$\begin{aligned} Q_\mu(x) = & \frac{i}{2}(\Omega_\mu^\dagger(x) - \Omega_\mu(x)) \\ & - \frac{i}{6}Tr(\Omega_\mu^\dagger(x) - \Omega_\mu(x)), \end{aligned}$$

and

$$\Omega_\mu(x) = \left(\sum_{\nu \neq \mu} \rho_{\mu\nu} \Sigma_{\mu\nu}^\dagger(x) \right) U_\mu^\dagger(x),$$

where $\Sigma_{\mu\nu}(x)$ denotes the sum of the two staples touching $U_\mu(x)$ which reside in the $\mu - \nu$ plane. The scheme of over-improvement requires $\Sigma_{\mu\nu}(x)$ to be replaced by a combination of plaquette and rectangular staples. This ratio is tuned by the parameter ϵ [146]. In the following we use a value of $\epsilon = -0.25$, with $\rho_\mu = \rho = 0.06$. We note that for a value of $\rho = 0.06$, the over-improved stout-link algorithm is roughly equivalent, in terms of UV filtering, to the standard stout-link smearing algorithm with the same $\rho = 0.06$.

5.2.1 Smearing and cooling

In the literature there are different naming conventions of smearing and cooling. Based on the dimensionality, the term ‘cooling’ can be used to mean the 4D iteration. The term ‘smearing’ is excluded to mean only 3D iterations on the spatial links of the interpolating fields used in the transfer matrix formalism. However, some authors [146, 148, 149, 147] distinguish between cooling and smearing based on the way the iteration updates proceed. The term cooling refers to an update of a single link based on its neighbours, effectively one at a time as one sweeps across the lattice. On the other hand, smearing is defined as a simultaneous update of all link variables based on neighbours at the previous iteration. The dimensionality of smearing can be 3D where only the spatial links are smeared, or 4D where temporal links are involved. Throughout this work we adopt the later nomenclature.

5.2.2 Smearing radius

In the standard APE smearing [101], a smearing sweep consists of a replacement of the link-variable $U_\mu(x)$ ($\mu = 1, 2, 3, 4$) by the $SU(3)_c$ projected link $\bar{U}_\mu(x)$ that

maximizes the trace

$$\text{Re Tr}\{\bar{U}_\mu(x)U_{s,\mu}^\dagger(x)\}, \quad (5.2.2)$$

where

$$\begin{aligned} U_{s,\mu}(x) = & (1 - \alpha) U_\mu(x) + \frac{\alpha}{6} \sum_{\mu \neq \nu} \{ U_\nu(x) U_\mu(x + \hat{\nu}) \\ & U_\nu^\dagger(x + \hat{\mu}) + U_\nu^\dagger(x - \hat{\nu}) U_\mu(x - \hat{\nu}) U_\mu(x + \hat{\nu} - \hat{\mu}) \}, \end{aligned} \quad (5.2.3)$$

and α is the smearing parameter. Consider by analogy, a scalar field $\phi(\mathbf{r}; n+1)$ similar to the $(n+1)$ -th smeared gauge link in the μ direction. It is related to the scalar field $\varphi(\mathbf{r}; n)$ at the n smearing time by correspondence to Eq. (5.2.3) via

$$\begin{aligned} \phi(\mathbf{r}; n+1) = & (1 - \alpha) \phi(\mathbf{r}; n) + \frac{\alpha}{6} \sum_{\nu \neq \mu} (\phi(\mathbf{r} + a\hat{\nu}; n) \\ & + \phi(\mathbf{r} - a\hat{\nu}; n)). \end{aligned} \quad (5.2.4)$$

Introducing a smearing time $\tau = n a_\tau$ with a spacing a_τ , the finite difference smearing operator can be approximated by $\Delta_n \simeq a_\tau \partial_\tau$. Applying this operator into Eq. (5.2.4) yields

$$\partial_\tau \phi(\mathbf{r}; \tau) \simeq \frac{a}{a_\tau} \frac{\alpha}{6} \sum_{\nu \neq \mu} (\partial_\nu \phi(\mathbf{r}; \tau) + \partial_\nu \phi(\mathbf{r} - a\nu; \tau)). \quad (5.2.5)$$

It follows that

$$\partial_\tau \phi(\mathbf{r}; \tau) = D \nabla^2 \phi(\mathbf{r}; \tau),$$

with the diffuseness

$$D \equiv \frac{\alpha}{6} \frac{a^2}{a_\tau}. \quad (5.2.6)$$

The unsmeared field corresponds to source

$$\phi(\mathbf{r}; n=0) = \delta(\mathbf{r}). \quad (5.2.7)$$

The solution of the above intial value problem Eq. (5.2.6) and Eq. (5.2.7) is a Green function of the heat PDE equation. This gives the evolution of the scalar field in the smearing time

$$G(\mathbf{r}; \tau) = \frac{1}{(4\pi D\tau)^{\frac{3}{2}}} \exp \left[-\frac{\mathbf{r} \cdot \mathbf{r}}{4D\tau} \right]. \quad (5.2.8)$$

The diffused field is Gaussian distributed through a sphere with a characteristic radius

$$\begin{aligned} R_s \equiv & \left(\frac{\int d^3 \mathbf{r} G(\mathbf{r}; \tau) \mathbf{r}^2}{\int d^3 \mathbf{r} G(\mathbf{r}; \tau)} \right)^{1/2}, \\ = & a \sqrt{\alpha n}. \end{aligned} \quad (5.2.9)$$

5.2.3 Calibration of smearing algorithms

Calibrating different smearing algorithms can proceed via comparing the respective number of smearing sweeps in each smearing scheme with respect to a certain threshold [149]. The reconstructed action-density [150] normalized to a single instanton action S/S_0 is the threshold adopted here. Fig. 5.1 shows the relative number of smearing sweeps for different values of the stout-link smearing parameter ρ compared to that at $\rho = 0.06$ in the improved stout-link smearing algorithm [146], with $\epsilon = -0.25$. Assuming that the number of smearing sweeps scales with the smearing parameter as

$$\frac{n_s(\rho_2)}{n_s(\rho_1)} = \left(\frac{\rho_1}{\rho_2}\right)^\delta, \quad (5.2.10)$$

the fit of the logarithm of both sides in Eq. (5.2.10) to straight line yields a slope $\delta = 1$ as it is depicted in Fig. 5.1. The number of sweeps in the improved stout-link smearing, therefore, scales inversely with the smearing parameters. The standard APE smearing shows also the same scaling behavior [149] and both algorithms can be calibrated through

$$\frac{\alpha n_{\text{ape}}(\alpha)}{\rho n_s(\rho)} = c. \quad (5.2.11)$$

Calibration with respect to APE smearing at $\alpha = 0.7$ yields the proportionality constant $c = 6.15(3)$. Using Eq. (5.2.9), $R_s = a\sqrt{\rho cn_s}$.

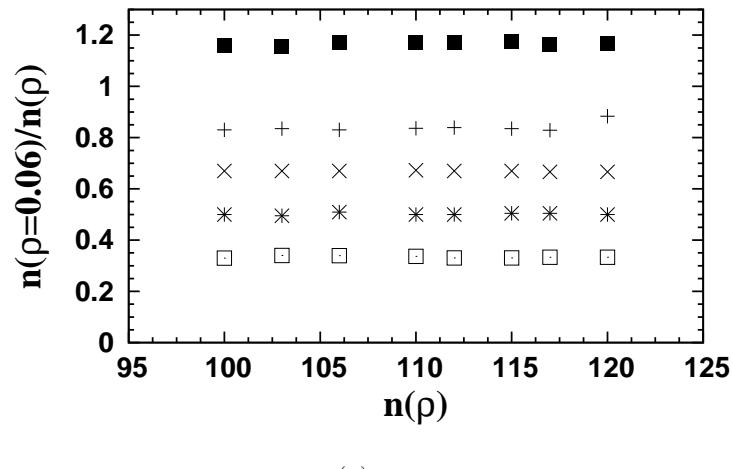
5.2.4 Quark–antiquark potential

Throughout this investigation, the technique adopted to enhance the signal to the noise ratio in the correlation function which characterizes the gluon flux involves smearing the gauge links by the over-improved stout-link smearing algorithm described above. In this section we study the limitations of this method.

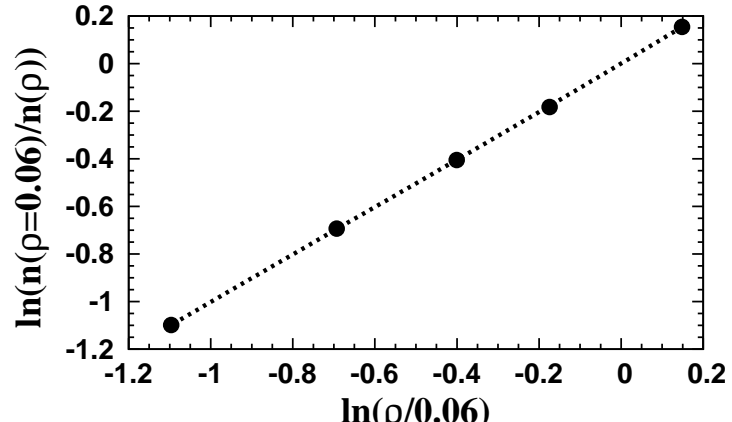
we consider 500 configurations of a $36^3 \times 10$ lattice at $\beta = 6$. The whole four dimensional torus is smeared for the consecutive levels of smearing corresponding to 20, 40, 60, and 80 sweeps, forming four data set of smeared-gauge configurations.

The choice of the appropriate data set (smeared-configuration) for the numerical evaluation of the expectation values in Eq. (3.3.3) at each distance scale, should be based on a compromise to simultaneously achieve two tasks, namely that the smearing level has a minimal effect on the physical observables, and a significant error reduction is gained. The larger the separation distance between the quark pair, the higher the smearing level required to gain good signal to noise in the correlations in Eq. (3.3.3). However, smearing has an effect on the observables similar to the increase of the lattice space-time cutoff, and a large enough number of smearing sweeps will result in a subsequent loss of the physics on the short distance scale.

The physical observable of direct relevance to the properties of the gluonic flux tube is the quark–antiquark potential. For each level of smearing, we numerically evaluate the quark anti-quark potential and the corresponding force. At fixed temperature T , the Monte Carlo evaluation of the quark–antiquark potential at each R



(a)



(b)

Figure 5.1: (a) Plot of the logarithm of the average value of $n(\rho = 0.06)/n(\rho)$ versus $\ln(\rho/0.06)$. The line corresponds to a fit to a straight line passing through the origin.

is calculated through the Polyakov-loop correlators according to

$$V(R, T) = \frac{-1}{T} \log(\langle P(0)P^\dagger(R) \rangle). \quad (5.2.12)$$

The jackknife error analysis for the data shows a significant decrease in the uncertainties associated with Polyakov-loop correlators on a short distance scale when measurements are taken after 20 sweeps of smearing. For large distances, a subsequent increase of 20 sweeps would provide error reduction by factors of $1.3 \leq x \leq 1.5$ for the corresponding distances $0.6 \text{ fm} \leq R \leq 1 \text{ fm}$. Table 5.1 summarizes the factors of error reduction for the Polyakov-loop correlator after each incremental increase of 20 sweeps of smearing. It is worth noting that by the use of a link integration method [151], one would not expect a factor of error reduction that can be more than $x \simeq 1.1$ in the middle region. For larger distances, however, the link integration method would be beneficial only if supplemented by a large number of measurements.

Table 5.1: The error reduction factor in the Polyakov-loop correlator, Eq. (3.5.29), by the increase of the number of 20 smearing sweeps for each smeared data set.

No. sweeps	20 – 40	40 – 60	60 – 80
$R = 6a$	1.3	1.1	1.1
$R = 8a$	1.4	1.2	1.2
$R = 10a$	1.5	1.3	1.2

To test the validity of the gauge-smearing approach, or equivalently, to determine the levels of smearing for which the physics is left intact, one is tempted to set a reference scale which signifies how the smeared data would behave with respect to it. Here, we set this reference to be the string model parametrization of Eq. (4.3.7). This approach of referencing the data to the string model is justified by the fits previously reported in Ref. [81], which has returned good χ^2 and shown stability to the fit range at large distances.

The numerical data obtained for the quark–antiquark potential, Eq. (5.2.12), on every smeared gauge configuration is fitted to the string picture $q\bar{q}$ potential of Eq. (4.3.7). The effects of smearing are expected to be more pronounced at short distances. For this reason the minimal fit distances are taken as large as possible, $R > 0.7 \text{ fm}$ for $T = 0.8 T_c$, and $R > 0.9 \text{ fm}$ for $T = 0.9 T_c$. The string tension has been taken as a fitting parameter. The fits are returning good χ^2 for all the smeared data sets considered.

The quark–antiquark potential and the corresponding fits are shown in Fig. 5.2. The fits to the data show almost equal slopes for all smearing levels. This is also manifest in Table 5.2, where the string tensions are measured in accord with Eqs. (4.3.7) and (4.3.10). Within the standard deviations of the measurement, the returned string tensions for all levels of smearing are equal. At temperature $T = 0.9 T_c$, our measurements for the string tension agree for all the data sets. Moreover, this value is in agreement with that reported in Ref. [81].

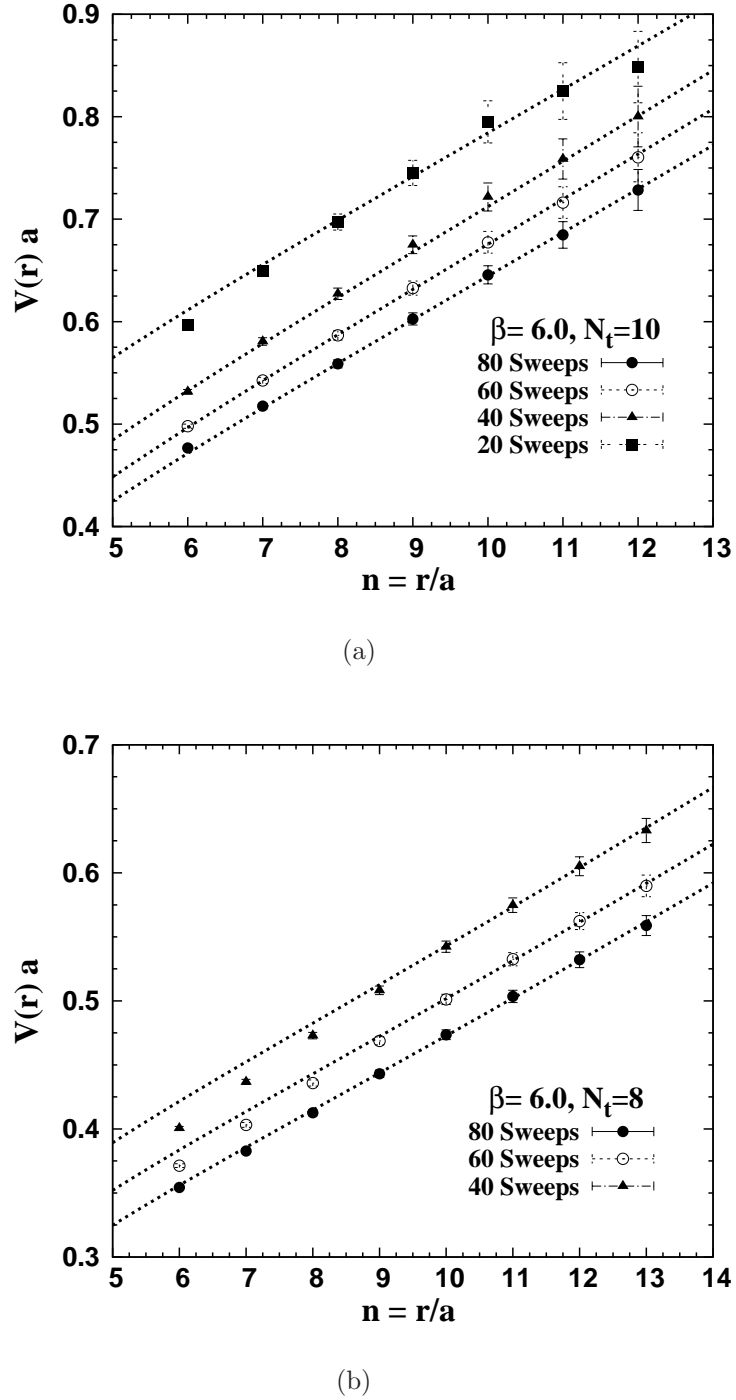


Figure 5.2: The quark-antiquark potential measured at each depicted smearing level. The lines correspond to fits of the potential obtained from the string picture of Eq. (4.3.7) for each data set as described in the text. The upper plot is at $T = 0.8 T_c$ while the lower plot is at $T = 0.9 T_c$.

Table 5.2: The string tension measured on all data sets corresponding to various levels of link smearing. The measurements are obtained from the fits to Eqs. (4.3.7) and (4.3.10).

No. sweeps	σa^2	Fit range $n = R/a$
$T = 0.8 T_c$		
20	0.047(3)	8-12
40	0.050(2)	8-12
60	0.0493(9)	8-12
80	0.0478(6)	8-12
$T = 0.9 T_c$		
40	0.0385(8)	10-13
60	0.0377(9)	10-13
80	0.0373(8)	10-13

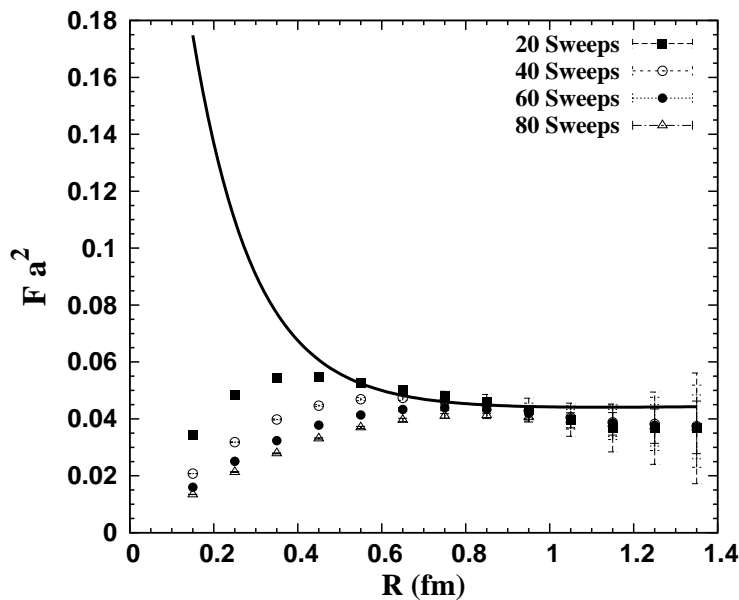


Figure 5.3: The $q\bar{q}$ force measured for all the smearing levels up to a distance of 1.4 fm. The temperature is $T = 0.8 T_c$, and $\beta = 6$. The line denotes the force as predicted by the string model at finite temperature, Eq. (4.3.7).

The factors of error reduction at higher temperature at $R = 1$ fm after 40 sweeps of smearing compares to the corresponding one at $T = 0.8 T_c$ after 80 sweeps. The noise tends to decrease with the increase of the temperature. This analysis shows that for the $q\bar{q}$ separation distance $R \geq 1.0$ fm as depicted in Table 5.2, all of the smeared configurations are appropriate for revealing the gluonic field.

On the other hand, it is clear that the data points for $R \leq 0.8$ fm shift upwards with the increase in the number of smearing sweeps. The removal of short distance physics is manifest here. The difference in the regularization brought about by the increasing of the space-time cutoff introduced by smearing, shifts the $q\bar{q}$ potential by a renormalization constant in Eq. (5.2.12). To illustrate the effect of smearing on the $q\bar{q}$ potential, the potential Eq. (5.2.12) has not been normalized. The $q\bar{q}$ force, however, can be calculated to eliminate these constant shifts. With the definition of the derivative on the lattice taken as in Refs. [62, 88], the force is computed as

$$F(r - \frac{a}{2}) = \frac{V(r) - V(r - a)}{a}. \quad (5.2.13)$$

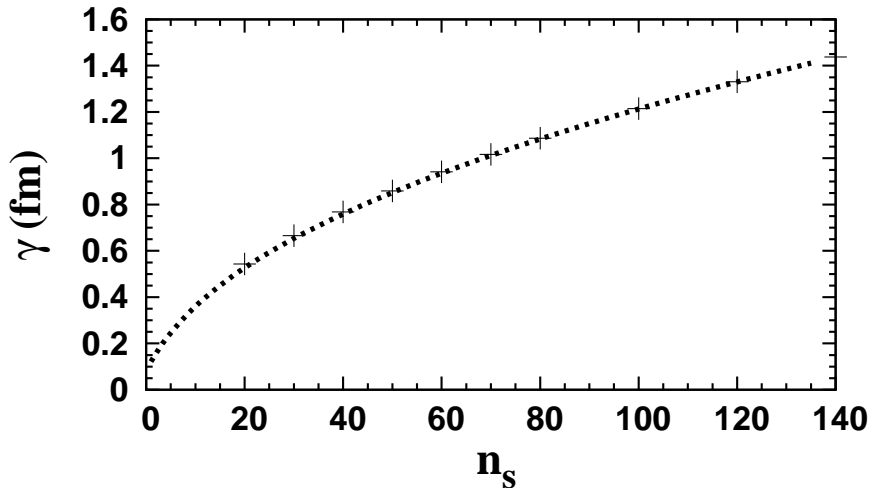


Figure 5.4: The diameter of smearing $2R_s$ versus the number of sweeps n_s for the improved stout-link algorithm with $\rho = 0.06$ as in Eq. (5.2.9).

Figure 5.3 shows the force calculated for all smearing levels for distances up to 1.4 fm. The force from the string picture, Eq. (4.3.7), with a fit parameter measured at 60 sweeps in Table 5.2 is illustrated. Inspection of Figs. 5.2 and 5.3 enables one to estimate a distance scale beyond which effects of smearing are negligible. For example, the results for 40 sweeps and 60 sweeps of smearing agree for $R \geq 0.76$ fm in Fig. 5.3. Similar comparisons of 40 and 60 sweeps or 60 and 80 sweeps provide the results, R_F , depicted in Table 5.3.

This also can be read in conjunction with the radius of Brownian motion or the so-called smearing radius. For the standard APE smearing [101], this quantity can be calculated analytically [3], and may then be calibrated [149] to the improved stout-link smearing algorithm used here. This gives a smearing radius of

$$R_s = \sqrt{c\rho n_s} a, \quad (5.2.14)$$

Table 5.3: The characteristic radii R_s and R_F at each smearing level.

Number of sweeps	R_F (fm)	R_s (fm)	$2 R_s$ (fm)
40	0.65	0.38	0.76
60	0.75	0.47	0.94
80	0.95	0.54	1.04

where n_s denotes the number of smearing sweeps and $c = 6.15(3)$ is the calibration constant calculated above. In Fig. 5.4 the smearing radius is plotted versus the number of smearing sweeps. R_s describes the characteristic scale of smearing, within which the gluon action density has been suppressed. Values for R_s are compared to R_F in Table 5.3, where the radius threshold for agreement of the $q\bar{q}$ force, R_F , lies close to the smearing diameter $2 R_s$ which is the minimal distance between two diffuse links in Polyakov-loop correlators. Therefore, a conservative range of trust for distance scales—where the essential features of the confinement remain unchanged for a given level of gauge-field smearing—can be provided by

$$\gamma = 2 R_s. \quad (5.2.15)$$

5.3 Link integration

The key idea of the link integration [152] is to reduce the statistical noise by substituting the link operator by an expression giving the same mean values with less variance. Let O_1 be an observable with variance proportional to $\langle O_1^2 \rangle$. We find another variable O_2 such that

$$\begin{aligned} \langle O_1 \rangle &= \langle O_2 \rangle, \\ \langle O_1^2 \rangle &\gg \langle O_2^2 \rangle. \end{aligned} \quad (5.3.1)$$

To apply this to correlation functions, the variables have to be mutually independent. Because of the locality of the action, this condition can be easily met in the case of Polyakov loop correlators because each link variable U which belongs to the P loops are mutually independent for separation distance greater than two. The link integration method can then be stated as

$$\langle \prod_{i \in p} U(i) \prod_{i' \in p'} U(i') \rangle = \langle \prod_{i \in p} \bar{U}(i) \prod_{i' \in p'} \bar{U}(i') \rangle. \quad (5.3.2)$$

We replace the temporal link variables U in the Polyakov loops with the new link variable

$$\bar{U} = \frac{\int dU U e^{-Tr(QU^\dagger + UQ^\dagger)}}{\int dU e^{-Tr(QU^\dagger + UQ^\dagger)}}, \quad (5.3.3)$$

where Q is the sum of the staples associated with the link U .

Heat bath method may be used to numerically evaluate the above integral. Although the result of the integration should not depend on the number of heated hits N , the statistical fluctuations decrease with N to a plateau value. However, fast numerical evaluation of an SU(3) link integration, through the evaluation of the one-link integral expressed as contour integrals [151], is more feasible from the practical point of view. The one-link integral is associated with

$$Z(Q) = \int dU \exp[-Tr(Q U^\dagger + U Q^\dagger)]. \quad (5.3.4)$$

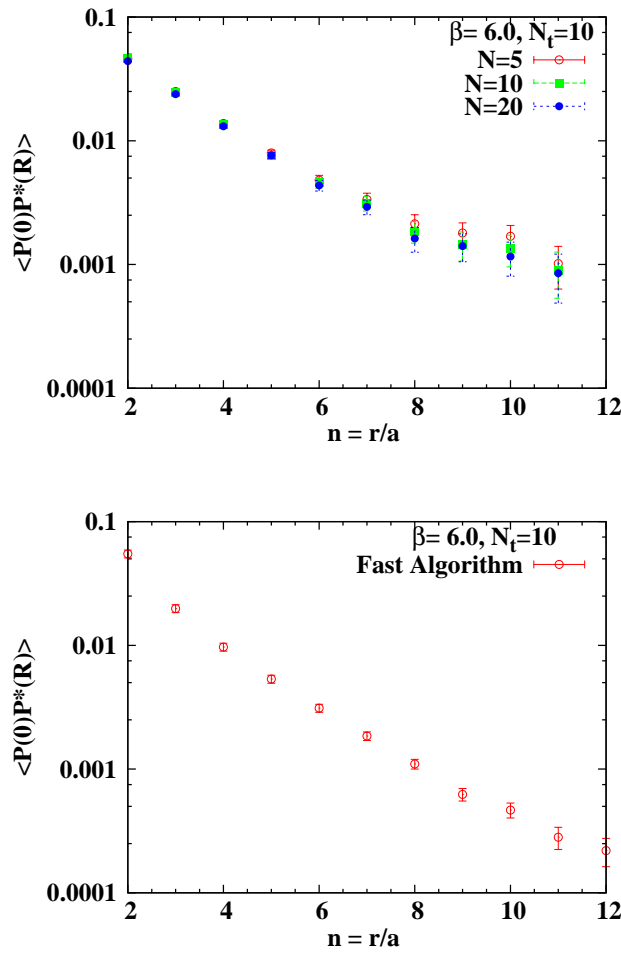


Figure 5.5: The Polyakov loop correlators measured using the heatbath integration (above), and fast link integration (below).

This defines an integral over one SU(3) matrix. The value of the integration depends on the neighboring links through the so-called source R . As discussed above, the integral can be evaluated through the heat-bath method. In this evaluation scheme, N heated hits are necessary to reduce statistical errors. This consumes large CPU time (one order of magnitude more than the Monte Carlo updating) and renders the method inefficient in some applications such as the calculations of

Table 5.4: The values of Polyakov loop correlators using the link integration method and the corresponding measured lattice spacing for various $q\bar{q}$ separations R . The table summarizes the obtained values using the heatbath algorithm with $N_{up} = 10$, $N_{meas} = 90$, and the fast link integration method.

Heatbath integration			Fast integration	
R	$\langle P P^\dagger \rangle$	a	$\langle P P^\dagger \rangle$	a
6	0.0045(4)	0.10	0.0053(4)	0.10
7	0.0031(4)	0.10	0.0031(2)	0.10
8	0.0018(3)	0.09	0.0018(1)	0.10
9	0.0014(3)	0.10	0.00109(9)	0.10

gluon flux. The above integral can be expressed in terms of contour integrals [151] involving Bessel functions and then evaluated numerically. The integrated SU(3) link reads

$$Z(Q) = \oint \frac{dx}{2\pi i} e^{xL} \left(\frac{x}{P(x)} \right)^{1/2} I_1 \left(\sqrt{\frac{2P(x)}{x}} \right), \quad (5.3.5)$$

where $L = \det(Q) + \det(Q)^\dagger$ and $P(x) = \det(1 + xQQ^\dagger)$, and I_k are Bessel functions of the second kind. The first moment would give the link averaged link

$$\bar{U} = \frac{\partial}{\partial Q^\dagger} (\log Z(Q)), \quad (5.3.6)$$

with

$$\begin{aligned} \frac{\partial Z}{\partial Q^\dagger} = & \det(Q^\dagger)(Q^{*-1}) \times \oint \frac{dx}{2\pi i} x e^{xL} \left(\frac{x}{P(x)} \right)^{1/2} I_1 \left(\left(\frac{2P(x)}{x} \right)^{1/2} \right) \\ & + \oint \frac{dx}{2\pi i} \frac{e^{xQ}}{P(x)} I_2 \left(\frac{2P(x)}{x} \right)^{1/2}. \end{aligned} \quad (5.3.7)$$

The integrals are evaluated numerically using Gaussian quadrature along a circle centered at the origin. The radius of the contour circle is chosen such that the asymptotic expansion of Bessel functions,

$$I_\nu(z) = e^z / \sqrt{2\pi z} [1 - (4\nu^2 - 1)/8z + (4\nu^2 - 1)(4\nu^2 - 9)/2!(8z)^2 - ..], \quad (5.3.8)$$

is a good approximation. Clever tuning is required to minimize the round off errors and at the same time the length of the asymptotic expansion. Using the Gauss-Kronrod quadrature formula, we reported an accuracy estimate of 10^{-6} for the lattice parameters considered here. Fig. 5.5 shows Polyakov loop correlators calculated using the heatbath and fast integration schemes. Saturation in the statistical noise using the heatbath method is reached after $N = \mathcal{O}(10)$ heated hits which increases the time of evaluations. The values of error reduction and measured lattice spacing are depicted in Table 5.4.

5.4 Multi-level algorithm

In non-abelian pure gauge theories, the expectation value of a product of Polyakov loops is notorious for being difficult to compute because the signal to noise ratio rapidly decays with the increase of the loop size. The link integration method discussed above will not be efficient when simulations are extended to the low temperature region of the theory. The multi-level scheme of integration exploits the locality of the theory, and results in an exponential suppression of the standard errors in the correlators. The expectation value of a product of Polyakov loops is

$$\langle \Gamma \rangle = \frac{1}{z} \int D[U] \Gamma e^{-S[U]}. \quad (5.4.1)$$

The factorization property of this functional integral is a result of the local structure of the theory and leads to the possibility of a multilevel simulation algorithm. The key objects in this factorizing are the tensor products of link variables. In the case of two Polyakov loops this will be the two-link operator

$$\mathbb{T}(t_0)_{\alpha\beta\gamma\delta} = U(x, t_0)_{\alpha\beta} U^\dagger(x + R, t_0)_{\gamma\delta}, \quad (5.4.2)$$

with $\mathbb{T} \in 3^* \otimes 3$ representation of $SU(3)$.

The Multiplication law of the tensors \mathbb{T} reads

$$\mathbb{T}(t_0)_{\alpha\lambda\gamma\epsilon} \mathbb{T}(t_0 + a)_{\lambda\beta\epsilon\delta} = M_{\alpha\beta\gamma\delta}. \quad (5.4.3)$$

The product of two Polyakov lines can be represented as a multiplication of the two-link operator as

$$\begin{aligned} P(x) P^\dagger(x + R) &= (\mathbb{T}(t_0) \mathbb{T}(t_0 + a) \cdots \mathbb{T}(T - a) \mathbb{T}(T))_{\alpha\beta\gamma\delta} \delta_{\alpha\beta} \delta_{\gamma\delta} \\ &= M_{\alpha\alpha\gamma\gamma}. \end{aligned} \quad (5.4.4)$$

The locality of the action

$$S[U] = \frac{1}{g^2} \sum_{x,\mu,\nu} Tr \{ 1 - U_\mu(x) U_\nu(x + a\hat{\mu}) U_\mu^\dagger(x + a\hat{\nu}) U_\nu^\dagger(x) \} \quad (5.4.5)$$

allows integrations to be performed on the level of sublattices with the spatial links on the boundaries held fixed. The sublattice expectation value reads

$$[\mathbb{T}(t_0) \cdots \mathbb{T}(t_0 + ma)] = \frac{1}{Z_{sub}} \int D[U] \mathbb{T}(t_0) \mathbb{T}(t_0 + a) \cdots \mathbb{T}(t_0 + ma) e^{-S[U]_{sub}}. \quad (5.4.6)$$

The sublattice integrals are a function of the links at the boundaries. The links in the interior, however, are dynamical degrees of freedom to be integrated over. This results in the hierarchical integration formula

$$\langle P(x) P^\dagger(x + R) \rangle = \langle [[\mathbb{T}(t_0) [\mathbb{T}(t_0 + a)]] \cdots [[\mathbb{T}(T - a) [\mathbb{T}(T)]]]_{\alpha\alpha\gamma\gamma} \rangle. \quad (5.4.7)$$

By virtue of the action locality, the integration

$$[\mathbb{T}(x_0)\mathbb{T}(x_0 + a)] = [[\mathbb{T}(x_0)][\mathbb{T}(x_0 + a)]], \quad (5.4.8)$$

is equivalent. The tensor $[\mathbb{T}(t_0)]_{n_{up}}$ is integrated over with the updates in the time slice $[t_0, t_0 + a]$, the tensor $[\mathbb{T}(t_0 + a)]_{n_{up}}$ is accordingly averaged for updates n_{up} within the time slice $[t_0 + a, t_0 + 2a]$, and so on.

$$[[\mathbb{T}(t_0 + a)]_{n_{up}}[\mathbb{T}(x_0)]_{n_{up}}]_{N_{up}} = [\mathbb{T}(x_0 + a)\mathbb{T}(x_0)]. \quad (5.4.9)$$

The multi-level algorithm proceeds through the following steps:

- A sequence of gauge field configurations is first generated using a hybrid heat-bath overrelaxation link updates.
- The product $[\mathbb{T}(t_0)\mathbb{T}(t_0 + 2a)]$ is estimated by updating the gauge field in the interior of the time-slice $[t_0, t_0 + 2a]$ a number of times followed by averaging $\mathbb{T}(t_0)\mathbb{T}(t_0 + a)$ over these configurations.
- Finally, we integrate the trace of the products in Eq. (5.4.7) via the lower level estimates calculated in the second step. That is, by averaging first within the level and then multiplying the averaged results, one gains a significant increase in the number of statistical samples as “cross terms” between levels in the averaging process contribute.

While the link integration method [152] provides efficient noise reduction at small quark separations for the expectation values of Polyakov loops in Eq. (5.2.12), noise remains problematic at large separations. The method is expected to be efficient for the $Q\bar{Q}$ source separation range $R \leq 0.5$ fm [151] but has to be supplemented with a large number of measurements for the calculations of the larger distance $q\bar{q}$ potential [81]. The number of measurements has to be increased significantly for the corresponding 3Q potential calculations with a three point correlator (as we will discuss in Chapter 9). On the other hand, the action density calculations are even more challenging in both cases [135].

The exponential reduction of noise provided by the leveling approach of the Lüscher Weiss (LW) requires the hierarchical integration to be carried out over time sub-slices larger than the deconfinement temporal extent $t_{sub} > 1/T_c$ [118]. For the temperatures considered here, the division of measurements into binned sub-measurements resembles a one level implementation of the LW method, with updating of the last time slice.

5.5 Conclusion

A combination of a large number of Monte Carlo updates followed by link averaging can be performed similarly to that performed in Ref. [81] to evaluate the $q\bar{q}$ potential for a range of temperatures above and below the confinement phase. This involves a large number of updating sweeps and measurements which makes it rather expensive in terms of the CPU time. Memory requirements have prevented an analysis of the baryon potential to date. This is even more problematic for the evaluation

of the gluonic flux distribution, since this evolves the Monte Carlo evaluation of not only the Polyakov-loop correlator, but also the three-point (four point in the case of baryon) correlation function in the numerator of Eq. (3.4.5). Throughout this work, four-dimensional gauge smearing is chosen as a fast and effective method for revealing the general topological features of the flux distribution which can be confronted with the predictions of the string model. We have been able to show in this chapter the ranges of the validity of this approach, through the measurements of the physical observables that have been previously reported in [81], i.e, the $q\bar{q}$ potential and the string tension. The combination of link integration and multi-level methods provides effective methods for probing the flux distribution at low temperatures. This is outside the scope of the present thesis, but is of merit for future work as computing resources allow.

Chapter 6

Gluonic Profile of Static Mesons

6.1 Outline

The distribution of the gluon action density in mesonic systems is investigated at finite temperature. The simulations are performed in pure SU(3) Yang-Mills gauge theory for two temperatures below the deconfinement phase. Unlike the gluonic profiles displayed at $T = 0$, the action-density isosurfaces display a prolate-spheroid-like shape. The curved width profile of the flux tube is found to be consistent with the prediction of the free bosonic string model at large distances.

6.2 Introduction

In the flux-tube model, the linearly rising potential between a pair of static colour sources is believed to be due to the formation of a thin gluonic flux tube of a constant cross-section. At high temperatures, lattice simulations on pure SU(3) gauge fields [81] have indicated a decrease of the effective string tension for the quark–antiquark potential with the rise of the temperature. The QCD vacuum structure around the sources is then expected to exhibit gluonic profiles with widths variant to the zero temperature case. The detailed geometry of the gluonic field at finite temperature and whether it holds the constant cross-section property is an interesting topic that has not yet been explored in lattice quantum chromodynamics.

The low-energy dynamics of the flux tubes in the infrared region of a confining gauge theory can be described in terms of an effective bosonic string. The thin flux tube between two widely separated static color sources fluctuates like a massless string. The linearly rising part of the potential arises from the classical configuration which corresponds to the flat world sheet of the string. The quantum fluctuations of the string lead to a universal subleading correction to the potential well known as the Lüscher term [67]. Lattice simulations for several gauge theories [63, 64, 65, 66, 119] have supported the existence and the universality of the string’s subleading effect. At high temperatures, the gluonic modes come into play and the effective string description of the temperature-dependent quark–antiquark potential has been worked out in Refs. [117, 125]. A further comparison with $SU(3)$ Monte Carlo lattice data for temperatures beginning from $T = 0.8 T_c$ [81] has shown a good parametrizing behaviour to the string picture formula for a minimal distance of

$RT = 0.5$. On the other hand, there have been numerical indications that the inclusion of the higher-order string effects beyond the Gaussian approximation, e.g, the NLO string's self-interaction term in the Nambu-Goto effective string action, has reproduced the correct temperature-dependent string tensions up to a temperature scale of $T = 0.5 T_c$ in the three-dimensional gauge Z_2 model [153].

The string model predictions of a logarithmic broadening [126] for the width of the string delocalization have also been observed in several lattice simulations corresponding to different gauge groups [63, 65, 138, 154]. As the temperature increases, substantial deviations from the logarithmic behaviour are expected, and the broadening turns eventually into a linear growth for large distances before the deconfinement is reached from below [129]. Apart from the peculiar features in the broadening of the flux tube when the temperature is raised, the string picture predicts an effect which is rather interesting from the geometrical point of view. The width calculated at each corresponding transverse plane to the line joining the two quarks is found to differ from that at the central plane by an amount that increases with the rise of the temperature. In other words, the mesonic string picture is implying a curvature in the gluonic profile that becomes more pronounced as higher temperatures are approached. The string self-interaction with the quark line causes a noticeable difference in the delocalizations beyond the central transverse plane and these aspects remain to be ascertained in lattice quantum chromodynamics. Moreover, revealing the whole profile of the glue at finite temperature provides a particularly interesting source of knowledge regarding the true geometry of the flux tube, since, naturally, at finite temperature one need not hold to any particular assumption for the shape of the gluonic source-wave functions in the relevant gauge-invariant objects representing the quark states. Probing the transverse profile of the glue might even be of relevance to the modeling of ground-state sector of the theory where the exact geometry of the flux tube seems to be not yet settled [155].

In this work, we investigate the distributions of the colour field inside a static meson at two temperatures below the deconfinement phase, $T \simeq 0.9 T_c$, and $T \simeq 0.8 T_c$. Since the bosonic string predictions are expected to be more relevant to pure Yang-Mills theories with static colour sources (rather than QCD with dynamical sea quarks where string breaking occurs), the lattice simulations are performed on the $SU(3)$ gauge group in the quenched approximation. The field strength inside the corresponding quark system will be revealed by correlating an improved action-density operator [150] to the mesonic state. The static mesonic state is accounted for by means of Polyakov-loop correlators. Gauge four-dimensional smearing [146, 147], in addition to a high statistics gauge-independent approach [2], will be employed to enhance the signal to the noise in the flux correlation function. This noise-reduction approach is variant to other approaches that utilize Abelian gauge-fixing [143] to reduce the noise. The obtained profile of the action density will then be compared to the prediction of the mesonic string models at several distances for the highest temperature near the deconfinement point $T \simeq 0.9 T_c$.

6.3 Colour field measurements

In this investigation we have taken our measurements on 500 quenched QCD gauge-field configurations for each set of lattice parameters considered. The gauge configurations were generated using the standard Wilson gauge action on lattices with spatial volume of 36^3 . We chose to perform our analysis with lattices as fine as $a = 0.1$ fm by adopting a coupling of value $\beta = 6.00$, with temporal extents of $N_t = 8$, and $N_t = 10$ slices, which correspond to temperatures $T \simeq 0.9 T_c$, and $T \simeq 0.8 T_c$, respectively. The gluonic gauge configurations were generated with a pseudo-heat bath algorithm [93, 94] updating the corresponding three SU(2) subgroup elements [95]. Each update step consists of one heat bath and 4 microcanonical reflections. The measurements are taken after each 2000 of updating sweeps.

The static mesonic state is constructed by means of a pair of Polyakov loops corresponding to an infinitely heavy quark–antiquark pair,

$$\mathcal{P}_{2Q}(\vec{r}_1, \vec{r}_2) = P(\vec{r}_1)P^\dagger(\vec{r}_2),$$

where the Polyakov loop is given by

$$P(\vec{r}_i) = \frac{1}{3} \text{Tr} \left[\prod_{n_t=1}^{N_t} U_{\mu=4}(\vec{r}_i, n_t) \right], \quad (6.3.1)$$

and the vectors \vec{r}_i define the positions of the quarks. The measurements that characterize the colour field are taken by a gauge-invariant action-density operator $S(\vec{\rho}, t)$ at spatial coordinate $\vec{\rho}$ of the three-dimensional torus corresponding to a Euclidean time t . The measurements are repeated for each time slice and then averaged,

$$S(\vec{\rho}) = \frac{1}{N_t} \sum_{n_t=1}^{N_t} S(\vec{\rho}, t). \quad (6.3.2)$$

The action-density operator is calculated via a highly improved $\mathcal{O}(a^4)$ three-loop improved lattice-field-strength tensor [150]. A dimensionless scalar field that characterizes the gluonic field can be defined as

$$\mathcal{C}(\vec{\rho}; \vec{r}_1, \vec{r}_2) = \frac{\langle \mathcal{P}_{2Q}(\vec{r}_1, \vec{r}_2) \rangle \langle S(\vec{\rho}) \rangle - \langle \mathcal{P}_{2Q}(\vec{r}_1, \vec{r}_2) S(\vec{\rho}) \rangle}{\langle \mathcal{P}_{2Q}(\vec{r}_1, \vec{r}_2) \rangle \langle S(\vec{\rho}) \rangle}, \quad (6.3.3)$$

where $\langle \dots \dots \rangle$ denotes averaging over configurations and lattice symmetries, and the vector $\vec{\rho}$ refers to the spatial position of the flux probe with respect to some origin. Cluster decomposition of the operators leads to $C \rightarrow 0$ away from the quarks.

6.4 Action density

6.4.1 Tube profile (qualitative picture)

The lattice operator which characterizes the gluonic field is usually taken as the correlation between the vacuum action density $S(\vec{\rho}, t)$, and a gauge-invariant operator

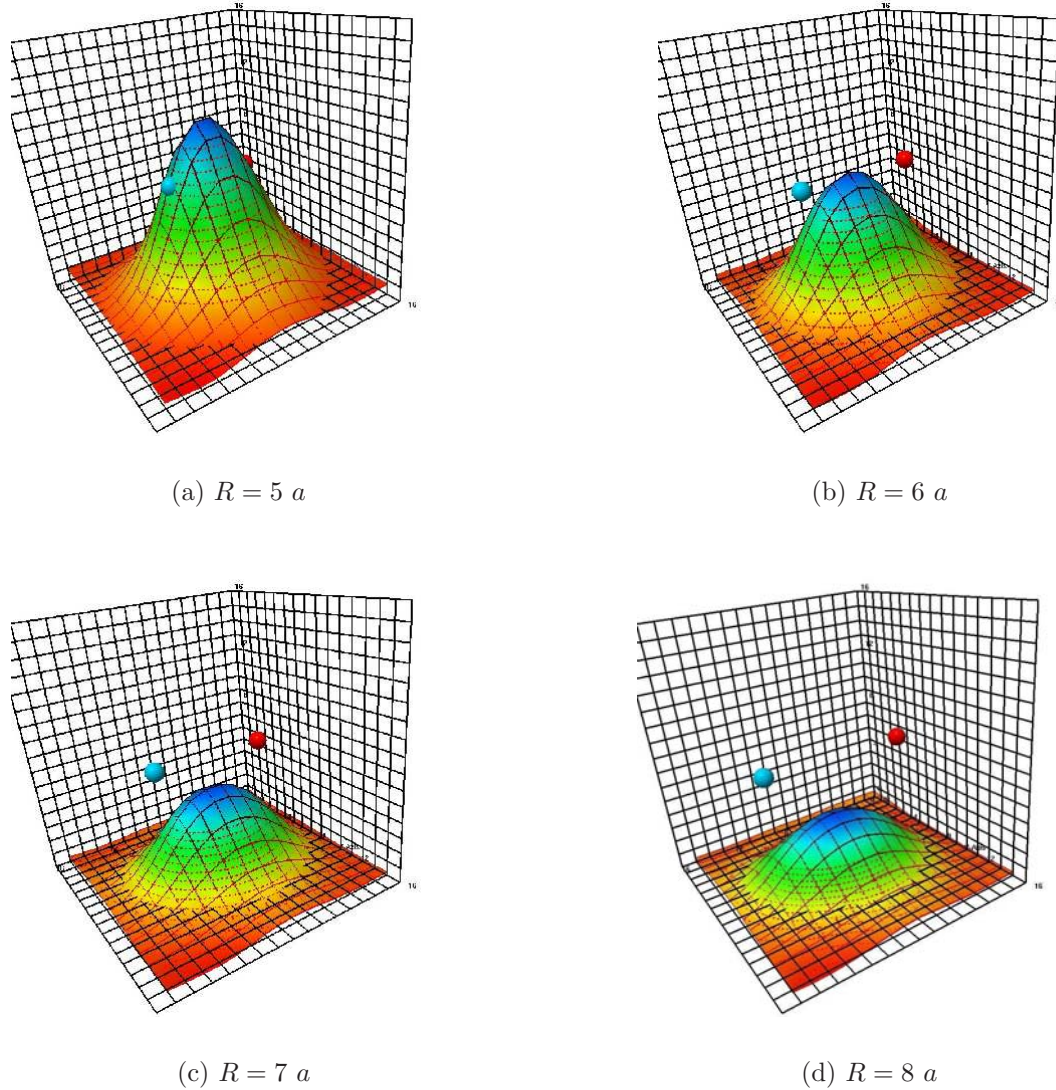


Figure 6.1: The flux-distribution $\bar{C}(\vec{\rho}, \vec{r}_1, \vec{r}_2)$ as given by the characterization Eq. (6.3.3) in the plane of the quark–antiquark pair $\vec{\rho}(x, y, z = z_0)$, for separation distances R (a) 0.5 fm, (b) 0.6 fm, to (d) 0.8 fm at $T = 0.8 T_C$. The spheres refer to the positions of the quark and antiquark.

representing the quark states. At finite temperature this must be a pair of Polyakov lines.

The action-density operator is calculated through an $\mathcal{O}(a^4)$ improved lattice version of the continuum field-strength tensor. Discretization errors are reduced by combining several clover terms complemented by tadpole improvement [150]. We take our measurements with a three-loop field-strength tensor given by

$$F_{\mu\nu}^{\text{Imp}} = \sum_{i=1}^3 w_i C_{\mu\nu}^{(i,i)}, \quad (6.4.1)$$

where $C^{(i,i)}$ is a combination of Wilson loop terms corresponding to loops with lattice extent i used to construct the clover term and w_i are weights [150]. The reconstructed action-density

$$S(\vec{\rho}) = \beta \sum_{\mu>\nu} \frac{1}{2} \text{Tr}(F_{\mu\nu}^{\text{Imp}})^2, \quad (6.4.2)$$

is accordingly measured on 20 sweeps of four-dimensional stout-link smearing. This has the effect of the removal of the divergence in the action density in the neighborhood of the quark positions. It is, however, very beneficial in obtaining a good signal to noise to display the flux strength. The correlation function Eq. (6.3.3) provides $\mathcal{C}(\vec{\rho}) > 0$, and $\mathcal{C} \simeq 0$ away from the quark position. The scaled flux distribution $\bar{\mathcal{C}}(\vec{\rho}) = 1 - \mathcal{C}(\vec{\rho})$ in the plane of the $q\bar{q}$ pair is plotted in Fig. 6.1, for several $q\bar{q}$ separation distances $R = |\vec{r}_1 - \vec{r}_2|$, at temperature $T = 0.8 T_c$. The Polyakov-loop correlator is measured on 40 sweeps of link smearing. The distribution shows a peak in the middle point between the $q\bar{q}$ pair at small separation distance $R = 0.5$ fm. As the two quarks are pulled apart, the distribution $\mathcal{C}(\vec{\rho})$ decreases rapidly, the peak behaviour diminishes and the distribution is almost constant at $R = 0.8$ fm. The qualitative description of these density plots suggests a two-dimensional Gaussian-like behaviour, however, as we will see in the next section, careful measurements of the widths at each perpendicular plane to the $q\bar{q}$ line, yield different widths for large distances.

The behaviour of the flux distribution around the outer edges of the density profile does depend on finite volume [156]. As a byproduct of performing the simulations on large lattice sizes to gain high statistics in a gauge-independent manner, the two lattices employed in this investigation are of a typical spatial size of 3.6^3 fm^3 which does minimize the volume effect.

The curvature in the flux lines is manifesting itself as is evident from the flux-contour plots in Fig. 6.2. The contour plots reveal the form of the flux tube just before the deconfinement phase $T = 0.9 T_c$, for $q\bar{q}$ sources separated by $R = 0.9$ fm and $R = 1$ fm, respectively. A similar plot of the action-density isosurface at $R = 0.9$ fm in Fig. 6.3 displays a three-dimensional version of Fig. 6.2 (prolate-spheroid-like shape) for the flux tube. This geometrical form of the density plot manifests itself at temperature $= 0.8 T_c$ which is known to be near the end of the plateau of the QCD-phase diagram [5].

It is worth noting, nevertheless, that at zero temperature, the correlation of the action density with the Wilson loop taken as a mesonic operator does not reveal

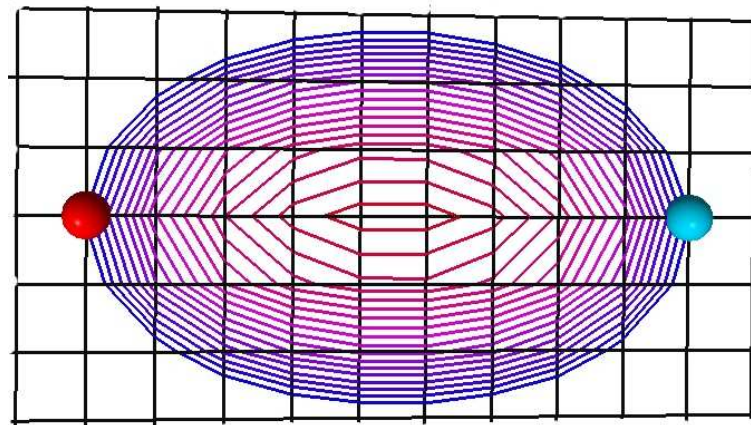
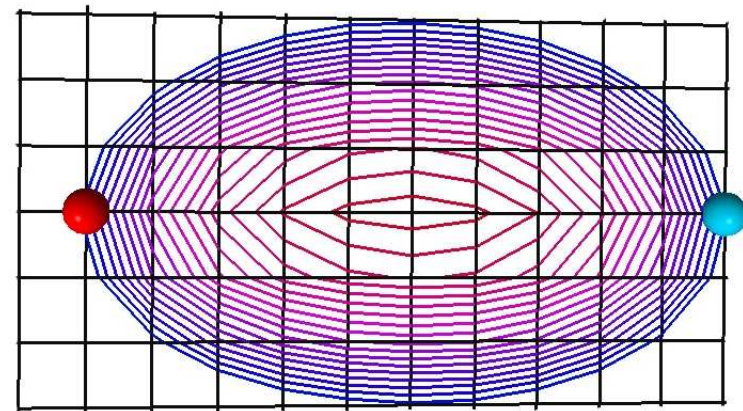
(a) $R = 9 a$ (b) $R = 10 a$

Figure 6.2: The flux-contour-line distribution in the plane of the quark-antiquark pair z_0 , for separation distances of (a) 0.9 fm, (b) 1.0 fm. The spheres denote the positions of the $q\bar{q}$ pair, $T = 0.9 T_C$.

this curvature of the flux lines in the inner region between the $q\bar{q}$ pair at large separation distance [63]. Thus we have illustrated the action-density correlations using Polyakov loops at finite temperature.

The ground-state source-wave functions in the Wilson-loop operator are trial-wave functions, and the state adopted is the one which maximizes the overlap with the ground state, usually by smearing the string of the glue connecting the quarks [63, 155]. Moreover, the calculations of gluonic distribution are plagued by systematic errors due to biasing by the shape of the source, and the corresponding limitations imposed by the statistical fluctuations upon the Euclidean-time evolution in the loop operator [2, 157].

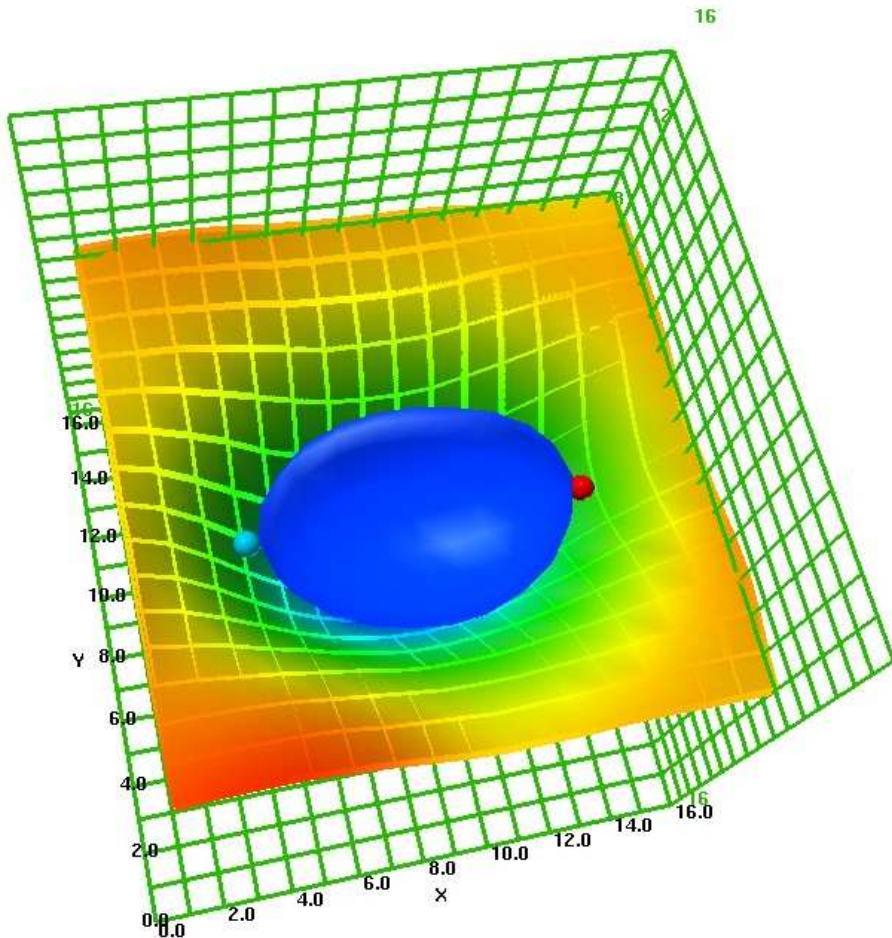


Figure 6.3: The flux iso-surface passing through the quarks, plotted together with a surface plot for the density distribution in the $q\bar{q}$ plane (inverted). The measurements are taken on 80 sweeps of smearing for separation distance $R = 9a$, and $T = 0.8 T_c$. The lattice spatial extent is 36^3 at $\beta = 6$, $a = 0.1$ fm.

Tube profile (quantitative aspects)

Usually studies carried out on the flux tube features of growth focus their measurements on the central plane transverse to the $q\bar{q}$ line. At $T = 0$, Wilson loops results

indicate a tube that has a uniform energy-density profile for large $q\bar{q}$ separations [63]. Nevertheless, at high temperature where the string tension is reported to decrease by a value around 10% at $T = 0.8 T_c$ [81], our calculations of the flux chromostrength inside the meson (Figs. 6.1, and 6.2) display a nonuniform action-density pattern around the whole $q\bar{q}$ line.

At high temperature, one would expect higher modes relevant to the collective degrees of freedom of the stringlike object to give rise to new, interesting measurable effects, which seem not only to be related to the properties of the growth of the tube's width [129], but also to the width's profile itself. The string model's solution, Eq. (4.3.17), informs us about how the tube would behave behind its symmetry point in the middle, and together with the observed chromofield profile (Figs. 6.1-6.2), one is tempted to investigate this string effect and establish a quantitative comparison between the model and the glue profile in QCD. This is the aim of this section.

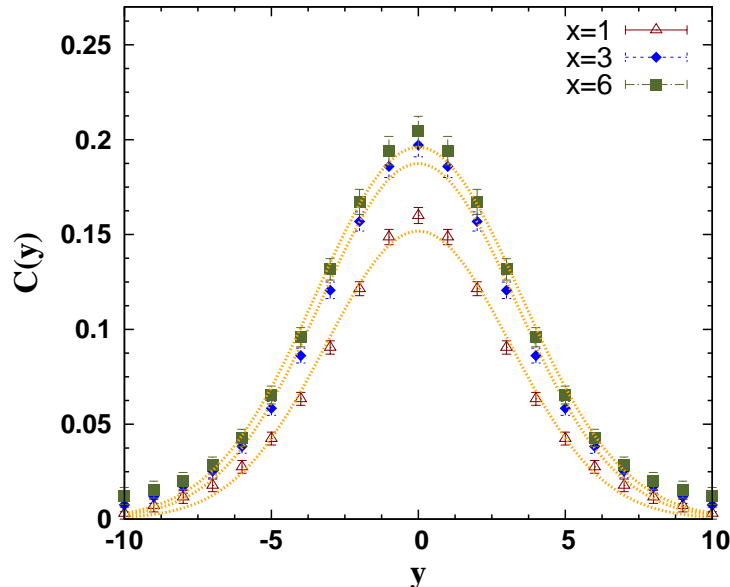


Figure 6.4: The density distribution $\mathcal{C}(\vec{\rho})$ for separation distance of $R = 12a$, $T = 0.9T_c$, plotted for the transverse planes $x = 1$, $x = 3$, and $x = 6$. The lines correspond to the Gaussian fits to the density in each plane $\vec{\rho}(x_i, y, z_0)$.

Different possible components of the field-strength tensor in Eq. (6.4.1) can separately measure the chromoelectric and magnetic components of the flux. The action density, however, is related to the chromofields via $\frac{1}{2}(E^2 - B^2)$ and is the quantity of direct relevance to the comparison with the string fluctuations [Eq. (4.3.17)].

The width of the flux tube may be then estimated through fitting the density distribution $\mathcal{C}(\vec{\rho})$ [Eq. (6.3.3)], in each selected transverse plane $\vec{\rho}(x_i, y, z_0)$ to a Gaussian [65, 126]. The width of the tube is defined as

$$W^2(x_i) = \frac{\int d^2 \eta \eta^2 e^{-(\eta^2/W^2)}}{\int d^2 \eta e^{-(\eta^2/W^2)}}. \quad (6.4.3)$$

The flux calculations with Polyakov lines as a mesonic operator are well known to be distorted by statistical noise. To take reliable measurements to reveal the tube's fine structure, we choose to perform our analysis on the tube's width at the highest temperature $T = 0.9 T_c$ where the scalar field $\mathcal{C}(\vec{\rho})$ has smaller jackknife error bars, even at very large distances. To further increase the signal to noise ratio, the number of measurements has been increased by a factor of 4. This has been done by updating each raw gauge configuration 3 times each separated by 70 sweeps of Monte Carlo updates as described in Sec. II.

Table 6.1: The width of the flux tube at each consecutive transverse planes x_i from the quark to the middle of the $q\bar{q}$ line. The measurements for sources separation distances $R = 6a$ to $R = 10a$, for the temperature $T = 0.9 T_c$.

Plane $n = R/a$	$x = 1$ $W^2 a^{-2}$	$x = 2$ $W^2 a^{-2}$	$x = 3$ $W^2 a^{-2}$	$x = 4$ $W^2 a^{-2}$
6	14.6(5)	14.4(5)	14.4(5)	
7	15.8(6)	15.6(4)	15.7(5)	
8	16.9(6)	17.0(5)	17.1(5)	17.2(5)
9	17.9(6)	18.2(6)	18.6(6)	18.8(6)

η is the set of vectors perpendicular to the $q\bar{q}$ line in the x_i plane.

To avoid artificial reduction of the error bars, each set of four configurations (original configuration together with three new ones) has been included in the same jackknife subensemble, such that the variances are calculated with respect to decorrelated bins (see also Refs. [81, 151]). The density distributions have been symmetrized around all the symmetry planes of the tube; the resultant average density $\mathcal{C}(\vec{\rho})$ is fit to a Gaussian of the form $A(x_i) e^{-(y-y_0)^2/W^2}$, with y_0 on the $q\bar{q}$ line (see, e.g., Fig. 6.4). The Gaussian fits to the data are for several transverse planes between two sources separated by a distance of $R = 12a$.

Table 6.2: Similar to Table 6.1, the widths of the flux tube are measured at each consecutive transverse planes x_i from the quark to the middle of the $q\bar{q}$ line. The measurements for sources separation distances $R = 10a$ to $R = 13a$.

Plane $n = R/a$	$x = 1$ $W^2 a^{-2}$	$x = 2$ $W^2 a^{-2}$	$x = 3$ $W^2 a^{-2}$	$x = 4$ $W^2 a^{-2}$	$x = 5$ $W^2 a^{-2}$	$x = 6$ $W^2 a^{-2}$
10	18.8(7)	19.4(6)	20.0(6)	20.4(6)	20.6(6)	
11	19.4(7)	20.3(7)	21.3(7)	22.0(7)	22.3(8)	
12	19.7(7)	21.0(7)	22.4(7)	23.4(8)	23.9(8)	24.1(9)
13	19.5(6)	21.0(7)	22.9(7)	24.4(8)	25.4(9)	25.8(9)

Tables 6.1, 6.2 and Table 6.3 summarize the measurements on both the widths $W^2(x_i)$ and the amplitudes $A(x_i)$ of the flux tube, in accord to these Gaussian fits

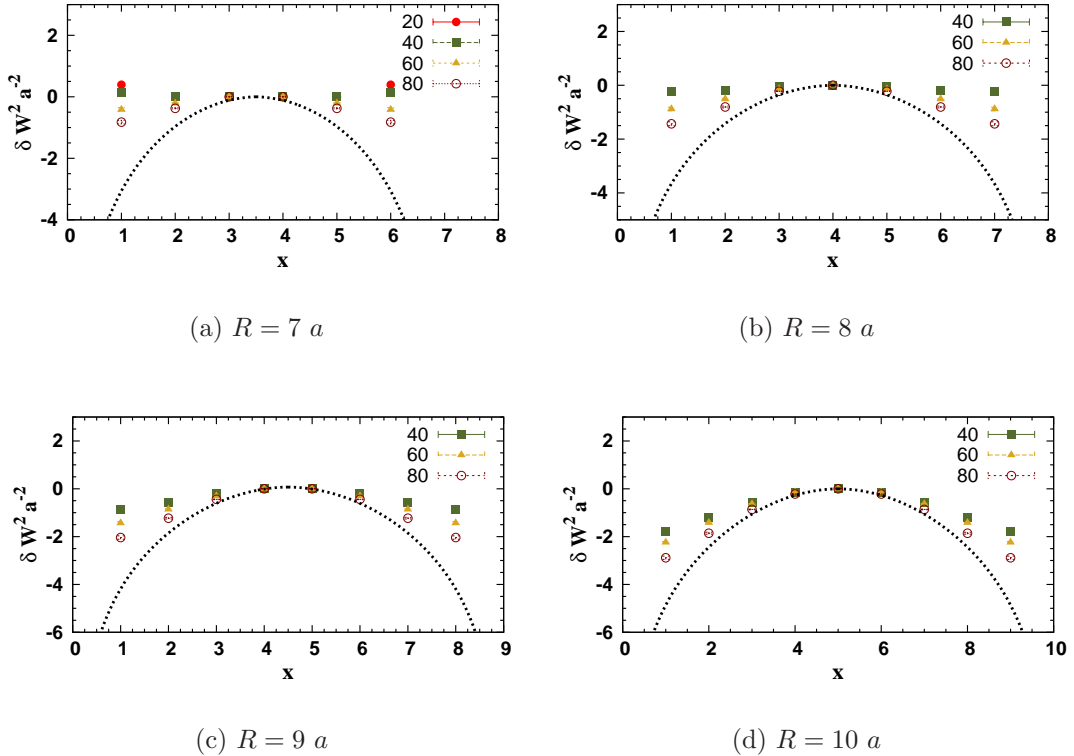


Figure 6.5: The width difference $\delta W^2 = W^2(x_i) - W^2(x_0)$ for $q\bar{q}$ separations (a) 0.7 fm, (b) 0.8 fm, (c) 0.9 fm, and (d) 1 fm, $\beta = 6$, $T = 0.9 T_C$ for each depicted smearing level. The line denotes the width difference δW^2 as predicted by the string model Eq. (4.3.17). The lowest smearing level provides the best estimate of the width difference.

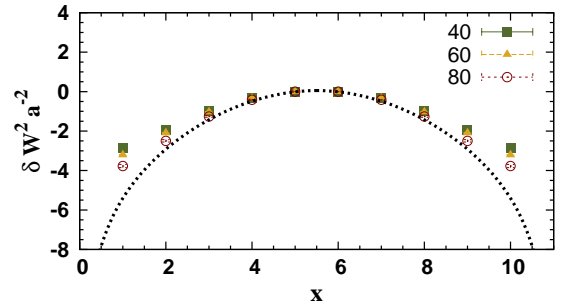
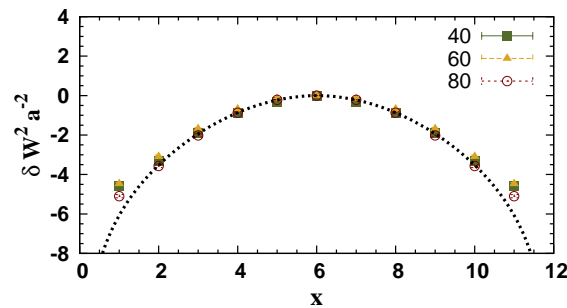
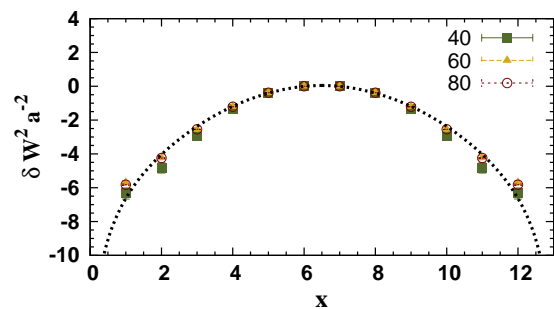
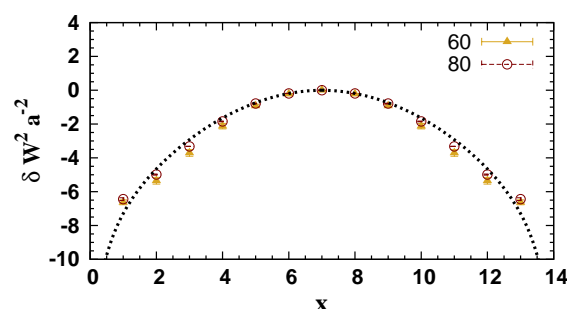
(a) $R = 11 a$ (b) $R = 12 a$ (c) $R = 13 a$ (d) $R = 14 a$

Figure 6.6: Similar to Fig. 6.5, the change in width is plotted for $q\bar{q}$ separations (a) 1.1 fm, (b) 1.2 fm, (c) 1.3 fm, and (d) 1.4 fm.

at each transverse plane x_i to the $q\bar{q}$ line. The coordinates x_i are lattice coordinates (lattice units) and are measured from the quark position $x = 0$. The uncertainties in width measurements at each transverse plane are the standard asymptotic errors in the Gaussian fits and are correlated. The flux-density measurements at each source separation are taken on all smeared sets of configurations. We will be mainly discussing results for the set of configurations corresponding to 40 sweeps of smearing. According to Sec. IV-A, this level of gauge-field smearing leaves the $q\bar{q}$ potential and force with insignificant effects for $R > 0.6$ fm. We also discuss the effects of smearing on the gluonic profile.

Table 6.3: The amplitude of the flux tube at each of the consecutive transverse planes x_i from the quark to the middle of the $q\bar{q}$ line. The measurements for sources' separation distances $R = 6a$ to $R = 10a$, for the temperature $T = 0.9T_c$.

Plane n=R/a	$x = 1$ A	$x = 2$ A	$x = 3$ A	$x = 4$ A
6	0.160(3)	0.191(3)	0.202(3)	
7	0.165(3)	0.199(3)	0.218(4)	
8	0.165(3)	0.199(3)	0.221(4)	0.229(4)
9	0.162(3)	0.195(3)	0.217(4)	0.228(4)

For a fixed source separation, the measured values in Table 6.1 and 6.2 (taken on 40 smearing sweeps) are indicating, generally speaking, changes in the tube width along the $q\bar{q}$ line. The maximum width is measured at the tube's symmetry point in the middle. At relatively small separations $R < 0.9$ fm, the change in tube width along the planes is subtle. The variation in the tube's width, however, is more pronounced at large source separation distances (see, e.g., Table 6.2) in general qualitative agreement with the predictions of the string picture Fig. 4.1. The growth in width with the increase of the source separation is also maximum at the tube's center point.

Since we focus here on comparing the tube geometry to the string profile rather than the feature of the growth, we measure the change in the width of the tube at each corresponding plane with respect to the central plane x_0 ,

$$\delta W^2 = W^2(x_i) - W^2(x_0). \quad (6.4.4)$$

This can provide a measure on how rounded or squeezed the flux tube would be compared to the width of the string fluctuations. Figure 6.5 shows the change in the tube width calculated for separation distance $R = 0.7$ fm to $R = 0.9$ fm, with uncertainties taken such that the standard errors in the Gaussian fits are correlated, i.e. $|e(x_i) - e(x_0)|$. In addition to that, the measured values of R_0 depend on the corresponding plane at which the lattice data is fitted to Eq. (4.3.17). The value of the fit parameter R_0 can be fixed for each plane using the lattice data at very large separations. The changes in R_0 it self from the central plane value is found to scale as, $-\frac{1}{2\pi\sigma} \log \left| \frac{\theta_2(\pi\xi_1/R; \tau)}{\theta'_1(0; \tau)} \right|$, (the second term in Eq. (4.3.17)), for $R > 1.2$ fm.

Thus, before comparing Eq. (4.3.17) with the corresponding change in flux tube's width one should take into account this change in R_0 [158], see also Table 6.4. This will be discussed in detail in the next chapter.

In contrast with the predictions of the string model, the tube has an almost constant width at $R \leq 0.8$ fm. The measured changes in width at the plane $x = 1$ deviate from that of the model at $R = 0.9$ fm by a large value of 75%. The deviations decrease as the sources are pulled apart to 50% at $R = 1.0$ fm, 25% at $R = 1.2$ fm, and good agreement between both profiles is reached at $R = 1.3$ fm and $R = 1.4$ fm as can be seen in Fig. 6.6. The change of the width measured at the inner-transverse planes, however, agrees with the model at shorter distances, $R = 1.2$ fm for the plane $x = 2$ and $x = 3$. In general, the four plots in Fig. 6.6 show significant improvement with respect to the model predictions compared to the four plots at shorter distances in Fig. 6.5. The flux tube shows an almost constant cross-section for $R = 0.8$ fm in disagreement with the string picture. At distances $0.8 < R < 1.1$ fm, the Lattice gluonic-distribution profile is, geometrically speaking, more squeezed than the free-string picture would imply. As the sources are pulled farther apart, the disagreement decreases gradually and the profiles of the glue and the string both compare well for sources' separations $R \gtrsim 1.2$ fm.

To show the effects of smearing on the tube profile, the data corresponding to all smearing levels are included in Figs. 6.5 and 6.6. The lattice data indicate similar topology for the flux tube for the analysis on 20 and 40 sweeps of smearing at distance $R = 0.7$ fm. For smearing levels of 40 and 60 sweeps, the measurements are revealing the same topology for $R \gtrsim 0.9$ fm. All smearing levels are yielding the same flux tube structure as can be seen in Fig. 6.6 for distance scales $R \gtrsim 1.1$ fm. This is consistent with our earlier assertion of a general distance scale, $\gamma = 2R_s$, which commences at 2 times the radius of the Brownian motion Eq. (5.2.14), as a range which is free of smearing effects. For source separations where the tube geometry is clearly affected by smearing, as can be seen in Fig. 6.5, the largest deviations from the model predictions do occur at the lowest level of smearing where the short distance physics is best preserved. The increase in agreement between the model prediction and lattice data at short distances $0.6 \leq R \leq 1.0$ fm for measurements taken on highly smeared gauge configurations is, however, an interesting observation in its own right with physical implications that will be studied in detail in the next chapter.

The thermal effects are manifest in the gluonic profile, giving rise to nonuniform widths. The string picture can parametrize these profiles only at large distances. At short distances on the other hand, the free-string picture does not model the gluonic interactions on the scale of short distances which may become even more relevant in the thermal regime.

6.4.2 Tube growth in width

The measured values in Tables 6.1 and 6.2 indicate a growth in the tube's mean-square width at all transverse planes x_i as the colour sources are pulled apart. The growth in flux tube width at each selected transverse plane can be compared to the corresponding growth in the string fluctuation Eq. (4.3.17); this comparison can be performed by fitting the formula of Eq. (4.3.17) to the tube measured widths.

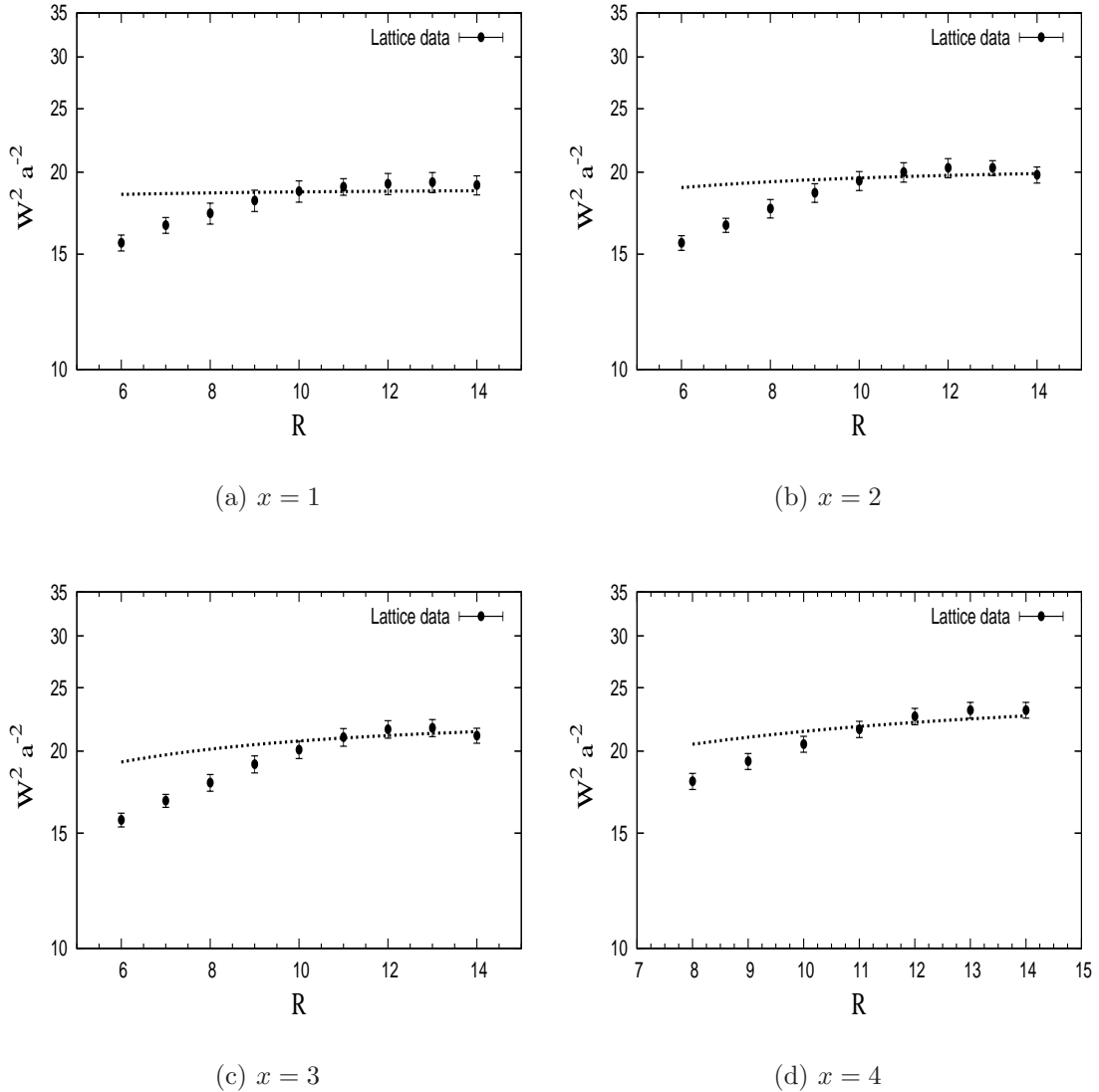


Figure 6.7: The width $W^2(x_i)$ for $q\bar{q}$ separations $R = 6a$ to $R = 13a$ at four consecutive planes (a) $x = 1$, (b) $x = 2$, (c) $x = 3$, and (d) $x = 4$. $\beta = 6$, $T = 0.9 T_C$. The line denotes the string model, Eq. (4.3.17), fit of R_0 to the data as described in the text.

Table 6.4: The resultant measurements of the scale $R_0 \times 100$ for the first four consecutive transverse planes x_i in accord to the fits of the tube width to the string model formula Eq. (4.3.17). The values of the fit parameter, R_0 , and the corresponding χ^2_{dof} are presented for variety of fit ranges.

Plane	$x = 1$		$x = 2$		$x = 3$		$x = 4$	
Range	$R_0 a^{-1}$	χ^2_{dof}						
6-10	0.0155(3)	4.3	0.028(5)	5.9	0.033(5)	5.5		
6-13	0.0126(2)	5.9	0.022(4)	8.9	0.027(4)	9.2		
7-13	0.0108(1)	3.1	0.019(3)	5.7	0.023(4)	7.1		
8-13	0.0093(8)	1.2	0.017(2)	2.4	0.019(3)	3.1	0.020(3)	4.7
9-13	0.0086(5)	0.4	0.014(1)	0.9	0.017(2)	1.7	0.018(3)	2.9
10-13	0.0081(2)	0.1	0.0129(6)	0.3	0.015(1)	0.7	0.015(1)	1.2

Table 6.4 summarizes the resultant measurements of the fit parameter and the corresponding χ^2_{dof} at four consecutive transverse planes $x = 1$ to $x = 4$. The fits show strong dependency on the fit range if the points at small sources' separations are included. The highest value of χ^2 is returned when fits include the whole range of sources separations, i.e., $R = 6a$ to $R = 13a$. With the first four points excluded from the fit, the returned χ^2_{dof} is smaller, indicating that only the data points at large source separation are parametrized by the string model formula. The value of the χ^2_{dof} gradually decreases as we exclude points at short distance separations, and stability in the fit is reached for widths measured for the plane $x = 1$ at sources' separations $R > 0.7$ fm, and at $R > 0.8$ fm for the plane $x = 2$. The fits are returning good χ^2_{dof} values for fits at the planes $x = 3, 4$ for sources' separations $R \geq 0.9$ fm. In the regions where the fits are returning good χ^2_{dof} , the values of the fit parameters are almost equal for the planes in the middle, $x = 2, 3, 4$. However, at the closest plane to the sources, $x = 1$, the value of the returned parameter, unsurprisingly, deviates from the corresponding one at other planes. This is another manifestation of the above observed deviations in the change in tube widths at this plane compared to the central plane as emphasized in the discussion surrounding Figs. 6.5 and 6.6.

Figure 6.7 shows data points and the corresponding best fits to the string model at each plane; the string model at finite temperature poorly describes the lattice data at short distances. The plots depict the fact that the flux tube observed in LGT has a more suppressed profile than the fluctuations of the free string would imply at short distances. On the other hand, the growth of the flux tube diameter is manifest in the lattice data.

6.5 Conclusion

The gluonic distribution inside the static meson has been revealed at finite temperature. The Monte Carlo simulations have been performed on the SU(3) gauge group

for temperatures $T \simeq 0.8 T_c$ and $T \simeq 0.9 T_c$. Noise reduction has been achieved by a gauge-independent high statistics approach, in addition to the employment of adequate levels of gauge-field smoothing that preserve the relevant physics at large distances. The flux tube, characterized as a correlation between the action density and the mesonic operator (Polyakov lines), has been displayed up to distances of 1.4 fm. The flux isolines and isosurfaces display a curved profile along the tube. The profile is showing a nonuniform action-density pattern unlike that observed using Wilson's loop as a mesonic operator at $T = 0$.

The flux-tube width profile is compared to the corresponding mean-square width of the free bosonic string fluctuations at all planes between the colour sources. For source separation distances $R > 0.8$ fm, measurements of the tube cross-section at each selected transverse plane show a nonconstant width for the tube, with maximum width at the symmetry point of the tube. At small $q\bar{q}$ source separations $0.8 < R < 1.1$ fm, the tube is seen to yield a more compact (squeezed) form than the string model would predict. The deviations of the tube width profile from the corresponding string profile decrease gradually as the source separation increases. The profiles commence to compare well at $R \simeq 1.2$ fm.

The gluonic width profiles displayed in this investigation are geometric manifestations of thermal effects on the $q\bar{q}$ potential (the measured decrease in the string tension). Moreover, the squeezed gluonic profile in comparison to the rounded string fluctuations provides a geometrical interpretation for the deviations of the predicted string tension based on the free string picture from the corresponding lattice results [81].

This study is motivating further investigations of the energy-density and chromoelectromagnetic distributions with methodological improvements that minimize the number of smearing sweeps and increase the number of measurements. It would also be interesting to confront these profiles with the bosonic string profiles in the context of string self-interactions. The string's geometrical effects (curved profiles) ought to be addressed in other gauge groups. Work is progressing in these directions. The detailed investigation of the thermal hadronic gluonic distributions by straight forward generalizations of the action density calculations to the static baryon will be presented in this thesis in Chapter 9.

Chapter 7

Bosonic Strings and the UV Filtering of QCD

7.1 Outline

The gluonic action density is calculated in static mesons at finite temperature just below the deconfinement point. Our focus is to elucidate the role of vacuum UV fluctuations which are filtered using an improved smearing algorithm. In the intermediate source separation distance, where the free string picture poorly describes the flux tube width profile, we find the topological characteristics of the flux tube converge and compare favorably with the predictions of the free bosonic string upon reducing the vacuum action towards the classical instanton vacuum. This result establishes a connection between the free string action and vacuum gauge fields and reveals the important role of UV fluctuations in understanding the lattice data at this temperature scale. As a byproduct of these calculations, we find the broadening of the QCD flux tube to be independent of the UV filtering at large distances. Our results exhibit a linearly divergent pattern in agreement with the string picture predictions.

7.2 Introduction

The string conjecture [62] follows as an intuitive realization of the squeezed color field (due to the dual superconductive medium). The major objective of the string formulation is to derive the leading and subleading properties of the flux tube in the infrared region of confining gauge theories. This effective description is expected to hold on distance scales larger than the intrinsic thickness of the flux tube $1/T_c$ [65] in the rough phase of lattice gauge theories (LGT). The linearly rising potential part arises from the classical configuration of the string, and the quantum fluctuations of the string lead to the presence of a long distance c/r term in the $q\bar{q}$ potential well known as the Lüscher term. The existence of the subleading term has been verified in high precision measurements of Polyakov loop correlators in the $SU(3)$ gauge group at zero temperature [119]. The fluctuations of the string render an effective width for the flux-tube which grows logarithmically [126] as the color sources are pulled apart. The logarithmic divergence has been verified in many lattice simulations

corresponding to a variety of confining gauge models [63, 65, 139, 154].

At high temperature, higher-order gluonic modes are present. The corresponding free bosonic string predicts a new set of measurable thermal effects. These include a decrease in the effective string tension [125, 117, 159], a change in the pattern of the tube's growth in width from a logarithmic divergence into a linear divergence [129], and a non-constant width profile [129, 158] along the $q\bar{q}$ line.

Unlike the situation at zero temperature, where also the lattice data linking perturbation theory with the string behavior has been reported in Ref. [160]. The thermal behavior of the free string manifests only at source separation distance scales larger than what one expects normally in the zero temperature regime [81, 129, 158]. The fact that the lattice data are poorly described by the free theory in the intermediate distance regime has been a subject of analytic and numerical studies which include higher-order terms of the effective string's action [161, 162] into the corresponding partition function. The consequences of such an approach have been studied on the level of the $q\bar{q}$ potential [153, 163] and, recently, extended to the flux tube width profile [138, 139, 140].

Apart from the linearly rising potential, the interesting physics of the effective confining string is mainly due to its quantum fluctuations. As we will see, remarkable features arise when the UV part of the fluctuations of the string-like flux tube is filtered out for intermediate quark separations at high temperatures. As it is not yet clear, at this distance scale, whether the deviations from the string picture are due to a non-Nambu-Goto action or the fact that a stringlike behavior has not yet set in, it seems interesting to address this problem in a variant context by reporting an observation regarding the role played by the UV fluctuations of vacuum in these discrepancies. We do this by tracking the response of the QCD vacuum which is subject to UV fluctuations filtering to the presence of external static color sources. This work extends the region for which the free string picture is of utility.

In the following we measure the gluonic action-density distribution by correlating an action density operator to Polyakov loop correlators. Measurements are taken on a set of $SU(3)$ pure gauge configurations. The configurations are generated using the standard Wilson gauge action S_w on two lattices of a spatial volume of 36^3 and temporal extents of $N_t = 10$ and $N_t = 8$, corresponding to temperatures $T \approx 0.8 T_c$ and $T \approx 0.9 T_c$ respectively. The simulations are performed for coupling value $\beta = 6.00$, at this value the lattice spacing is $a = 1.0$ fm to reproduce the standard value of the string tension $\sqrt{\sigma} = 440$ MeV [164]. The Monte Carlo updates are implemented with a pseudo-heatbath algorithm [95] using Fabricius-Haan and Kennedy-Pendleton (FHKP) [93, 94] updating. Each update step consists of one heat bath and 5 over-relaxations. The measurements are taken on 500 bins separated with 2000 updating sweeps. Averaging inside each bin is performed on 5 measurements separated by 70 updating sweeps. This leads to a hierarchical integration, that is apart from updating the last time slice, similar to implementing a one-level Lüscher Weisz (LW) algorithm [118].

The measurements are taken after smearing the gauge field by an over-improved stout-link smearing algorithm [146]. Smearing the gauge field reduces the action towards the action minimum or the classical instanton solution [165]. The UV effects of smearing can be calibrated using a family of ultraviolet filtered topological charge densities. The topological density can be formally obtained [166] from the trace of

the overlap Dirac operator

$$q(x) = -Tr[\gamma_5 (1 - \frac{a}{2} D(0; x, x))]. \quad (7.2.1)$$

The spectral representation of the above overlap Dirac operator can be used to label the ultraviolet filtered topological charge densities labeled by λ_{cut} [167]. It can be shown [148] that the above family of densities is well represented by the gluonic topological charge density after an appropriate number of iterations of stout-link smearing. In this way, smearing can be considered as a UV filter, removing UV modes ¹ of the Dirac operator.

In this chapter we use the value of the stout-link smearing parameters of $\epsilon = -0.25$ and $\rho_\mu = \rho = 0.06$ that we used in the last chapter. The measurements are taken on sets of smeared gauge configurations with increasing levels of smearing. This way we are able to investigate the limit where the QCD vacuum response to the presence of an external static color sources asymptotically approaches the low energy free effective theory behavior.

7.3 Quark–antiquark potential

At fixed temperature T , the Monte Carlo evaluation of the quark–antiquark potential at each R is calculated through the Polyakov loop correlators

$$\begin{aligned} \mathcal{P}_{2Q} &= \int d[U] P(0) P^\dagger(R) \exp(-S_w), \\ &= \exp(-V(R, T)/T). \end{aligned} \quad (7.3.1)$$

In the string picture, the Polyakov loop correlator assumes the functional form of the partition function of the two-dimensional bosonic string and the quark anti-quark potential is given by Eq. (4.3.8).

The numerical evaluation of the quark anti-quark potential, Eq. (7.3.1), using a four dimensional smearing scheme leads to a systematic ambiguity in regard to the transfer matrix interpretation which allows one to identify the expectation values of the Polyakov loop correlators with $\exp(-V(R)/T)$. We recourse, instead, to three dimensional smearing keeping the temporal-links unsmeared. The same smearing parameters as above are used.

Our approach is as follows:

- We start with 500 configurations. Each configuration is smeared only altering the spatial directions of the links, as depicted in Fig. 7.1
- For every 3D smeared configuration, an update sweep is applied. It consists of a heat-bath step and four overrelaxation steps on the lattice. The hit proceeds as an update of every single link based on its neighbours, effectively one at a time as one sweeps across the lattice in all four directions.

¹In this thesis, we will often use the terminology Ultraviolet (UV) modes to refer to high-energy fluctuations on the lattice which are removed in the process of smearing. The smearing operation will be referred to as UV filtering.

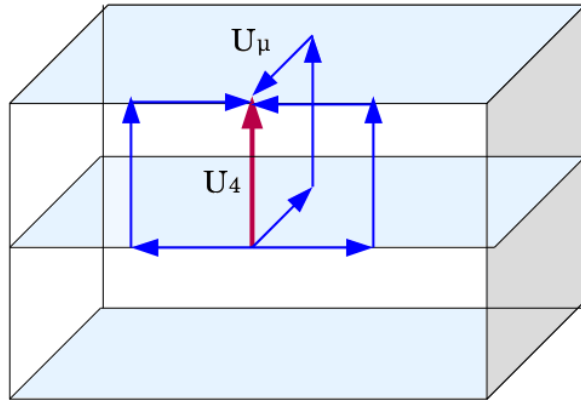


Figure 7.1: (a) The temporal link U_4 is updated based on the neighboring links. The shaded area represents the 3D spatial smeared lattice. The heat bath starts from links of a low action configuration. The overrelaxation or reflection steps starts updates the time links based on action minimal

- The update sweep and measurement is repeated three more times on each configuration. This results in four measurements out of each of the original configurations.

The measurements proceed as follows:

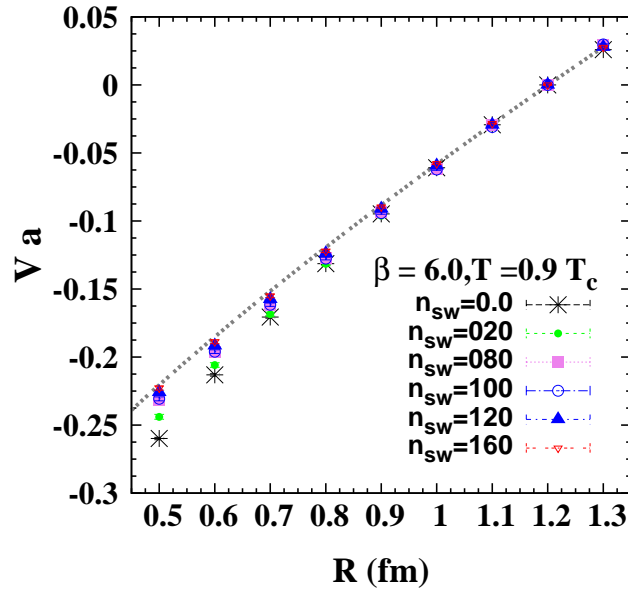
- The temporal links in each of these newly created configurations are then integrated out using a source Q sum of staples. The temporal link variables U_t are replaced with the new link variable \bar{U}_t using the link-integration method [152, 151]

$$\bar{U} = \frac{\int dU U e^{-Tr(QU^\dagger + UQ^\dagger)}}{\int dU e^{-Tr(QU^\dagger + UQ^\dagger)}}. \quad (7.3.2)$$

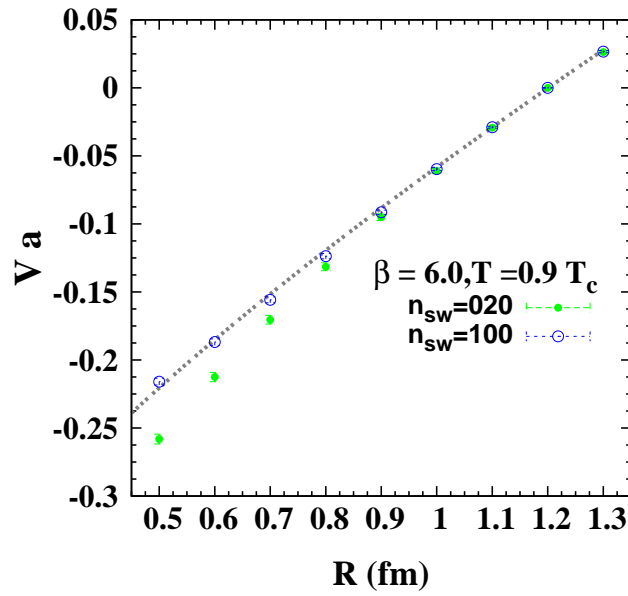
- Finally, the Polyakov loop correlators are calculated on each of the four generated configurations. The result is averaged and binned as a single jackknife entry to avoid artificial error reduction. The 500 decorrelated bins are then averaged.

The Monte Carlo update step starts from a low action configuration in the spatial directions due to smearing. The above described update procedure brings in a newly updated time-link such that the local action reduction that was only in the spatial torus takes place in the four-dimensional lattice. In this way, the UV filtering is implemented as systematic integration over the path integral (7.2), thus, preserving the transfer matrix interpretation.

In Fig. 7.2 the value of the potential measured on various levels of spatially smeared configurations, normalized to its value at $R = 12 a$, are plotted. Fig. 7.2 (a)



(a) 3 D smearing



(b) 4 D smearing

Figure 7.2: (a) The quark-antiquark potential measured at each depicted smearing level for 3 dimensional smearing (above) and 4 dimensional smearing (below). The lines correspond to the string picture predictions of Eq. (4.3.8). The standard value of the string tension is used.

shows the numerical behaviour of the data using the above described 3D smeared heat bath/overrelaxation driven updates. On the other hand, Fig. 7.2 (b) shows the corresponding numerical behaviour of the data measured on standard four-dimensional smeared configurations. The data corresponding to the unsmeared lattice and the string model predictions of Eq. (4.3.8) at $T = 0.9 T_c$ are also included.

The discrepancies between the unsmeared lattice data and the free string model occur in the intermediate distances $0.5 \leq R \leq 1 \text{ fm}$. The numerical results for the quark–antiquark potential evaluated on the 3D smeared updated configurations show an interesting behaviour with respect to the number of smearing sweeps (see Fig. (7.2)(a)). The data at large distances show no response to the filtering of the UV fluctuations of the gauge field. The data at intermediate separation distance converge for a large number of smearing sweeps. Moreover, the data approach the free string model predictions.

It is interesting to compare these results to those obtained from the four-dimensional smearing illustrated in Fig. 7.2 (b), where 20 and 100 sweeps of smearing are compared. The results for 100 sweeps of smearing coincide very well with the convergence toward the string model predictions observed in Fig. 7.2. Thus, the four dimensional smearing (4D) approach can be used as an efficient method for exploring the more demanding three-point functions required to determine the distribution of gluon flux, and this is used in the following. Similar results are observed at $T = 0.8 T_c$.

7.4 The Gluonic profile

The transverse degrees of freedom of the stringlike flux tube render an effective width for the tube. The mean-square width of the free bosonic string in D dimensions [129, 138] reads

$$W^2(\xi_1, \tau) = \frac{D-2}{2\pi\sigma} \log \left(\frac{R}{R_0} \right) + \frac{D-2}{\pi\sigma} \log \left| \frac{\eta_2(\pi \xi_1/R; \tau)}{\eta_1'(0; \tau)} \right|. \quad (7.4.1)$$

One can easily see that the above formula is equivalent to Eq. 4.3.17 through the standard relation between η and θ Jacobi elliptic functions. This solution gives the mean square width at all the planes transverse to the quark-antiquark line, and hence, is describing the topological shape of the fluctuating flux tube and its dependence on the temperature as well as its evolution with the increase of color source separation. Using a modular transform $\tau \rightarrow 1/\tau$ [129, 138], Eq. (7.4.1), at $R \gg \frac{1}{T}$, in four dimensions [140] becomes

$$W^2(R/2) = \frac{1}{\pi\sigma} \log \left(\frac{T_c}{T} \right) + \frac{1}{2\sigma} TR - \frac{1}{\pi\sigma} e^{-2\pi RT}, \quad (7.4.2)$$

which indicates linear growth of the tube’s width at large distance.

The width of the action density of the free bosonic string can be compared to the width of the action density of the corresponding flux tube of the lattice gauge theory. In the calculations of the gluonic profile through out this section, we adopt the usual four-dimensional smeared configurations.

After constructing the color-averaged infinitely-heavy static-mesonic state,

$$\mathcal{P}_{2Q} = P(\vec{r}_1)P^\dagger(\vec{r}_2),$$

with the Polyakov loop given by Eq. (6.3.1)

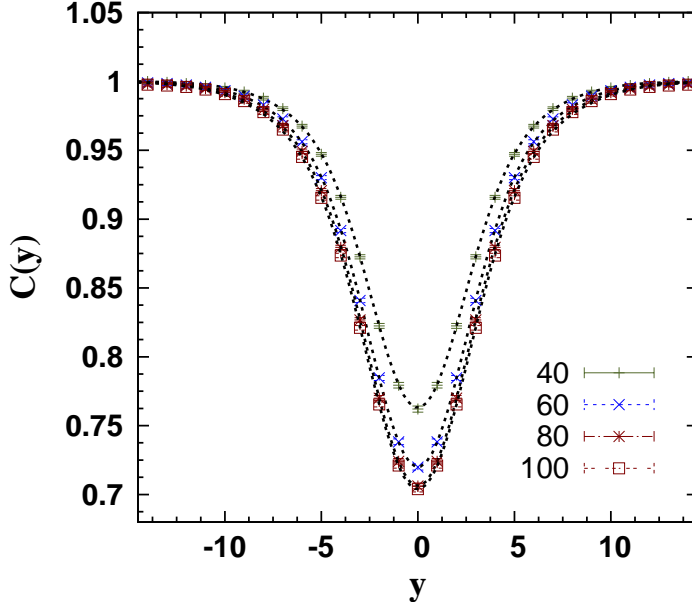


Figure 7.3: Plot of the density distribution $\mathcal{C}(\vec{\rho})$ in the middle plane for source separation $R = 9a$, $T = 0.9T_c$.

Subsequent measurement by an action density operator $\frac{1}{2}(E^2 - B^2)$ is taken at each point of the three-dimensional torus at each corresponding Euclidean time slice for every source configuration. The action density operator is constructed via a highly-improved $\mathcal{O}(a^4)$ three-loop improved lattice field-strength tensor [150]. The measurements taken are averaged over the time slices. A scalar field that characterizes the gluonic action-density distribution field can be then measured using the definition [2]

$$\mathcal{C}(\vec{\rho}; \vec{r}_1, \vec{r}_2) = \frac{\langle \mathcal{P}_{2Q}(\vec{r}_1, \vec{r}_2) S(\vec{\rho}) \rangle}{\langle \mathcal{P}_{2Q}(\vec{r}_1, \vec{r}_2) \rangle \langle S(\vec{\rho}) \rangle}, \quad (7.4.3)$$

where $\langle \dots \dots \rangle$ denotes averaging over configurations and lattice symmetries, and the vector $\vec{\rho}$ refers to the spatial position of the flux probe with respect to some origin. To further suppress the statistical fluctuations, the density distributions have been symmetrized around all the symmetry planes of the tube.

A measurement of the width of the flux-tube's action density may be taken through fitting the density distribution $\mathcal{C}(\vec{\rho})$, Eq. (7.4.3), in each selected transverse plane $\vec{\rho}(x_i, y, z_0)$ to the Gaussian of the form

$$\mathcal{C}(y) = 1 - a_1 e^{-y^2/W^2(x_i)}. \quad (7.4.4)$$

$x_i = 0$ denotes the position of the quark.

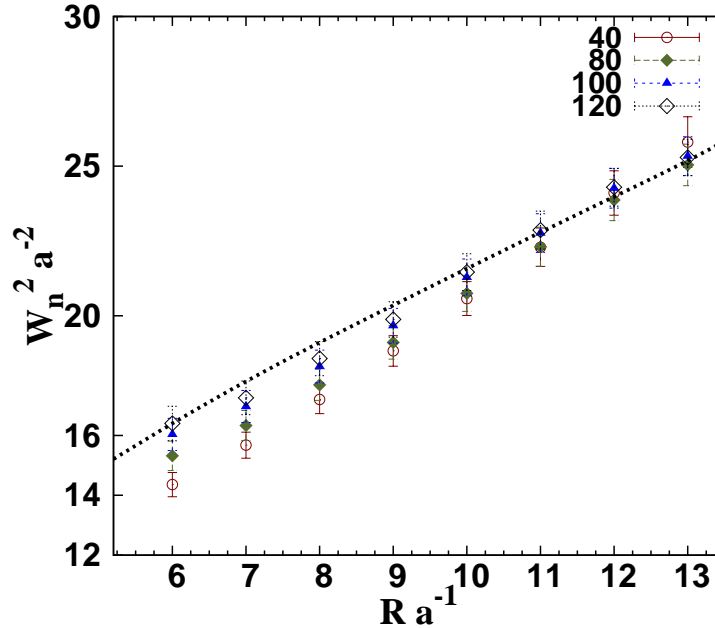


Figure 7.4: The mean square width of the flux tube $W_n^2(R/2)$ in the middle plane between the quarks. The lattice data, corresponding to the action density minimization, approach the string model predictions at short distances. At large distances the predicted linear divergence of the flux tube width is manifest in lattice data.

The decrease in $C(y)$ with the increase of the smearing sweeps is depicted in Fig. 7.3. The action-density asymptotically converges to a minimum for values around $n_{sw} = 80$ to 100 sweeps of smearing.

The mean square width of the flux tube is measured via the second moment of the flux density with respect to the central plane given by Eq. (6.4.3). The measured values of the mean square width in the middle plane $R/2$ of the tube versus the source separation are plotted in Fig. 7.4. Similar plots at three consecutive transverse planes $x = 2$, $x = 3$, and $x = 4$ to the line joining the two color sources are illustrated in Figs. 7.5 and 7.6.

To unambiguously identify the tube broadening pattern, the second term of Eq. (7.4.1) has to be isolated. The width is defined normalized with respect to the ultraviolet cutoff R_0 (Eq.(7.4.1)) which does scale with smearing

$$W_n^2 = W^2 + \frac{1}{\pi \sigma} \log(R_0). \quad (7.4.5)$$

In plotting Fig. 7.4, R_0 has been measured for each smearing level by fitting Eq. (7.4.1) to the last five data points corresponding to $R > 1$ fm where good χ^2 is obtained.

At large distances, in the middle plane of the flux tube, the tube shows a width broadening pattern for increasing R that does not depend strongly on the corresponding smearing level. The data at large distances is increasing linearly in agreement with the string model predictions [138, 139, 140]. The UV effects, on the other hand, are manifest in the data points at shorter distances. The width of the flux

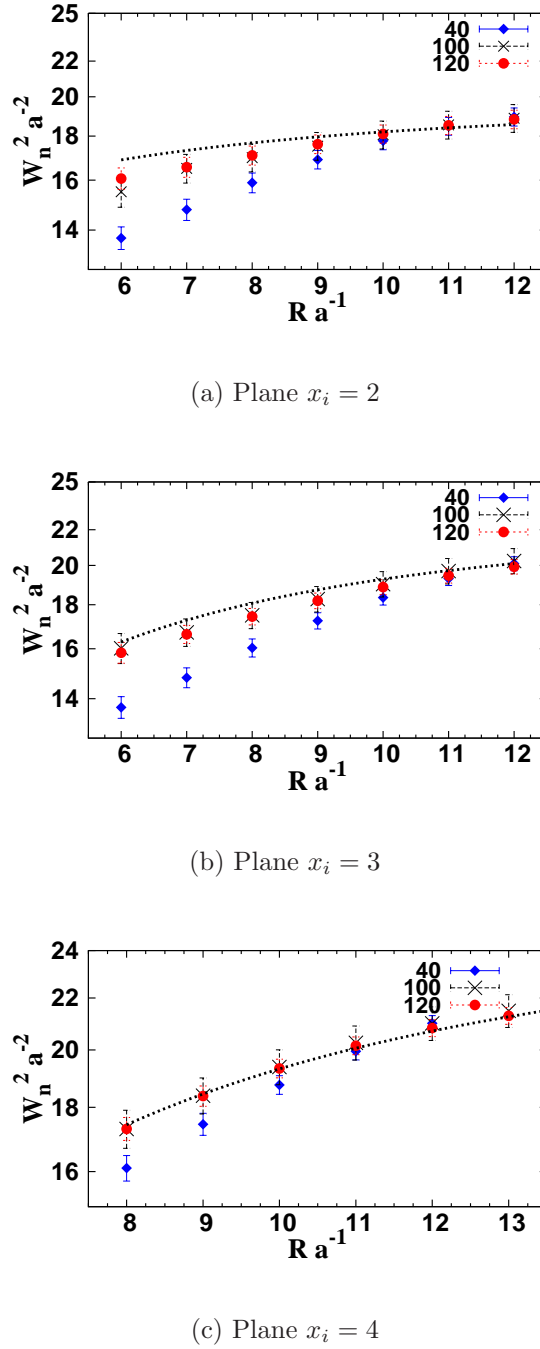


Figure 7.5: The normalized width of the flux tube $W_n^2(x_i)$ versus $q\bar{q}$ separations measured in the planes (a) $x = 2$, (b) $x = 3$, (c) $x = 4$. $\beta = 6$, $T = 0.9 T_C$. The coordinates x_i are lattice coordinates (lattice units) and are measured from the quark position $x = 0$. The line denotes the one parameter string model, Eq. (7.4.1), fit to lattice data for $R \geq 1$ fm. The numbers in the legend denote the number of smearing sweeps.

Table 7.1: The returned χ_{dof}^2 by the fit of lattice data for measurement on the flux tube width in the middle plane between quark–antiquark to the effective string model predictions Eq. (7.4.1), the lattice data correspond to smearing levels from $n_{\text{sw}} = 40$ to $n_{\text{sw}} = 120$.

No.sweeps	40	60	80	100	120
χ_{dof}^2	3.2	1.6	1.20	0.98	0.96

tube measured on the lowest smearing level, where the short distance physics is best preserved, is poorly described by the free bosonic string model at short distances. As higher smearing levels are considered, the subsequent removal of the short distance physics from the gauge sector regulates the fast rate of growth of the flux tube width. However, this does not continue uncontrollably. The data ultimately converge near 100 sweeps of smearing, in accord with the saturation in the action density of Fig. 7.3. Moreover, the UV-filtered results converge to the free string predictions.

Table 7.1 summarizes the measured χ_{dof}^2 for fits of Eq. (7.4.1) for the fit range $R \geq 0.5$ fm. With the increase of the number of smearing sweeps the returned values of the χ_{dof}^2 improves and becomes stable near the action saturation of approximately 100 sweeps.

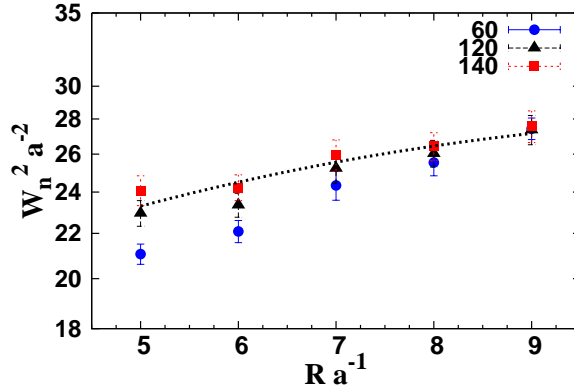


Figure 7.6: The normalized width of the flux tube $W_n^2(x_i)$ versus $q\bar{q}$ separations measured in the plane $x = 3$. The temporal links have not been smeared in the evaluation of Polyakov loops, rather the temporal links have been integrated out. This time, the Polyakov loops are taken from the unsmeared configurations and correlated with the smeared action density. The legend denotes the number of smearing sweeps of the QCD vacuum.

To clarify this point further, we investigate the response of the QCD vacuum to the presence of infinitely heavy sources that are not constructed using smeared temporal links. Instead, the Polyakov lines are evaluated in the calculations of the flux strength, Eq. (7.4.3), using the link integration procedure of Refs. [152] and [151] for noise reduction. For our analysis performed on 500 configurations, we observe

that the data corresponding to the width profile of the flux tube measured on high levels of vacuum UV filtering do display similar behavior to the results in Fig. 7.5. Fig. 7.6 presents results for the plane $x = 3$. Again systematically converge with a large number of smearing sweeps and approach the string model predictions. Note that the evaluation of the correlation function using this method involves a three point correlation function which becomes noisy at large distance.

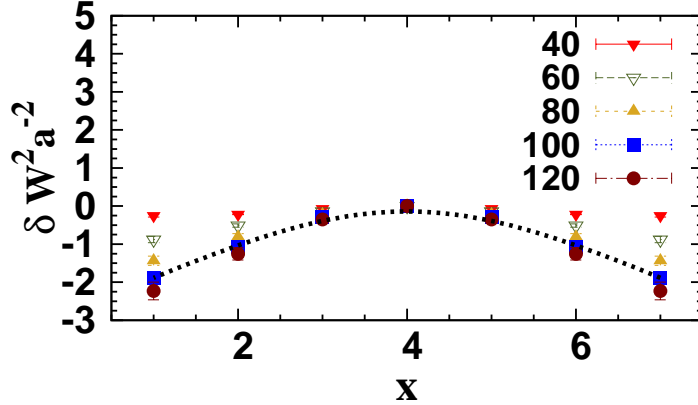
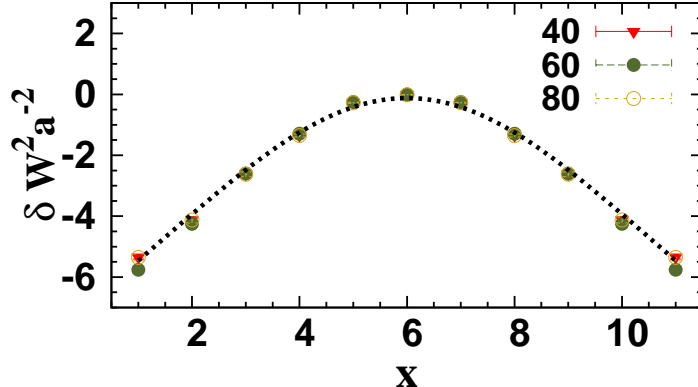
(a) $R = 0.8 \text{ fm}$ (b) $R = 1.2 \text{ fm}$

Figure 7.7: The change of the tube's width $\delta W^2 = W^2(x_i) - W^2(x_0)$ measured from the central plane for the depicted $q\bar{q}$ separations. The smearing level of the lattice data is illustrated. $\beta = 6$, $T = 0.9 T_C$. The line denotes the width difference δW^2 as predicted by the string model Eq. (7.4.1).

The topological aspects of the fluctuating free string are contained mainly in the second term of Eq. (7.4.1) and can be isolated by considering the difference in the mean square width at a given plane with respect to the central plane, $\delta W^2 = W^2(x_i) - W^2(x_0)$. The measured value of R_0 , however, depends on the corresponding plane at which the lattice data is fitted to Eq. (7.4.1). The value of the fit parameter

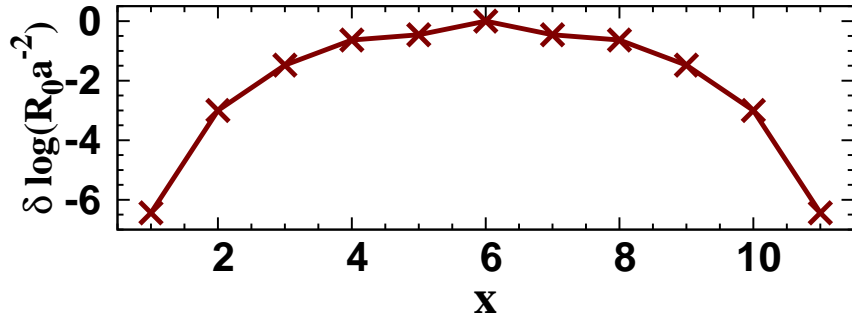


Figure 7.8: The measured change in the ultraviolet cutoff R_0 along the flux tube normalized by a factor $(\pi\sigma)^{-1}$.

R_0 is fixed for each plane using lattice data at large separations $R = 1.1\text{fm}$ and $R = 1.2\text{ fm}$, a comparison of the second term of Eq. (7.4.1) with the corresponding change in flux tube's width on the lattice obtained from fits of , Eq. (7.4.3), is shown in Fig. 7.7 for a source separation in the intermediate distance $R = 0.8\text{ fm}$ and at large distance $R = 1.2\text{ fm}$. The changes in R_0 with respect to the central plane is plotted separately in Fig. 7.8. Taking into account the changes in R_0 [158].

Lattice data for each gauge-field smoothing level is depicted in Fig. 7.7. The jackknife uncertainties associated with the change in the mean squared width of the tube reveal correlated errors between the adjacent planes. Only subtle changes are observed in the tube's width along the transverse planes with respect to the central plane for the analysis performed on smeared gauge configurations of the lowest smearing level $n_{\text{sw}} = 40$ sweeps. The tube tends to exhibit larger curvatures as higher levels of gauge-field smoothing are considered. At large values of UV fluctuations filtering, the tube profile converges and approaches the geometrical shape of the free-Bosonic string. At large distances, on the other hand, the flux tube displays a curved width profile which compares well with the bosonic string profile and is not affected by smearing, as is evident in Fig. 7.7 at $R = 1.2\text{ fm}$.

7.5 Conclusion

The presence of a pair of static external sources in the QCD vacuum induces the response of an effective free bosonic string for source separations in the intermediate separation region, provided the short distance vacuum fluctuations are filtered out. The flux tube, measured as a correlation between the mesonic operator and the vacuum action density is found to exhibit a broadening pattern with increasing R and a transverse structure similar to the free Bosonic string for measurements taken near the saturation in action density minimization under smearing even at intermediate distances. At large distances, the short distance fluctuations do not affect the tube growth, which exhibits a linear divergent pattern consistent with the string model predictions.

To systematically study the effects of UV filtering of the QCD vacuum on the quark-antiquark potential, we introduced a novel method that avoids the ambigu-

ties that might arise due to smearing the temporal links, i.e, preserving the transfer matrix interpretation. Instead, three-dimensional spatial smearing is combined with single pseudo-heat bath driven updates. This means that the Polyakov loop correlators are evaluated after applying a Monte Carlo update on lattices with the three-dimensional spatial links smeared.

There are many observations on the behaviour of the numerical data when evaluating the Polyakov loop correlator using this method:

1. The time links have not been smeared. Heat-bath updates are more systematic and allow us to identify the Polyakov loop correlator as $\exp(-V/T)$. The UV filtering is complemented by a systematic integration in the path integral Eq. (7.3.1).
2. The data corresponding to the quark–antiquark potential at large distances do not show a dependence on the UV physics, as expected.
3. The data at short distances converge at large number of smearing sweeps displaying little sensitivity to the precise number of sweeps of smearing. This merit is not obtained with standard 4D smearing smearing.
4. The data approach the string model predictions at short distances.

While the consideration of smeared temporal links in Polyakov lines is often criticized, the results obtained with our novel 3D smearing method are similar to those obtained from traditional four dimensional smearing. Any ambiguities associated with smeared temporal links are subtle. 4D smearing is acceptable for revealing long distance physics and is used in the flux-tube calculations using the correlator Eq. 7.4.3.

The analysis performed at short distances provides an extension of the QCD vacua where the free string picture is of utility. The infrared large distance part of the physics in the intermediate distance region can be described merely on the basis of a free string picture. This fact is relevant and complements recent investigations including higher-order self interactions to match lattice results.

Chapter 8

On The Ground State of Yang-Mills Theory

8.1 Outline

We investigate the overlap of the ground state meson potential with sets of mesonic-trial wave functions corresponding to different gluonic distributions. We probe the transverse structure of the flux tube through the creation of non-uniform smearing profiles for the string of glue connecting two color sources in Wilson loop operator. The non-uniformly UV-regulated flux-tube operators are found to optimize the overlap with the ground state and display interesting features in the ground state overlap.

8.2 Introduction

A fundamental property of the non-perturbative regime of confining pure-gauge theories is the linear increase in the ground state potential between a pair of static color sources. In addition to that, lattice gauge simulations have recently confirmed the existence of a sub-leading non-Coulombic long range correction to the mesonic ground-state potential in Yang-Mills theory [64, 65, 66, 119]. These features are connected with the underlying gluonic picture and the subsequent energy distribution profile. Although the properties of the ground state potential have been unambiguously measured to a subleading order in the infrared region of the non-abelian gauge, the geometrical aspects of the associated energy density profile at low temperatures remains to be completely resolved.

Lattice calculations of the gluon-field distribution in static mesons using Wilson loop operators reveal uniform energy and action density profiles along the line joining the static $q\bar{q}$ pair at large distances [63]. These measurements, however, may be vulnerable to systematic errors associated with excited-state contamination [157]. The non-ground state components manifest themselves in the revealed gluonic profiles as a bias reflecting the form of spatial links of the Wilson loop operator. The bias by the geometry of spatial links in the L shape baryon operator provides a clear example where the flux distribution mimics the source [2, 157]. The height and the width of the distribution also depend on the ultraviolet properties of the

gauge links in the source [2]. Apart from the arbitrariness in adopting the source that best approximates the ground state, the statistical fluctuations impose a practical constraint on the Euclidean time evolution in the loop operator to isolate the physically interesting energy-density profile of the ground state. The excited-state contamination is more challenging in the case of field distribution calculations which involve three-point correlations rather than the potential which is extracted in the large time limit of a two point correlation [157].

In the finite-temperature regime, the static meson can be constructed using a pair of Polyakov lines. These hadronic operators provide a systematically unbiased stringless gauge-invariant objects in the calculations of field-distribution correlations. This means that one need not adopt specific geometric or UV properties for the gluonic string between the color sources.

Current investigations of the flux-tube profile in the finite-temperature regime of QCD have revealed action-densities of non-uniform distribution along the flux-tube [158]. The action density displays a two dimensional Gaussian-like profile and isosurfaces of a curved prolate spheroid-like shape [158] in the intermediate source separation distance region $0.6 \leq R \leq 1$ fm. This has been observed near the deconfinement point $T \approx 0.9 T_c$ and remain manifest at the temperature $T \approx 0.8 T_c$ close to the end of the plateau region of the QCD phase diagram [5]. The measurements of the tube's mean square width profile indicate, however, almost constant width 7.6(a,b,c). Variation in the amplitude give rise to curved isosurfaces. At larger distances, the tube changes width along the $q\bar{q}$ plane and this width profile is predictable on accord with a free bosonic string picture [158]. The gluonic distributions obtained at finite temperature by correlating two Polyakov lines constitute an interesting source of knowledge for investigating the possibility that non-uniform densities provide the true geometry of the ground state in the static meson. The viability of considering finite temperature results as an indication for the field distribution of the system's ground state can be justified by arguing also that the change in the string tension is small [81, 135] at $T \approx 0.8 T_c$.

In addition to this observation, it has been found recently that a model of Coulombic trial states provides a good overlap with the ground state in the continuum limit [155]. Moreover, the free bosonic string model predicts observable edge-effects at zero temperature for the width profile of the tube given by Allais and Caselle [129]

$$\frac{1}{\pi\sigma} \log \left| \cos\left(\frac{\pi\xi}{R}\right) \right|, \xi \in [-R/2, R/2]. \quad (8.2.1)$$

The above term describes the geometrical shape of the flux tube and it indicates subtle changes in the tube's mean square radius in the middle of the tube and more pronounced changes near the quark positions. The success of the string picture in accounting for the flux-tube curvature at high temperature at large distances is remarkable, and one may investigate such effects at zero temperature. Apart from the string's width effects, a non-uniform action density amplitude pattern along the tube has been observed at finite temperature whether the tube exhibits a non-constant width profile or not [158]. The bag model is also another scheme that predicts an ellipsoidal-like [168] shape for the tube in the infrared region.

At zero temperature, correlating a pair of Polyakov lines with an action density

operator is very noisy and requires substantial numerical simulations using special techniques such as the Multi-level algorithm [118]. Nevertheless, standard Wilson loop operators do not exhaust the possibility of investigating the transverse structure of the field distribution. We can introduce the non-uniformity by employing the idea of constructing the flux-tube operator as a product of locally smeared links with varying smearing extents. This corresponds to imposing a local transverse cutoff on the lattice parallel transporters between the fermionic fields. By extending the space of mesonic states constructed in Wilson loop this way, we investigate the existence of states such that the overlap with the ground state is maximized. This is the objective of the present report.

8.3 Wilson loop operator

In the mesonic Wilson loop, a mesonic state is described by fermionic fields connected by the parallel transporters \mathcal{G} that is an element of the corresponding local gauge group G

$$|\Psi\rangle = \bar{\psi}(x_2) \mathcal{G} \psi(x_1) |\Omega\rangle. \quad (8.3.1)$$

The spectral expansion of the Wilson loop operator reads

$$\langle W(R, t) \rangle = \sum_n C_n(R) e^{-V_n(R)t}. \quad (8.3.2)$$

The overlaps, $C_n(R)$, obey the normalization condition

$$\sum_n C_n(R) = 1. \quad (8.3.3)$$

For large t , the so-called overlap with the system ground state can be measured as

$$C_0(R) = \frac{\langle W(R, t) \rangle^{t+1}}{\langle W(R, t+1) \rangle^t}. \quad (8.3.4)$$

The mesonic state with an infinitesimally thin flux tube operator between quarks

$$\mathcal{G} = \mathcal{P} \exp \left[\int_{x_2}^{x_1} d\mathbf{z} \cdot \mathbf{A}(\mathbf{z}) \right], \quad (8.3.5)$$

is poorly overlapping with the ground state in the continuum [155]. Analogy with an Abelian analytically solvable case [169] shows that the infinitesimal thickness of the gauge links corresponds to the removal of UV cutoff on the transverse direction of the tube causing a vanishing overlap with the ground state.

Applying a smearing operator on a gauge link in a certain local gauge group would alter its UV properties. Smearing introduces a transverse UV regulator into the flux-tube operator and this results in the enhancement of the overlap with the ground state. Define a smearing operator $\mathcal{S} : \oplus_x G \rightarrow \oplus_x G$. A standard APE [101] smearing sweep $(\mathcal{S}U)_\mu(x)$ consists of a replacement of the spatial link-variable $U_\mu(x)$ ($\mu = 1, 2, 3$) with the angular part of

$$\begin{aligned} U_{s,\mu}(x) = & (1 - \alpha) U_\mu(x) + \frac{\alpha}{4} \sum_{\mu \neq \nu} \{ U_\nu(x) U_\mu(x + \hat{\nu}) \\ & U_\nu^\dagger(x + \hat{\mu}) + U_\nu^\dagger(x - \hat{\nu}) U_\mu(x - \hat{\nu}) U_\mu(x + \hat{\nu} - \hat{\mu}) \}, \end{aligned} \quad (8.3.6)$$

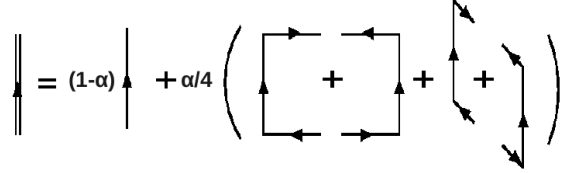


Figure 8.1: Schematic representation of link-blocking

where α is the smearing parameter as illustrated Fig. 8.1. In QCD, this corresponds to the projected link $\bar{U}_\mu(x) \in \text{SU}(3)_c$ that maximizes

$$\Re \text{Tr}\{\bar{U}_\mu(x)U_{s,\mu}^\dagger(x)\}. \quad (8.3.7)$$

The geometrical characteristics of smearing can be described by analogy to the Brownian motion associated with a diffusing scalar field [3]. Given a scalar field $\phi(\mathbf{r}; n+1)$ similar to the $(n+1)$ -th smeared gauge link in the μ direction, and a smearing time $\tau = na_\tau$ with a spacing a_τ . The smearing operation will then correspond to the three-dimensional version of the diffusion initial value problem [Eq. (5.2.6) and Eq. (5.2.7)]. In three dimension, the characteristic radius of the Gaussian distributed field

$$G(\mathbf{r}; \tau) = \frac{1}{(4\pi D\tau)} \exp\left[-\frac{\mathbf{r} \cdot \mathbf{r}}{4D\tau}\right], \quad (8.3.8)$$

is given by

$$r \equiv \left(\frac{\int d^3\mathbf{r} G(\mathbf{r}; \tau) \mathbf{r}^2}{\int d^3\mathbf{r} G(\mathbf{r}; \tau)} \right)^{1/2} = 2a\sqrt{\alpha n}, \quad (8.3.9)$$

and the amplitude

$$A = \frac{1}{(4\pi D\tau)}. \quad (8.3.10)$$

Applying the local smearing operator \mathcal{S} at each spatial link in Wilson loop operator

$$\mathcal{G} = (\mathcal{S}^{n_1} U)(x_1) (\mathcal{S}^{n_2} U)(x_1 + a) \cdots. \quad (8.3.11)$$

The sequence of numbers of smearing sweeps applied at each link $\{n_1, n_2, n_3, \dots, n_N\}$ fixes the gluonic distribution along the spatial links in Wilson loop. This sequence of numbers maps into the geometrical space of the corresponding radii $r(x_i)$ and the amplitudes $A(x_i)$ given by Eqs. (8.3.9) and (8.3.10). For a mesonic state n_i or $r(x_i)$, the projection on the system's ground state is measured as,

$$\langle \Psi_0 | \Psi_{\{n\}} \rangle = \langle \Psi_0 | \bar{\psi}(\mathbf{x}_2) \mathcal{G} \psi(\mathbf{x}_1) | \Omega \rangle. \quad (8.3.12)$$

The mesonic state constructed by operators corresponding to a rectangular shape given by a constant sequence $\{r_i\}$ has been considered to provide a good approximation for the potential ground state [63]. The understanding of the geometry of the flux-tube, nevertheless, would be increased by constructing trial states without this

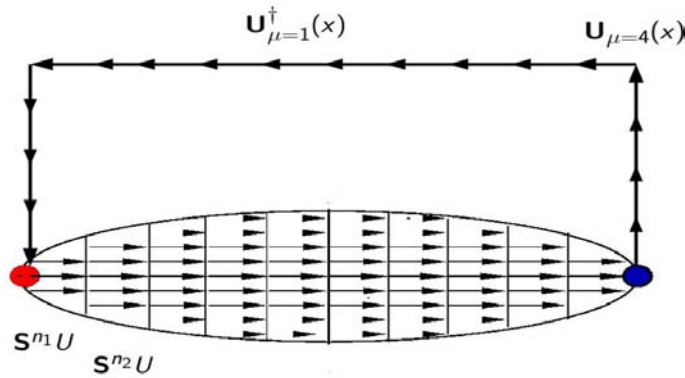


Figure 8.2: Schematic representation of smearing the spatial links in the Wilson loop. Each spatial link $U_\mu(x), \mu \neq 4$ is smeared with the operators $(S^n)U$. The temporal links are left unsmeared. While not indicated in the figure, the links U^\dagger at the top of the figure are also smeared.

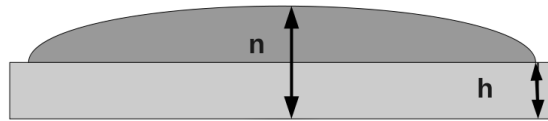


Figure 8.3: Schematic diagram of the smearing profile. h is the minimum number of smearing sweeps applied at the last link giving rise to smearing radius L_1 . n is the maximum number of smearing sweeps in the middle resulting in the radius L_2 .

constraint. We expect based on the results in Refs. [155, 158] that the best possible approximation of the ground state may be approached this way.

For a Wilson loop with N spatial links, we consider a class of distributions characterized by the radii $r = f(x) + L_1$, with an ellipsoidal constraint

$$\frac{f^2(x_i)}{b^2} + \frac{x_i^2}{a^2} = 1. \quad (8.3.13)$$

The abscissa x are lattice coordinates and are measured from the middle plane between the two quarks $x = 0$. The shape is fixed by the minimum number of smearing sweeps at the last spatial link $n_N = h$ and the maximum number of sweeps at the middle links $n_{N/2} = n$. The shape consists of a base defined by the family of rectangles of height $L_1 \propto \sqrt{h}$ and ellipsoidal caps with $a = R/2$ and $b^2 \propto (n - h)$, thus, the radius at middle link is $L_2 = b + L_1$. This parametrizes the geometrical shape schematically represented in Fig. 8.3. Among a variety of heuristic shapes, this particular prescription is found to be especially useful for maximizing the overlap with the ground state by variations of the tuning parameters h and n .

8.4 Numerical results and discussions

We take our measurements on 200 SU(3) pure-gauge configurations. The configurations are generated as described in Chapter 6 for lattice volume of $36^3 \times 32$ with the same coupling value of $\beta = 6.00$.

The APE smearing operation Eq. (8.3.6) and Eq. (8.3.7) is locally applied on spatial links of the Wilson loop with smearing parameter $\alpha = 0.7$. That is, the number of smearing sweeps at each link as one moves from the quark to the anti-quark is not necessarily equal. The smeared links are drawn from sets of smeared configurations corresponding to 1 to 40 sweeps of APE smearing. The spatial links in the Wilson loop are drawn from these sets.

For noise reduction, the Wilson loop is calculated at each node of the lattice and then averaged over the 4-volume of the hypertoroid. The overlap with the ground state C_0 of Eq. (8.3.4) is measured using Wilson loops of temporal extent of 2 and 3 slices for source separations $R = 10a$ and $R = 12a$.

The sequence of the numbers of smearing sweeps applied at each link defines a trial state. Here, we consider measurements of C_0 for states in the parameter space $\{5 \leq n \leq 40, 1 < h < 30\}$. The state is uniquely determined by n and h . The number of sweeps at each link in between is obtained from Eqs. (8.3.13) and (8.3.9). The smearing profile is symmetric with respect to the middle point between the quarks.

Figure 8.4 indicates the measurements of the overlap of the ground state for three selected lines in the parametric space correspond to $\{n, h = 1\}$, $\{n, h = 5\}$, $\{n, h = 13\}$. The shape is elliptic with the quark source at the end of the ellipse for $h = 1$ (one smearing sweep at the last link). The values of C_0 are small for ellipses with number of sweeps in the middle $5 \leq n \leq 17$. With further increase in the height n , the value of C_0 increases and lies approximately in the range $[0.80, 0.85]$ for $n \geq 17$. However, if the height of the rectangular shape in the base increases to $h = 5$ in terms of sweeps, the overlap with the ground state is in the range

$0.90 < C_0 < 0.93$ for $n = 19$ to $n = 33$. Further increase of h causes subtle increases in the value of C_0 until an optimum value for $h \simeq 13$ is reached.

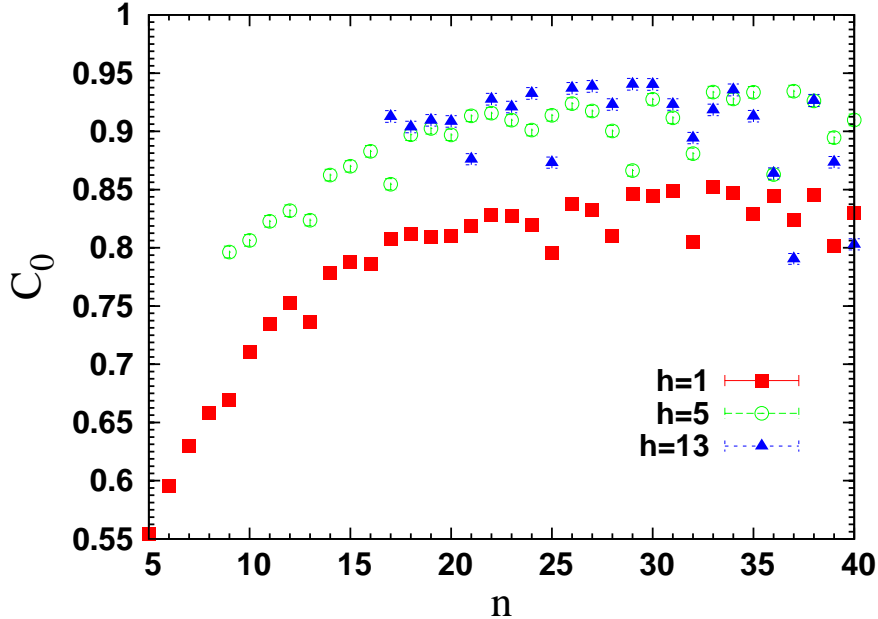


Figure 8.4: The overlap with the ground state C_0 , the distance between the quark anti-quark source is $R = 10 a$, $\beta = 6$.

The flux tube modeled as an ellipsoid with the color source at the far end of the prolate shaped gluonic bag does not provide the optimal overlap with the ground state in static mesons. The subsequent increase in the ground state overlap value C_0 observed by introducing this rectangular base of height h can be understood by considering a model of an elliptic-like shaped flux tube in which the quark positions are shifted from the edges to the inside. The bag model, for example, leads to an ellipsoidal approximation for the gluonic field distribution around the color source [168]. The above result would indicate that the ground state gluonic bag would have the position of quarks not exactly at the edges. Indeed the elliptical shapes revealed at small quark separations in Ref. [2] contained the quarks.

The retrieved values of the overlap for parameter values corresponding to the two lines $\{n, h = 15, 18\}$ are illustrated in Fig. 8.5. The overlap with the ground state exhibits a pronounced oscillatory behavior versus n for $h > 13$. Nevertheless, the measured data are not randomly scattered in the graph.

The data are seen to arrange themselves to lie ultimately within what resembles a band structure. This branching is more evident when plotting a denser region of the parametric space as in Fig. 8.6 for sweeps $n > 25$. The data appear to line up into five bands with the continuous variation of n indicating that this observed oscillatory behavior by changing n for a given h as in Fig. 8.5 may not be arbitrary. This is likely to arise from the discrete nature of n_i and h in constructing the source and the sink, and the inclusion of spatial link configurations which systematically probe excited states of the glue.

There is, however, a variety of states of interest that maximize the overlap value

at $C_0 \approx 0.94$. These states line up in the first band from above as in Fig. 8.6. The form of the corresponding operators for four of these parametric states are shown in Fig. 8.7.

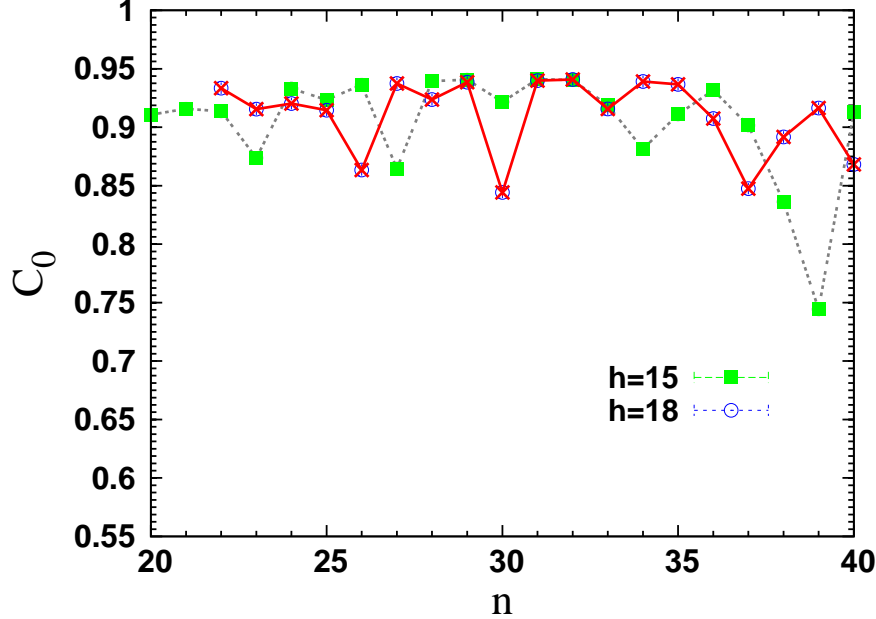


Figure 8.5: The overlap with the ground state C_0 , for $R = 1$ fm. The lines connect the states corresponding to variation of the ellipse semi-major axis for each rectangular base corresponding to sweeps $h = 15$ and $h = 18$.

It is evident that the states with very large values of h , for example, $(h = 24, n = 32)$ tend to assume a more flat shape rather than the clear difference in amplitude along the tube as in the state $(h = 13, n = 34)$. Nevertheless, the four operators overlap with the ground state equivalently.

For comparison, the values of C_0 corresponding to the uniformly smeared (flat) states, $n = h$, is also depicted in Fig. 8.6. In this case, C_0 is a smoothly varying function of n . In addition, the curve interestingly crosses through the states of the second band from above. Inspection of Fig. 8.6 shows that states constructed by non-uniformly smeared links can maximize the overlap with the ground state in a comparative way to the mesonic states with uniform flux tubes $\{n = h\}$.

In general, we observe that neither smearing approach can overlap optimally higher with the ground state for all the variables of the considered parametric spaces. In the far region (large values of n or h), however, there exists many states belonging to the highest band in Fig. 8.6 for which the overlap with the ground state, C_0 , is higher than the corresponding flat smearing. This observation indicates that smearing near the quark anti-quark pair, for sweeps greater than 30, increases the excited-state contamination. The links near the quark positions exhibit different UV behavior from the links at the middle with respect to the ground state overlap. The measured data provide an explanation why the usual flat APE smearing decreases

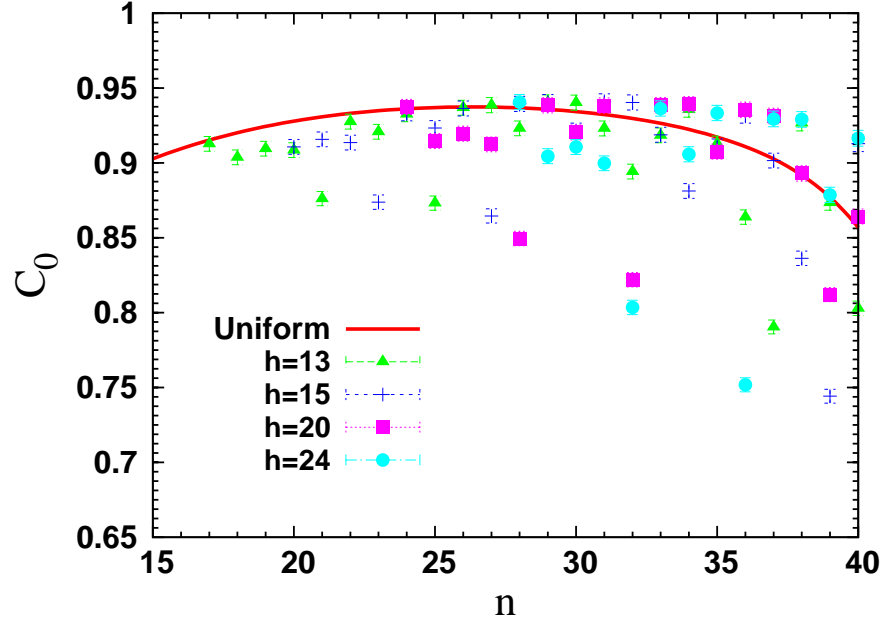


Figure 8.6: Comparison between non-uniformly smeared profiles $n \neq h$ and flat states $n = h$ represented by the smooth line. The quark source separation distance $R = 1.0$ fm.

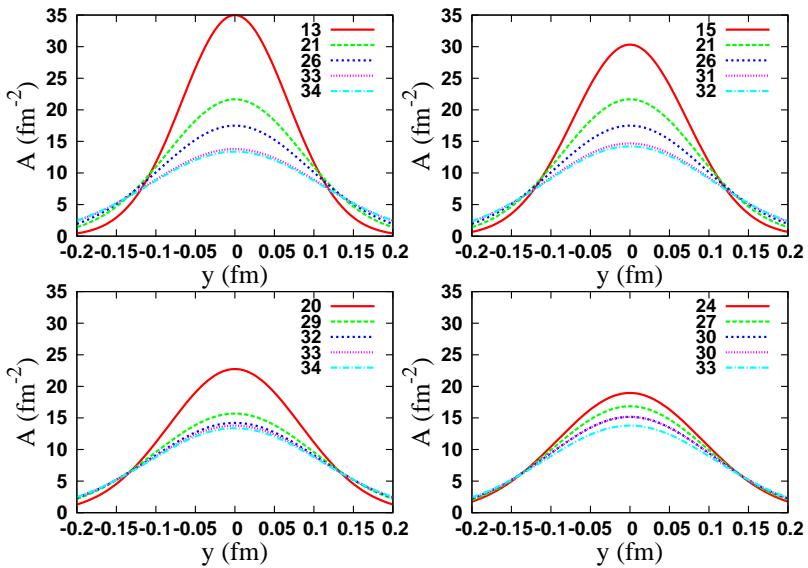


Figure 8.7: The flux tube operator Eq. (8.3.8). Each operator consists of a family of five Gaussians. The operators correspond to the states $(h = 13, n = 34)$, $(h = 15, n = 32)$, $(h = 20, n = 34)$ and $(h = 24, n = 33)$. These states maximize the value of the overlap with the ground state. The source separation distance $R = 1.0$ fm.

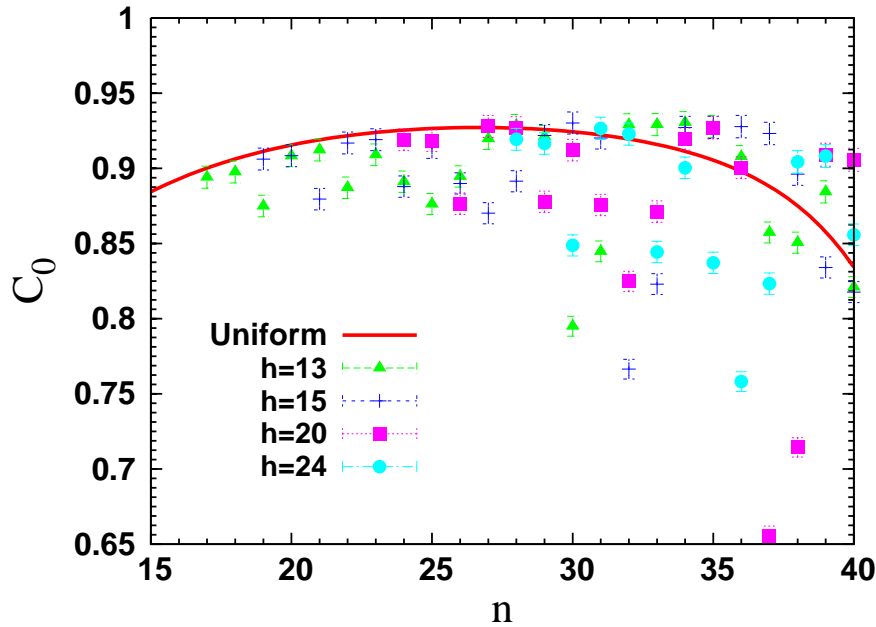


Figure 8.8: Same as Fig. 8.6, for quark-antiquark separation distance $R = 1.2$ fm.

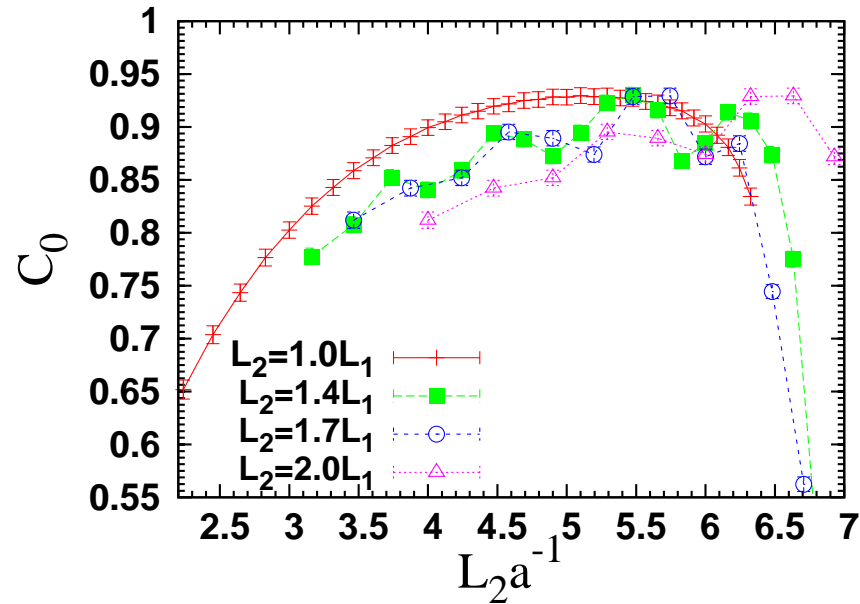


Figure 8.9: The overlap with the ground state C_0 versus the physical width of the flux-tube operator in the middle L_2 of the tube. Each line corresponds to a fixed ratio between the width of the tube in the middle and at the last link L_1 . The quark-antiquark separation distance of $R = 1.2$ fm is considered here.

the overlap with the ground state for large number of smearing sweeps.

Recalling that the local smearing operator $\mathcal{S}^n U$ not only alters the width of the fat link at each locus which is proportional to \sqrt{n} , but also decreases the amplitude as indicated in Eq. (8.3.10). We see that some of these states that maximize the ground state overlap show in addition to the variation in the amplitude a sensible variation in the amplitude of the flux tube operator near the quark source.

At larger source separation $R = 1.2$ fm, the collection of C_0 in branching bands is less obvious as can be seen in Fig. 8.8. The observable difference between the overlaps value at $R = 1.2$ fm in Fig. 8.8 and for $R = 1.0$ fm in Fig. 8.5 is that the states $\{h = 24, n > 32\}$, having a flatter and more uniform profile, do not optimize the overlap with the ground state.

We replot the points in the parametric space which correspond to a fixed ratio between the radii at the end and middle points of the flux tube L_1/L_2 in Fig. 8.9. The lines pass through trial states that approximately have the same non-trivial topology for the case $L_1 \neq L_2$. The flat states, $L_1 = L_2$, are smoothly varying in comparison to the non-uniformly smeared states which in general assume the same behavior except for an obvious existence of fluctuation along each curve. These arise due to the fact that non-uniform states, because of the lattice structure, do not have exactly the same non-trivial topology in comparison to the flat states.

The optimization of the ground state overlap with the nonuniformly smeared flux-tube operators suggests a similarity between the effects observed at the end of the plateau in the QCD phase diagram and at zero temperature. Nevertheless, this does not weaken the conclusions we have made in the earlier chapters on the finite temperature effects. Indeed, there are significant differences in the flux-tube width profile between the results at $T = 0.8 T_c$ at the end of the plateau in the QCD phase diagram and at $T = 0.9 T_c$ just below the phase transition. This is where the finite temperature effects are manifest. The suggestion made in this chapter is that very little happens between $T = 0.8 T_c$ and $T = 0$. This is further supported by the similarity of the string tension observed at the end of the plateau in the QCD phase diagram and at zero temperature.¹

8.5 Conclusion

The overlap with ground state static mesons has been measured for a variety of trial mesonic states corresponding to non-uniform gluonic distributions. An optimal ground state overlap for non-uniform flux-tube operators as well as flat smeared operators has been found. This supports the possibility that the true ground state flux tube is not uniform but rather has a curved flux strength profile larger in the middle with higher action-density suppression. Such a result resembles the profile revealed at finite temperature near the end of the QCD plateau. The findings of this work motivate the use of a Multi-level approach to explore the action-density profile of a static meson at zero temperature. This is the focus of the forthcoming

¹This suggested similarity between both profiles, at $T = 0$ and at the end of the plateau of QCD phase diagram, is understood in the context of small changes in the width along the tube and an observed nonuniform profile due to changes in the amplitude of the Gaussian shape along the flux tube (see for example Figs. 6.3 and 6.4).

investigation. It is remarkable that highly non-uniform trial states produce values of C_0 equally as good as the traditional uniform smearing approach. This result indicates that it is the smearing extent is the most critical in obtaining optimal overlap with the ground state. However, it is important to note that the shape of the non-uniform sources is critical to obtaining large values for C_0 . Our investigation of other source shapes complementary to Fig. 8.3 did not produce values for C_0 as large as favorable case studied here in detail.

Chapter 9

Gluonic Profile of Static Baryons

9.1 Outline

The gluon flux distribution of a static three quark system has been revealed at finite temperature in the pure SU(3) Yang-Mills theory. An action density operator is correlated with three Polyakov loops representing the baryonic state at temperatures near the end of the QCD plateau, $T/T_c \approx 0.8$, and another just before the deconfinement point, $T/T_c \approx 0.9$. The flux distributions at short distance separations between the quarks display an action-density profile consistent with a rounded filled Δ shape iso-surface. However the Δ shape action iso-surface distributions are found to persist even at large inter-quark separations. The action density distribution in the quark plane exhibits a nonuniform pattern for all quark separations considered. This result contrasts with the Y-shaped uniform action density gluonic-flux profile obtained using the Wilson loop as a quark source operator at zero temperature. We systematically measure and compare the main aspects of the profile of the flux distribution at the two considered temperature scales for three sets of isosceles triangle quark configurations. The radii, amplitudes and rate of change of the width of the flux distribution are found to reverse their behavior as the temperature increases from the end of the QCD plateau towards the deconfinement point. Remarkably, we find the mean square width of the flux distribution shrinks and localizes for quark separations larger than 1.0 fm at $T/T_c \approx 0.8$ which results in an identifiable Y-shaped radius profile. Near the deconfinement point, the action-density delocalizes and the width broadens linearly at large quark separations.

The profile of the baryonic gluonic distribution is compared with the width of the string picture's junction fluctuations. Despite the observation that the gluonic flux is always Δ shaped even at large distances, the comparison reveals that the best fits to the junction fluctuations of the baryonic string are returned when the profile of the flux-tube junction is near the fermat point of the triangle made up by the quarks as the distance of one quark from the other two is varied. This result supports the underlying gluonic picture of Y-shaped string-like flux tubes connected at a junction whose position is such that the total string length is minimized.

9.2 Introduction

Revealing the colour field distribution in the nucleon is a subject of fundamental importance to quantum chromodynamics (QCD) and confinement. Lattice QCD simulations provide a first principle source of knowledge about how the energy distribution manifests itself among a system of three static quarks (3Q). This has to do with the relevant ansatz that accurately parametrizes and models the non-abelian force that binds the nucleon. The colour distribution due to a 3Q system has been of a problem of reviving interest of lattice simulations and has been revisited with a variety of lattice techniques [2, 157, 143, 170]. However, an important aspect of this problem yet remains to be thoroughly investigated. That is, the energy distribution associated with the 3Q system at finite temperature. Tackling the problem of the gluonic distribution from this perspective involves the employment of a methodologically different set of unbiased hadronic operators. In addition to this, revealing the changes of the gluonic profile of the (3Q) system under various temperature conditions would certainly contribute to our perception of the underlying gluonic picture and the associated gluon dynamics. In fact, the distribution of gluonic fields in the baryon at high temperature, before quantum chromodynamics (QCD) undergoes a phase transition, is unknown in detail and has not yet been scrutinized by the lattice approach.

Most of our current understanding of the (3Q) confining force is based on analysis at zero temperature [3, 100, 171, 172, 173, 174, 175]. The parametrization which provides the best possible fits of the lattice data of the measured 3Q system potentials has been controversial for a long period of time [171, 176, 177, 100]. However, recent lattice QCD findings regarding the three quark potential are settled to support the so-called Δ -ansatz parametrization for small quark separation distances of $R < 0.7$ fm and the Y-ansatz for $0.7 < R < 1.5$ fm [100]. The Δ -ansatz accounts for a confining potential built up as a sum of two-body forces; the string tension is half that in the corresponding $Q\bar{Q}$ system and the confining part of the baryonic potential is in proportion to the perimeter of the triangle set up by the 3Q system. On the other hand, if the confining potential is proportional to the sum of the distances from the quarks to the Fermat point with a string tension the same as that in the $Q\bar{Q}$ system, then due to its shape, this potential is known as the Y-ansatz, giving rise to a three-body term relevant to a genuine interaction channel of the non-abelian force.

Ambiguities are known to arise, however, in the calculations of the gluonic distribution in the 3Q system at zero temperature. The energy distribution may be vulnerable to systematic errors associated with excited-state contamination [157] when constructing the static baryon using a Wilson loop operator. The configuration of the spatial links that best minimize the potential has to be adopted before hand. Associated with this arbitrariness in tuning the ground state operator are the excited state potentials which manifest themselves in the revealed gluonic profiles as a bias reflecting the form of spatial links of the Wilson loop operator [157]. The L shape baryon operator provides a pronounced evidence where the flux distribution mimics the source [2].

The isolation of the ground state is challenging in the case of field-distribution calculations which involve four-point correlations rather than the ground state po-

tential which is extracted in the large time limit of a three-point correlation [157]. For example, Euclidean time evolution in the 3-quark Wilson loop operator results in observable broadening of the junction in the Y-shaped configuration [2]. Statistical noise, nevertheless, imposes a practical constraint on any further increase in the exponentially decaying operator.

In this investigation, the static baryonic states are accounted for by means of Polyakov loops. This provides a gauge invariant operator which acquires a methodological importance [143] due to the ability to construct an unbiased 3-quark operator without recourse to a particular assumption regarding the form of the configuration of the spatial links in Wilson loops or the ultraviolet properties of these parallel transporters [178]. While carrying out energy density calculations into the zero temperature regime requires substantial numerical simulations with regard to the CPU time as well as the memory storage, the use of these stringless hadronic operators for revealing the energy distribution at finite temperature is still an attractive idea from the practical feasibility point of view. This can be studied in conjunction with the thermal effects.

At finite temperature, pure Yang-Mills $SU(3)$ lattice simulations for the action density in the mesonic sector display a flux distribution with a vibrating string-like shape. The density distribution shows a non-uniform pattern with an almost constant cross section in the intermediate distance region $0.5 \leq R \leq 1$ fm and non-constant cross section at larger quark separations [158]. The non-uniformity of the action density coincides with only a small decrease in the $Q\bar{Q}$ effective string tension σ [81] suggesting the ground state may also display a nonuniform action density distribution [178].

In this chapter, we generalize this analysis to the distribution of the colour field inside the baryon. We consider one temperature near the end of the QCD plateau region at $T/T_c \approx 0.8$, and other just before the deconfinement point at $T/T_c \approx 0.9$. The three infinitely heavy quarks are accounted for by means of Polyakov loops of the same time orientation. The field strength inside the corresponding quark system is revealed by correlating an improved action density operator [150] to these gauge-invariant hadronic operators. Gauge-field smoothing [147], in addition to a high statistics gauge-independent [2] averaging is employed to enhance the signal to the noise. This noise reduction approach can be employed in a controlled and systematic manner that has been proved effective in keeping the physics intact in the case of the static meson [158]. The analysis on either the $Q\bar{Q}$ force or the action density shows that smearing leaves no effect on the corresponding measurements taken for quark source separation distance scales greater than the diameter of the Brownian motion of a diffused link, i.e. the characteristic diameter of smearing. Moreover, the systematic effects associated with this UV filtering procedure on the gluonic profile has been reported in detail in Ref. [135].

The analysis on the smearing effects is revisited in this work for the 3Q force. The relevant distance scale where the physics is preserved is established. After identifying this scale, the characteristics of the action density profile are presented for selected 3Q configurations and contrasted at the two considered temperatures.

The map of this chapter is as follows: In Section 9.3 and Section 9.4, the details of the simulations and noise reduction techniques are described. The force in the 3Q system for selected configurations is evaluated in Section 9.5. In Section 9.6,

the main aspects of the gluonic profile of the baryonic action density is analyzed and contrasted at the two temperatures. In the last Section 9.7, we compare the junction profile with the predictions of the string model derived in Chapter 4.

9.3 Measurements

The infinitely heavy quark state is constructed by means of Polyakov loop correlators. As discussed in chapter(3) the baryonic correlator reads,

$$\langle \mathcal{P}_{3Q}(\vec{r}_1, \vec{r}_2, \vec{r}_3) \rangle = \langle P(\vec{r}_1) P(\vec{r}_2) P(\vec{r}_3) \rangle ,$$

where the Polyakov loop is given by Eq. (6.3.1). The above correlator corresponds to three Polyakov lines all in the same time direction.

After the construction of the gauge-invariant colour-averaged quark states, subsequent measurement by a gauge-invariant action density operator $S(\vec{\rho}, t)$ is taken at the spatial coordinate $\vec{\rho}$ of the three dimensional torus corresponding to each Euclidean time slice. The action density operator is calculated, in the usual way used in the previous chapters, via a highly-improved $\mathcal{O}(a^4)$ three-loop improved lattice field strength tensor [150].

A scalar field that characterizes the gluonic field can be defined as

$$\mathcal{C}(\vec{\rho}, \vec{r}_1, \vec{r}_2, \vec{r}_3) = \frac{\langle \mathcal{P}_{3Q}(\vec{r}_1, \vec{r}_2, \vec{r}_3) S(\vec{\rho}) \rangle}{\langle \mathcal{P}_{3Q}(\vec{r}_1, \vec{r}_2, \vec{r}_3) \rangle \langle S(\vec{\rho}) \rangle}, \quad (9.3.1)$$

for baryonic systems, where $\langle \dots \dots \rangle$ denotes averaging over configurations and lattice symmetries, the vectors \vec{r}_i define the positions of the quarks and $\vec{\rho}$ the position of the flux probe. Cluster decomposition implies $C \rightarrow 1$ away from the quarks.

In this investigation, we have taken 10,000 measurements at temperature $T/T_c = 0.8$, and 6,000 measurements at temperature $T/T_c = 0.9$. The measurements are taken on hierarchically generated configurations. The gauge configurations are generated using the standard Wilson gauge action on lattices with a spatial volume of 36^3 . Gauge configurations are generated with a coupling value of $\beta = 6.00$. The lattice spacing at this coupling is $a = 0.1$ fm [164]. After each 1000 updating sweeps, $n_{\text{sub}} = 20$ or 12 measurements separated by 70 sweeps of updates are taken for the two lattices corresponding to $T/T_c \approx 0.8$ and $T/T_c \approx 0.9$ respectively. These sub measurements are binned together in evaluating Eq. (9.3.1). The total measurements are taken on 500 bins.

The gluonic gauge configurations are generated with a pseudo-heat bath algorithm [95]. As has been done in the previous chapters, the heat bath is implemented by (FHKP) [93, 94] updating on the corresponding three SU(2) subgroups. Each update step consists of one heat bath sweep and 4 micro-canonical reflections.

9.4 Statistics

In the same way as described in the last chapters, gauge-independent noise reduction can be employed by making use of the space-time translation invariance of the hyper-

toroid. Also, local action reduction by cooling the gauge field with an over-improved stout-link (4D-smearing) algorithm [146], as described in Chapter 4, is employed.

Local action reduction by smearing the gauge links has been performed on the whole four-dimensional lattice. This procedure can be applied for correlating operators with Polyakov loops. For example, the correlations with the topological charge has been studied in Ref. [145] using the Cabbibo-Marinari cooling. Smearing the gauge field can be particularly helpful in reducing the statistical noise associated with evaluating the Polyakov loop correlators.

However this step may result in the elimination of short distance physics and one has to be careful with regard to the number of smearing sweeps and the relevant distance scale where the physical observables are extracted. In the next section, we extend the study of Chapter 4 of the effects of gauge field four-dimensional smearing to the 3Q force and determine the distance scale and corresponding smearing level where the physical observables are left intact. We smear the gauge field with an over-improved stout-link four-dimensional smearing algorithm [146], with the same parameters used in the measurement setup of the Chapters 6 and 7.

9.5 Forces in the static baryon

Unlike the force which is extracted from a three point correlator, the flux characterization Eq. (9.3.1), involves a four-point correlation function in the numerator presenting additional challenges with respect to the signal to noise level. The lattice space-time and configuration space symmetries can be auxiliary in enhancing the signal to noise ratio; however, a four dimensional gauge smoothing has to be employed to obtain a signal.

The force in the 3Q system is a physical observable of direct relevance to the properties of the underlying energy distribution. In the following we consider the effects of the gauge smoothing procedure on the force experienced by a test colour charge. This can give indications on the relationship between source separation distance and the number of smearing sweeps where the changes in physics is minimal. Similar techniques have been adopted in Ref. [144] in the determination of the large distance $Q\bar{Q}$ force in vacuum with different levels of hyperbolic (HYP) smearing [158]. In the following, we consider the evaluation of the force via three Polyakov loop correlators.

For several levels of smearing corresponding to $n_{sw} = \{20, 40, 60, 80\}$, we numerically evaluate the force on a test colour charge, assuming the transfer matrix interpretation is preserved as justified in Ref. [135], the 3Q potential can be identified via a three loop correlator as

$$\begin{aligned}\langle \mathcal{P}_{3Q} \rangle &= \langle \mathcal{P}(\vec{r}_1) \mathcal{P}(\vec{r}_2) \mathcal{P}(\vec{r}_3) \rangle \\ &= \exp(-V_{3Q}(\vec{r}_1, \vec{r}_2, \vec{r}_3)/T).\end{aligned}$$

The force on the third quark Q_3 for the isosceles triangle configuration illustrated in

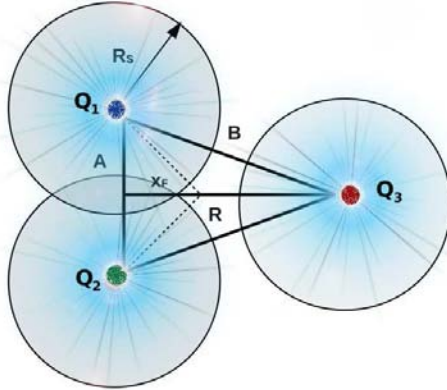


Figure 9.1: Schematic diagram for the isosceles configuration of the 3Q system. The large spheres represent the motion of the diffused field of characteristic smearing radius of R_s centred at the quarks (small spheres).

Fig. 9.1 is measured through the definition of the derivative on the lattice [88, 119]

$$\begin{aligned} F_{Q_3} &= -\frac{\partial V(R; A)}{\partial R} \Big|_{R+\frac{a}{2}} \\ &= \frac{1}{2 a T} \log \left(\frac{\langle P(0, 0) P(0, A) P(R, A/2) \rangle}{\langle P(0) P(0, A) P(R + 1, A/2) \rangle} \right). \end{aligned} \quad (9.5.1)$$

The numerical values of the force measured on smeared configurations are reported in Fig. 9.2 for three isosceles bases, $A = 0.6, 0.8$ and 1.0 fm. The repeated measurements on the data sets corresponding to increasing smearing levels indicate, in general, invariance of the force experienced by the test charge Q_3 under smearing at large distances. The loss of short distance physics is pronounced at small values of R which decreases as we increase the length of the isosceles base quark configuration. In the following, our consideration of different isosceles 3Q configurations enable a systematic identification of the distance scale beyond which a given level of smearing has little effect on the physical observables.

We define $R_F(n_{\text{sw}})$ to be the minimal distance beyond which a smearing sweeps up to n_{sw} does not affect the force Eq. (9.5.1). The values of R_F can be read from Fig. 9.2. Table 9.1 summarizes the values of R_F for each isosceles configuration and smearing level. Since the effects of smearing relate also to the length of the isosceles base, we list for comparison the values of the corresponding effective range, B_F , defined as $B_F = \sqrt{R_F^2 + A^2/4}$, and also the distance from a quark at the base of the triangle to the Fermat point of the triangle L_F (see Fig. 9.1).

Clearly the range R_F is decreasing with the increase of the length of the isosceles base, A , indicating that smearing around the charges residing on the isosceles base decreases the force exerted on the colour test charge Q_3 as the charges Q_1 and Q_2 become closer as in Fig. 9.1. Inspection of the corresponding values of the above defined B_F , on the other hand, show that the decrease of R_F with the increase of A is such that the length of B_F is approximately constant. To gain an insight to what

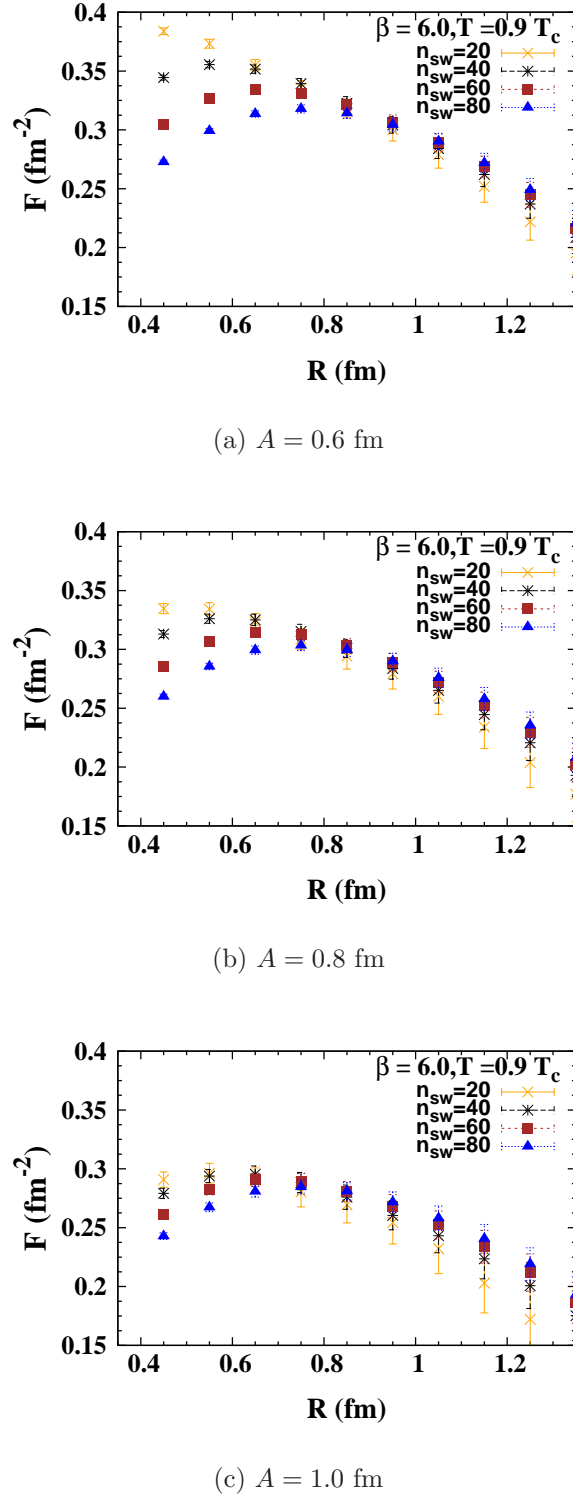


Figure 9.2: The force for the isosceles 3Q configurations with base lengths (a) $A = 0.6$ fm, (b) $A = 0.8$ fm and (c) $A = 1.0$ fm, respectively. The x -axis denotes the position R of the third quark. Smearing effects are manifest for $R < 0.95$ fm, $R < 0.85$ fm and $R < 0.75$ fm for $A = 0.6$ fm, $A = 0.8$ fm, and $A = 1.0$ fm. Only subtle smearing effects remain beyond these distance scales.

Table 9.1: The characteristic radii $B_F = \sqrt{R_F^2 + A^2/4}$ for the baryonic system at each smearing level for each configuration of Fig. 9.2.

Config	$A = 0.6$ $L_F = 0.35$		$A = 0.8$ $L_F = 0.46$		$A = 1.0$ $L_F = 0.58$	
	n_{sw}	R_F	B_F	R_F	B_F	R_F
40	0.65	0.63	0.55	0.68	0.45	0.67
60	0.75	0.80	0.65	0.76	0.55	0.74
80	0.85	0.90	0.75	0.85	0.65	0.82

these observations may imply, we study the characteristics of the Brownian motion of the diffused field, and also the analogous values of smearing threshold $R_F(n_{sw})$ measured for the $Q\bar{Q}$ system.

The diffuse field is Gaussian distributed [3] through a ball centered at position \mathbf{r} whose evolution with a smearing time τ , in a four-dimensional smearing scheme [158] is given by Eq. (5.2.9)

The diffused field characteristic radius is defined as

$$R_s = a\sqrt{\rho c n_{sw}}. \quad (9.5.2)$$

The proportionality constant c scales the number of smearing sweeps n_{sw} in the improved stout-link smearing algorithm defined above with respect to APE four-dimensional smearing as defined for instance in Refs. [2, 178]. The calibration proceeds via comparing the respective number of smearing sweeps in each smearing scheme with respect to a given threshold [149] (the reconstructed action-density [150] normalized to a single instanton action S/S_0). This yields a value of $c = 6.15(3)$ [158] (see also Chapter 6). With $\rho = 0.06$, the number of smearing sweeps in the improved stout-link smearing algorithm scales as half the number of the corresponding smearing sweeps in APE smearing with the smearing parameter $\alpha = 0.7$.

After identifying this characteristic smearing range, the values of $R_s(n_{sw})$ are compared to the corresponding values of $R_F(n_{sw})$ for the $Q\bar{Q}$ system [158] in Table 5.3. Inspection of the values reported for the mesonic force unveils that R_F is roughly equivalent to twice the smearing radius R_s . This suggests that the mesonic force is invariant under the smearing operation applied on the whole four dimensional lattice as long as the fuzzed balls centred at the quark source links are non-overlapping. Similar analysis on the action density shows that the region free of smearing effects obeys the same invariance criterion [158].

The distance B_F describes the minimal distance from the quarks $Q_{1,2}$ to Q_3 for which the measured force is invariant under a given number of smearing sweeps. The values of B_F in Table 9.1 compare favourably with the values calculated for the quark-antiquark system in Table 5.3. This indicates that the smearing effects are immaterial as long as the length of the isosceles side is such that the fuzzed balls around any of the colour charges $Q_{1,2}$ and that around the test charge Q_3 are non-overlapping.

For the smearing radii considered here, a slight overlap of the fuzzed ball around each quark $Q_{1,2}$ on the base of the isosceles is seen to have no observable effect on

the force experienced by the test charge Q_3 . This observation does not exclude the possibility of the three body channel of the interaction in the (3Q) system. The locus of the center of interaction may still be outside the two overlapping spheres in the base of the triangle.

In Table 9.1, the distance from the quarks $Q_{1,2}$ to the Fermat point is indicated for each configuration. Simple variation calculus shows that for an isosceles triangle, the position of the Fermat point does not depend on the height of the triangle, R , and the locus is fixed merely by the length of the base of the triangle such that, $x_F = A/(2\sqrt{3})$.

In summary, for the quark position geometry considered in this work, the above analysis on the measured values of the force among a system of three quarks for each smeared data set of configurations suggest a conservative distance scale γ beyond which the confining force on a given source is unchanged to be

$$\gamma = 2 R_s. \quad (9.5.3)$$

This restricts the number of smearing sweeps to be such that the characteristic diameter of smearing does not exceed the distance between at most two quarks. To take into account the distance between other sources, an additional conservative measure will be to keep the distance to the Fermat point from any of the quarks of a given configuration outside the radius of smearing. However, in the present case this may be immaterial since the differences in the force measurements are well within the statistical errors. Equation (9.5.3) indicates the distance scales where a specific characteristic of the action density might be affected by gauge field smoothing. The corresponding effects of gauge field smoothing on the revealed gluonic profile will be discussed also on several occasions below.

9.6 Action Density

9.6.1 Flux iso-surface profile

The flux strength is measured as the correlation between the vacuum action-density, $S(\vec{\rho}, t)$, and a gauge-invariant operator representing the quark states as provided by Eq. (9.3.1). The action density operator

$$S(\vec{\rho}) = \beta \sum_{\mu > \nu} \frac{1}{2} \text{Tr}(F_{\mu\nu}^{\text{Imp}})^2, \quad (9.6.1)$$

is calculated through the $\mathcal{O}(a^4)$ improved lattice version of the continuum field-strength tensor [150]

$$F_{\mu\nu}^{\text{Imp}} = \sum_{i=1}^3 w_i C_{\mu\nu}^{(i,i)}. \quad (9.6.2)$$

where $C_{\nu\mu}^{(i,i)}$ are $i \times i$ link products in the $\nu\mu$ plane and w_i are coefficients selected to remove $\mathcal{O}(a^2)$ and $\mathcal{O}(a^4)$ errors. The evaluation of this operator on smeared configurations filters out the UV divergences around the quark positions. The origin

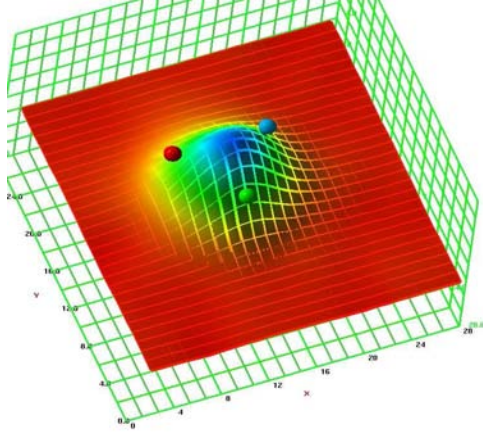
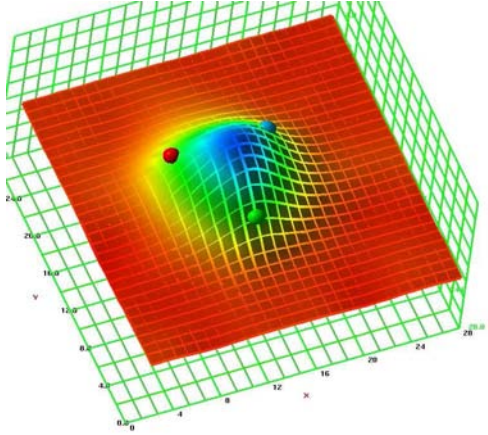
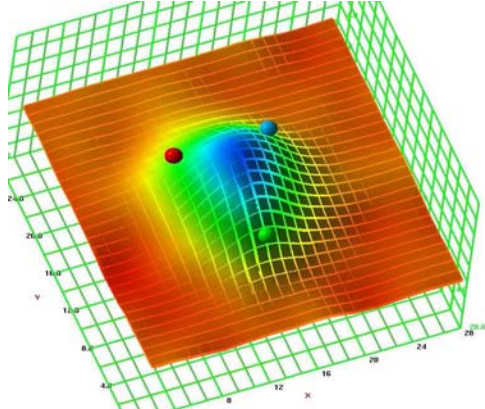
(a) $R = 0.6$ fm, $n_{\text{SW}} = 60$.(b) $R = 0.8$ fm, $n_{\text{SW}} = 60$.(c) $R = 1.0$ fm, $n_{\text{SW}} = 80$.

Figure 9.3: Surface plot (inverted) of the flux distribution $\mathcal{C}(\vec{\rho})$ of Eq. (9.3.1) evaluated in the plane of the (3Q) system $\vec{\rho}(x, y, 0)$, for isosceles configuration of base length $A = 0.4$ fm and separation distances (a) $R = 0.6$ fm, (b) $R = 0.8$ fm and (c) $R = 1.0$ fm, at $T = 0.8 T_C$. The spheres refer to the positions of the quarks.

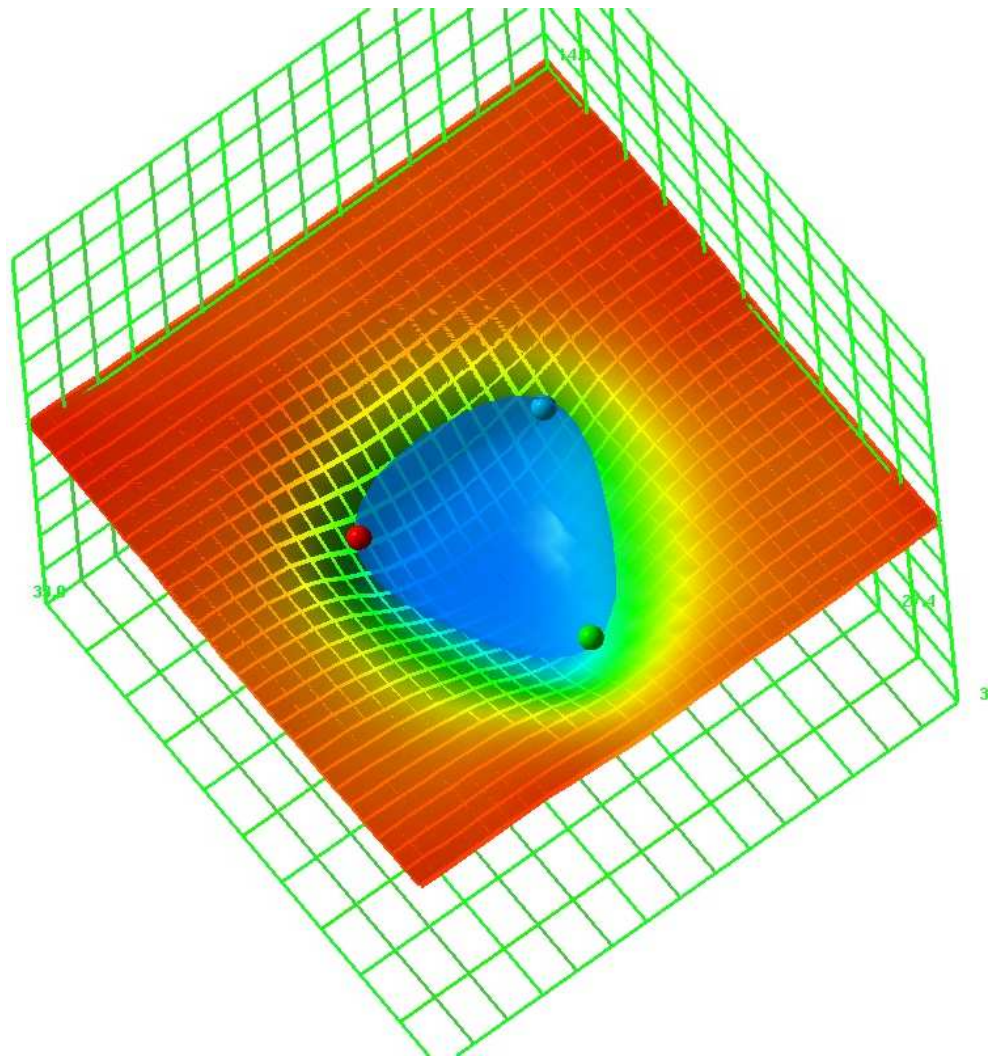


Figure 9.4: The flux action iso-surface at the quark positions, plotted together with a surface plot for the density distribution $\mathcal{C}(\vec{\rho})$, in the 3Q plane at temperature $T = 0.9 T_c$, for equilateral triangular configuration $R = 1.1$ fm and $A = 1.0$ fm.

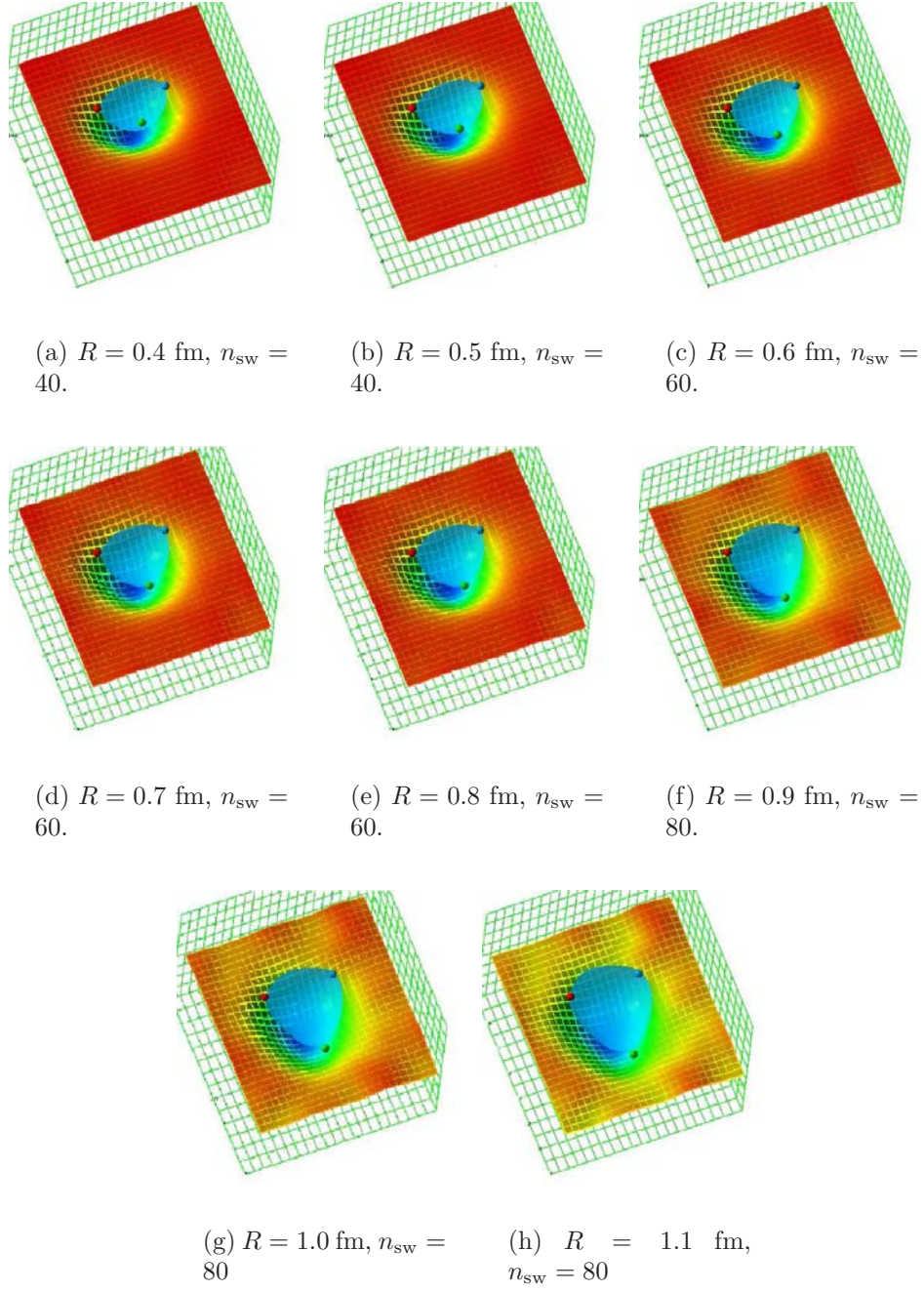


Figure 9.5: Surface plot in the plane of the 3Q system $\vec{\rho}(x, y, z = 0)$ and iso-surface of the flux distribution $\mathcal{C}(\vec{\rho}; \vec{r}_1, \vec{r}_2, \vec{r}_3)$ for the isosceles configuration with $A = 1$ fm and the third quark separation distance R as indicated. $T = 0.8 T_C$.

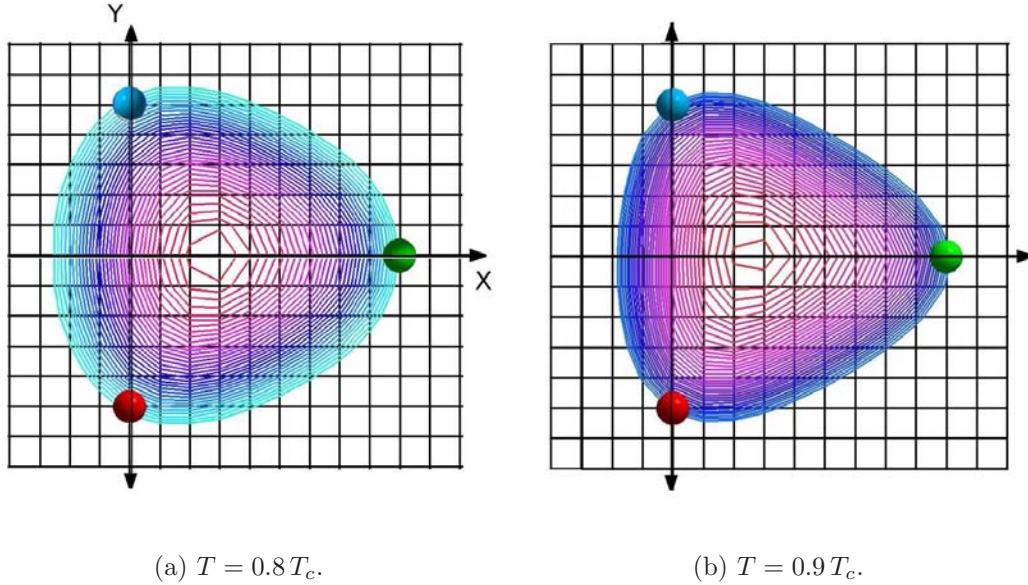


Figure 9.6: Comparison of the flux contour lines of the density distribution in the 3Q plane \mathcal{C} for triangular base $A = 1.0$ fm and third quark separation $R = 0.9$ fm at (a) $T = 0.8 T_c$ and (b) $T = 0.9 T_c$, in the $z = 0$ plane. As illustrated in Fig. 9.3, the maximal effect is near the Fermat point.

of the co-ordinate system is placed at the middle between the two quarks $Q_{2,3}$ on the y axis at positions $\vec{\rho}(0, \pm \frac{A}{2}, 0)$ and at distance R from the third quark, Q_3 , at $\vec{\rho}(x = R, 0, 0)$. The quarks reside on the plane $\vec{\rho}(x, y, 0)$.

On calculating Eq. (9.3.1), we find $\mathcal{C}(\vec{\rho}) < 1$, and $\mathcal{C} \simeq 1$ away from the quark positions. The density distribution in the plane of the quarks is plotted in Fig. 9.3. In general, the action density distribution is non-uniformly distributed as revealed in Fig. 9.3 through 9.5. The distribution $\mathcal{C}(\vec{\rho}(x, y, z = 0))$ has an action density maximal curve along the middle line $\vec{\rho}(x, y = 0, z = 0)$ between the two quarks $Q_{1,2}$. With the increase of source Q_3 separation, the peak point along the maximal curve $\mathcal{C}(\vec{\rho}(x, y = 0, z = 0))$ shows only subtle movement, remaining near the Fermat point of the triangle. These results contrast with the Wilson loop results at large separations [2] where the action density assumes a constant amplitude along each arm of the Y-shaped profile. A convex curvature in the contour plot of flux density is manifest in Fig. 9.4(b). This also contrasts with the density plots obtained using the Wilson loop where the flux density assumes a concave curvature.

Figure 9.4 discloses the flux surface plot of \mathcal{C} in the 3Q plane and associated iso-surface for an isosceles configuration corresponding to a base $A = 1.0$ fm at the temperature $T/T_c = 0.9$. The flux iso-surface displays a clear filled Δ shape distribution. By moving the third quark further away, i.e. by increasing R , the Δ shape is found to persist. The sequence of frames in Fig. 9.5 displays similar results, this time at $T = 0.8 T_c$. It is important to note that this geometrical form of the density plot manifests itself at a temperature near the end of the plateau of the QCD-phase diagram [5] where the string tension has been reported to decrease only

by a value around 10% [81].

The contour lines and iso-surface of the flux do not exhibit a significant change with the temperature scale. Similarly, the effects of smearing do not cause deformations of the iso-surface profile outside of smoothing the interpolation of the flux-lines. This has been observed [179] at relatively short distances employing the link integration for evaluating Polyakov lines in the flux strength characterization (9.3.1). Even though the number of smearing sweeps selected for each graph are larger than the limits set by the invariance of the force analysis of the last sections, the rendered graphs are not sensitive to increased levels of smearing.

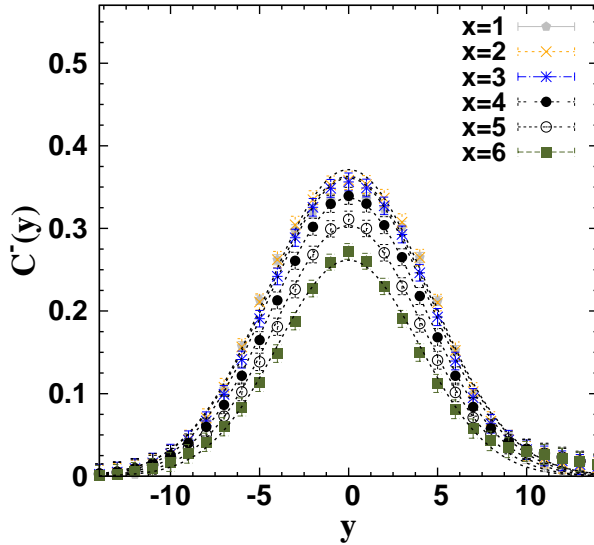


Figure 9.7: The density distribution $\mathcal{C}'(\vec{\rho})$ for the isosceles configuration with the base, $A = 1.0$ fm, and height $R = 0.8$ fm at $T/T_c = 0.8$ ($n_{\text{sw}} = 60$ sweeps). Data are plotted for the transverse planes $x = 1$ to $x = 6$. The lines correspond to the Gaussian fits to the density in each plane $\vec{\rho}(x_i, y, 0)$. The highest amplitude lies close to the Fermat point plane $x = 2.88$ of this 3Q configuration.

The flux distribution acquires a non-trivial transverse structure along the lines perpendicular to the x -axis. The fits of the transverse distribution along the lines $\vec{\rho}(x_i, y, 0)$ is returning good χ^2 for a Gaussian distribution with varying amplitudes and widths from the third quark Q_3 position, R , to the y -axis as shown for instance in Figs. 9.3 or 9.6. This symmetry about the y -axis in the $x - y$ plane also exists in the perpendicular z direction.

In a mesonic system, the width of the flux distribution is cylindrically symmetric around the line joining the two quarks. However, the existence of a third quark away from the y -axis breaks the symmetry of the width profile and the measured widths perpendicular to the plane of the quarks do indeed differ from the widths in the quark plane. In the forth coming section, we focus on dissecting the profile properties of the flux distribution within the quark plane, while the asymmetry aspect ratios are reported separately in the last section.

Table 9.2: The amplitude, $H_y(x_i)$ (scaled by a factor of 10^1) of the flux distribution at each consecutive transverse plane x_i from the quarks forming the base, A , of an isosceles triangle. The measurements for base source separation distance $A = 0.6, 0.8$ and 1.0 fm for the temperature $T/T_c = 0.8$ are indicated as a function of the third quark position, Q_3 .

Plane	$x = 1$	$x = 2$	$x = 3$	$x = 4$	$x = 5$	$x = 6$	$x = 7$	$x = 8$	$x = 9$	$x = 10$	$x = 12$	$x = 13$
$Q_3 = R/a$												
$A=0.6$ fm												
07	4.12(2)	4.34(1)	4.28(1)	3.97(2)	3.48(2)	2.84(2)						
08	4.24(2)	4.53(2)	4.56(2)	4.36(3)	4.00(3)	3.49(3)	2.85(3)					
09	4.31(2)	4.63(3)	4.73(3)	4.63(4)	4.37(4)	3.99(4)	3.49(4)	2.85(3)				
10	4.35(3)	4.67(5)	4.82(5)	4.79(6)	4.62(6)	4.33(5)	3.95(4)	3.46(3)	2.83(2)			
11	4.36(5)	4.66(7)	4.84(7)	4.85(8)	4.74(8)	4.53(7)	4.24(5)	3.86(4)	3.39(3)	2.80(3)		
12	4.35(6)	4.6(1)	4.7(1)	4.8(1)	4.8(1)	4.59(9)	4.35(7)	4.06(4)	3.72(4)	3.29(3)	2.73(3)	
13	4.30(7)	4.4(1)	4.6(1)	4.7(1)	4.7(1)	4.5(1)	4.3(1)	4.06(6)	3.81(4)	3.53(4)	3.14(4)	2.64(3)
$A=0.8$ fm												
07	4.71(5)	4.92(3)	4.80(1)	4.40(2)	3.80(3)	3.07(3)						
08	4.79(5)	5.08(3)	5.06(3)	4.78(3)	4.31(4)	3.71(4)	3.01(3)					
09	4.83(5)	5.14(4)	5.22(4)	5.03(4)	4.68(5)	4.22(4)	3.66(4)	2.98(3)				
10	4.84(5)	5.13(5)	5.27(5)	5.18(5)	4.93(6)	4.58(5)	4.13(4)	3.60(4)	2.95(4)			
11	4.84(5)	5.06(5)	5.24(5)	5.23(6)	5.08(6)	4.80(5)	4.44(4)	4.02(5)	3.51(6)	2.88(6)		
12	4.84(5)	4.92(5)	5.12(5)	5.18(6)	5.12(6)	4.92(5)	4.61(3)	4.23(6)	3.8(1)	3.4(1)	2.75(9)	
13	4.84(5)	4.70(4)	4.88(3)	5.00(3)	5.04(5)	4.92(5)	4.64(2)	4.27(8)	3.9(1)	3.5(1)	3.1(1)	2.6(1)
$A=1.0$ fm												
07	5.17(9)	5.43(6)	5.33(3)	4.86(1)	4.15(2)	3.31(2)						
08	5.22(9)	5.56(7)	5.58(5)	5.25(2)	4.69(1)	3.99(2)	3.19(3)					
09	5.2(1)	5.58(9)	5.72(7)	5.53(5)	5.11(3)	4.55(2)	3.89(4)	3.14(4)				
10	5.2(1)	5.5(1)	5.8(1)	5.71(9)	5.43(7)	4.99(6)	4.45(6)	3.82(7)	3.08(7)			
11	5.26(1)	5.3(1)	5.7(1)	5.8(1)	5.7(1)	5.3(1)	4.9(1)	4.3(1)	3.7(1)	3.0(1)		
12	5.4(1)	5.1(1)	5.5(1)	5.7(1)	5.8(1)	5.6(1)	5.1(1)	4.6(1)	4.0(1)	3.4(1)	2.7(1)	
13	5.7(1)	4.7(1)	5.0(1)	5.4(1)	5.6(1)	5.7(1)	5.3(1)	4.6(1)	4.0(1)	3.4(1)	2.9(1)	2.4(1)

Table 9.3: The squared width, r_y^2 , in lattice units, of the flux distribution as in Table 9.2.

Plane $Q_3 = R/a$	$x = 1$	$x = 2$	$x = 3$	$x = 4$	$x = 5$	$x = 6$	$x = 7$	$x = 8$	$x = 9$	$x = 10$	$x = 12$	$x = 13$
A=0.6 fm												
	07	9.7(1)	9.6(0)	9.3(0)	9.0(1)	8.6(1)	8.2(1)					
	08	10.0(1)	9.9(1)	9.7(1)	9.5(1)	9.2(1)	8.7(1)	8.2(1)				
	09	10.2(1)	10.3(1)	10.2(1)	10.0(1)	9.7(2)	9.3(2)	8.8(2)	8.2(1)			
	10	10.6(1)	10.8(2)	10.6(2)	10.5(2)	10.3(2)	9.9(2)	9.4(2)	8.8(2)	8.0(1)		
	11	10.9(2)	11.5(3)	11.2(3)	11.1(3)	10.9(3)	10.6(3)	10.2(2)	9.5(2)	8.6(1)	7.8(1)	
	12	11.3(2)	12.5(5)	12.1(4)	11.8(4)	11.6(4)	11.3(4)	11.0(3)	10.3(2)	9.4(2)	8.4(2)	7.7(1)
	13	11.7(3)	13.9(7)	13.2(6)	12.7(6)	12.4(6)	12.3(6)	12.1(5)	11.5(3)	10.4(2)	9.2(2)	8.3(2)
A=0.8 fm												
	07	12.2(2)	11.9(1)	11.3(0)	10.8(1)	10.2(1)	9.5(2)					
	08	12.4(2)	12.2(1)	11.7(1)	11.2(1)	10.6(1)	10.0(2)	9.2(2)				
	09	12.8(2)	12.6(1)	12.1(1)	11.6(1)	11.1(2)	10.5(2)	9.7(2)	8.8(2)			
	10	13.2(2)	13.1(2)	12.5(2)	11.9(2)	11.4(2)	10.9(2)	10.2(2)	9.3(2)	8.2(2)		
	11	13.6(2)	13.6(2)	12.8(2)	12.1(2)	11.5(2)	11.0(2)	10.4(1)	9.6(2)	8.5(3)	7.5(3)	
	12	14.1(2)	14.0(2)	12.9(2)	12.1(2)	11.3(2)	10.8(2)	10.3(1)	9.6(2)	8.6(4)	7.6(4)	6.8(4)
	13	14.8(2)	14.2(2)	12.7(1)	11.4(1)	10.6(2)	10.1(1)	9.8(1)	9.3(3)	8.5(5)	7.6(6)	6.9(6)
A=1.0 fm												
	07	15.4(4)	14.6(3)	13.7(1)	12.9(0)	12.2(1)	11.4(2)					
	08	15.7(4)	14.8(3)	13.8(2)	13.0(1)	12.3(0)	11.5(1)	10.6(2)				
	09	16.1(5)	15.0(4)	13.8(3)	12.9(2)	12.1(1)	11.5(1)	10.6(2)	9.5(2)			
	10	16.6(5)	15.1(5)	13.7(4)	12.6(3)	11.7(2)	11.0(2)	10.4(2)	9.4(3)	8.1(4)		
	11	17.0(6)	14.9(6)	13.3(6)	12.0(5)	10.9(4)	10.2(4)	9.6(5)	9.0(6)	7.9(6)	6.6(6)	
	12	17.2(7)	13.9(5)	12.2(5)	10.8(5)	9.7(7)	8.9(7)	8.3(8)	7.8(9)	7(1)	6(1)	5(1)
	13	17.1(9)	12(1)	10(1)	9(1)	8(1)	7(1)	6(1)	6(1)	6(1)	5(1)	4(1)

Table 9.4: The amplitude, $H_y(x_i)$ (scaled by a factor of 10^1), of the flux distribution at each consecutive transverse plane x_i from the quarks forming the base, A , of an isosceles triangle. The measurements for base source separation distance $A = 0.6, 0.8$ and 1.0 fm for the temperature $T/T_c = 0.9$ are indicated as a function of the third quark position, Q_3 .

Plane	$x = 1$	$x = 2$	$x = 3$	$x = 4$	$x = 5$	$x = 6$	$x = 7$	$x = 8$	$x = 9$	$x = 10$	$x = 12$	$x = 13$
$Q_3 = R/a$												
$A=0.6$ fm												
07	2.73(1)	2.83(1)	2.77(1)	2.58(1)	2.27(2)	1.88(2)						
08	2.71(1)	2.79(0)	2.75(1)	2.62(1)	2.42(2)	2.14(2)	1.79(2)					
09	2.68(0)	2.73(0)	2.67(0)	2.56(0)	2.41(1)	2.24(1)	2.01(2)	1.71(1)				
10	2.64(0)	2.64(1)	2.55(1)	2.43(0)	2.30(0)	2.19(1)	2.06(1)	1.89(1)	1.63(1)			
11	2.59(0)	2.55(2)	2.42(2)	2.27(1)	2.14(0)	2.05(0)	1.99(1)	1.91(1)	1.77(1)	1.56(1)		
12	2.53(1)	2.45(3)	2.29(3)	2.10(2)	1.95(2)	1.86(1)	1.83(1)	1.81(0)	1.77(1)	1.67(1)	1.49(1)	
13	2.46(2)	2.35(3)	2.15(3)	1.93(3)	1.76(3)	1.66(3)	1.63(2)	1.64(1)	1.64(0)	1.63(1)	1.56(2)	1.43(1)
$A=0.8$ fm												
07	2.88(2)	2.93(1)	2.85(0)	2.64(0)	2.33(1)	1.94(1)						
08	2.84(2)	2.86(2)	2.79(0)	2.63(0)	2.41(1)	2.14(1)	1.81(1)					
09	2.80(3)	2.77(3)	2.68(1)	2.52(0)	2.35(0)	2.18(1)	1.97(1)	1.70(1)				
10	2.74(2)	2.66(4)	2.53(3)	2.36(1)	2.20(0)	2.07(0)	1.96(1)	1.82(1)	1.60(1)			
11	2.67(2)	2.54(5)	2.38(4)	2.18(3)	2.00(2)	1.89(1)	1.83(0)	1.78(1)	1.69(1)	1.51(2)		
12	2.59(1)	2.44(5)	2.23(4)	2.00(4)	1.81(3)	1.69(2)	1.64(1)	1.64(0)	1.63(1)	1.58(2)	1.46(2)	
13	2.51(1)	2.35(4)	2.11(4)	1.85(4)	1.64(4)	1.50(3)	1.45(2)	1.46(1)	1.50(1)	1.52(2)	1.50(3)	1.42(3)
$A=1.0$ fm												
07	2.85(5)	2.84(4)	2.78(2)	2.59(0)	2.31(0)	1.96(0)						
08	2.79(6)	2.74(5)	2.68(3)	2.52(1)	2.33(0)	2.10(0)	1.82(1)					
09	2.72(6)	2.61(6)	2.52(4)	2.36(2)	2.20(1)	2.06(0)	1.91(0)	1.69(1)				
10	2.64(6)	2.46(7)	2.33(5)	2.15(3)	1.99(2)	1.89(0)	1.83(0)	1.74(1)	1.58(1)			
11	2.55(6)	2.31(7)	2.14(6)	1.93(5)	1.75(3)	1.66(1)	1.63(0)	1.63(0)	1.60(1)	1.48(1)		
12	2.46(5)	2.19(7)	1.98(6)	1.73(5)	1.54(4)	1.43(2)	1.41(1)	1.44(0)	1.49(1)	1.49(1)	1.43(2)	
13	2.39(5)	2.12(7)	1.86(6)	1.59(5)	1.38(4)	1.25(3)	1.21(2)	1.25(1)	1.32(1)	1.39(2)	1.43(3)	1.38(4)

Table 9.5: The squared width, r_y^2 , in lattice units, of the flux distribution as in Table 9.3.

Plane $Q_3 = R/a$	$x = 1$	$x = 2$	$x = 3$	$x = 4$	$x = 5$	$x = 6$	$x = 7$	$x = 8$	$x = 9$	$x = 10$	$x = 12$	$x = 13$
<hr/>												
A=0.6 fm												
07	13.2(1)	12.8(1)	12.5(0)	12.0(1)	11.4(2)	10.9(3)						
08	13.5(1)	13.0(1)	12.9(0)	12.6(1)	12.1(1)	11.4(2)	10.7(3)					
09	13.8(1)	13.2(1)	13.2(0)	13.0(0)	12.7(1)	12.1(2)	11.4(2)	10.6(3)				
10	14.2(1)	13.3(2)	13.4(1)	13.4(0)	13.2(0)	12.8(1)	12.2(2)	11.3(2)	10.5(3)			
11	14.6(1)	13.3(2)	13.5(2)	13.6(1)	13.6(1)	13.4(1)	13.0(1)	12.2(2)	11.2(2)	10.2(3)		
12	15.1(2)	13.3(3)	13.5(2)	13.7(2)	13.9(2)	13.9(1)	13.7(1)	13.1(1)	12.1(2)	10.9(2)	9.8(2)	
13	15.6(2)	13.2(3)	13.4(3)	13.7(3)	14.0(3)	14.3(3)	14.3(2)	13.9(1)	13.1(1)	11.9(2)	10.5(2)	9.3(2)
A=0.8 fm												
07	16.6(4)	15.8(3)	15.1(1)	14.3(0)	13.3(2)	12.4(3)						
08	16.9(4)	16.1(3)	15.6(1)	14.9(0)	14.0(1)	13.0(2)	12.0(3)					
09	17.3(4)	16.3(4)	15.9(2)	15.4(1)	14.7(0)	13.8(1)	12.7(2)	11.7(3)				
10	17.9(5)	16.5(5)	16.2(3)	15.8(2)	15.4(1)	14.7(1)	13.7(2)	12.5(2)	11.3(3)			
11	18.5(5)	16.7(5)	16.4(4)	16.2(3)	15.9(2)	15.5(1)	14.7(1)	13.5(2)	12.2(3)	10.9(3)		
12	19.3(5)	16.8(6)	16.7(5)	16.6(4)	16.5(3)	16.2(2)	15.7(2)	14.7(1)	13.4(2)	11.8(3)	10.5(3)	
13	20.0(5)	17.0(6)	17.0(5)	17.0(5)	17.0(4)	16.9(4)	16.6(3)	15.9(2)	14.7(2)	13.1(3)	11.4(3)	9.9(3)
A=1.0 fm												
07	21.4(9)	20.1(7)	18.8(3)	17.4(0)	15.9(1)	14.5(3)						
08	21.9(9)	20.4(8)	19.3(5)	18.1(2)	16.7(0)	15.2(2)	13.8(3)					
09	22(1)	20.7(9)	19.7(6)	18.7(3)	17.5(1)	16.1(1)	14.5(2)	13.0(3)				
10	23(1)	21(1)	20.2(7)	19.3(5)	18.3(2)	17.1(1)	15.6(1)	13.9(2)	12.4(3)			
11	24(1)	22(1)	20.7(9)	19.9(6)	19.1(4)	18.1(2)	16.8(1)	15.1(2)	13.4(3)	11.7(3)		
12	25(1)	22(1)	21.4(1)	20.8(7)	20.1(5)	19.2(4)	18.1(3)	16.5(2)	14.7(2)	12.8(3)	11.2(4)	
13	27(1)	23(1)	22.4(1)	22.0(8)	21.4(7)	20.7(5)	19.7(4)	18.2(3)	16.4(3)	14.3(3)	12.3(4)	10.5(4)

9.6.2 Flux radius profile

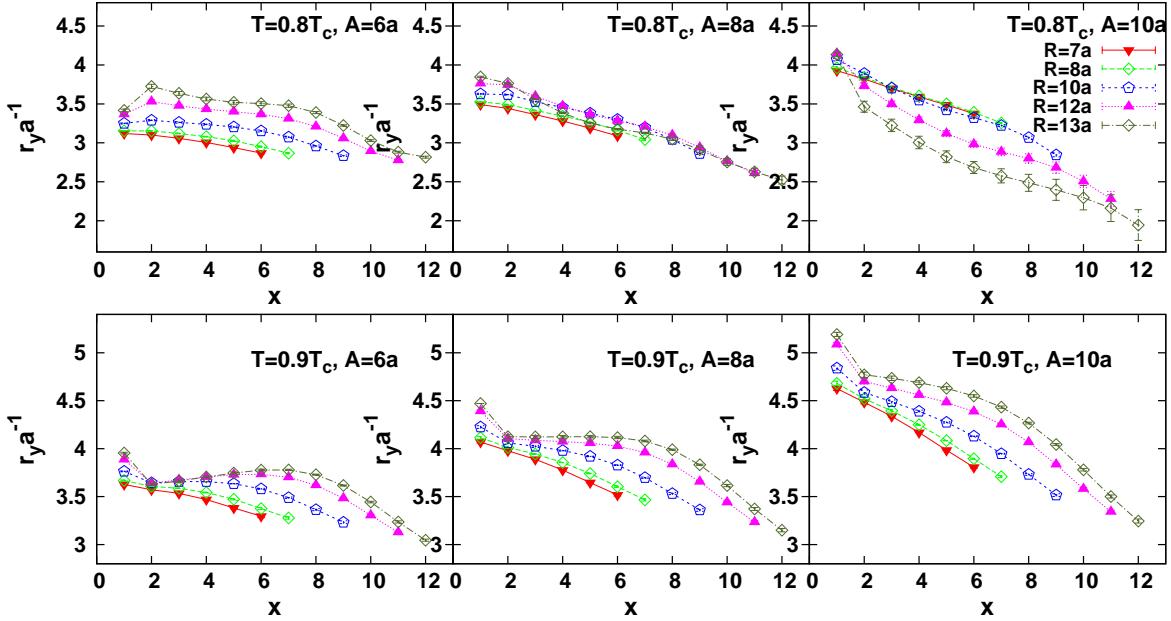


Figure 9.8: The radius profile of the flux-tube measured in the plane of the quarks for each isosceles configuration with base $A = 6a$, $A = 8a$ and $A = 10a$ ($a = 0.1$ fm), at two temperatures $T/T_c = 0.8$ (above) and $T/T_c = 0.9$ (below). The legend (in the upper right corner graph) signifies the third quark's position.

At large quark separation, the revealed flux tube profile using the 3Q Wilson loop operator at zero temperature exhibits a uniform tube amplitude with a radius that is only slightly increasing up to the position of the junction [2]. Although the bias of the energy distribution by the shape of the configurations of the spatial links [2, 157] leaves these rendered energy distributions somewhat uncertain, this flux distribution has been considered consistent with the parametrization of the 3Q ground state potential with a Y -ansatz at large distance [171]. The Y -shaped gluonic distribution has also been considered in consonance with the dual superconductivity picture [49, 52, 109] of the QCD vacuum. The flux is squeezed into a thin region dual to the Abrikosov vortex [180] resulting in the formation of Y -shaped string-like flux tube [181, 182, 183, 184].

At finite temperature, on the other hand, one intuitively would expect the quantum vibrations of the underlying three string system [133, 134, 185] to give rise to a nonuniform action density distribution in a similar fashion to the results revealed in the meson [158]. The thin string-like Y -shaped flux tube may delocalize away from its classical configuration and span the whole region though out the bulk of the triangular 3Q configuration, giving rise to a rounded concentric family of Δ action iso-surfaces (equi-action surfaces of Fig. 9.4). Each surface is weighted by a temperature-dependent amplitude intensity distribution. In this non-uniform action density context, the radius topology is not fixed merely based on the distribution of equi-action surfaces, as there can be an infinite number of iso-surface topologies

of the action density that all correspond to the same measured square root of the second moment of the distribution.

The second moment, $r_y^2(x)$, and the amplitude, $H_y(x)$, of the flux density at each line $\vec{\rho}(x_i, y, 0)$ is measured by means of Gaussian fits to the complementary distribution $\mathcal{C}' = 1 - C$

$$\mathcal{C}'(\vec{\rho}(x_i, y, 0)) = H_y(x_i) e^{-y^2/2r^2} \quad (9.6.3)$$

The fits to this Gaussian form are illustrated in Fig. 9.7. The mean square width in the 3Q plane at position, x_i , is measured via

$$r_y^2(x_i) = \frac{\int dy y^2 \mathcal{C}'(\vec{\rho}(x_i, y, 0))}{\int dy \mathcal{C}'(\vec{\rho}(x_i, y, 0))}, \quad (9.6.4)$$

eliminating dependence on $H_y(x_i)$. The values of the measurements of $H_y(x_i)$ and $r_y(x_i)$ are listed in Tables 9.2 through 9.5. The radius profile in the quark plane, $z = 0$, is measured at each lattice co-ordinate x_i . The data points corresponding to radii along the x -axis for a given quark configuration are interpolated with a continuous line up to the third quark, Q_3 , with position $\vec{\rho}(R, 0, 0)$ as in Fig. 9.8.

The first row of graphs in Fig. 9.8 correspond to radii measurements at the temperature $T/T_c = 0.8$ with base length running from $A = 0.6$ fm to $A = 1.0$ fm. For $A = 0.6$ fm, the radius profile draws almost constant lines with small declination indicating a subtle decrease along the x -axis up to the third quark position. The difference in radii between the very first planes and the planes close to the third quark Q_3 becomes more pronounced with the increase of the third quark Q_3 separation R as well as the increase of the distance between the two quarks $Q_{1,2}$ in the base.

At the same temperature scale $T/T_c = 0.8$ and small isosceles base $A = 0.6$ fm, the tube's radius, $r_y(x_i)$, at a given point broadens slowly with the increase of the quark separation Q_3 . This behaviour changes as the length of the isosceles base A becomes wider. The change in radius along the x -axis with R approaches near a stagnation in the broadening for $A = 0.8$ fm indicating an inflection point.

This is evident from the profile at the widest base length $A = 1.0$ fm. The radius at a given point typically decays with the increase of the third quark Q_3 separation R . The geometrical area spanned by the triangle made up by the 3Q system becomes significantly large as the third quark Q_3 steps farther away. In response, the gluonic energy condenses in narrower extents around the x -axis. In fact, we see a clearly identifiable Y-shaped profile of the gluon flux emerging at $R = 1.3$ fm as well as at $R = 1.2$ fm.

For illustration, the action contours and radius profile have been superimposed in Fig. 9.9. The action contours are concentric convex Δ -shaped action isolines, and the corresponding radii measured along the x -axis are not coinciding with any of the action isolines and have a convex Y-shaped-like profile. Variation of the amplitude, H_y , hides the underlying Y-shape revealed through the consideration of r_y . We see from the corresponding last graph of the bottom row in Fig. 9.8 that the contour lines and the radius profile have similar concave curvatures at the temperature $T/T_c = 0.9$.

This analysis may render the widely used terms such as the Y and Δ shaped gluon flux linguistically ambiguous if their usual usage is brought to the regime

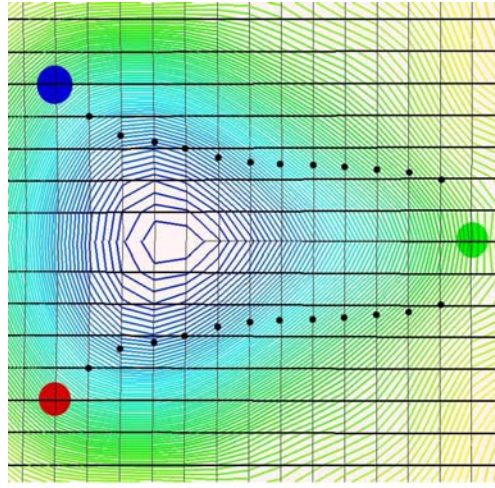


Figure 9.9: The radius profile of the flux-tube displaying a Y-shape like profile for quark configurations of base $A = 1.0$ fm and the third quark position $R = 1.3$ fm at temperature $T/T_c = 0.8$. In the background are the corresponding flux action-density contours.

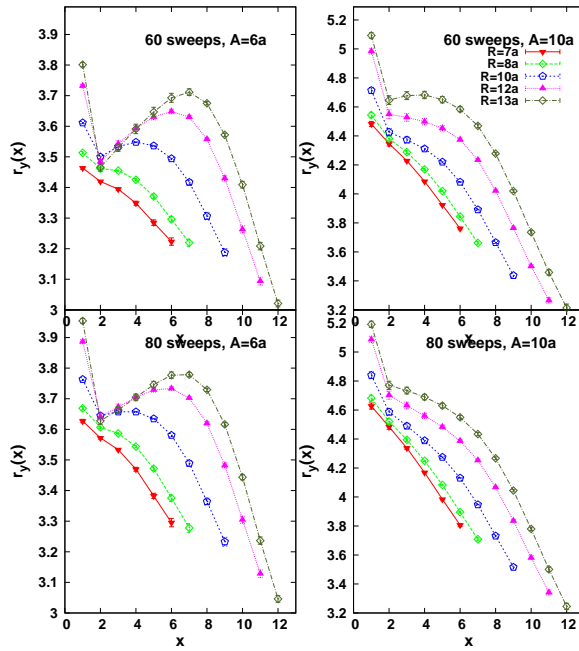


Figure 9.10: Same as Fig. 9.8 for isosceles configuration bases of $A = 0.6$ fm, and $A = 1.0$ fm. The upper and lower figures compare the measured radius profile for two levels of smearing, 60 sweeps and 80 sweeps, respectively. The radius is in lattice units.

of non-uniform action density profiles with position-dependent (local) amplitudes distribution, H_y . One can speculate that the observation of the simultaneous co-existence of both the Y and the Δ aspects of the profile opens the possibility that the ground-state baryon state may exhibit a similar action isosurface behaviour even with the success of the Y -ansatz in the parametrization of the large distance potential. This may be sound plausible especially if we take into account the fact that the gluonic junction broadens with the evolution of Euclidean time in the Wilson loop operator [2]. In addition, non-uniformly UV regulated Wilson loop operators have optimized the ground state overlap at zero-temperature in the mesonic sector [178]. At the same time, and along the line of the above argument, the observation of a Y -shape current distribution following abelian gauge fixing [143] at $T/T_c = 0.8$ should not be taken by as contradictory to the Δ -shaped action density in QCD observed without gauge fixing.

Inspection of the bottom row of the graphs in Fig. 9.8 reveals how thermal effects on the tube's radius profile take place as we get closer to the deconfinement point at $T/T_c = 0.9$. In general, there is an increase in the radius of the flux with the increase of the temperature. The tube's topology is almost the same, with an expansion of the size as we get to wider triangular bases. The radii flatten out through the planes $x \leq 6$ for large quark separations. The change in radius along the x -axis increases also with the increase of the temperature for small quark separations. Minimum growth in the radius for increasing R is noticeably manifesting near the Fermat point of the configurations $x = 1.7, 2.3$ and 2.9 for the isosceles bases $A = 0.6, 0.8$ and 1.0 fm, respectively. Another distinguishable feature for the profile at $T/T_c = 0.9$ is that the radius shows no sign of squeezing at any quark configuration. The increase in energy resulting from the increase of the temperature is now large enough to accommodate the corresponding enlargement in the geometrical area of the triangle set up by the quarks. We focus on detailed aspects of the flux broadening patterns separately in Sec. D.

In addition to the force measurements in Sec. 9.5 taken as a guiding analysis to set a trusted distance scale for each level of smearing, we now report the effects of smearing on the radius profile of the action density along the tube. Fig. 9.10 compares the radii of the flux at each plane x measured on 60 and 80 sweep smeared gauge configurations. The values of the measured radii do not change at distant planes from the isosceles base. Smearing causes a subtle shifting rather than lensing effect on the radius at the planes near the quarks in the base $Q_{1,2}$. An increment of 20 sweeps of smearing from 60 sweeps to 80 sweeps causes a maximum increase of the radius by a subtle factor of 1.04. This effect diminishes as we consider far planes $x > 6$ from the $Q_{1,2}$ quarks on the base.

9.6.3 Flux amplitude profile

At zero temperature, the revealed vacuum structure inside the static baryon constructed via the Wilson loop operator has a maximum vacuum suppression at the center of the triangle made up by the 3Q system at small separations [2]. At large distances, the Wilson loop operator of the minimum spatial string length has been found to minimize the potential [2], indicating a junction position at the Fermat point of the configuration. However, a peak in the action density at zero temper-

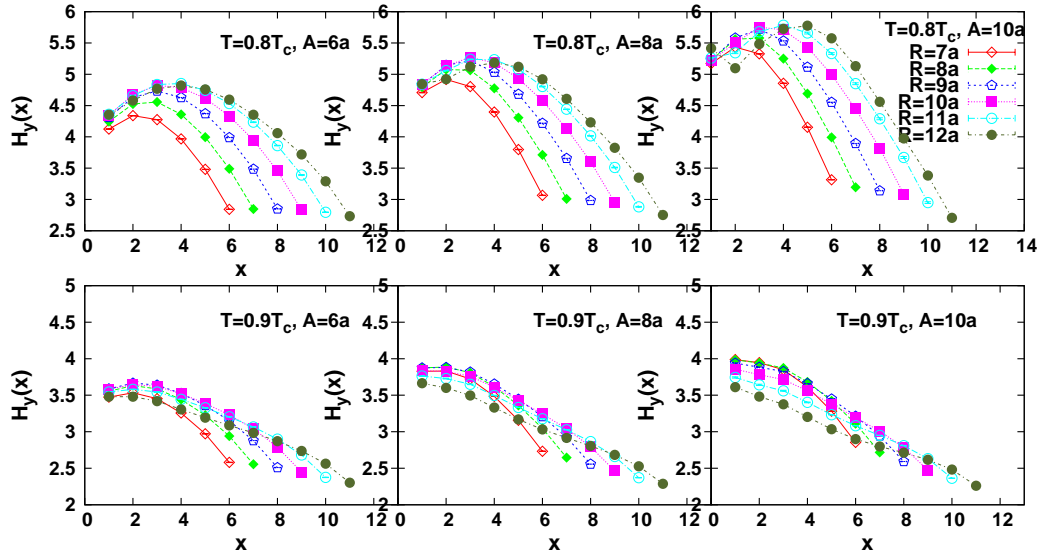


Figure 9.11: The profile of the action density amplitude, $H_y(x_i)$ (scaled by a factor of 10^1) for each isosceles configuration with base $A = 0.6$ fm, $A = 0.8$ fm and $A = 1.0$ fm, for the two temperatures $T/T_c = 0.8$ (upper), $T/T_c = 0.9$ (lower). The legend signifies the third quark position.

ature does not manifest but rather the distribution assumes a constant amplitude. The analysis performed here for the density distributions using Polyakov lines as hadronic operators, nevertheless, reveals density amplitude peaks which manifest at short as well as large source separation distances. In this section, the amplitude profile is investigated and contrasted for the two considered temperatures.

Tables 9.2 and 9.4 summarize the measured amplitudes, $H_y(x)$, in accord with the Gaussian fits of Eq. (9.6.3). The corresponding plots are shown in Fig. 9.11, for the isosceles configurations with base $A = 0.6$ fm, $A = 0.8$ fm and $A = 1.0$ fm at two temperatures $T/T_c = 0.8$ (top row) and $T/T_c = 0.9$ (bottom row), respectively. At all considered planes, the height of the distribution $H_y(x)$ decreases with the increase of the temperature, which reciprocates the changes of the radius of the flux with the temperature. The decrease of the distribution height together with the associated increase in the distribution moment indicates the spread of the gluonic energy with the increase of the temperature.

At $T/T_c = 0.8$, the amplitude also increases at most planes when moving the third quark Q_3 farther from the base of the isosceles configuration. Recalling the corresponding decrease in the radii along the x-axis, one infers the gluonic behaviour undergoes a localization rather than a decay of the flux tube. The amplitudes at $T/T_c = 0.9$ show similar increase up to small quark separation. However, a noticeable turnover to decreasing amplitude with the increase of the third quark Q_3 separation manifests for $R \geq 10a$. The behaviour of the amplitude and radius at $T/T_c = 0.8$ resembles, respectively, the behaviour of the radius and amplitude at $T/T_c = 0.9$. The analysis of the flux amplitude shows different qualitative behaviour as we transit from the end of the QCD plateau to just before the deconfinement point

and this behaviour is reciprocal to the radius profile, indicating a delocalization of the gluonic distribution with the increase of the temperature and the subsequent decrease in the string tension.

In addition to the position of the amplitude maximum along the x -axis at $y = 0$ and the corresponding trigonometric aspects of the triangular setup. The maxima localize around the second and third planes $x = 2, x = 3$, for third quark Q_3 separations $R < 10a$. However, this localization of the maxima of the vacuum suppression around the Fermat points ceases as the third quark is pulled away further. The density maximum moves in the same direction of third quark at $T/T_c = 0.8$ and moves in the opposite direction (towards the triangle base) for the higher temperature $T/T_c = 0.9$.

9.6.4 The broadening of the flux width

In this section, we focus on the broadening aspects of the mean-square width of the flux. We restrict our analysis to the mean square width in the 3Q plane at the two considered temperature scales. The lattice data for the mean square width, $r_y^2(x_i)$, at planes x_i along the x -axis are summarized in Tables 9.3 and 9.5. For convenience, we have considered the tube's width for an analysis performed on gauge configurations of 80 sweeps of smearing, where we obtain the best signal to noise ratio with only a relatively small elimination of short distance points which are affected by smearing.

In the last section, we reported the effects of gauge-smoothing on the radius of the gluon flux. Smearing shifts the width by a subtle constant near the base of the isosceles triangle, as in Fig. 9.12. This shift diminishes at distant planes from the base. To further examine the rate of broadening of the flux distribution, we fit the mean square width to the simple linear ansatz

$$r_y^2(R; x_i) = b_1(x_i) R + b_2(x_i) \quad (9.6.5)$$

Table 9.6: The slope of the growth in the mean square width, r_y^2 , measured for isosceles base $A = 1.0$ fm on two levels of link smearing. The measurements are obtained from the fits to the linear form Eq. (9.6.5).

n_{sw}	b_1	Fit range Ra^{-1}
x=2		
60	0.76(4)	4-13
80	0.83(3)	4-13
x=7		
60	2.3(1)	8-13
60	2.8(2)	10-13
80	2.2(1)	8-13
80	2.5(1)	10-13

The returned values of the slope of the growth in the flux width with the increase of the isosceles height, R , display small systematic errors associated with the selection of parameters as indicated in Table 9.6.

The profile of the broadening of the glue at various planes, the for isosceles base, $A = 0.8$ fm, is plotted in Fig. 9.13 with a similar plot for, $A = 1.0$ fm, in Fig. 9.14, respectively. Each set of data describes how the width of the gluonic flux vary at a given plane x_i for the triangle base as the third quark Q_3 moves to larger values of R . Evidently, the increase of the temperature dramatically increases the rate of the broadening of the glue at all planes.

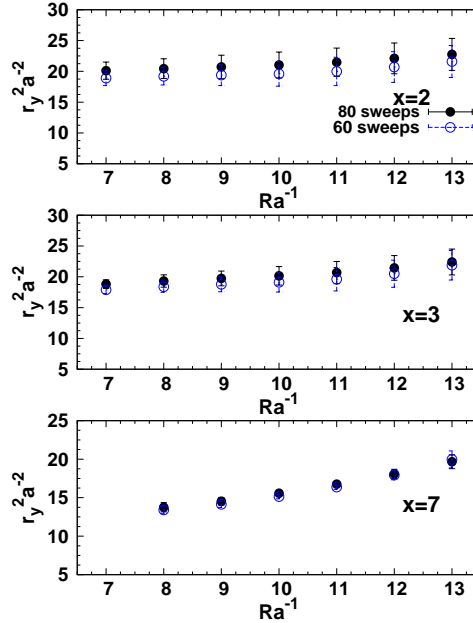


Figure 9.12: The squared flux distribution width at the depicted planes, $x_i = 2, 3$ and 7 , are compared for two smearing levels. The isosceles configuration base length is $A = 1.0$ fm at temperature $T/T_c = 0.9$. Smearing merely shifts the profile by a constant. The broadening pattern is not affected.

Apart from the pronounced thermal effects near the deconfinement point, we see the rates of broadening at $T/T_c = 0.8$ are decreasing as one proceeds to the more distant planes from the base of the triangle. Moreover, the wider the base of the isosceles triangle, the more pronounced is the corresponding decrease in the width, indicating that the gluonic tend to become more localized as the geometrical area enclosed by the quarks positions becomes larger.

The shrinking of the width of the flux tube is a peculiar property of certain geometrical configurations of the Multi-quark system. The decrease in the width with the increase of the inter-quark separation has never been observed in the meson either using Polyakov lines at finite temperature [158] or Wilson's loop at zero temperature [63]. The analysis of the Wilson loop based energy distribution at zero temperatures does not seem to indicate shrinking of the width of the flux tube [2].

Near the deconfinement point, the broadening of the mean square width, r_y^2 , exhibits a clear linear divergence at distant planes from the base of the isosceles triangle for large separations, $R > 1.0$ fm of the third quark Q_3 . This result resembles the observed linear growing in the flux distribution width at the same temperature in the meson [135]. The slope of the growing width at distant planes from the base,

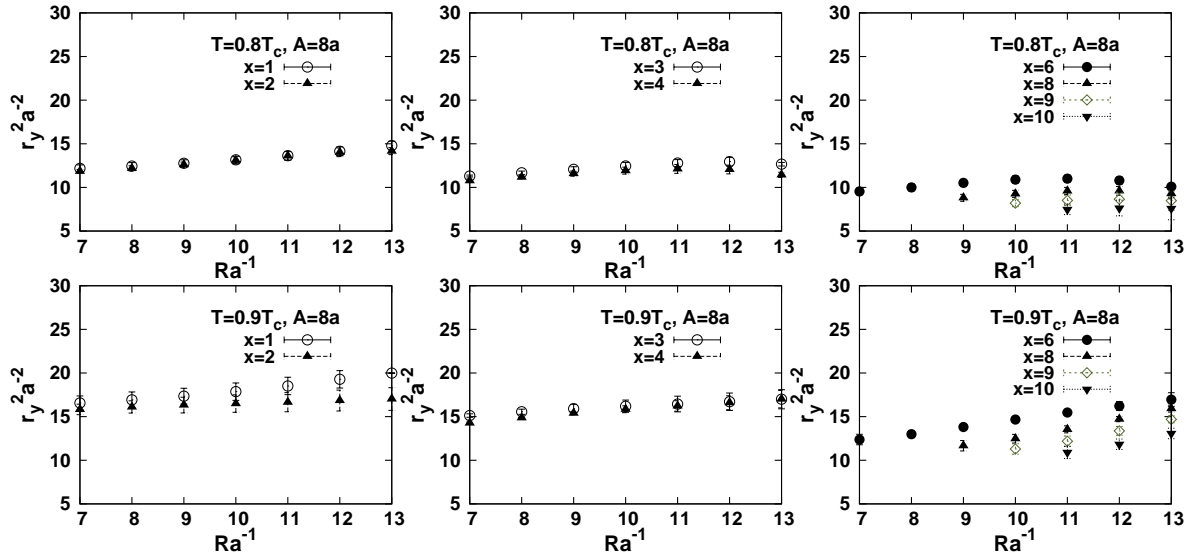


Figure 9.13: The squared flux-tube width at the depicted planes for the isosceles configuration $A = 0.8$ fm compared at two temperatures $T/T_c = 0.8$ (top) and $T/T_c = 0.9$ (bottom). The plane coordinates are indicated in the legend.

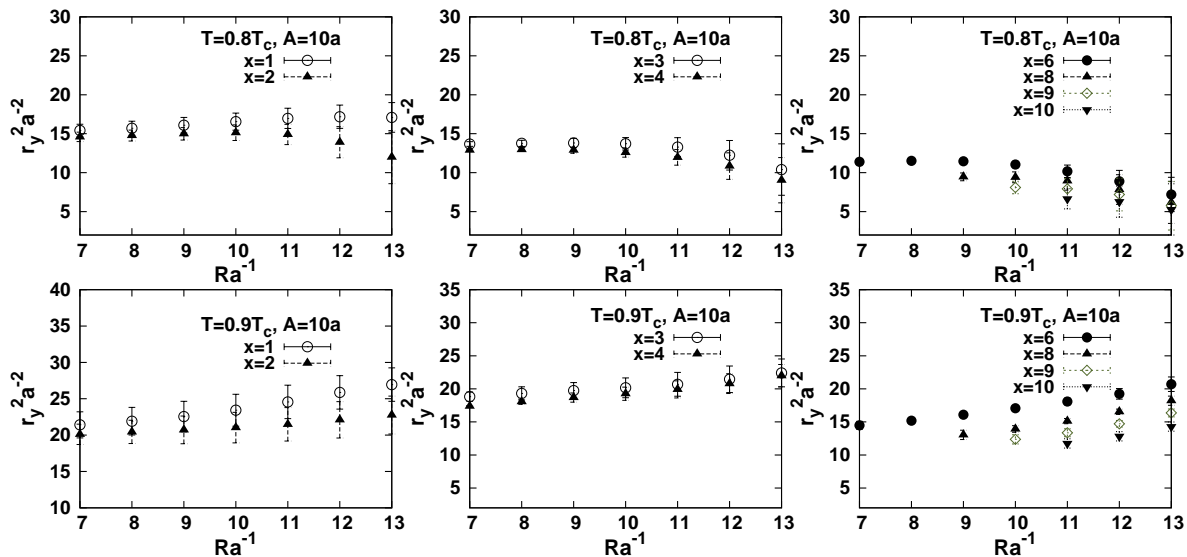


Figure 9.14: Same as Fig. 9.13 for a larger isosceles base length of $A = 1.0$ fm.

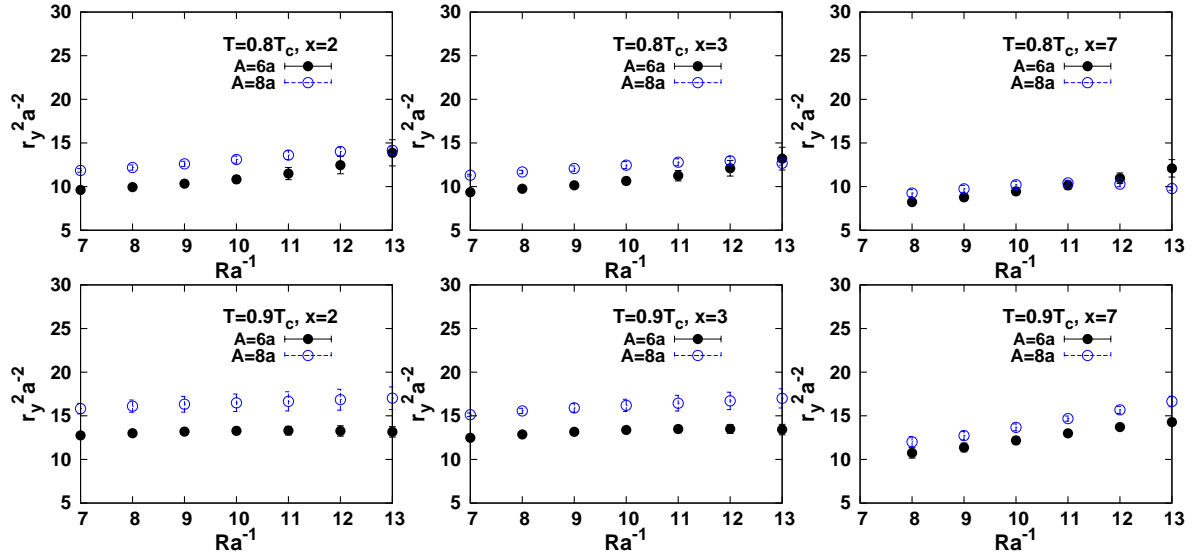


Figure 9.15: Comparison of the mean square width of the flux distribution at three distinct planes, $x = 2, 3$, and 7 , for two isosceles bases $A = 0.6$ fm and $A = 0.8$ fm. The upper graphs show the comparison at $T/T_c = 0.9$ whereas the lower are at $T/T_c = 0.8$.

$x > 6$, from plane to plane show only subtle changes. This indicates that the effects of the boundary and the junction fluctuations decays away by proceeding to large quark separations. Fig. 9.15 displays the effects of increasing the distance between the two quarks $Q_{1,2}$ on the rate of change of the width versus the motion of the source Q_3 . At $T/T_c = 0.9$ the wider the base the faster the rate of growth. This behaviour is the reciprocal of the corresponding one at $T/T_c = 0.8$.

9.6.5 Planes aspect ratio

The gluonic flux in the 3Q system does not exhibit a symmetry between the width measured in the quark plane and that in the perpendicular direction. This is related to the underlying gluonic structure and the associated fluctuations. For example, the string picture indicates an asymmetry in the mean square width between the two planes [134]. We report for completeness the general qualitative features of this ratio of the action density in the two perpendicular planes. The width of the tube in the perpendicular direction is measured through Gaussian fits as

$$r_z^2(x_i) = \frac{\int dz z^2 \mathcal{C}'(\vec{\rho}(x_i, 0, z))}{\int dz \mathcal{C}'(\vec{\rho}(x_i, 0, z))}. \quad (9.6.6)$$

We measure the ratio between the width in the quark plane and that in the perpendicular plane to the quarks

$$\alpha(x_i) \equiv \frac{r_x^2(x_i)}{r_z^2(x_i)}. \quad (9.6.7)$$

It is interesting to consider this quantity since the predictions of the string model at zero temperature indicate asymmetric width pattern near the junction [134]. In a similar way to the characteristics of the flux that we have studied in the previous sections, we plot in Fig. 9.16 the aspect ratio at the two temperatures for the same quark position configurations.

Generally, the value of the aspect ratio indicates that the fluctuations in the quark plane are always larger than the perpendicular fluctuations for both temperatures. Further inspection of Fig. 9.16 shows only subtle dependence on the temperature for the small isosceles bases. The aspect ratio is changing slowly as we move through the planes up to the third quark position for the smallest isosceles bases. However, at larger bases the asymmetry throughout the gluonic cone becomes pronounced. The results of the aspect ratio indicate greater restoring forces for the gluonic distribution in the perpendicular direction to the quark plane. This effect diminishes as we consider planes away from the Fermat point of the triangle quark configuration. Near the deconfinement point $T/T_c = 0.9$, the aspect ratio increases with the base length showing only a subtle dependency on R . This behaviour is reversed at the lower temperature $T/T_c = 0.8$ for large quark separation. Indeed we see at $T/T_c = 0.8$, for the bases $A = 0.8$ fm and $A = 1.0$ fm, a decrease in the aspect ratio at all planes with the increase of the third quark separation $R > 1.0$ fm.

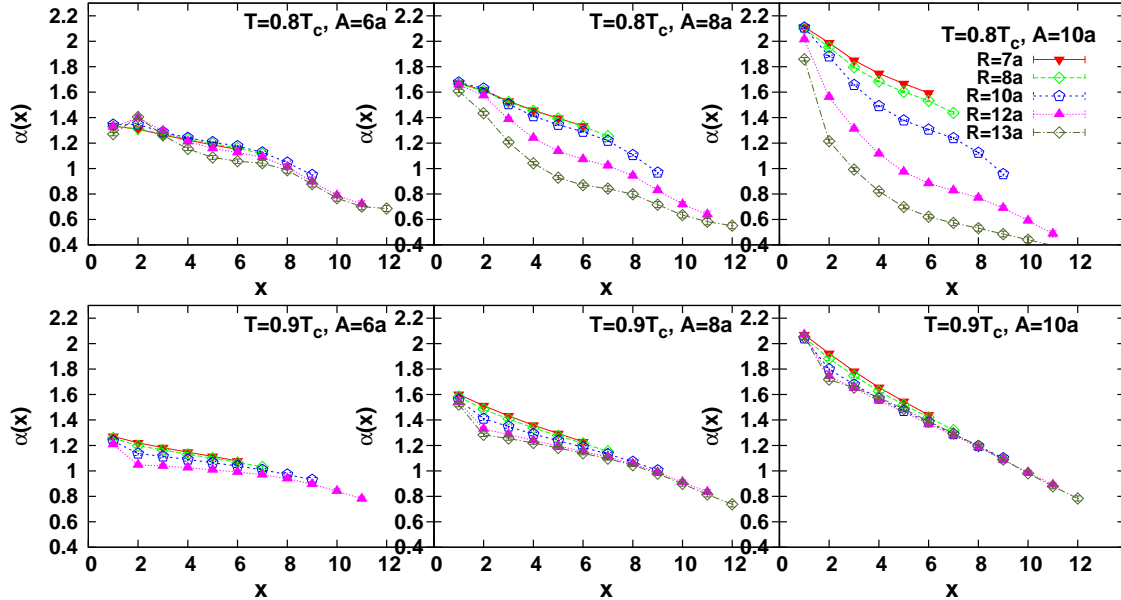


Figure 9.16: Comparison of the ratio, α (Eq. (9.6.7)), of the mean squared width of the flux distribution parallel and perpendicular to the quark plane for three isosceles bases $A = 0.6$ fm, $A = 0.8$ fm and $A = 1.0$ fm. The upper graphs show comparison at $T/T_c = 0.8$ whereas the lower are at $T/T_c = 0.9$.

Within the underlying gluonic picture of three squeezed string-like flux tubes meeting at a junction and assuming a Y-shaped form, the predictions of this string model for the ratio of the mean square width of the flux distribution in the quark

planes and the perpendicular direction at position of the junction has been worked out in Ref. [134]. However, one should carefully consider the geometrical aspects of the configuration and take into account any remnant ($T/T_c = 0.8$) or pronounced ($T/T_c = 0.9$) thermal effects before pursuing a complete confrontation with the predictions of the baryonic bosonic string models. We included the thermal effects [186] into the predictions that have been worked out earlier in Ref. [134]. However, this comparison of the lattice data with the predictions of the models lies beyond the scope of the present presentation of the gluonic profile, and will be reported in details elsewhere [187].

Finally, it is worth noting that the flux strength distribution revealed with the action density using the Wilson loop does not appear to produce an asymmetric gluonic pattern. For instance, in Ref. [2] the radius of the tube is calculated with cylindrical coordinates assuming a cylindrical symmetry of the tube. The analysis provided here for the aspect ratio of the mean-square width provides another distinct feature of the glue, as revealed by Polyakov loops rather than a manifestation of temperature effects.

9.7 Delocalization of the junction

The strong coupling results [130, 131, 132] indicate that the Y-ansatz is the most relevant in the IR region. This is also consistent with the dual superconductivity picture of the QCD vacuum. Three strings with a junction whose equilibrium position is at the Fermat point are preferred. The consequence of this picture has been elucidated at both the level of the potential [133] and the mean square width of the delocalized junction at zero temperature [134]. The relevant string effects in the baryon at finite temperature are yet to be investigated.

At zero temperature, a gluonic Y-shaped profile is formed with a ground state configured such that the length of the flux tube [2] is minimal. In contrast, the revealed flux distribution for the considered planar configurations, at finite temperature, did not exhibit a formation of three separate flux tubes of almost constant width and uniform density profile that meet at a junction whose position is determined by the requirement of minimizing the total flux-tube length. The observation of a filled delta-shaped gluonic distributions with non-uniform density distribution (varying amplitudes), nevertheless, do not necessarily exclude or contradict that the true underlying gluonic picture might consist of three string-like flux tubes connected at the Fermat point. For example, in the last section we found that the radius of the tube in the quark plane shows an underlying Y -shape for some quark configurations which is characteristic of the zero temperature Y shapes. This strongly suggests that the observed Δ shapes of the action iso-surface come about through the vibration of an underlying Y -shaped Baryonic string. Indeed, Fig. 9.17 exposes the underlying Y -shape rather well.

In Chapter 4 we rederived an expression for the junction's perpendicular and parallel profiles for a system of three bosonic strings whose classical configuration coincides with the ground state of the corresponding zero temperature three quark system. The thermal effects have been included using a consistency framework between two string actions; the string action which represents one whole complete

string and string action that is obtained by dividing the string into two with a junction mass in the middle. This resulted in expressions for the junction fluctuations in the quark plane. In particular, parallel fluctuations give rise to the mean-square width of Eq. (4.4.29).

In this section, the broadening of the flux tube with the increase of the source separation is compared to the corresponding string model predictions of Eq. (4.4.29). This can provide a first indication of the compatibility of our proposed finite-temperature baryonic string model with the measured LGT junction profile, the position of the junction and its proposed insight.

The analyzed lattice gauge data for the flux tube mean square width in the 3Q plane for isosceles triangle configurations display the property of having a fixed position of the Fermat point (the point that minimize the length of the flux tube) and is given by $R = A/(2\sqrt{3})$. The position of the Fermat point is fixed by the length of the base of the isosceles triangle and is not affected by the height of the triangle, i.e. the position of the third quark. Considering this planar quark set up results in a great simplification the study of the baryonic junction on the lattice. As illustrated in Fig. 9.18, the baryonic blades of length L_1, L_2, L_3 are measured from the position of the junction.

As we have discussed in Chapter 4, the string model parameter introduces a constant shift to the profile of the flux-tube mean square width. For convenient optimization, we have provided Eq. (4.4.26) and Eq. (4.4.29) in a two parameter form

$$\begin{aligned}\langle \varphi_{\parallel}^2 \rangle &\rightarrow \langle \varphi_{\parallel}^2 \rangle + \mu_1, \\ \langle \varphi_{\perp}^2 \rangle &\rightarrow \langle \varphi_{\perp}^2 \rangle + \mu_2,\end{aligned}\tag{9.7.1}$$

by shifting the parameter $m \rightarrow k$. The formulas of Eq. (4.4.26) and Eq. (4.4.29) account for the tube's mean-square width in the parallel and perpendicular directions to the 3Q plane, respectively. In the present work we restrict our analysis to the width parallel to the 3Q plane. The measured lattice data are fit to the string model formula Eq. (4.4.29). The position of the Fermat point for isosceles configurations $A = 6a$ is $x_F = 1.7$, $x_F = 2.3$ for that of a base length $A = 8a$. Assuming the junction lies at the Fermat point of the configuration, this entails taking the length of the blade L_3 related to the third quark position as $L_3 = R - x_F$. We fit the string model formula Eq. (4.4.29) to the measured mean square width at the three planes $x = 1$, $x = 2$ and $x = 3$. The returned value of the fit parameters k and μ_1 in addition of the corresponding values of the χ^2 are summarized in Tables 9.7, 9.8 and 9.9.

The returned values of the χ^2_{dof} for the isosceles base $A = 0.6a$ indicate the acceptable fits to the string model formula are for plane quark separations $R \geq 0.6$ fm for each corresponding plane. The string model formula fits the lattice data well for distances $R \geq 0.6$ fm reflecting the applicability of the string picture only at large quark separations. Recalling that the Fermat point of this particular configuration lies at $x \approx 1.7$, this is the only plane where Eq. (4.4.29) can be expected to describe the data well. We conclude that the string picture of the formation of three thin flux tubes that meet at the point that minimize the length of the flux tube is compatible with the lattice data at $T = 0.9 T_c$.

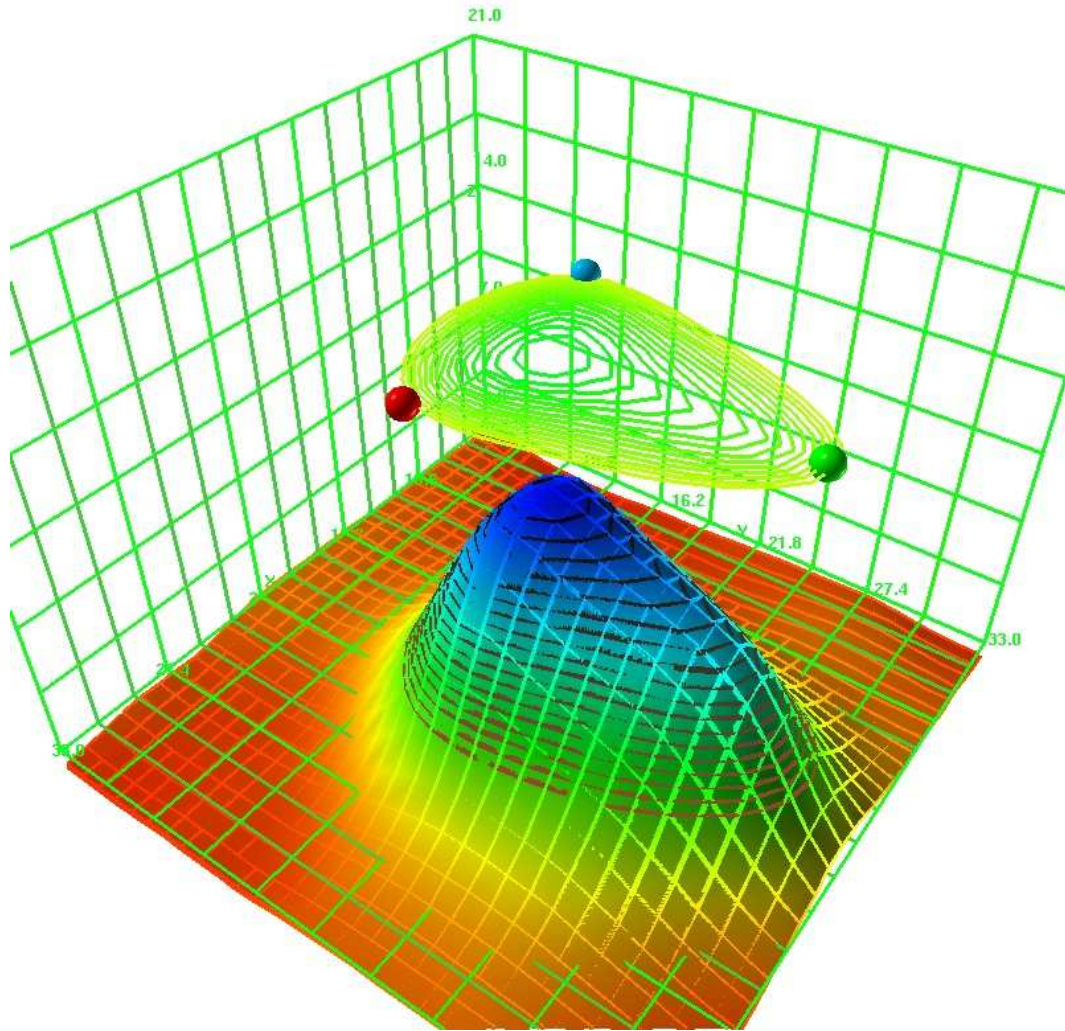


Figure 9.17: Surface plot of the flux density surface in the quark plane, $\rho(x, y, z = 0)$, together with contour lines. The contour lines are projected onto the surface plot. The density of the contour lines increases near the edges in accord with the gradient of the density scalar field along the x -axis. The flux contours of the maximum value are the inner most lines inside the triangle. As the density plot illustrates, the flux-tube configuration is a filled Δ -shape with maximum action expulsion inside the triangle near the Fermat point of the configuration. These measurements are taken for an isosceles quark geometry of base $A = 0.8$, height $R = 1.2$ fm and temperature $T = 0.9 T_c$.

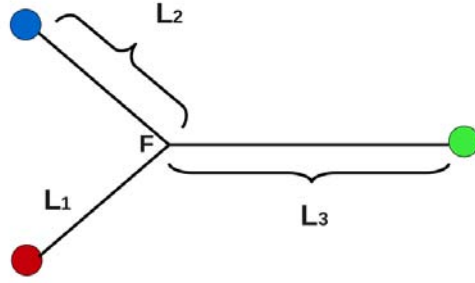


Figure 9.18: Schematic diagram for the isosceles configuration of the 3Q system. L_1 , L_2 and L_3 are distances from the Fermat point to the quark positions.

Table 9.7: The returned fit parameters of formula Eq. (4.4.29) and the corresponding χ^2_{dof} for the width of the flux tube of the isosceles 3Q configuration with the base $A = 6a$, at the plane $x = 1$, $T = 0.9T_c$. The fit range describes the values of the third quark position, R , considered in the fit.

Fit range	χ^2	χ^2_{dof}	k	μ_1
4-09	10.3	2.57	0.0110	2.061
4-10	24.14	4.82	0.0113	2.104
4-11	58.47	9.74	0.0112	2.225
4-13	140.76	17.59	0.0111	2.397
6-13	117.24	19.54	0.0105	2.638
7-13	92.47	18.49	0.0103	2.801
8-13	67.49	16.87	0.0101	2.979

Table 9.8: The same as Table 9.7 for base $A = 6a$, and plane $x = 2$, $T = 0.9T_c$.

Fit range	χ^2	χ^2_{dof}	k	μ_1
4-9	9.11	2.27	0.01092	1.602
4-10	10.65	2.13	0.01106	1.587
4-11	11.30	1.88	0.01109	1.587
4-13	11.45	1.43	0.01110	1.588
6-13	7.02	1.17	0.01103	1.639
7-13	2.65	0.53	0.01079	1.740
8-13	0.83	0.21	0.01345	1.400

Table 9.9: Same as above tables for base $A = 6 a$, and plane $x = 3$, $T = 0.9 T_c$.

Fit range	χ^2	χ^2_{dof}	k	μ_1
4-9	23.09	5.77	0.11745	1.194
4-10	37.56	7.51	0.01165	1.297
4-11	45.20	7.53	0.01158	1.351
4-13	50.05	6.25	0.01153	1.393
6-13	28.98	4.83	0.01082	1.651
7-13	13.01	2.60	0.01052	1.811
8-13	4.05	1.01	0.01031	1.951

Table 9.10: Same as above tables for base $A = 8 a$, and plane $x = 1$, $T = 0.9 T_c$.

Fit range	χ^2	χ^2_{dof}	k	μ_1
4-13	47.85	5.98	0.0117	5.614
6-13	41.71	6.95	0.0111	5.824
7-13	33.81	6.76	0.0110	6.076
8-13	24.47	6.11	0.0107	6.381

Table 9.11: Same as above tables for base $A = 8 a$, and plane $x = 2$, $T = 0.9 T_c$.

Fit range	χ^2	χ^2_{dof}	k	μ_1
4-09	4.04	1.01	0.00316	6.815
4-10	5.12	1.03	0.00370	6.598
4-11	6.23	1.04	0.00419	6.405
4-13	8.92	1.12	0.00511	6.070
5-09	1.19	0.39	0.01295	3.896
5-10	1.74	0.44	0.01279	3.937
5-11	2.42	0.48	0.01264	3.976
5-13	4.90	0.70	0.01234	4.070
6-13	3.65	0.61	0.01168	4.259
7-13	1.97	0.39	0.01121	4.457
8-13	0.98	0.25	0.01089	4.626

Table 9.12: Same as above tables for base $A = 8a$, and plane $x = 3$, $T = 0.9T_c$.

Fit range	χ^2	χ^2_{dof}	k	μ_1
5-9	20.54	6.84	0.01331	2.899
5-10	29.75	7.44	0.01314	2.935
5-11	39.37	7.87	0.01326	2.965
5-13	69.97	9.99	0.01179	3.464
6-13	44.44	7.41	0.01126	3.899
7-13	21.03	4.21	0.01088	4.301
8-13	7.907	1.98	0.01272	3.034

Tables 9.10, 9.11 and 9.12 summarize the returned fit parameters for the isosceles configuration with base $A = 8a$. The values indicate also the smallest χ^2_{dof} occurs at the plane $x = 2$ which is the closest plane to the Fermat point of this configuration i.e $x_F = 2.3$. With the larger base $A = 0.8$ fm, smaller values of R provide acceptable fits. This time $R = 0.4$ fm is acceptable.

9.8 Conclusion

The gluon flux distribution of a three quark system in pure SU(3) Yang-Mills vacuum has been revealed at finite temperature. This analysis is an extension of the calculations of the action density correlations obtained recently for the $Q\bar{Q}$ [158] system to three quark systems. The infinitely heavy baryonic state has been constructed by three Polyakov loops. The gluon flux is measured as a correlation between the action density operator and three traced (gauge-invariant) Polyakov lines. Measurements have been taken near the end of QCD phase diagram, $T/T_c \approx 0.8$ and just before the deconfinement point $T/T_c \approx 0.9$.

We have revealed the characteristics of the flux action-density measured for three sets of geometrical 3-quark configurations and the corresponding changes on the behaviour due to the temperature. Each set corresponds to isosceles triangle bases of length $A = 0.6$ fm, $A = 0.8$ fm and $A = 1.0$ fm. The characteristics of the isosurface, the radius and the amplitude profiles of the action density correlations, in addition to the broadening (or the shrinking) pattern of the flux distribution, can be summarized in the following main points:

A. The iso-surface of the flux action-density displays a family of concave Δ shapes at small as well as large quark separations. These Δ -shaped gluonic distributions persist and do not change into a Y-shape as the distances between the quark sources are increased. The density plots in the quark plane display a nonuniform distribution at all distance separations. This contrasts with the Wilson loop results at zero temperature which exhibit uniform action density along each arm of the Y-shaped profile. A remarkable feature of the revealed map of the contour lines of the flux strength is that the shape of the contour lines do not show significant sensitivity to

the temperature for the two temperatures considered here.

B. The radius profiles give indications on the spread of the energy inside the baryon. At the lowest temperature near the end of the plateau, $T/T_c = 0.8$, the measurements of the radius indicate localization of the action density in narrow regions for quarks separations greater than 1.0 fm. The radius of the tube decreases and draws a Y-shaped like profile even though the action isosurface and isolines are Δ shaped. Near the deconfinement point, on the other hand, the energy tends to spread as we see the radius increases at all considered distance scales.

C. The amplitude profile analysis of the flux density shows a maximum vacuum fluctuations suppression at the plane nearest to the Fermat point of the planar three-quark configurations for intermediate separation distances. The distribution's peak ceases localizing around the Fermat point of the 3Q isosceles configurations when the height, R , is greater than 1.0 fm. The peak shifts to the outside of the triangle made at $T/T_c \approx 0.9$ and shifts in the reverse direction to the inside of the triangle for $T/T_c \approx 0.8$. That is, the amplitude gets higher when the radius shrinks at $T/T_c \approx 0.8$ and the reverse is manifest at $T/T_c \approx 0.9$.

D. The flux mean-square width does not always broaden with the increase of the quark source separation as is the case in the meson. For the lowest temperature, $T/T_c \approx 0.8$, the flux distribution shrinks in width for large quark separations. The change in the width of the flux tube shows a non-broadening aspect which is a property of certain configurations of the multi-quark system. The width, however, grows linearly near the deconfinement point, $T/T_c \approx 0.9$, with the increase of the height of the triangle. In general, the slope of the decrease or increase in the width, at both temperatures, depends on the length of the triangle base. The wider the base of the triangle set up by the quarks positions, the lower or higher is the slope at temperatures $T/T_c = 0.8$ and $T/T_c = 0.9$, respectively.

E. The aspect ratio between the mean square width of the flux distribution in the quark plane and the width in the perpendicular plan exhibits an asymmetry. The gluonic fluctuations in the plane of the quarks are greater than that in the perpendicular directions around Fermat point, indicating a greater restoring force for the system in the plane of the quarks. The ratio between the two components of the mean square width decreases as we consider planes further from the locus of the Fermat point of the quark configuration. The temperature dependence for the aspect ratio is more pronounced at large quark separations while we see almost the same profiles for small isosceles bases. The deviation of the aspect ratio from unity is implied by the predictions of the string models and does not manifest using Wilson loop operator in the action correlations.

F. The profile of the junction

We compared the growth of the mean square width of the flux tube measured on the lattice with our finite-temperature extension of the baryonic string model for the width of the baryonic junction. The string model formula fits the lattice data well for the mean square width in the plane of the quarks for transverse planes near

the Fermat point of the considered configurations.

Future work

To the best of our knowledge, this is the world's first work presenting a detailed investigation of the flux distribution of the 3Q system at finite temperature. There are many promising avenues of investigation remaining. For example, additional quark configurations could be examined in detail. Lower temperatures remain to be investigated. We compare [187] the growth of the mean square width of the flux distribution measured on the lattice with finite-temperature extensions of the baryonic string model [186, 187] for the width of the baryonic junction [134]. We can also study the relevant ansatz for the measured potentials at each temperature. Methodological improvements based on increasing the number of measurements and decreasing the number of gauge smoothing sweeps are always desirable. The method pursued here may prove effective in a calculation framework that includes the effects of the dynamical quarks.

Chapter 10

Summary and Conclusion

In this work, I studied the profiles of the gluonic flux distribution in both mesons and baryons in pure Yang-Mills theory at finite temperature. The obtained lattice gauge theory results are then compared to predictions of bosonic string models for the flux-tube profile at finite temperature.

As introductory material for this investigation, the theory of measurements for the gluonic distributions and the consequent construction of the quark states by means of Wilson loop and Polyakov line operators have been reviewed. The use of the Wilson loop approach introduces systematic errors due to the bias of the shape of the gluonic source. Polyakov loop correlators provide an unbaised set of operators that can be used to construct static mesons and baryons. Polyakov loop correlators are well known, however, to suffer from a bad signal to noise ratio. The loop operator is exponentially suppressed with the increase of the separation distance between the sources and the temporal extent of the lattice. This brings us inevitably to study the gluonic distribution in lattices of short temporal extents. Consequently, this leads to the study of the thermal effects on the profile of the glue.

The low-energy dynamics of the flux-tubes in the infrared region of a confining gauge theory can be understood in terms of an effective bosonic string. The thin flux-tube between two widely-separated static color sources fluctuates like a massless string. The predictions from bosonic string models for the mean square width of the flux tube and the potential on both the baryonic and mesonic levels have been reviewed. The extension of the baryonic string model for the mean-square width of the baryonic junction to finite temperature is proposed. The string model predicts a temperature-dependent string tension and hence a decrease of the slope of the linearly rising potential. Also, the string model predictions of a logarithmic broadening for the width of the string delocalization dramatically changes into a linear growth for large separation distances before the deconfinement temperature is reached from below.

The string picture predicts geometrical effects on the profile of the flux tube. The mesonic string picture implies a curvature in the gluonic profile that becomes more pronounced as higher temperatures are approached. The string self-interaction with the quark line causes a noticeable difference in the delocalizations beyond the central transverse plane. The focus of this thesis is to ascertain these features using the lattice approach.

Link smearing techniques can be used to enhance the signal to noise ratio in the

gluonic flux strength function. Nevertheless, link smearing results in a loss of short distance physics and one has to be careful when extracting the correct physics at each distance scale. We have been able to show the ranges of validity of this noise reduction technique by studying the effects of gauge field smearing on Polyakov loop correlators. We find that the physical observables are left intact for measurements carried out on distance scales larger than the diameter of the Brownian motion of a diffused link. Link-integration is also a popular method for noise reduction that is powerful at short distance scales. Link integration methods have, however, the advantage of preserving the transfer matrix interpretation which allows one to identify the Polyakov loop correlators as the exponential function of the potential. This method has been employed when studying the effects of filtering out the UV fluctuations of the gauge theory on the quark–antiquark potential. Through this work, gauge-field smearing is chosen as a cheap and effective method to reveal the general topological features of the flux distribution which can be compared with the predictions of the string model. The distance scales for which this approach is valid has been studied, through the measurements of the physical observables on the level of the potential and also the action density.

The distribution of the gluon action density in mesonic systems is revealed at finite temperature. The simulations are performed in pure Yang-Mills theory for two temperatures below the deconfinement phase. Unlike the gluonic profiles displayed at $T = 0$, the action density iso-surfaces display a prolate-spheroid like shape. The flux tube, characterized as a correlation between the action-density and the mesonic operator (Polyakov-lines), has been displayed up to distances of 1.4 fm. The flux iso-lines and iso-surfaces display a curved profile along the tube. The profile is showing a non-uniform action-density pattern unlike that observed using Wilson’s loop as a mesonic operator at $T = 0$. At $T = 0.9 T_c$ the flux tube width profile is compared to the corresponding mean-square width of the free bosonic string fluctuations at all planes between the color sources. For source separation distances $R > 0.8$ fm, measurements of the tube cross-section at each selected transverse plane show a non-constant width for the tube, with maximum width at the symmetry point of the tube. At $q\bar{q}$ source separations $0.8 \text{ fm} < R < 1.1 \text{ fm}$, the tube is seen to yield a more compact (squeezed) form than the string model would predict. The deviations of the tube width profile from the corresponding string profile decrease gradually as the source separation increases. The profiles compare well at $R \geq 1.2$ fm. The curved width profile of the flux-tube is found to be consistent with the prediction of the free bosonic string model at large distances and finite temperature.

In the intermediate source separation distance, the free string picture poorly describes the flux tube width profile. Our focus is to elucidate the role of high-energy vacuum fluctuations which are filtered using an improved smearing algorithm. We find that the topological characteristics of the flux-tube converge and compare favourably with the predictions of the free bosonic string upon reducing the vacuum action towards the action minimum or the classical instanton vacuum. This result establishes a connection between the free string action and vacuum gauge fields and reveals the important role of higher energy fluctuations in understanding the lattice data at this temperature scale. As a byproduct of these calculations, we find the broadening of the QCD flux tube to be independent of the UV filtering at large distances. Our results exhibit a linearly divergent pattern in agreement with the

string picture predictions. The analysis performed at short distances provides an extension of the QCD vacua where the free string picture is of utility. This result complements the recent research [138, 139, 140] which includes effects of higher order-self interactions to the free action to match lattice results.

The investigation of the flux-tube profile in the finite-temperature regime of QCD has revealed action-densities of non-uniform distribution along the flux-tube. The action density displays a two dimensional Gaussian-like profile and isosurfaces of a curved prolate spheroid-like shape in the intermediate source separation distance region $0.6 \leq R \leq 0.9$ fm. This has been observed near the deconfinement point $T \approx 0.9T_c$ and remains manifest at the temperature $T \approx 0.8T_c$ close to the end of the plateau region of the QCD phase diagram. The measurements of the tube's mean square width profile indicate, however, only a small variation in the width. Variation in the amplitude gives rise to curved isosurfaces. At larger distances, the tube changes width along the $q\bar{q}$ plane and this width profile is predicted by the free bosonic string picture.

The gluonic distributions obtained at finite temperature by correlating two Polyakov lines constitute an interesting source of knowledge for investigating the possibility that non-uniform densities provide the true geometry of the ground state in the static meson at $T = 0$. The viability of considering finite temperature results as an indication for the field distribution of the system's ground state can be justified by arguing also that the change in the string tension is small, about 10% at $T \approx 0.8T_c$. Moreover, the free bosonic string model predicts observable edge-effects at zero temperature for the width profile of the tube of $\frac{1}{\pi\sigma} \log \left| \cos\left(\frac{\pi\xi}{R}\right) \right|$, $\xi \in [-R/2, R/2]$. The success of the string picture in accounting for the flux-tube curvature at high temperature at large distances is remarkable, and one may investigate such effects at zero temperature.

Apart from the string's width effects, a non-uniform action density amplitude pattern along the tube has been observed at finite temperature, whether the tube exhibits a non constant width profile or not. This leads us to investigate the overlap of the ground state meson potential with sets of mesonic-trial wave functions corresponding to a variety of gluonic distributions with transverse profile. We probe the transverse structure of the flux tube through the creation of non-uniform smearing profiles for the string of glue connecting two color sources in Wilson loop operator at $T = 0$. The non-uniformly UV-regulated flux-tube operators are found to also provide strong overlap with the ground state. These results support the possibility that the true ground state flux-tube is not uniform but rather has a curved flux strength profile larger in the middle with greater action-density suppression.

Extending the analysis to the static baryon reveals a delocalization of the baryonic node in the Y-shape gluonic configuration observed at zero temperature. At finite temperature, filled delta-shaped action iso-surfaces are observed, even at large distances. The density distribution in the 3Q system shows non-uniformity of the action density and a variation in the amplitude of the flux along each arm. This result does not manifest in the current zero temperature calculations using the Wilson loop operator. There, only a small variation in the tube width is observed in moving from a quark up to the junction. The gluonic flux is thus Y-shaped from the width profile point of view. The study of the broadening of the flux-tube in the

baryon shows a linearly growing pattern for large quark separation distances near the deconfinement point. The profile of the baryonic junction as predicted by the baryonic string model is compared to the measured lattice data for the junction. The lattice data are found to compare well with the predictions of the string model at large distances.

This study is motivating further investigations of the energy-density and chromo-electromagnetic distributions with methodological improvements that minimize the number of smearing sweeps and increase the number of measurements. It would also be interesting to confront these profiles with the bosonic string profiles in the context of the string's self-interactions. The findings of this work motivate also the use of a multi-level approach to explore the action-density profile of the static meson and static baryon at low and zero temperature. The gauge-field smearing method for noise reduction provides a suitable method for the rapid generalization of the calculations presented here to include the dynamical quarks QCD.

Appendix A

Transition Form Factors

A.1 Introduction

The recent available high-precision experimental data, and the forthcoming measurements on hadrons form factors and structure functions, impose a challenge to the theoretical efforts to explain these fine structures from the basic principles of QCD. This comparison with the experimental data would introduce research opportunities to the lattice QCD to create new knowledge and explore the lattice techniques as well.

An interesting and important source of exploring the structure of hadrons, is to study the electromagnetic transition processes between a pseudo-scalar and a vector meson. Even more, understanding these reaction may be important in analyzing certain reaction mechanisms [188]. As is well known, studying these reactions within the lattice QCD framework is motivated by the need to consider the quarks' bound-state effects, and the non-perturbative character of the transition form factors. The first lattice QCD study of the rho to pi transition reaction has been conducted by Edwards [188], a hybrid calculation with domain wall valence quarks and improved staggered (Asqtad) sea quarks has been used. However, it is still interesting to use different lattice techniques to study the same reaction, and compare the results to the experimental data [189]. Since the determinations of light hadron physics properties has become of considerable interest to experimental labs such as the Jefferson Lab, it would be also important to conduct lattice QCD calculation for different transition reactions channels. In the following, the phenomenological formalism for extracting the transition form factors from the correlation function is described. This work provides a framework for studying pseudo-scalar to vector meson electromagnetic transition reactions. The calculations can be applied to transition channels such as $K\gamma^* \rightarrow K^*$, $K^+\gamma^* \rightarrow K^0$, $\bar{K}^0\gamma^* \rightarrow K^-$ and $\pi\gamma^* \rightarrow \rho$ reactions. .

A.2 The Vector-current-Hadron vertex function

The momentum-space three point function is defined by [190]

$$\langle G_{\nu(\pi \rightarrow \rho)}^{\mu[AB]}(t_2, t_1, \vec{p}_2, \vec{p}_1) \rangle = \sum_{\vec{x}_1, \vec{x}_2} e^{-i\vec{p}_2 \cdot \vec{x}_2} e^{i(\vec{p}_2 - \vec{p}_1) \cdot \vec{x}_1} \langle \Omega | \hat{\chi}_\nu^B(x_2) \hat{J}^\mu(x_1) \hat{\phi}^{\dagger A}(0) | \Omega \rangle$$

(A.2.1)

where \hat{J}^μ is the vector current operator, $\hat{\phi}^\dagger(0)$ and $\hat{\chi}_\nu(x_2)$ are the operators of the interpolating fields of the pseudoscalar and vector meson, respectively. The brackets $\langle \dots \dots \rangle$ denote the ensemble average, the indices $A, B(L, S)$ indicate that the operator can either be L (local) or S smeared.

The momentum representation of the operators is achieved by projecting on to complete sets of relativistically-normalized pseudo-scalar and vector mesonic intermediate states

$$\begin{aligned} \mathcal{I} &= \sum_i \sum_{\vec{p}_\pi} \frac{1}{2E_{\vec{p}_\pi}^{(i)}} |i, \vec{p}_\pi\rangle \langle i, \vec{p}_\pi| , \\ \mathcal{I} &= \sum_k \sum_{\vec{p}_\rho} \sum_s \frac{1}{2E_{\vec{p}_\rho}^{(k)}} |k, \vec{p}_\rho, s\rangle \langle k, \vec{p}_\rho, s|. \end{aligned} \quad (\text{A.2.2})$$

These two subsets of eigen-states span the whole Hilbert space.

The energy tower of the final multi-particle excited states is constrained by

$$E_{\vec{p}_\rho}^{(k)} = \sqrt{|\vec{p}_\rho|^2 + m_{\rho,k}^2}, \quad (\text{A.2.3})$$

with $m_{\rho,k}$ the energy of the zero-momentum k th-particle eigenstate. This constraint corresponds to a hyperboloid of one particle states and a grid of multi-particle excited states bounded from below by the hyperboloid of the two-particle states. The same constraint holds on the pseudo-scalar channel.

The correlation function after insertion of the intermediate states is

$$\begin{aligned} G_{\nu(\pi \rightarrow \rho)}^{\mu[AB]}(t_2, t_1, \vec{p}_2, \vec{p}_1) &= \sum_{\vec{x}_2 \vec{x}_1} \sum_{\vec{p}_\rho \vec{p}_\pi} \sum_{i,k} \sum_s \frac{1}{4E_{\vec{p}_\rho}^{(k)} E_{\vec{p}_\pi}^{(i)}} e^{-i\vec{p}_2 \cdot \vec{x}_2} e^{-i(\vec{p}_2 - \vec{p}_1) \cdot \vec{x}_1} \\ &\quad \langle \Omega | \hat{\chi}_\nu^A | k, \vec{p}_\rho, s \rangle \langle k, \vec{p}_\rho, s | \hat{J}^\mu | i, \vec{p}_\pi \rangle \langle i, \vec{p}_\pi | \hat{\phi}^{\dagger B}(0) | \Omega \rangle. \end{aligned} \quad (\text{A.2.4})$$

Using the rule of changing the field operators under spatial and temporal translations

$$\hat{O}(x) = e^{i\hat{H}t} e^{-i\hat{P} \cdot \vec{x}} \hat{O}(0) e^{-i\hat{H}t} e^{i\hat{P} \cdot \vec{x}}, \quad (\text{A.2.5})$$

where \hat{P} is the operator of total momentum of the system.

The correlation function now reads

$$\begin{aligned} \langle G_{\nu(\pi \rightarrow \rho)}^{\mu[AB]}(t_2, t_1, \vec{p}_2, \vec{p}_1) \rangle &= \sum_{\vec{x}_2 \vec{x}_1} \sum_{\vec{p}_\rho \vec{p}_\pi} \sum_{i,k} \sum_s \frac{1}{4 E_{\vec{p}_\rho}^{(k)} E_{\vec{p}_\pi}^{(i)}} e^{-i E_{\vec{p}_\rho}^{(k)} t_2} e^{i E_{\vec{p}_\rho}^{(k)} t_1} e^{-i E_{\vec{p}_\pi}^{(i)} t_1} \times \\ &e^{i(\vec{p}_2 - \vec{p}_1 - \vec{p}_\rho + \vec{p}_\pi) \cdot \vec{x}_1} e^{-i(\vec{p}_2 - \vec{p}_\rho) \cdot \vec{x}_2} \langle \Omega | \hat{\chi}_\nu^A | k, \vec{p}_\rho, s \rangle \langle k, \vec{p}_\rho, s | \hat{J}^\mu | i, \vec{p}_\pi \rangle \langle i, \vec{p}_\pi | \hat{\phi}^{\dagger B}(0) | \Omega \rangle. \end{aligned} \quad (\text{A.2.6})$$

Performing summation over \vec{x}_2

$$\begin{aligned} \langle G_{\nu(\pi \rightarrow \rho)}^{\mu[AB]}(t_2, t_1, \vec{p}_2, \vec{p}_1) \rangle &= \sum_{\vec{x}_1} \sum_{\vec{p}_\rho \vec{p}_\pi} \sum_{i,k} \sum_s \frac{1}{4 E_{\vec{p}_\rho}^{(k)} E_{\vec{p}_\pi}^{(i)}} \\ &e^{-i E_{\vec{p}_\rho}^{(k)} t_2} e^{i E_{\vec{p}_\rho}^{(k)} t_1} e^{-i E_{\vec{p}_\pi}^{(i)} t_1} e^{-i(\vec{p}_1 - \vec{p}_\pi) \cdot \vec{x}_1} \delta_{\vec{p}_2 \vec{p}_\rho} \\ &\langle \Omega | \hat{\chi}_\nu^B | k, \vec{p}_\rho, s \rangle \langle k, \vec{p}_\rho, s | \hat{J}^\mu | i, \vec{p}_\pi \rangle \langle i, \vec{p}_\pi | \hat{\phi}^{A\dagger} | \Omega \rangle. \end{aligned} \quad (\text{A.2.7})$$

Similarly, summing over \vec{x}_1 , then the momenta yields

$$\begin{aligned} \langle G_{\nu(\pi \rightarrow \rho)}^{\mu[AB]}(t_2, t_1, \vec{p}_2, \vec{p}_1) \rangle &= \sum_{i,k} \sum_s \frac{1}{4 E_{\vec{p}_2}^{(k)} E_{\vec{p}_1}^{(i)}} e^{-i E_{\vec{p}_2}^{(k)} t_2} e^{i E_{\vec{p}_2}^{(k)} t_1} e^{-i E_{\vec{p}_1}^{(i)} t_1} \\ &\times \langle \Omega | \hat{\chi}_\nu^B | k, \vec{p}_2, s \rangle \langle k, \vec{p}_2, s | \hat{J}^\mu | i, \vec{p}_1 \rangle \langle i, \vec{p}_1 | \hat{\phi}^{\dagger A} | \Omega \rangle. \end{aligned} \quad (\text{A.2.8})$$

Since any eigenstate of the Hamiltonian with a definite-momentum can be written as a boost of some zero-momentum eigenstate

$$\begin{aligned} \langle i, \vec{p}_1 | \hat{\phi}^{\dagger}(0) | \Omega \rangle &= \langle i, \vec{p}_1 = 0 | U^\dagger(\Lambda) \hat{\phi}^{\dagger}(0) U(\Lambda) | \Omega \rangle, \\ &= \langle i, \vec{p}_1 = 0 | \hat{\phi}^{\dagger}(0) | \Omega \rangle, \\ &= Z_\pi^{(i)}. \end{aligned} \quad (\text{A.2.9})$$

$|Z_\pi^{(i)}|^2$ is the field strength renormalization, which depends only on the mass of the eigenstate, and the smearing of the operator and corresponds to the probability for creating or annihilating an eigenstate of the Hamiltonian. The above relation is a consequence of the Lorentzian invariance of the vacuum and the operator $\hat{\phi}^{\dagger}(0)$,

$$U^\dagger(\Lambda) \hat{\phi}^{\dagger}(0) U(\Lambda) = \hat{\phi}^{\dagger}(0) \quad (\text{A.2.10})$$

The vector field does not transform trivially under Lorentz transforms

$$\begin{aligned} \langle \Omega | \hat{\chi}_\nu(0) | k, \vec{p}_2, s \rangle &= \langle \Omega | U^\dagger(\Lambda) \hat{\chi}_\nu(0) U(\Lambda) | k, \vec{p}_2 = 0, s \rangle \\ &= \langle \Omega | U^\dagger(\Lambda) \hat{\chi}_\nu(0) U(\Lambda) | k, \vec{p}_2 = 0, s \rangle \\ &= (\Lambda_\nu^\alpha)^{-1} \langle \Omega | \hat{\chi}_\alpha(0) | k, \vec{p}_2 = 0, s \rangle \\ &= Z_\rho^{(k)*} (\Lambda_\nu^\alpha)^{-1} \epsilon_\alpha(k, \vec{p}_2 = 0, s) \\ &= Z_\rho^{(k)*} \epsilon_\nu(p_2, s) \end{aligned} \quad (\text{A.2.11})$$

In a finite sample, however, imperfect discrete symmetry [191] would lead to a non-vacuum contaminations in the Z factors. In the following formalism, therefore, we will have to indicate whether the averaging is done over a finite sample of N configurations, or the ensemble average $N \rightarrow \infty$, where we expect the restoration of the space-time symmetries of the continuum Euclidean field theory. That is,

$$\begin{aligned}\langle O \rangle &= \lim_{N \rightarrow \infty} \langle O \rangle_N, \\ &= \lim_{N \rightarrow \infty} \frac{1}{N} \sum_{i=1}^N O_i.\end{aligned}\tag{A.2.12}$$

thus, a momentum dependence in the Z factors will be assumed as long as finite sample averaging is considered.

$$\langle i, \vec{p} | \phi^{\dagger A} | \Omega \rangle_N = Z_{(\pi)}^{(i)A}(\vec{p}),\tag{A.2.13}$$

$$\langle \Omega | \phi^A | i, \vec{p} \rangle_N = \tilde{Z}_{(\pi)}^{(i)B}(\vec{p}).\tag{A.2.14}$$

For $A \equiv B \equiv L$,

$$\tilde{Z}^L(\vec{p}) = Z^{L*}(\vec{p}),\tag{A.2.15}$$

In the ensemble average,

$$\lim_{N \rightarrow \infty} Z^L(\vec{p}) = Z^L,\tag{A.2.16}$$

$$\lim_{N \rightarrow \infty} \tilde{Z}^L(\vec{p}) = Z^{L*}.\tag{A.2.17}$$

Similarly in the vector case,

$$\langle k, \vec{p}, s | \chi^{\dagger B} | \Omega \rangle_N = Z_{(\rho)}^{(k)B}(\vec{p}) \epsilon_{\nu}^*(p, s),\tag{A.2.18}$$

$$\langle \Omega | \chi^B | k, \vec{p}, s \rangle_N = \tilde{Z}_{(\rho)}^{(k)B}(\vec{p}) \epsilon_{\nu}(p, s).\tag{A.2.19}$$

Plugging the Z factors of Eqs. A.2.11 and Eq. A.2.12 into the correlation function of Eq. A.2.8, and analytically continuing to Euclidean space-time, the three point correlation function reads

$$\begin{aligned}\langle G_{\nu(\pi \rightarrow \rho)}^{\mu[AB]}(t_2, t_1, \vec{p}_2, \vec{p}_1) \rangle_N &= \sum_{k,i} \frac{1}{4 E_{\vec{p}_2}^{(k)} E_{\vec{p}_1}^{(i)}} e^{-E_{\vec{p}_2}^{(k)} t_2} e^{E_{\vec{p}_2}^{(k)} t_1} e^{-E_{\vec{p}_1}^{(i)} t_1} \times \\ &\quad \tilde{Z}_{\rho}^{(k)B}(\vec{p}_2) \epsilon_{\nu}(p_2, s) \langle k, \vec{p}_2, s | \hat{J}^{\mu} | i, \vec{p}_1 \rangle Z_{\pi}^{(i)A}(\vec{p}_1),\end{aligned}\tag{A.2.20}$$

Similar calculations give for the three-point function with the vector meson (four-momentum p_2) in the input channel

$$\begin{aligned} \langle G_{\nu(\rho \rightarrow \pi)}^{\mu[AB]}(t_2, t_1, \vec{p}_1, \vec{p}_2) \rangle_N = & \sum_{i,k} \sum_s \frac{1}{4E_{\vec{p}_2}^{(k)} E_{\vec{p}_1}^{(i)}} e^{-E_{\vec{p}_1}^{(i)} t_2} e^{E_{\vec{p}_1}^{(i)} t_1} e^{-E_{\vec{p}_2}^{(k)} t_1} \times \\ & \langle \Omega | \hat{\phi}_{\nu}^B | i, \vec{p}_1 \rangle \langle i, \vec{p}_1 | \hat{J}^{\mu} | k, \vec{p}_2, s \rangle \langle k, \vec{p}_2, s | \hat{\chi}^{\dagger A} | \Omega \rangle \end{aligned} \quad (\text{A.2.21})$$

or equivalently

$$\begin{aligned} \langle G_{\nu(\rho \rightarrow \pi)}^{\mu[AB]}(t_2, t_1, \vec{p}_1, \vec{p}_2) \rangle_N = & \sum_{k,i} \frac{1}{4E_{\vec{p}_2}^{(k)} E_{\vec{p}_1}^{(i)}} e^{-E_{\vec{p}_1}^{(k)} t_2} e^{E_{\vec{p}_1}^{(k)} t_1} e^{-E_{\vec{p}_2}^{(i)} t_1} \times \\ & \tilde{Z}_{\pi}^{(i)A}(\vec{p}_1) \langle i, \vec{p}_1 | \hat{J}^{\mu} | k, \vec{p}_2, s \rangle Z_{\rho}^{(k)B}(\vec{p}_2) \epsilon_{\nu}^*(p_2, s). \end{aligned} \quad (\text{A.2.22})$$

A.2.1 Transition form factors

The formal structure of the electromagnetic transition matrix $\gamma^* \pi \rightarrow \rho$ and $\gamma^* \rho \rightarrow \pi$ can be deduced by collecting all linearly independent possible combinations of contracted tensors that give rise to the vector current and encoding the functional dependence on the scalars (which is only the four-momentum transfere q^2) into the so-called form factors. Choosing the physically relavant combinations by imposing the requirements of Gauge invarince (Ward identy), the transition matrix then takes the form

$$\langle p_2, s | \hat{J}^{\mu} | p_1 \rangle = -i e F(Q^2) \varepsilon^{\mu\beta\eta\sigma} \mathcal{H}_{\beta\sigma} \epsilon_{\eta}^* . \quad (\text{A.2.23})$$

Here, ϵ is the polarization vector of the meson, $\varepsilon^{\mu\nu\eta\sigma}$ the Levi-Civita tensor because of the pseudo-scalar nature of the pion and $\mathcal{H}_{\nu\sigma}$ is the hadronic tensor defined by

$$\mathcal{H}_{\beta\sigma} = \mathcal{P}_{\beta} q_{\sigma} , \quad (\text{A.2.24})$$

where, $\mathcal{P}_{\beta} = (p_{1,\beta} + p_{2,\beta})$, and $q_{\sigma} = (p_{2,\sigma} - p_{1,\sigma})$ is the momentum transfer of the off-shell photon, $q^2 = -Q^2$.

The vector-current operator is hermitian,

$$\langle p_1 | \hat{J}^{\mu} | p_2, s \rangle = -i e F(Q^2) \varepsilon^{\mu\beta\eta\sigma} \mathcal{H}_{\beta\sigma} \epsilon_{\eta} , \quad (\text{A.2.25})$$

with $q_{\sigma} = (p_{1,\sigma} - p_{2,\sigma})$. This transition form factor contains the complete information about the response of the transit mesonic system to the external electromagnetic field.

Decomposing the hadronic tensor into its symmetric and anti-symmetric parts,

$$\begin{aligned} \mathcal{H}_{\beta\sigma} &= \mathcal{S}_{\beta\sigma} + \mathcal{A}_{\beta\sigma}, \\ \mathcal{S}_{\beta\sigma} &= (p_{1,\beta} p_{1,\sigma} - p_{2,\beta} p_{2,\sigma}), \\ \mathcal{A}_{\beta\sigma} &= (p_{2,\beta} p_{1,\sigma} - p_{1,\beta} p_{2,\sigma}) , \end{aligned} \quad (\text{A.2.26})$$

only the anti-symmetric part of the hadronic tensor survives in the transition current matrix, because of the Levi-Civita anti-symmetric tensor

$$\langle p_2, s | \hat{J}^\mu | p_1 \rangle = -i e F(Q^2) \varepsilon^{\mu\eta\beta\sigma} \epsilon_\eta^* \mathcal{A}_{\sigma\beta}. \quad (\text{A.2.27})$$

Now, we will show how to extract the transition form factors from correlation functions. Substituting the electromagnetic transition matrix Eq. A.2.15 into the three point function Eq. A.2.12

$$\begin{aligned} \langle G_{\nu(\pi \rightarrow \rho)}^{\mu[AB]}(t_2, t_1, \vec{p}_2, \vec{p}_1) \rangle_N &= -e \sum_{k,i} \sum_s \frac{1}{4 E_{\vec{p}_2}^{(k)} E_{\vec{p}_1}^{(i)}} e^{-E_{\vec{p}_2}^{(k)} t_2} e^{E_{\vec{p}_2}^{(k)} t_1} e^{-E_{\vec{p}_1}^{(i)} t_1} \\ &\quad \times \tilde{Z}_\rho^{(k)B}(\vec{p}_2) Z_\pi^{(i)A}(\vec{p}_1) \epsilon_\nu \epsilon_\eta^* \varepsilon^{\mu\eta\beta\sigma} A_{\sigma\beta} F(Q^2). \end{aligned} \quad (\text{A.2.28})$$

Summing over the spin of the vector meson and making use of the completeness relation of the polarization vectors

$$\sum_s \epsilon_\nu(p, s) \epsilon_\eta^*(p, s) = -(g_{\nu\eta} - \frac{p_\nu p_\eta}{m^2}) \quad , \quad (\text{A.2.29})$$

the correlation now is

$$\begin{aligned} \langle G_{\nu(\pi \rightarrow \rho)}^{\mu[AB]}(t_2, t_1, \vec{p}_2, \vec{p}_1) \rangle_N &= e \sum_{k,i} \frac{1}{4 E_{\vec{p}_2}^{(k)} E_{\vec{p}_1}^{(i)}} e^{-E_{\vec{p}_2}^{(k)} t_2} e^{E_{\vec{p}_2}^{(k)} t_1} e^{-E_{\vec{p}_1}^{(i)} t_1} \\ &\quad \times \tilde{Z}_\rho^{(k)B}(\vec{p}_2) Z_\pi^{(i)A}(\vec{p}_1) \Upsilon_\nu^\mu(p_2, p_1) F(Q^2) \quad , \end{aligned} \quad (\text{A.2.30})$$

where we have collected all of the Lorentzian indexed quantities in one term

$$\Upsilon_\nu^\mu(p_2, p_1) = g_{\nu\eta} \varepsilon^{\mu\eta\beta\sigma} \mathcal{A}_{\sigma\beta} - \frac{1}{m_\rho^2} \varepsilon^{\mu\eta\beta\sigma} p_{2,\nu} p_{2,\eta} \mathcal{A}_{\sigma\beta} \quad . \quad (\text{A.2.31})$$

Analogously, the correlation $G_{(\rho \rightarrow \pi)}$ is,

$$\begin{aligned} \langle G_{\nu(\rho \rightarrow \pi)}^{\mu[AB]}(t_2, t_1, \vec{p}_1, \vec{p}_2) \rangle_N &= e \sum_{k,i} \frac{1}{4 E_{\vec{p}_2}^{(k)} E_{\vec{p}_1}^{(i)}} e^{-E_{\vec{p}_1}^{(i)} t_2} e^{E_{\vec{p}_1}^{(i)} t_1} e^{-E_{\vec{p}_2}^{(k)} t_1} \\ &\quad \times Z_\rho^{(k)B}(\vec{p}_1) \tilde{Z}_\pi^{(i)A}(\vec{p}_2) \Upsilon_\nu^\mu(p_1, p_2) F(Q^2) \quad . \end{aligned} \quad (\text{A.2.32})$$

In the above equation,

$$\Upsilon_\nu^\mu(p_1, p_2) = -\Upsilon_\nu^\mu(p_2, p_1) \quad (\text{A.2.33})$$

A.2.2 The ratio method

The 3 to 2 point function ratio is a convenient and conventional method for the removal of the time exponents and the Z factors from the correlation functions. In a form similar to the one used by J.Hedditch [192] for vector mesons, the ratio for $t_1, t_2 \rightarrow \infty$, can be defined as

$$R_{[\mu\nu,\alpha\beta]}^{[1]} = \sqrt{\frac{\langle G^{[AB]\mu}_{\nu(\pi\rightarrow\rho)}(t_2, t_1, \vec{p}_2, \vec{p}_1) \rangle_N \langle G^{[CD]\mu}_{\nu(\rho\rightarrow\pi)}(t_2, t_1, \vec{p}_1, \vec{p}_2) \rangle_N}{\theta \langle G^{[CB]}_{(\rho)}(t_2, \vec{p}_2) \rangle_N \langle G^{[AD]}_{(\pi)}(t_2, \vec{p}_1) \rangle_N}} \quad (\text{A.2.34})$$

where $\theta = \pm 1$. The vector and pseudo-scalar meson two-point functions in the denominator are

$$\begin{aligned} \langle G_{(\rho)}^{[CB]}(t_2, \vec{p}_2) \rangle_N &= \sum_{k,s} \frac{1}{2 E_{\vec{p}_2}^{(k)}} e^{-E_{\vec{p}_2}^{(k)} t_2} \langle \Omega | \chi_\nu^C | k, \vec{p}_2, s \rangle \langle k, \vec{p}_2, s | \chi_\nu^{\dagger B} | \Omega \rangle, \\ &= \sum_{k,s} \frac{1}{2 E_{\vec{p}_2}^{(k)}} e^{-E_{\vec{p}_2}^{(k)} t_2} \tilde{Z}_\rho^{(k)C}(\vec{p}_2) Z_\rho^{(k)B}(\vec{p}_2) \epsilon_\nu^*(p_2, s) \epsilon_\nu(p_2, s), \\ &= \sum_k \frac{-1}{2 E_{\vec{p}_2}^{(k)}} e^{-E_{\vec{p}_2}^{(k)} t_2} \tilde{Z}_\rho^{(k)C}(\vec{p}_2) Z_\rho^{(k)B}(\vec{p}_2) (g_{\alpha\beta} - \frac{p_{2,\alpha} p_{2,\beta}}{m_{\rho,k}^2}), \end{aligned} \quad (\text{A.2.35})$$

and

$$\begin{aligned} \langle G_{(\pi)}^{[AD]}(t_2, \vec{p}_1) \rangle_N &= \sum_i \frac{1}{2 E_{\vec{p}_1}^{(i)}} e^{-E_{\vec{p}_1}^{(i)} t_2} \langle \Omega | \phi^D | i, \vec{p}_1 \rangle \langle i, \vec{p}_1 | \phi^{\dagger A} | \Omega \rangle, \\ &= \sum_i \frac{1}{2 E_{\vec{p}_1}^{(i)}} e^{-E_{\vec{p}_1}^{(i)} t_2} Z_\pi^{(i)A}(\vec{p}_1) \tilde{Z}_\pi^{(i)D}(\vec{p}_1), \end{aligned} \quad (\text{A.2.36})$$

$$(\text{A.2.37})$$

respectively.

Substituting Eqs. A.2.23, A.2.25, A.2.28, and Eq. A.2.29, into the ratio Eq. A.2.27

$$\begin{aligned} R_{[\mu\nu,\alpha\beta]}^{[1]} &= \sqrt{\frac{e^{-E_{\vec{p}_2} t_2} e^{E_{\vec{p}_2} t_1} e^{-E_{\vec{p}_1} t_1} e^{-E_{\vec{p}_1} t_2} e^{E_{\vec{p}_1} t_1} e^{-E_{\vec{p}_2} t_1} Z_\rho^C(\vec{p}_2) \tilde{Z}_\rho^B(\vec{p}_2) \tilde{Z}_\pi^D(\vec{p}_1) Z_\pi^A(\vec{p}_1)}{\theta e^{-E_{\vec{p}_2} t_2} e^{-E_{\vec{p}_1} t_1} Z_\rho^C(\vec{p}_2) \tilde{Z}_\rho^B(\vec{p}_2) Z_\pi^A(\vec{p}_1) \tilde{Z}_\pi^D(\vec{p}_1) (-g_{\alpha\beta} + \frac{p_{2,\alpha} p_{2,\beta}}{m_{\rho,k}^2})}}, \\ &\times \frac{e}{2 \sqrt{E_{p_1} E_{p_2}}} (\Upsilon_\nu^\mu) F(Q^2), \\ &= \frac{e}{2 \sqrt{\theta E_{p_1} E_{p_2} (-g_{\alpha\beta} + \frac{p_{2,\alpha} p_{2,\beta}}{m_\rho^2})}} \Upsilon_\nu^\mu F(Q^2). \end{aligned} \quad (\text{A.2.38})$$

In the last equation we have dropped the multi-particle eigenstates label, since we assume the dominance of the ground state in the limit of large Euclidean time.

Now, let us find the ratio $R^{[1]}$ in the frame where, $p_1 = (m_\pi, 0, 0, 0)$ and $p_2 = (E_x, p_x, 0, 0)$, since the only non-vanishing Lorentzian terms Υ_μ^ν are

$$\begin{aligned} \Upsilon_2^3 = -\Upsilon_3^2 &= \varepsilon^{32\sigma\beta} A_{\sigma\beta}, \\ &= (p_{\rho,1}p_{\pi,0} - p_{\pi,1}p_{\rho,0}), \\ &= 2m_\pi p_x. \end{aligned} \quad (\text{A.2.39})$$

In the following, the form factors in terms of the R ratio for $\mu = 3$, $\nu = 2$, and different values of α and β are evaluated. The sign factor θ is chosen such that the quantity under the square root is positive.

- $\alpha = 0, \beta = 0$,

$$e F(Q^2) = \frac{(R_{[32,\alpha=0\beta=0]}^{[1]})}{m_\rho m_\pi p_x} \sqrt{E_x(2m_\rho^2 - p_x^2)}, \quad (\text{A.2.40})$$

- $\alpha = 1, \beta = 1$,

$$e F(Q^2) = \frac{(R_{[32,\alpha=1\beta=1]}^{[1]})}{m_\rho m_\pi p_x} \sqrt{m_\pi E_x(2m_\rho^2 + p_x^2)}, \quad (\text{A.2.41})$$

- $\alpha = 2, \beta = 2$,

$$e F(Q^2) = \frac{(R_{[32,\alpha=2\beta=2]}^{[1]})}{m_\pi p_x} \sqrt{m_\pi E_x}, \quad (\text{A.2.42})$$

- $\alpha = 3, \beta = 3$,

$$e F(Q^2) = \frac{(R_{[32,\alpha=3\beta=3]}^{[1]})}{m_\pi p_x} \sqrt{m_\pi E_x}, \quad (\text{A.2.43})$$

- $\alpha = 0, \beta = 1$,

$$e F(Q^2) = \frac{(R_{[32,\alpha=0\beta=1]}^{[1]})}{m_\pi p_x} \sqrt{m_\pi/m_\rho E_x p_x}. \quad (\text{A.2.44})$$

Bibliography

- [1] F. Bissey et al., Gluon field distribution in baryons, *Nucl. Phys. Proc. Suppl.* 141 (2005) 22, hep-lat/0501004.
- [2] F. Bissey et al., Gluon flux-tube distribution and linear confinement in baryons, *Phys. Rev. D* 76 (2007) 114512, hep-lat/0606016.
- [3] T.T. Takahashi et al., Detailed analysis of the three quark potential in SU(3) lattice QCD, *Phys. Rev. D* 65 (2002) 114509, hep-lat/0204011.
- [4] A.D. Kennedy et al., Where is the continuum in lattice quantum chromodynamics?, *Phys. Rev. Lett.* 54 (1985) 87.
- [5] T. Doi et al., The lattice QCD simulation of the quark-gluon mixed condensate at finite temperature and the phase transition of QCD, *Nucl. Phys. B - Proc. Suppl.* 140 (2005) 559 .
- [6] A. Casher, Gauge fields on the null plane, *Phys. Rev. D* 14 (1976) 452.
- [7] E. Tomboulis, Quantization of the Yang-Mills field in the null-plane frame, *Phys. Rev. D* 8 (1973) 2736.
- [8] V.A. Franke, Y.V. Novozhilov and E.V. Prokhvatilov, On the light cone quantization of non-abelian gauge theory, *Lett. Math. Phys.* 5 (1981) 437.
- [9] G. Leibbrandt, The light cone gauge in Yang-Mills theory, *Phys. Rev. D* 29 (1984) 1699.
- [10] F.J. Dyson, The S matrix in quantum electrodynamics, *Phys. Rev.* 75 (1949) 1736.
- [11] J. Schwinger, On the Green's functions of quantized fields. I, *Proceedings of the National Academy of Science* 37 (1951) 452.
- [12] R. Alkofer and L. von Smekal, The infrared behavior of QCD Green's functions: Confinement, dynamical symmetry breaking, and hadrons as relativistic bound states, *Phys. Rept.* 353 (2001) 281, hep-ph/0007355.
- [13] C.D. Roberts and A.G. Williams, Dyson-Schwinger equations and their application to hadronic physics, *Prog. Part. Nucl. Phys.* 33 (1994) 477, hep-ph/9403224.

- [14] G. Zweig, An $SU(3)$ model for strong interaction symmetry and its breaking; Part II, (1964) 80 p.
- [15] M. Gell-Mann, Symmetries of baryons and mesons, Phys. Rev. 125 (1962) 1067.
- [16] C.N. Yang and R.L. Mills, Conservation of isotopic spin and isotopic gauge invariance, Phys. Rev. 96 (1954) 191.
- [17] M.E. Peskin and D.V. Schroeder, An introduction to quantum field theory (Addison-Wesley, Reading, 1995).
- [18] R. Utiyama, Invariant theoretical interpretation of interaction, Phys. Rev. 101 (1956) 1597.
- [19] J.J. Sakurai, Theory of strong interactions, Annals Phys. 11 (1960) 1.
- [20] Y. Ne'eman, Derivation of strong interactions from a gauge invariance, Nucl. Phys. 26 (1961) 222.
- [21] R.L. Arnowitt and S.I. Fickler, Quantization of the Yang-Mills field, Phys. Rev. 127 (1962) 1821.
- [22] J.S. Schwinger, Non Abelian gauge fields. Relativistic invariance, Phys. Rev. 127 (1962) 324.
- [23] J.S. Schwinger, Non-Abelian gauge fields. Lorentz gauge formation, Phys. Rev. 130 (1963) 402.
- [24] A. Salam, Renormalizability of gauge theories, Phys. Rev. 127 (1962) 331.
- [25] L. Landau, On the quantum theory of fields, In Niels Bohr and the Development of Physics. Wolfgang Pauli, Leon Rosenfeld, and Victor Weisskopf, eds., Oxford: Pergamon, pp. 52-69 .
- [26] D.J. Gross and F. Wilczek, Asymptotically free gauge theories. I, Phys. Rev. D 8 (1973) 3633.
- [27] H.D. Politzer, Reliable perturbative results for strong interactions?, Phys. Rev. Lett 30 (1973) 1346.
- [28] H.L. Anderson et al., Measurement of nucleon structure function in muon scattering at 147 GeV/c, Phys. Rev. Lett. 37 (1976) 4.
- [29] A. Benvenuti et al., Further data on the high- y anomaly in inelastic antineutrino scattering, Phys. Rev. Lett. 36 (1976) 1478.
- [30] P.H. Frampton and J.J. Sakurai, Model for scaling violation, Phys. Rev. D 16 (1977) 572.
- [31] W. Greiner, S. Schramm and E. Stein, Quantum chromodynamics, Berlin, Germany: Springer (2007) 553 p. (2007).

- [32] K.G. Wilson, Confinement of quarks, *Phys. Rev. D* 10 (1974) 2445.
- [33] P. Faccioli and T.A. DeGrand, Evidence for instanton induced dynamics, from lattice QCD, *Phys. Rev. Lett.* 91 (2003) 182001, hep-ph/0304219.
- [34] F. Lenz, J.W. Negele and M. Thies, Confinement from merons, *Phys. Rev. D* 69 (2004) 074009.
- [35] J.V. Steele, Can merons describe confinement?, (2000), hep-lat/0007030.
- [36] H. Shiba and T. Suzuki, Monopoles and string tension in $SU(2)$ QCD, *Phys. Lett.* B333 (1994) 461, hep-lat/9404015.
- [37] J. Ambjorn and P. Olesen, A color magnetic vortex condensate in QCD, *Nucl. Phys.* B170 (1980) 265.
- [38] D. Diakonov and V. Petrov, Confining ensemble of dyons, *Phys. Rev. D* 76 (2007) 056001.
- [39] G. 't Hooft, Monopoles, instantons and confinement, (1999), hep-th/0010225.
- [40] F.S. Henyey and A. Patrascioiu, Instantons, tunnelling, and confinement, *Phys. Rev. D* 18 (1978) 2962.
- [41] C.G.A. Jr., R. Dashen and D.J. Gross, A mechanism for quark confinement, *Phys. Lett. B* 66 (1977) 375 .
- [42] J.W. Negele, F. Lenz and M. Thies, Confinement from instantons or merons, *Nucl. Phys. Proc. Suppl.* 140 (2005) 629, hep-lat/0409083.
- [43] Y.A. Simonov, Dyons in QCD: Confinement and chiral-symmetry breaking, (1995), hep-ph/9509403.
- [44] D. Diakonov and V. Petrov, Confinement and deconfinement for any gauge group from dyons viewpoint, *AIP Conference Proceedings* 1343 (2011) 69.
- [45] L. Del Debbio et al., Center dominance and $Z(2)$ vortices in $SU(2)$ lattice gauge theory, *Phys. Rev. D* 55 (1997) 2298, hep-lat/9610005.
- [46] M. Engelhardt et al., Deconfinement in $SU(2)$ Yang-Mills theory as a center vortex percolation transition, *Phys. Rev. D* 61 (2000) 054504, hep-lat/9904004.
- [47] H.B. Nielsen and P. Olesen, Vortex-line models for dual strings, *Nucl. Phys. B* 61 (1973) 45 .
- [48] M. Creutz, The Higgs mechanism and quark Confinement, *Phys. Rev. D* 10 (1974) 2696.
- [49] G. 't Hooft, High Energy Physics, edited by A. Zichichi, Palermo, 1975, EPS International Conference.
- [50] A. Jevicki and P. Senjanovic, Stringlike solution of Higgs model with magnetic monopoles, *Phys. Rev. D* 11 (1975) 860.

- [51] S. Mandelstam, Vortices and quark confinement in nonabelian gauge theories, *Phys. Rept.* 23 (1976) 245.
- [52] G. Parisi, Quark imprisonment and vacuum repulsion, *Phys. Rev. D* 11 (1975) 970.
- [53] V.L. Ginzburg and L.D. Landau, On the theory of superconductivity, *Zh. Eksp. Teor. Fiz.* 20 (1950) 1064.
- [54] E.T. Akhmedov et al., Quantum theory of strings in abelian Higgs model, *Phys. Rev. D* 53 (1996) 2087, hep-th/9505070.
- [55] A. Di Giacomo et al., Colour confinement and dual superconductivity of the vacuum. I, *Phys. Rev. D* 61 (2000) 034503, hep-lat/9906024.
- [56] A. Di Giacomo et al., Colour confinement and dual superconductivity of the vacuum. II, *Phys. Rev. D* 61 (2000) 034504, hep-lat/9906025.
- [57] J.M. Carmona et al., Color confinement and dual superconductivity of the vacuum. III, *Phys. Rev. D* 64 (2001) 114507, hep-lat/0103005.
- [58] G.S. Bali et al., Dual superconductor scenario of confinement: A Systematic study of Gribov copy effects, *Phys. Rev. D* 54 (1996) 2863, hep-lat/9603012.
- [59] P.A.M. Dirac, The theory of magnetic poles, *Phys. Rev.* 74 (1948) 817.
- [60] G. t Hooft, Topology of the gauge condition and new confinement phases in non-abelian gauge theories, *Nucl. Phys. B* 190 (1981) 455 .
- [61] T. Suzuki and I. Yotsuyanagi, Possible evidence for Abelian dominance in quark confinement, *Phys. Rev. D* 42 (1990) 4257.
- [62] M. Luscher and P. Weisz, Quark confinement and the bosonic string, *JHEP* 0207 049 (2002).
- [63] G.S. Bali, C. Schlichter and K. Schilling, Observing long color flux tubes in SU(2) lattice gauge theory, *Phys. Rev. D* 51 (1995) 5165.
- [64] K.J. Juge, J. Kuti and C. Morningstar, Fine structure of the QCD string spectrum, *Phys. Rev. Lett.* 90 (2003) 161601, hep-lat/0207004.
- [65] M. Caselle et al., Width of long colour flux tubes in lattice gauge systems, *Nucl. Phys. B* 460 (1996) 397, hep-lat/9510019.
- [66] M. Caselle, M. Pepe and A. Rago, Static quark potential and effective string corrections in the (2+1)-d SU(2) Yang-Mills theory, *JHEP* 10 (2004) 5, arXiv:hep-lat/0406008.
- [67] M. Luscher, K. Symanzik and P. Weisz, Anomalies of the free loop wave equation in the WKB approximation, *Nucl. Phys. B* 173 (1980) 365.
- [68] T. Banks and A. Casher, Chiral symmetry breaking in confining theories, *Nucl. Phys. B* 169 (1980) 103 .

- [69] M. Creutz, Confinement, chiral symmetry, and the lattice, (2011), 1103.3304.
- [70] M. Creutz, Anomalies and chiral symmetry in QCD, *Annals Phys.* 324 (2009) 1573, 0901.0150.
- [71] R.G. Edwards, U.M. Heller and R. Narayanan, A study of chiral symmetry in quenched QCD using the overlap-Dirac operator, *Phys. Rev. D* 59 (1999) 094510, hep-lat/9811030.
- [72] F. Bruckmann et al., Quantitative comparison of filtering methods in lattice QCD, *Eur. Phys. J. A* 33 (2007) 333, hep-lat/0612024.
- [73] J. Goldstone, A. Salam and S. Weinberg, Broken Symmetries, *Phys. Rev.* 127 (1962) 965.
- [74] J.M. Cornwall, Dynamical mass generation in continuum quantum chromodynamics, *Phys. Rev. D* 26 (1982) 1453.
- [75] J. Engels et al., High temperature SU(2) gluon matter on the lattice, *Phys. Lett.* B101 (1981) 89.
- [76] A.D. Linde, Infrared problem in thermodynamics of the Yang-Mills gas, *Phys. Lett.* B96 (1980) 289.
- [77] F.R. Brown et al., Nature of the deconfining phase transition in SU(3) Lattice Gauge Theory, *Phys. Rev. Lett.* 61 (1988) 2058.
- [78] J. Kuti, J. Polonyi and K. Szlachanyi, Monte Carlo study of SU(2) gauge theory at finite temperature, *Phys. Lett.* B98 (1981) 199.
- [79] H. Bohr and H.B. Nielsen, Hadron production from a boiling quark soup : A thermodynamical quark model predicting particle ratios in hadronic collisions, *Nucl. Phys. B* 128 (1977) 275 .
- [80] L. McLerran, Chiral-symmetry order parameter, the lattice, and nucleosynthesis, *Phys. Rev. D* 36 (1987) 3291.
- [81] O. Kaczmarek et al., Heavy quark potentials in quenched QCD at high temperature, *Phys. Rev. D* 62 (2000) 034021.
- [82] H.J. Rothe, Lattice gauge theories: An introduction, *World Sci. Lect. Notes Phys.* 74 (2005) 1.
- [83] I. Montvay and G. Munster, Quantum fields on a lattice (, 1994), Cambridge, UK: Univ. Pr. (1994) 491 p. (Cambridge monographs on mathematical physics).
- [84] M. Creutz, Asymptotic-freedom scales, *Phys. Rev. Lett.* 45 (1980) 313.
- [85] I. Montvay, Numerical calculation of hadron masses in quantum chromodynamics, *Rev. Mod. Phys.* 59 (1987) 263.

- [86] D.J.E. Callaway and A. Rahman, Lattice gauge theory in the microcanonical ensemble, *Phys. Rev. D* 28 (1983) 1506.
- [87] S. Gottlieb et al., Hybrid-molecular-dynamics algorithms for the numerical simulation of quantum chromodynamics, *Phys. Rev. D* 35 (1987) 2531.
- [88] R. Sommer and J. Wosiek, Baryonic loops and confinement in the three quark channel, *Phys. Lett. B* 149 (1984) 497 .
- [89] SESAM Collaboration, G.S. Bali et al., Observation of string breaking in QCD, *Phys. Rev. D* 71 (2005) 114513.
- [90] J.M. Hammersley and D.C. Handscomb, Monte Carlo Methods (Chapman and Hall, 1964).
- [91] N. Metropolis et al., Equation of State Calculations by Fast Computing Machines, *J. Chem. Phys.* 21 (1953) 1087.
- [92] M. Creutz, Overrelaxation and Monte Carlo simulation, *Phys. Rev. D* 36 (1987) 515.
- [93] K. Fabricius and O. Haan, Heat bath method for the twisted Eguchi-Kawai model, *Phys. Lett. B* 143 (1984) 459.
- [94] A.D. Kennedy and B.J. Pendleton, Improved heat bath method for Monte Carlo calculations in lattice gauge theories, *Phys. Lett. B* 156 (1985) 393.
- [95] N. Cabibbo and E. Marinari, A new method for updating $SU(N)$ matrices in computer simulations of gauge theories, *Phys. Lett. B* 119 (1982) 387.
- [96] J.W. Flower and S.W. Otto, The field distribution in $SU(3)$ lattice gauge theory, *Physics Letters B* 160 (1985) 128 .
- [97] R.W. Haymaker et al., Distribution of the color fields around static quarks: Flux tube profiles, *Phys. Rev. D* 53 (1996) 389.
- [98] H. Ichie et al., The flux distribution of the three quark system in $SU(3)$, *Nucl. Phys. Proc. Suppl.* 119 (2003) 751, hep-lat/0212024.
- [99] F. Okiharu and R.M. Woloshyn, An alternate smearing method for Wilson loops in lattice QCD, *Eur. Phys. J. C* 35 (2004) 537, hep-lat/0402009.
- [100] C. Alexandrou, P. de Forcrand and O. Jahn, The ground state of three quarks, *Nucl. Phys. Proc. Suppl.* 119 (2003) 667, hep-lat/0209062.
- [101] APE, M. Albanese et al., Glueball masses and string tension in lattice QCD, *Phys. Lett. B* 192 (1987) 163.
- [102] T.T. Takahashi et al., Detailed analysis of the three quark potential in $SU(3)$ lattice QCD, *Phys. Rev. D* 65 (2002) 114509.
- [103] A.M. Polyakov, Thermal properties of gauge fields and quark liberation, *Physics Letters B* 72 (1978) 477 .

- [104] L. Susskind, Lattice models of quark confinement at high temperature, *Phys. Rev. D* 20 (1979) 2610.
- [105] A.J. Niemi and G.W. Semenoff, Finite-temperature quantum field theory in Minkowski space, *Annals of Physics* 152 (1984) 105.
- [106] T. Doi et al., The lattice QCD simulation of the quark-gluon mixed condensate at finite temperature and the phase transition of QCD, *Nucl. Phys. B Proc. Suppl.* 140 (2005) 559.
- [107] R. Gupta, Introduction to lattice QCD, (1997), hep-lat/9807028.
- [108] G. Veneziano, Construction of a crossing - symmetric, Regge behaved amplitude for linearly rising trajectories, *Nuovo. Cim.* A57 (1968) 190.
- [109] S. Mandelstam, II. Vortices and quark confinement in non-Abelian gauge theories, *Phys. Rep.* 23 (1976) 245 .
- [110] E.V. Thuneberg, Ginzburg-Landau theory of vortices in superfluid 3He-B, *Phys. Rev. B* 36 (1987) 3583.
- [111] M.G. Alford and G. Good, Flux tubes and the type-I/type-II transition in a superconductor coupled to a superfluid, *Phys. Rev. B* 78 (2008) 024510.
- [112] K. Kasamatsu and M. Tsubota, Quantized vortices in atomic Bose-Einstein condensates, ArXiv e-prints (2007), 0709.1042.
- [113] A.S. Lo and E.L. Wright, Signatures of cosmic strings in the cosmic microwave background, (2005), astro-ph/0503120.
- [114] Y. Nambu, QCD and the string model, *Phys. Lett. B* 80 (1979) 372 .
- [115] O. Alvarez, Static potential in string models, *Phys. Rev. D* 24 (1981) 440.
- [116] J. Ambjorn, P. Olesen and C. Peterson, Observation of a string in three-dimensional SU(2) lattice gauge theory, *Phys. Lett. B* 142 (1984) 410.
- [117] P. de Forcrand et al., The string and its tension in SU(3) lattice gauge theory: Towards Definitive Results, *Phys. Lett. B* 160 (1985) 137.
- [118] M. Luscher and P. Weisz, Locality and exponential error reduction in numerical lattice gauge theory, *JHEP* 09 (2001) 010, hep-lat/0108014.
- [119] M. Luscher and P. Weisz, Quark confinement and the bosonic string, *JHEP* 07 (2002) 049, hep-lat/0207003.
- [120] K. Dietz and T. Filk, Renormalization of string functionals, *Phys. Rev. D* 27 (1983) 2944.
- [121] S. Naik, Improved heavy quark potential at finite temperature from anti-de Sitter supergravity, *Phys. Lett. B* 464 (1999) 73, hep-th/9904147.

- [122] B. Lucini and M. Teper, Confining strings in $SU(N)$ gauge theories, *Phys. Rev. D* 64 (2001) 105019.
- [123] J. Polchinski and A. Strominger, Effective string theory, *Phys. Rev. Lett.* 67 (1991) 1681.
- [124] P. Olesen, Strings and QCD, *Phys. Lett.* B160 (1985) 144.
- [125] M. Gao, Heavy quark potential at finite temperature from a string picture, *Phys. Rev. D*40 (1989) 2708.
- [126] M. Luscher, G. Munster and P. Weisz, How thick are chromoelectric flux tubes?, *Nucl. Phys.* B180 (1981) 1.
- [127] F. Gliozzi, Quantum behavior of the flux tube: A Comparison between QFT predictions and lattice gauge theory simulations, (1994), hep-lat/9410022.
- [128] J.S. Schwinger, The theory of quantized fields. I, *Phys. Rev.* 82 (1951) 914.
- [129] A. Allais and M. Caselle, On the linear increase of the flux tube thickness near the deconfinement transition, *JHEP* 01 (2009) 073, 0812.0284.
- [130] J. Kogut and L. Susskind, Hamiltonian formulation of Wilson's lattice gauge theories, *Phys. Rev. D* 11 (1975) 395.
- [131] S. Capstick and N. Isgur, Baryons in a relativized quark model with chromodynamics, *Phys. Rev. D* 34 (1986) 2809.
- [132] N. Brambilla, G.M. Prosperi and A. Vairo, Three-body relativistic flux tube model from QCD Wilson-loop approach, *Phys. Lett. B* 362 (1995) 113 .
- [133] O. Jahn and P.D. Forcrand, Baryons and confining strings, *Nucl. Phys. B - Proc. Suppl.* 129-130 (2004) 700 , Lattice 2003.
- [134] M. Pfeuffer, G.S. Bali and M. Panero, Fluctuations of the baryonic flux-tube junction from effective string theory, *Phys. Rev. D* 79 (2009) 025022.
- [135] A.S. Bakry, D.B. Leinweber and A.G. Williams, Bosonic string behavior in UV filtered QCD, (2010), 1011.1380.
- [136] O. Andreev, Some multi-quark potentials, pseudo-potentials and AdS/QCD, *Phys. Rev. D*78 (2008) 065007, 0804.4756.
- [137] P. de Forcrand and O. Jahn, The baryon static potential from lattice QCD, *Nucl. Phys. A*755 (2005) 475, hep-ph/0502039.
- [138] F. Gliozzi, M. Pepe and U.J. Wiese, The width of the confining string in Yang-Mills theory, (2010), 1002.4888.
- [139] F. Gliozzi, M. Pepe and U.J. Wiese, The width of the color flux tube at 2-loop order, (2010), 1006.2252.

- [140] M. Caselle, Flux tube delocalization at the deconfinement point, JHEP 08 (2010) 063, 1004.3875.
- [141] A.S. Bakry, D.B. Leinweber and A.G. Williams, Gluonic profile of the static baryon at finite temperature, (2011), 1107.0150.
- [142] V. Dmitrasinovic, T. Sato and M. Suvakov, On the smooth cross-over transition from the Delta-string to the Y-string three-quark potential, Phys. Rev. D80 (2009) 054501, 0908.2687.
- [143] V.G. Bornyakov et al., Baryonic flux in quenched and two-flavor dynamical QCD after Abelian projection, Phys. Rev. D 70 (2004) 054506.
- [144] W. Detmold and M.J. Savage, Color screening by pions, Phys. Rev. Lett. 102 (2009) 032004.
- [145] S. Thurner et al., Correlations of topological objects and quarks in hadrons, Phys. Rev. D 54 (1996) 3457.
- [146] P.J. Moran and D.B. Leinweber, Over-improved stout-link smearing, Phys. Rev. D77 (2008) 094501, 0801.1165.
- [147] C. Morningstar and M. Peardon, Analytic smearing of $SU(3)$ link variables in lattice QCD, Phys. Rev. D 69 (2004) 054501.
- [148] E.M. Ilgenfritz et al., Vacuum structure revealed by over-improved stout-link smearing compared with the overlap analysis for quenched QCD, Phys. Rev. D 77 (2008) 074502.
- [149] F.D.R. Bonnet et al., Improved smoothing algorithms for lattice gauge theory, Phys. Rev. D 65 (2002) 114510.
- [150] S.O. Bilson-Thompson, D.B. Leinweber and A.G. Williams, Highly-improved lattice field-strength tensor, Ann. Phys. 304 (2003) 1, hep-lat/0203008.
- [151] P. de Forcrand and C. Roiesnel, Refined methods for measuring large-distance correlations, Phys. Lett. B 151 (1985) 77.
- [152] G. Parisi, R. Petronzio and F. Rapuano, A measurement of the string tension near the continuum Limit, Phys. Lett. B128 (1983) 418.
- [153] M. Caselle et al., String effects in Polyakov loop correlators, Nucl. Phys. Proc. Suppl. 119 (2003) 499, hep-lat/0210023.
- [154] P. Pennanen, A.M. Green and C. Michael, Flux-tube structure and beta-functions in $SU(2)$, Phys. Rev. D56 (1997) 3903, hep-lat/9705033.
- [155] T. Heinzl et al., Is the ground state of Yang-Mills theory coulombic?, Phys. Rev. D78 (2008) 034504, 0806.1187.
- [156] Y. Peng and R.W. Haymaker, $SU(2)$ flux distributions on finite lattices, 47 (1993) 5104, arXiv:hep-lat/9302009.

- [157] F. Okiharu and R.M. Woloshyn, A study of colour field distributions in the baryon, *Nucl. Phys. B - Proc. Suppl.* 129-130 (2004) 745 , Lattice 2003.
- [158] A.S. Bakry et al., String effects and the distribution of the glue in static mesons at finite temperature, *Phys. Rev. D* 82 (2010,hep-lat/1004.0782) 094503.
- [159] R.D. Pisarski and O. Alvarez, Strings at finite temperature and deconfinement, *Phys. Rev. D* 26 (1982) 3735.
- [160] N.H. Dass and P. Majumdar, Continuum limit of string formation in 3d SU(2) LGT, *Phys. Lett. B* 658 (2008) 273 .
- [161] O. Aharony and E. Karzbrun, On the effective action of confining strings, *JHEP* 06 (2009) 012, 0903.1927.
- [162] M. Luscher and P. Weisz, String excitation energies in SU(N) gauge theories beyond the free-string approximation, *JHEP* 07 (2004) 014, hep-th/0406205.
- [163] M. Caselle, M. Hasenbusch and M. Panero, Comparing the Nambu-Goto string with LGT results, *JHEP*. 03 (2005) 026. 25 p.
- [164] G.S. Bali and K. Schilling, Running coupling and the Λ parameter from SU(3) lattice simulations, *Phys. Rev. D* 47 (1993) 661.
- [165] P. de Forcrand, Localization properties of fermions and bosons, *AIP Conf. Proc.* 892 (2007) 29, hep-lat/0611034.
- [166] F. Niedermayer, Exact chiral symmetry, topological charge and related topics, *Nuclear Physics B - Proceedings Supplements* 73 (1999) 105 .
- [167] I. Horváth et al., Local structure of topological charge fluctuations in QCD, *Phys. Rev. D* 67 (2003) 011501.
- [168] K.J. Juge, J. Kuti and C.J. Morningstar, Bag picture of the excited QCD vacuum with static Q source,, *Nucl. Phys. B - Proc. Suppl.* 63 (1998) 543 , Proc. of the XVth Intern. Symp. on LFT.
- [169] T. Heinzl et al., Probing the ground state in gauge theories, *Phys. Rev. D*77 (2008) 054501, 0709.3486.
- [170] H. Ichie et al., Flux tubes of two- and three-quark system in full QCD, *Nuclear Physics A* 721 (2003) C899 .
- [171] T.T. Takahashi et al., The three-quark potential in the SU(3) lattice QCD, *Phys. Rev. Lett.* 86 (2001) 18, hep-lat/0006005.
- [172] G.S. Bali, QCD forces and heavy quark bound states, *Phys. Rept.* 343 (2001) 1, hep-ph/0001312.
- [173] C. Alexandrou, P. De Forcrand and A. Tsapalis, The static three-quark SU(3) and four-quark SU(4) potentials, *Phys. Rev. D*65 (2002) 054503, hep-lat/0107006.

- [174] D.S. Kuzmenko and Y.A. Simonov, Field distributions in heavy mesons and baryons, *Phys. Lett.* B494 (2000) 81, hep-ph/0006192.
- [175] D.S. Kuzmenko and Y.A. Simonov, Triangular and Y-shaped hadrons with static sources, *Phys. Atom. Nucl.* 67 (2004) 543, hep-ph/0302071.
- [176] R. Sommer and J. Wosiek, Baryonic loops and confinement in the three quark channel, *Physics Letters B* 149 (1984) 497 .
- [177] H. Thacker, E. Eichten and J. Sexton, The three-body potential for heavy quark baryons in lattice QCD, *Nucl. Phys. B - Proc. Suppl.* 4 (1988) 234 .
- [178] A.S. Bakry, D.B. Leinweber and A.G. Williams, On the ground state of Yang-Mills theory, *Annals Phys.* 326 (2011) 2165, 1102.3477.
- [179] A.S. Bakry, T(R)OPICAL QCD(II), Cairns, 2010, Thermal delocalization of the flux tubes in mesons and baryons finite temperature.
- [180] M.S. Cardaci et al., Chromoelectric flux tubes in QCD, *Phys. Rev. D* 83 (2011) 014502, 1011.5803.
- [181] H. Suganuma, S. Sasaki and H. Toki, Color confinement, quark pair creation and dynamical chiral-symmetry breaking in the dual Ginzburg-Landau theory, *Nuclear Physics B* 435 (1995) 207 .
- [182] H. Suganuma et al., Instantons and monopoles in the nonperturbative QCD, *Prog. Theor. Phys. Suppl.* 131 (1998) 559, hep-lat/9804027.
- [183] H. Suganuma et al., Quark confinement physics from quantum chromodynamics, *Nucl. Phys. A* 670 (2000) 40, hep-lat/0407017.
- [184] H. Suganuma, M. Fukushima and H. Toki, Quantum chromodynamics and color confinement, World Scientific (2001).
- [185] T.T. Takahashi and H. Suganuma, Detailed analysis of the gluonic excitation in the three-quark system in lattice QCD, *Phys. Rev. D* 70 (2004) 074506.
- [186] A.S. Bakry, D.B. Leinweber and A.G. Williams, The thermal delocalization of the flux tubes in mesons and baryons, *AIP Conference Proceedings* 1354 (2011) 178.
- [187] A.S. Bakry, D.B. Leinweber and A.G. Williams, Quantum fluctuations of the baryonic junction, (2011), In preparation, ADP-11-16/T738.
- [188] H. Ito and F. Gross, Isoscalar meson exchange currents and the deuteron form-factors, *Phys. Rev. Lett.* 71 (1993) 2555.
- [189] D. Berg et al., Radiative width of the ρ^- meson, *Phys. Rev. Lett.* 44 (1980) 706.
- [190] T. Draper et al., Electromagnetic form-factors of hadrons, *Nucl. Phys. Proc. Suppl.* 9 (1989) 175.

- [191] T. Draper, R.M. Woloshyn and K.F. Liu, Electromagnetic properties of nucleons from lattice QCD, *Phys. Lett. B* 234 (1990) 121.
- [192] J.N. Hedditch et al., Pseudoscalar and vector meson form factors from lattice QCD, *Phys. Rev. D* 75 (2007) 094504.